TECHNISCHE UNIVERSITÄT DRESDEN

In-depth Surface Studies of p-GaN:Cs Photocathodes by Combining *Ex-Situ* Analytical Methods with *In-Situ* X-Ray Photoelectron Spectroscopy

---

Dissertation

Zur Erlangung des akademischen Grades

Doctor rerum naturalium
(Dr. rer. nat.)

vorgelegt

dem Bereich Mathematik und Naturwissenschaften
der Technischen Universität Dresden

von

M. Sc. Jana Schaber
geboren am [redacted] in [redacted]

Tag der Einreichung: 25.11.2022
Tag der Verteidigung: 24.05.2023

Gutachter:
Prof. Dr. Nikolai Gaponik
Prof. Dr. Xin Jiang
Prof. Dr. Eike Brunner

Die Dissertation wurde in der Zeit von Juni 2018 bis November 2022 im Institut für Strahlenphysik (ELBE) am Helmholtz Zentrum Dresden Rossendorf angefertigt.

to my beloved grandparents

Abstract

The photocathode is one of the key components of particle accelerator facilities that provides electrons for experiments in many disciplines such as biomedicine, security imaging, and condensed matter physics. The requirements for the electron-emitting material, the so-called photocathode, are rather high because these materials should provide a high quantum efficiency, a low thermal emittance, a fast response, and a long operational lifetime. At present, none of the state-of-the-art photocathodes can fully meet all the desired requirements. Therefore, new materials that can be used as potential photocathodes are urgently needed for future developments in accelerator research.

Semiconductor photocathodes such as cesium telluride are the preferred materials in particle accelerators. These photocathodes provide high quantum efficiencies of above 10 %, making them highly attractive. The crystal growth of cesium telluride, as a compound semiconductor photocathode, requires the deposition of cesium and tellurium on a suitable substrate with an ideal chemical ratio, which seems elaborate and difficult to handle.

In contrast, III-V semiconductors, such as gallium arsenide and gallium nitride (GaN), represent another type of semiconductor photocathode. These commercially available semiconductors are already grown on a substrate and only require a thin film of cesium and optional oxygen to obtain a photocathode. An atomically clean surface is necessary to achieve a negative electron affinity surface, which is the main prerequisite for high quantum efficiency.

In this work, p-GaN grown on sapphire by metal-organic chemical vapor deposition was wet chemically cleaned and transferred into an ultra-high vacuum chamber, where it underwent a subsequent thermal cleaning. The cleaned p-GaN samples were activated with Cs to obtain p-GaN:Cs photocathodes and their performance was monitored with respect to their quality, especially concerning their quantum efficiency and storage lifetime.
The surface topography and morphology were examined *ex-situ* by atomic force microscopy and scanning electron microscopy in combination with energy dispersive X-ray spectroscopy.

The presence of oxygen during the sample handling and the temperature applied during the thermal cleaning significantly influenced the surface morphology and affected the quantum efficiency and lifetime. Atomic force microscope measurements confirmed the adsorption of oxygen when the freshly cleaned samples were exposed to air. Consequently, it is crucial to protect the p-GaN sample from exposure to air in the environment to avoid such oxidation. Thus, the cleaning process was carried out under dry nitrogen in a glovebox, and the p-GaN samples were further transported under a nitrogen atmosphere in a ultra-high vacuum chamber.

Treatments at different temperatures resulted in various quantum efficiency values and storage lifetimes. Moderate temperatures of 400–500 °C were found to be more beneficial for the p-GaN surface quality, which was reflected by achieving higher quantum efficiency values. After the thermal cleaning, the samples were activated with a thin layer of cesium at an average pressure of 1×10^{-9} mbar. The surface morphology was studied with scanning electron microscopy and energy dispersive X-ray spectroscopy after the samples were thermally cleaned and activated with cesium. The results showed that the surface appeared inhomogeneous when

the samples were cleaned at a high temperature above 600 °C. A thermal cleaning from the backside through the substrate represented another possibility but did not yield higher quantum efficiency values.

An *in-situ* analysis method facilitates following and understanding the changes in the surface electronic states before, during, and after any treatment of p-GaN:Cs photocathodes. For this purpose, an X-ray photoelectron spectrometer was applied that was built into an ultra-high vacuum system to prepare and characterize photocathodes. It allowed the *in-situ* monitoring of the photocathode surfaces beginning immediately after their cleaning and throughout the activation and degradation processes.

The realization of the adaption of an X-ray photoelectron spectroscopy chamber to the preparation chamber presented a significant constructional challenge. Thus, this work paid special attention to the technical aspects of *in-situ* sample transportation between these chambers without leaving the ultra-high vacuum environment.

The p-GaN surface was cleaned with different solutions and studied by X-ray photoelectron spectroscopy and atomic force microscopy, revealing that cleaning with a so-called "piranha" solution in combination with rinsing in ethanol works best for the p-GaN surface. A cleaning step that solely uses ethanol is also possible and represents a simple cleaning procedure that is manageable in all laboratories. Afterward, the cleaned p-GaN samples underwent a subsequential thermal vacuum cleaning at various temperatures to achieve an atomically clean surface. Each treatment step was followed by X-ray photoelectron spectroscopy analysis without leaving the ultra-high vacuum environment, revealing residual oxygen and carbon on the p-GaN surface. A thermal treatment under vacuum did not entirely remove these organic contaminations, although the thermal cleaning reduced their peak intensities. The remaining oxygen and carbon contaminants were assumed to be residuals derived from the metal-organic chemical vapor deposition process.

The complete removal of carbon and oxygen contaminants was only achieved by argon ion sputtering, which was accompanied by a strong depletion of the nitrogen atoms on the p-GaN surface. The treatments caused a large number of defects on the semiconductor surface, which was validated by *ex-situ* scanning electron microscopy, energy dispersive X-ray spectroscopy, and *in-situ* X-ray photoelectron spectroscopy. However, although a few atomic percentages of carbon and oxygen, representing undesired impurities from the metal-organic chemical vapor deposition, remained on the surface, p-GaN could still form a negative electron affinity surface when exclusively activated with cesium.

After the cesium activation, a shift toward a higher binding energy was observed in the X-ray photoelectron spectroscopy spectra of the related photoemission peaks. This shift indicated that the cesium was successfully adsorbed to the p-GaN surface. Before the cesium activation, adventitious carbon at a binding energy of approximately 284 eV was found, which was also present after the cesium activation but did not shift in its binding energy. It was also shown that the presence of remaining carbon significantly influenced the photocathode's quality. After the cesium deposition, a new carbon species at a higher binding energy (approximately 286 eV) appeared in the carbon 1s spectrum. This new species showed a higher binding energy than adventitious carbon and was identified as a cesium carbide species. This cesium carbide species grew over time, resulting in islands on the surface. The X-ray photoelectron spectroscopy data facilitated the elucidation of the critical role of this

cesium carbide species in photocathode degradation.

Residual photocurrents were measured after the samples were thermally cleaned before the next cesium activation. The X-ray photoelectron spectroscopy measurements revealed that the cesium was not entirely removed from the samples' surfaces. However, the remaining cesium seemed beneficial for the re-activations because higher quantum efficiency values were achieved than in the first activations.

Typically, the quantum efficiency of photocathodes decays exponentially. Conversely, an immense quantum efficiency loss was observed after the p-GaN:Cs photocathodes were studied by X-ray photoelectron spectroscopy. The origin of the quantum efficiency loss derived from X-rays as an external influence and was not caused by the sample's transportation. Therefore, potential X-ray damages to the p-GaN:Cs photocathodes were investigated. These experiments showed that the adsorbed cesium and its adhesion to the p-GaN surface were strongly influenced by X-ray irradiation. The cesium photoemission peaks shifted toward a lower binding energy, while the relative cesium concentration did not. This shift indicated that X-ray irradiation accelerated the external aging of the p-GaN photocathodes and thus it was proposed to use lower X-ray beam power or cool the samples to prevent X-ray damage to cesiated photocathodes.

Furthermore, the potential of applying p-GaN to other substrates such as silicon and titanium nitride as possible photocathodes was studied. The quantum efficiency values and storage lifetimes for p-GaN:Cs on silicon and titanium nitride were significantly shorter than those achieved for p-GaN:Cs on sapphire, which is related to the p-GaN crystal quality that is influenced by the substrate.

This work shows that an exclusive activation with cesium is feasible and that a re-activation of the same sample is possible. Quantum efficiency values of 1–12 % were achieved when the p-GaN, grown on sapphire, was activated. The capability of an X-ray photoelectron spectroscopy analysis allowed the *in-situ* monitoring of the photocathode surface and shed light on the surface compositions that changed during the photocathodes' degradation process.

Contents

1 Introduction **1**
- 1.1 Motivation . . . 2
- 1.2 ELBE SRF Gun II . . . 3
- 1.3 Goals of the Thesis . . . 5
- 1.4 Structure and Scope of the Thesis . . . 6

2 Theoretical Fundamentals I: Analytical Methods of Surface Characterization **9**
- 2.1 *In-Situ* X-ray Photoelectron Spectroscopy (XPS) . . . 9
  - 2.1.1 Working Principle and Scheme of *in-situ* XPS at HZDR . . . 9
  - 2.1.2 Options for Photoelectron Spectra . . . 10
  - 2.1.3 Surface Sensitivity and Quantification . . . 12
- 2.2 *Ex-situ* Surface Characterization Methods . . . 13
  - 2.2.1 Atomic Force Microscopy (AFM) . . . 13
  - 2.2.2 Scanning Electron Microscopy (SEM) . . . 15
  - 2.2.3 Energy Dispersive X-ray Spectroscopy (EDX) . . . 16

3 Theoretical Fundamentals II: Photocathodes **19**
- 3.1 Definition of Photocathode Properties . . . 19
  - 3.1.1 Photoemission Model and Quantum Efficiency . . . 19
  - 3.1.2 Storage Lifetime of Photocathodes . . . 23
  - 3.1.3 Electrical Conductivity . . . 23
- 3.2 Semiconductor Photocathodes . . . 25
  - 3.2.1 p-type Gallium Nitride (GaN) . . . 25
    - 3.2.1.1 Crystal Structure of p-GaN . . . 26
    - 3.2.1.2 Influence of the Substrate on the GaN Crystallinity . . . 27
    - 3.2.1.3 Band Structure and Surface Requirements . . . 28
    - 3.2.1.4 Performance as a Photocathode . . . 28
  - 3.2.2 p-type Gallium Arsenide (GaAs) . . . 29
  - 3.2.3 Cesium Telluride (Cs_2Te) . . . 33

4 Technical Aspects of the Realization of *In-Situ* XPS Capability **35**
- 4.1 Setup of Preparation Chamber and Challenges . . . 35
  - 4.1.1 Preparation Chamber with Ultra-High Vacuum . . . 35
  - 4.1.2 Thermal Cleaning and Temperature Measurement . . . 36
  - 4.1.3 Anode Drawbacks and Improvements . . . 37
  - 4.1.4 Ultraviolet Light Sources for Photoelectron Excitation . . . 38
  - 4.1.5 Sample Holder and Manipulator . . . 40
  - 4.1.6 Loading Chamber with Transportable Sample Suitcase . . . 41
  - 4.1.7 Software for Controlling the Preparation Process . . . 42
- 4.2 Introduction of *In-Situ* XPS Analysis . . . 43
  - 4.2.1 Adaption Challenges between Preparation and XPS Chambers 43
  - 4.2.2 Sample Transportation under Ultra-High Vacuum . . . 44
  - 4.2.3 XPS Sample Puck Modification . . . 45
- 4.3 Procedure for Ultra-High Vacuum Achievement . . . 46
  - 4.3.1 Preparation Chamber . . . 46

4.3.2 XPS Chamber . . . 47
4.4 Status-Quo . . . 47

5 Materials and Experimental Parameters 49
5.1 p-GaN . . . 49
5.1.1 Specifications of the Samples Used . . . 49
5.1.2 Wet Chemical Cleaning . . . 49
5.1.3 Thermal Cleaning . . . 50
5.1.4 Activation Process . . . 50
5.1.5 Re-activation Process . . . 51
5.2 Crystal Growth of Cs_2Te . . . 51
5.2.1 Preparation Chamber of Cs_2Te without Analytical Capabilities 51
5.2.2 Substrate Preparation . . . 52
5.2.3 Preparation of Cs_2Te . . . 52
5.3 Instrumental Parameters of the Analytical Methods . . . 55
5.3.1 *In-Situ* XPS . . . 55
5.3.2 *Ex-Situ* AFM . . . 55
5.3.3 *Ex-Situ* SEM/EDX . . . 55

6 Surface Characterization of p-GaN on Sapphire 57
6.1 Surface Analysis of As-received p-GaN Wafer . . . 57
6.2 Influence of the Wet Chemical Cleaning . . . 58
6.2.1 Surface Analysis after Solvent Cleaning . . . 58
6.2.2 Hydrofluoric Acid (HF) Cleaning . . . 59
6.2.3 "Piranha" Cleaning . . . 60
6.3 Influence of the Thermal Cleaning . . . 63
6.3.1 Surface Analysis after Halogen Lamp Irradiation . . . 63
6.3.2 Surface Analysis after Backside Heating . . . 64
6.3.3 QE Performance Depending on Surface Quality . . . 65
6.3.4 Storage Lifetime vs. Thermal Cleaning Temperature . . . 67
6.4 Influence of Argon Ion Irradiation . . . 68
6.4.1 On p-GaN Surface . . . 68
6.4.2 On p-GaN:Cs Photocathode Surface . . . 68
6.4.3 Surface Morphology after Thermal Cleaning, Argon Ion Irradiation and Activation . . . 70
6.5 Surface Analysis of the p-GaN Surface after Cesium Activation . . . 71
6.5.1 Spectral Response of the p-GaN:Cs Photocathode . . . 74
6.5.2 Surface Composition after YoYo Activation . . . 75
6.6 Degradation of p-GaN:Cs Photocathodes . . . 78
6.6.1 Influence of Surface Carbon on the QE Decay . . . 78
6.6.2 Surface Model of Cesium-Carbide Island Growth . . . 80
6.6.3 Influence of X-ray Irradiation . . . 81
6.7 Influence of Re-activations on the p-GaN Surface . . . 83
6.7.1 After Thermal Cleaning . . . 83
6.7.2 Influence of Cesium after the Re-activation . . . 84
6.7.3 Surface Morphology . . . 85

7 p-GaN:Cs Photocathode Performance on other Substrates 87
7.1 QE vs. Thermal Cleaning Temperature 88
7.2 Storage Lifetime of p-GaN:Cs Photocathodes on Si 90
7.3 Surface Morphology after Cleaning and Activation 91

8 Analytical Methods applied on other Photocathodes 93
8.1 Surface Characterization of GaAs Photocathodes 93
8.1.1 Surface Composition Depending on Cleaning Process 93
8.1.2 QE vs. Surface Conditions 95
8.1.3 Influence of Carbon Impurities on QE Decay 96
8.1.4 Surface Behavior in Re-activations 100
8.2 Surface Characterization of Cs_2Te Photocathodes 102
8.2.1 Surface Analysis of Cu Substrates 102
8.2.2 QE Performance of Cs_2Te during Operation in SRF Gun II . . 104
8.2.3 Analysis of the Degraded Cs_2Te Surface 105

9 Conclusions 111

10 Outlook 114

References 127

List of Figures 136

List of Tables 137

11 Acknowledgments 139

A Appendix I

List of Abbreviations

AFM atomic force microscopy

BE binding energy

BNL Brookhaven National Laboratory

BSE backscattered secondary electrons

CB conduction band

CBM conduction band minimum

DC direct current

DBR distributed Bragg reflector

DESY Deutsches Elektronen-Synchrotron

EA electron affinity

EAL effective attenuation length

EDX energy dispersive X-ray spectroscopy

ELBE electron linear accelerator with high brightness and low emittance

ERL energy recovery lines

ESP electron spin-polarization yield

FEL free-electron laser

HV high voltage

HVPE hydride vapor phase epitaxy

HZDR Helmholtz Zentrum Dresden Rossendorf

IE ionization energy

IMFP inelastic mean free path

INFN Istituto Nazionale di Fisica Nucleare

IR infrared

LED light-emitting diode

LMM electron transition between L- and M- shells

LN liquid nitrogen

MBE molecular beam epitaxy

MOCVD metal-organic chemical vapor deposition

MSE magnetron sputtering epitaxy

NEA negative electron affinity

NEG non-evaporable getter

NIR near infrared

PEA positive electron affinity

PSD position-sensitive photodetector

QE quantum efficiency

RF radio-frequency

RMS root mean square

SE secondary electrons

SEM scanning electron microscopy

SRF superconducting radio-frequency

SLAC Stanford Linear Accelerator Center

THz terahertz

UHV ultra-high vacuum

UV ultraviolet

VB valence band

VBM valence band minimum

WF work function

XPS X-ray photoelectron spectroscopy

XRD X-ray diffraction

List of Chemical Element Symbols and Formulae

Ag silver

Al aluminum

AlN aluminum nitride

Al_2O_3 sapphire

Ar argon

Ar^+ argon ion

As arsen

As_2O_3 arsen oxide

Au gold

B boron

C–OH hydroxyl

C=O carbonyl

C carbon

CH_4 methane

CH_3OH methanol

C_6H_6 benzol

C_3H_6O acetone

C_3H_8O iso-propanol

$C_6H_8O_7$ citric acid

Cp_2Mg bis-cyclopentadienyl magnesium

CO carbon monoxide

CO_2 carbon dioxide

Cs cesium

Cs_xC_y cesium carbide

Cs_2O_2 cesium peroxide

CsOH cesium hydroxide

Cs_2Te cesium telluride

Cu copper

EtOH ethanol

Fe iron

Ga gallium

GaAs gallium arsenide

GaN gallium nitride

$\mathbf{Ga}_x\mathbf{O}_y$ gallium oxide

$\mathbf{H}_2$ molecular hydrogen

$\mathbf{H}^+$ hydrogen ion

HCl hydrochloric acid

He helium

$\mathbf{He}^+$ helium ion

HF hydrofluoric acid

$\mathbf{H}_2\mathbf{O}$ water

$\mathbf{H}_2\mathbf{O}_2$ hydrogen peroxide

$\mathbf{H}_2\mathbf{SO}_4$ sulfuric acid

In indium

Mg magnesium

$\mathbf{MgAl}_2\mathbf{O}_4$ spinel

Mo molybdenum

N nitrogen

$\mathbf{N}_2$ molecular nitrogen

Nb niobium

$\mathbf{NF}_3$ nitrogen tri-fluoride

$\mathbf{NH}_3$ ammonia

O oxygen

$\mathbf{O}_2$ molecular oxygen

$\mathbf{O}_2^{2-}$ peroxide ion

$\mathbf{O}_3$ ozon

P phosphorous

Pb lead

Si silicon

SiC silicon carbide

SiN silicon nitride

Te tellurium

TeO_2 tellurium oxide

TeO_3 tellurium trioxide

TiN titanium nitride

TMG trimethylgallium

Zn zinc

1 Introduction

Electron sources are the key components in modern technologies such as microscopes [1–3], radio transmitters, and X-ray tubes for medical diagnostic devices [4]. Electron sources are also used in accelerator-based light sources that have a wide range of applications in biomedicine, security imaging, and condensed matter physics. The improvement of the existing electron sources is directly linked to the increased demand for higher electron currents, higher repetition rates, or high-brightness beams. These requirements for accelerator-based light sources, such as free-electron laser (FEL) and terahertz (THz), can be provided by an essential material, namely a so-called photocathode. The quality of all of the applications outlined above relies on the photocathode's performance. Great demands are placed on these photocathodes because they should provide a high quantum efficiency (QE), a low thermal emittance, a fast response, and a long operational lifetime. Apart from these basic requirements, the choice of a suitable cathode as a high-brightness electron source depends on many additional factors, and, at present, none of the existing state-of-the-art photocathodes can fulfill all of the desired requirements [5]. Therefore, new materials that can be used as potential photocathodes are urgently needed for future developments in particle accelerator research.

Metal cathodes such as copper (Cu), magnesium (Mg), and lead (Pb) were the first cathodes used in electron injectors in particle accelerators. They are the photocathodes of choice for the commissioning of a new electron source because their preparation is simple and they work robustly. However, they are not able to provide high QEs. In contrast, semiconductor photocathodes, such as cesium telluride (Cs_2Te) offer more advantages, such as higher QE and lower thermal emittance than pure metal photocathodes [6–8]. Cs_2Te could provide QE values between 5–20 %, a long lifetime, and low thermal emittance. However, this photocathode type is very sensitive to any kind of vacuum instability. Thus, the search for new materials with better photo-emitting properties led to the promising field of III-V semiconductor photocathodes [9, 10].

III-V nitride semiconductors are in high demand in many application fields and have garnered increasing interest, especially since the Nobel Prize was awarded for developing the gallium nitride (GaN) light-emitting diode (LED) in 2014 [11]. Since then, III-V semiconductors have been widely used in ultraviolet (UV) detectors and LEDs [11].

As a potential photocathode, p-type III-V semiconductors have the extraordinary ability to form a negative electron affinity (NEA) surface when they are activated with a thin layer of alkali metal, such as cesium (Cs) [12, 13]. The Cs on the semiconductor surface introduces a band-bending, while a high p-doping (e.g., Mg or zinc (Zn)) of the semiconductor is also beneficial as the photoelectrons can overcome the energy barrier and enter into the vacuum more easily [14, 15].

One important III-V semiconductor photocathode is gallium arsenide (GaAs), which is already established as a spin-polarized electron source in direct current (DC) particle accelerators for many years [16–18]. The activation of GaAs photocathodes is special as they are activated in a so-called YoYo process, where molecular oxygen (O_2) and Cs are alternately applied several times until a maximum photocurrent is achieved [19, 20]. GaAs photocathodes are extremely sensitive to residual vacuum gases and have a short lifetime of only several hundred hours [18, 21, 22].

GaN is another important III-V semiconductor that can possibly be used as a photocathode. It promises to be more robust [23] and it can potentially achieve extremely high QE values of approximately 70 % [24]. With its wide band gap of 3.4 eV (360 nm) a slight relief of the excitation laser is possible, while other photocathodes, such as Cs_2Te, mostly require more energetic UV-light at 260 nm. Therefore, p-GaN shows great potential to become a new electron source. Because the treatment with O_2 should not necessarily be involved in the activation of p-GaN:Cs photocathodes, the activation of p-GaN is easier than that of GaAs photocathodes [15, 25, 26].

The most important requirement for achieving the NEA surface and thus a high QE is an atomically clean surface, which is an important factor for all semiconductor photocathodes [27–29]. Detailed surface characterizations need to be performed which will help to determine these surface conditions and their QE dependence so that GaN can be used as an electron source in the future.

1.1 Motivation

The electron linear accelerator with high brightness and low emittance (ELBE) superconducting radio-frequency (SRF) Gun II at the Helmholtz Zentrum Dresden Rossendorf (HZDR) is a continuous wave multi-purpose radiation source that is used for various international research projects. The electron beam is used by many researchers around the world from medicine, materials science, physics, or chemistry for their experiments. Therefore, the continuous improvement of the ELBE SRF Gun II is of great interest to the user community [30–33].

The currently used photocathodes for the SRF Gun II are Mg and Cs_2Te. The Mg photocathode is easy to prepare but it cannot provide a high QE. In contrast, Cs_2Te is the preferred cathode in the SRF Gun II because it provides a higher QE and can be used for the generation of medium beam currents. The Cs_2Te photocathode can be operated for several months in the SRF Gun II but loses its QE during the operation under a radio-frequency (RF) field. The photoemissive Cs_2Te layer that is deposited on a Cu substrate is sensitive to any residual gas that will cause a surface change. Thus, the Cs_2Te layer is very sensitive to any vacuum instabilities. The strong desire for higher beam currents from a more robust photocathode leads to the research field of III-V semiconductors as potential novel photocathodes. The idea to use GaN as a potential electron source gained increasing interest in recent years. Preliminary studies on the photoemission surface properties have to be carried out to help determine the potential use of GaN as an electron source. At HZDR, there are no analytical capabilities for a detailed surface study on photocathodes, and especially no *in-situ* analysis method exists. In the last 20 years, Mg and Cs_2Te photocathodes were applied but neither had been characterized in terms of their surface qualities nor in their chemical surface composition. The photocathode performance and the degradation are hardly understandable without a reliable *in-situ* analytical method. So far, only assumptions have been made concerning the photocathode surfaces. Significantly, *ex-situ* methods are not suitable for examine air-sensitive materials because the surface oxidizes on exposure to the air in the environment. The extension of a ultra-high vacuum (UHV) preparation chamber with an *in-situ* analytical chamber is thus necessary to realize the analytical research for photocathodes at HZDR whereby the material surface is studied in its chemical composition and every surface change is observable without leaving the essential

vacuum environment. The capability of using such an *in-situ* analytical method helps to improve surface treatments with the effect of pushing the application of p-GaN photocathodes toward the future.

1.2 ELBE SRF Gun II

Electron sources for accelerator facilities can be distinguished into two different injector types, according to the field applied to the cathode [7, 34–37]. One type uses the application of a DC electric field between the cathode and anode. Depending on the DC voltage applied, the electrons gain energies between 100–500 keV, although they cannot be accelerated to relativistic energies.
Instead of a DC field, an RF field can be applied, in which the cathode is surrounded by a specially shaped cavity.

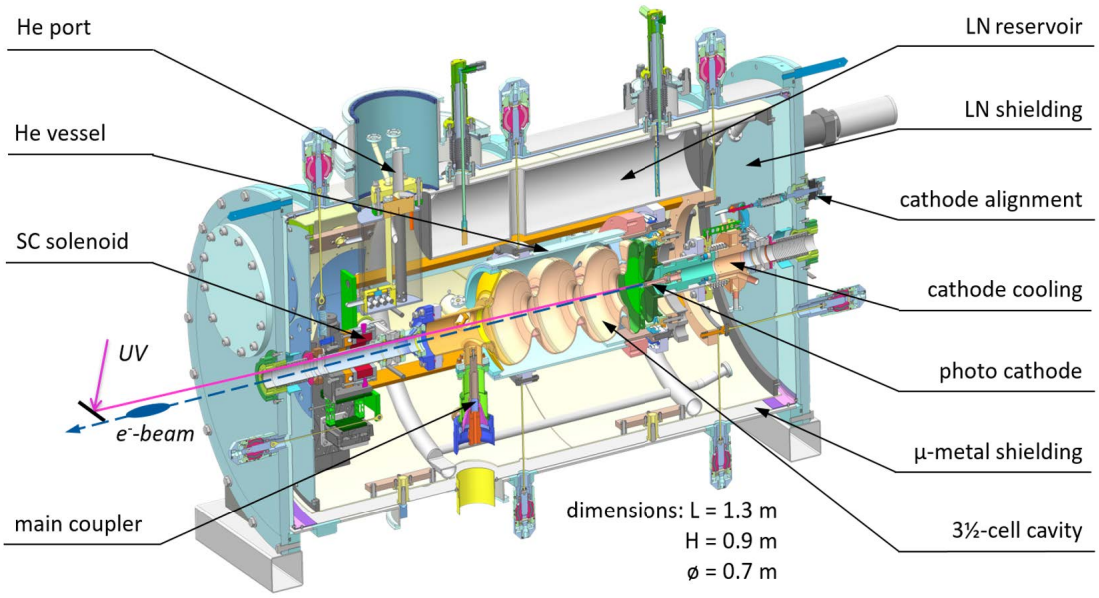

Fig. 1 3D model of the ELBE SRF Gun II at HZDR showing the incident UV laser pathway (violet) hitting the photocathode in the back wall that ejects electrons. The electrons are subsequently accelerated downstream (blue).

The SRF injector is a special type of RF injector that contains a niobium (Nb) resonance cavity that turns into a superconducting state below a critical temperatures. The cavity is therefore surrounded by a cryostat system and cooled down to 2 K with liquid helium (He) [30, 33].

Figure 1 shows a 3D model of the ELBE SRF Gun II. The core of the gun is a 3.5 cell fine grain Nb cavity to which a 1.3 GHz RF field can be applied [38, 39]. The cathode is placed in the cavity back wall and cooled with liquid nitrogen (LN), and thus it operates at 77 K [30, 33]. For the generation of photoelectrons from the cathode, an energy source is required to excite electrons above the work function (WF). The necessary energy can be supplied thermally with either an electric field or photons. Thermionic emission and field emission are mature methods and work robustly [40]. However, the photoemission offers more advantages than these mature methods because the electron bunches can be accurately time structured. In the

ELBE SRF Gun II, a UV laser (258 nm) illuminates the cathode surface to produce an initial electron bunch. The maximum power of the laser is approximately 400 mW, and works at 13 MHz with a pulse length of 2.4 ps.

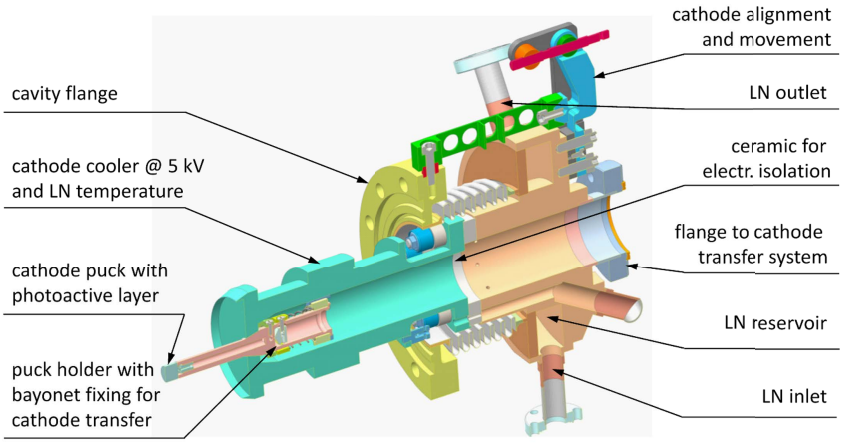

Fig. 2 3D model of the photocathode inside the SRF Gun II, showing its cooling system with a LN supply [33].

In the ELBE SRF Gun II, the cathode is mounted on a Cu cathode body which is externally cooled with LN [41]. Figure 2 shows the photocathode Cu body including its bayonet holder that is used for its transportation. The cathode plug is located at the front of the cathode body and is made of Mg or Cu onto which the Cs_2Te is deposited as a photoemissive layer.

As mentioned, Mg photocathodes were used in the SRF Gun II in the past but due to their low QE, they were replaced by Cs_2Te [40–42]. Cs_2Te is the photocathode of choice as it is able to provide a QE of over 1 % after it was transported into the SRF Gun II, and can be used in operation for several months [42].

The superconducting cavity is very sensitive to any contamination, which means that the right choice of photocathode is highly relevant. The potential release of photocathode compounds into the cavity, especially from semiconductor photocathodes, is a possible risk. Thus, the prevention of a potential overheating of the photocathode is a technical challenge. Laser irradiation and RF dissipation are possible reasons for an overheating that can be prevented by a proper thermal contact and a cooling with LN of the photocathode.

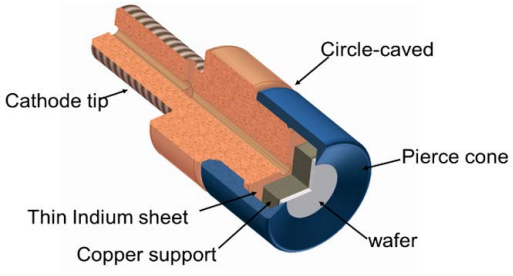

Fig. 3 Specialized 3D model for the adaption of p-GaN semiconductor photocathodes onto the SRF Gun II Cu body with the help of a Cu support, pierce cone and In sheet.

The improvement of the SRF Gun II and its beam quality is connected to the improvement of the photoemission properties such as a higher QE and a lower

thermal emittance. Thus, photocathode research is always being pushed forward. On the one hand, it is possible to improve the existing cathodes, while on the other hand, investigations to identify novel photoemissive materials can be conducted. Other semiconductor photocathodes such as GaAs and GaN show great potential and suitability to be tested for high current applications in the future [40]. To adapt the next generation of photocathode materials in the ELBE SRF Gun II, a special plug system combining the semiconductor with the cathode plug was developed, as shown in Figure 3. The semiconductor is surrounded by a pierce cone and contacted with the Cu body by an indium (In) sheet. Thus, a proper thermal contact to the Cu cathode body is guaranteed. The plug including the semiconductor can be screwed onto the Cu body with a bayonet holder and transported into the SRF Gun II.

1.3 Goals of the Thesis

A home-built photocathode preparation chamber that has a UHV environment was commissioned and systematically improved to always ensure the best conditions for photocathode research. An *in-situ* analytical method that measures the p-GaN surfaces after each treatment step was highly desirable to understand the photocathode processes. This *in-situ* method enables the traceability of the changes in the semiconductor surface in its chemical composition which affects the photocathode's properties.

This thesis describes different cleaning processes and their influence on a successful formation of an NEA surface to obtain a p-GaN:Cs photocathode. The photocathodes that were produced were characterized according to their photoemission properties such as QE and storage lifetime. Furthermore, the samples were characterized by *ex-situ* analytical tools such as atomic force microscopy (AFM), scanning electron microscopy (SEM), and energy dispersive X-ray spectroscopy (EDX). The surface changed during the transportation under air and, consequently, the "real" surface as it would be under UHV conditions, could not be characterized.

One of the main goals of this work was to establish a suitable surface characterization method that could be adapted to a UHV preparation chamber, so that the samples are measured and constantly kept in a UHV environment. A refurbished X-ray photoelectron spectroscope, operating under UHV conditions, was the solution to this aspect. It is worth noting that the adaption and sample transportation between the two UHV chambers (preparation and X-ray photoelectron spectroscopy (XPS) chamber) was very challenging and thus this work pays special attention to describing how to cope with this constructional challenge. Vacuum sample transportation followed by XPS measurements of the photocathodes were enabled by the successful adaption of the XPS chamber to the preparation chamber. Therefore, the research on semiconductor photocathodes at HZDR reached a milestone with the newly acquired ability to trace the photocathodes' surface changes and thus the degradation from an analytical point of view.

A detailed study of the p-GaN:Cs photocathode surface and its quality was realized with the help of the new *in-situ* XPS system. Therefore, another goal of this thesis involved gaining insights into the treatments and their effects on the p-GaN surface, which helped to continuously improve these treatments. Special attention was paid to the surface study to understand the degradation mechanism of this new type of p-GaN:Cs photocathode.

1.4 Structure and Scope of the Thesis

This thesis is an inter-disciplinary work that combines chemistry, physics, material science, and engineering. It deals with analytical methods that are used for photocathode characterization, separated into *in-situ* and *ex-situ* methods. The theoretical fundamentals for both analytical methods are provided in Section 2, while Section 3 introduces the photocathodes as subjects that can be analyzed and characterized by applying them. The thesis hereby describes the basic theory of photoemission and focuses on those materials that are later also relevant as potential photocathodes, especially semiconductor materials. Metal photocathodes are only mentioned briefly because they are not such promising candidates for future electron sources as the semiconductor ones.

The *in-situ* XPS connected to the preparation chamber – with all its challenges and difficulties – is discussed in detail in Section 4. The adaption of the XPS chamber to the preparation chamber represents the key component of this work, while the *ex-situ* methods such as SEM and AFM were used as alternative methods as long as *in-situ* XPS measurements were not yet available.

The thesis focusses on p-GaN on sapphire as a potential photocathode, which is presented and discussed in Section 6. The p-GaN:Cs photocathodes are studied in terms of their surface properties and compared regarding their surface cleaning process. A series of p-GaN:Cs photocathodes were compared concerning their QE, storage lifetimes, and surface qualities. However, the lifetime and thus QE decay was not measured for each sample until the QE vanished entirely because it is not feasible within a limited working time. For most of the samples, an extrapolation of the lifetime was feasible to estimate the "real" storage lifetime. Furthermore, a few YoYo activations were carried out, but they play a minor role because an activation with Cs alone is more practical.

The Mg concentration, related to the carrier concentration, also has a significant impact on the photocathode performance but a comparison in different carrier concentrations would have exceeded the scope of this thesis. The industrial suppliers are mostly not able to provide low quantities of p-GaN samples with the desired Mg concentrations.

No studies were conducted on cooled p-GaN photocathodes as they would be used in the SRF Gun II because the ability to cool the p-GaN sample was determined by the improvement of a preparation chamber during the thesis and the measurements would have exceeded the time available for completion. The Cs activation and QE measurements were therefore always carried out at room temperature.

A comparison of p-GaN grown by other methods than metal-organic chemical vapor deposition (MOCVD) and thus a comparison of different p-GaN qualities from different suppliers is not covered by this thesis. Besides sapphire, some experiments were also done on p-GaN on silicon (Si) or titanium nitride (TiN) in Section 7 but this can be regarded as a potential outlook for future research. Section 8 deals with the surface characterization of GaAs and Cs_2Te photocathodes which are regarded as comparable materials to p-GaN.

Section 8.1 highlights the difficulties involved in GaAs preparation and activation. The GaAs photocathode degradation is subsequently studied with *in-situ* XPS measurements.

Section 8.2 deals with Cs_2Te that is used in the ELBE SRF Gun II, which is described in its crystal growth process and studied after its degradation with *ex-situ*

methods. Additionally, the Cs_2Te photocathodes were inserted into the XPS chamber but showed an oxidized surface because the surface was exposed to air.

2 Theoretical Fundamentals I: Analytical Methods of Surface Characterization

2.1 *In-Situ* X-ray Photoelectron Spectroscopy (XPS)

2.1.1 Working Principle and Scheme of *in-situ* XPS at HZDR

The principle of XPS involves the irradiation of a sample in a vacuum with soft X-rays and the analysis of the emitted electrons depending on their energy. The spectrum obtained is a plot of electron counts versus their kinetic energy (E_{kin}). XPS analysis is a surface-sensitive method because the incident photons, usually from an X-ray dual anode of Mg or aluminum (Al), penetrate a few μm into the solid and interact with the solid's atoms. The emitted electrons have a limited inelastic mean free path (IMFP) of only several nm and thus the detected electrons originate from the top surface layers [43–47].
Kai Siegbahn used Einstein's idea of the photoelectric effect of the conversion from light into energy quanta for his photoelectron spectroscopy studies. He showed that the E_{kin} of the electrons depend on the binding energy (E_{B}) when the material is irradiated with X-rays as seen in Equation 1. He investigated the variation of the E_{kin} depending on the X-ray energy and was able to distinguish whether electrons derive from the core levels or outer valence orbitals. His studies comprise the first milestone of XPS development [44, 45].

$$E_{\mathrm{kin}} = h \cdot v - E_{\mathrm{B}} - \phi \tag{1}$$

The binding energy (BE) is regarded as the energy difference between the initial and final states after a photoelectron has left the atom. For this reason, each element has a unique set of BEs. Auger and fluorescence are competing processes that occur in parallel to the photoemission process. Fluorescence, which is commonly used for EDX analysis, only represents a minor process and is preferred in lighter elements ($Z = 30$) [45, 48].

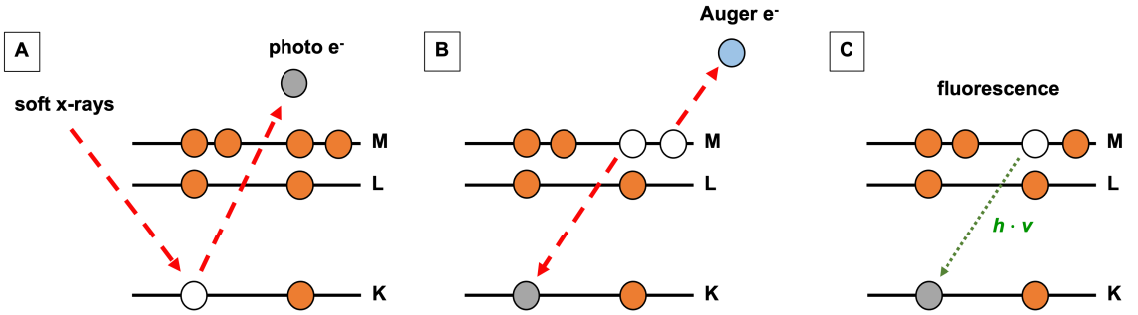

Fig. 4 Schematic of different processes including a) X-ray photoemission, and subsequent relaxation by b) Auger electron emission, and c) fluorescence.

An Auger electron is released when an inner electron fills up a vacancy and consequently a secondary electron is emitted that carries the excess energy. As a consequence, in most cases, photoionization leads to the emission of two electrons, one photoelectron and one Auger electron [44, 45, 47]. The incident source for the

generation of Auger electrons usually comprises primary electrons from an electron beam and not X-ray photons. The three processes are illustrated in Figure 4.

XPS experiments are carried out using an electron spectrometer that works at an average pressure of 5.3×10^{-9} mbar. A PHI Model 5600 as a multi-technique system is shown as a scheme on the left side of Figure 5, which illustrates the major components (1 = hemispherical analyzer, 2 = X-ray source, and 3 = argon ion gun) [43].

The XPS chamber at HZDR is not equipped with a monochromator. The XPS system is generally delivered as a stand-alone system which means that the supplier set-up is in place and and all the parts are calibrated. The XPS chamber was connected together with the supplier to our existing UHV preparation chamber for photocathodes, as shown on the right side of Figure 5. This ensures an *in-situ* sample transport and surface characterization measurement without leaving UHV conditions.

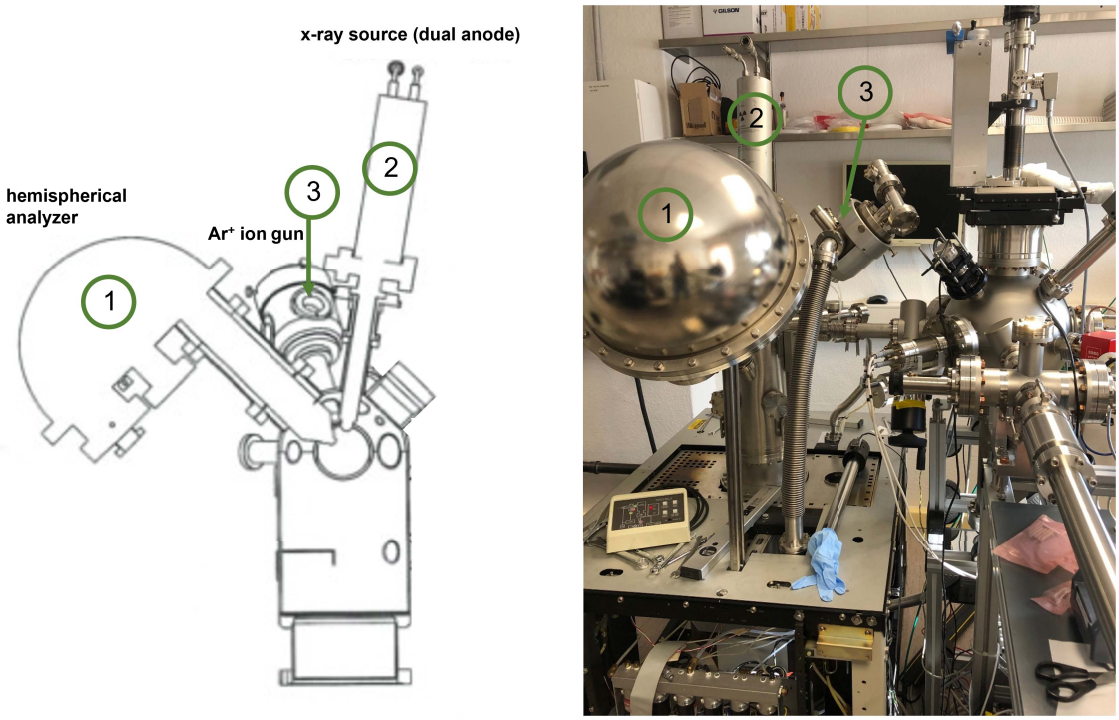

Fig. 5 Drawing of a PHI 5600 XPS spectrometer taken from [43] but without X-ray monochromator (left side). A photo of the adapted XPS chamber, connected to the UHV preparation chamber at HZDR (right side).

2.1.2 Options for Photoelectron Spectra

The photoelectron spectrum represents the shell structure of the atomic electrons of the specimen and thus the XPS spectrum can be displayed in E_B or E_{kin} on the x-axis [45, 49]. It shows discrete peaks that derive from photoelectrons ejected from atoms in the solid. The photoelectrons were able to escape the solid surface without an energy loss. Photoelectrons from valence band levels are located at a BE close to 0, while photoelectron peaks from core levels and Auger electrons appear at higher BEs. Auger transitions appear from the de-excitation of core holes from photoemission and lead to a series of Auger peaks. The overlap between Auger and

photoemission peaks usually results in a more challenging evaluation of the XPS spectra. The Auger positions can be varied when the BE scale is plotted and the excitation energy is changed, which can subsequently solve the overlap problem.

The peaks are located on a background that increases with increasing BE. This step-like increase of the background is caused by extrinsic inelastically scattering events which means that the photoelectrons lose some energy on their way to the analyzer [44, 45, 47, 50]. The survey spectrum is often used for elemental analysis and contains the qualitative information of an element. An example of a survey and detailed spectrum is shown in Figure 6.

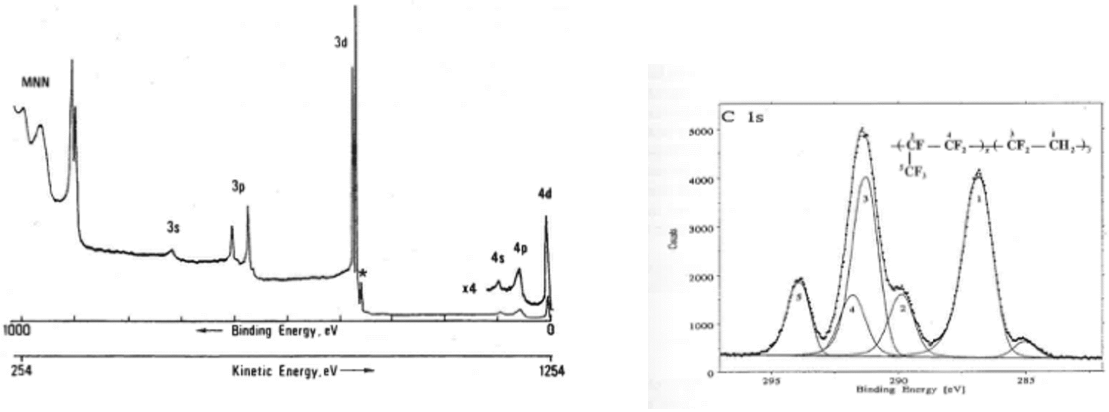

Fig. 6 X-ray photoelectron spectrum (survey spectrum) of silver (Ag) showing an increasing background (left) and an X-ray photoelectron spectrum (detailed spectrum) of the carbon (C) 1s peak of a polymer (right), showing the influence of electronegativity on the BE ("chemical shift") [45].

Furthermore, the BE gives information about the chemical state because the BE is influenced by the chemical environment. The atom is regarded as an electron sphere that carries a certain electron density. Any influence from the outside environment on this electron density can be followed in the BE. For example, the BE increases when the adjacent atom is more electronegative. Therefore, the BE is also called a "chemical shift" [45].
In contrast, a detailed spectrum of a photoelectron peak is used for deriving quantitative information. The quantification relies on many different factors such as the surface roughness, spectrometer used, cross-sections made, and many more [45, 47, 51]. A simple relationship to describe this process is shown in Equation 2 whereby the largest contribution to errors results from the assumption of the homogenous in-depth distribution of the atoms that depends on the peak intensity. If the solid is homogenous to a depth of several nm, the surface concentration would be proportional to the peak intensities. Significantly, the samples are often inhomogeneous and thus the quantification should be always performed with careful considerations [45, 52].

$$I_{\mathrm{A}} = \int \sigma_{\mathrm{A}} \cdot n_{\mathrm{A}} \cdot k \cdot F_{hv} \cdot e^{-\left(\frac{z}{\lambda_{\mathrm{A}} \cdot \cos\theta}\right)} dz \tag{2}$$

In the equation, I_{A} is the intensity of the photoemission peak of substance A, σ_{A} represents the effective cross-section, and n_{A} is the density of A. Furthermore, k is the instrumental factor which includes, for example, the solid angle, detection

sensitivity, illuminated area, and other instrument-specific factors. $F_{h\nu}$ represents the flux of photons, λ_A represents the IMFP for sample A, and θ is the emission angle.

2.1.3 Surface Sensitivity and Quantification

The surface sensitivity of XPS measurements greatly depends on several factors but mostly on the ability of the photoelectron to travel to the surface. The sensitivity depends on the attenuation of electrons because they interact with matter stronger than photons and therefore electrons do not travel very long distances. In general, the photoelectrons are generated at a depth of 5–30 Å, which means a few atomic layers. The surface sensitivity is element-specific but can be influenced by the incident photon energy because the IMFP increases with higher photon energy. Therefore, the photoelectrons carry larger E_{kin} and have a higher probability to pass through the material and move toward the surface. Furthermore, the surface sensitivity is enhanced by the angle of emission (θ). For angles of approximately 70° (in relation to the surface) the IMFP is about three times higher than those for angles at 0° [43, 45, 47, 51]. Most XPS measurements are thus performed at a higher angle to be more sensitive to the surface. An overview of the attenuation length that depends on the element and the electron energy is shown in Figure 7.

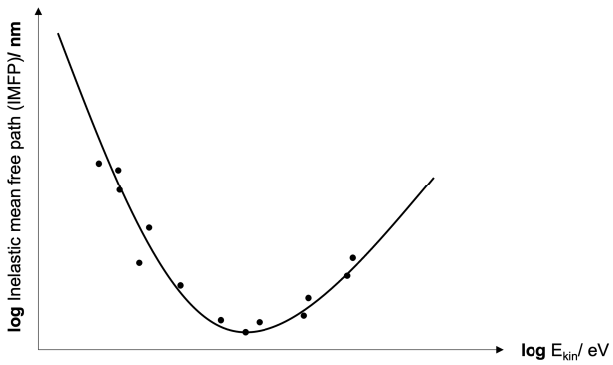

Fig. 7 Illustration of the IMFP of photoelectrons as a function of E_{kin} (also known as "universal curve").

The peak intensity is derived from the probability of an electron and its ability to leave the solid surface without an energy loss. Therefore, the origin of the photoelectrons including their attenuation during their travel to the surface must be considered in the peak intensity for a reliable quantification. The peak intensities I_z are exponentially attenuated with the excitation depth z [45, 51]. This relation obeys the Lambert-Beer law as shown in Equation 3:

$$I_z(z) = I_0 \cdot e^{-\left(\frac{z}{\lambda_i \cdot \sin\theta}\right)} \tag{3}$$

I_z means the intensity of the atoms at a depth z, while I_0 represents the intensity of the atoms at the surface. λ_i is the IMFP and θ represents the angle of emission. The IMFP is the average distance that an electron with a certain energy can travel until inelastic collision occurs. Inelastic scattering was long believed to be responsible for the electron attenuation. However, newer models also take elastic scattering

and non-exponential attenuation into account and thus λ_i can be replaced by the effective attenuation length (EAL) [45].

2.2 *Ex-situ* Surface Characterization Methods

2.2.1 Atomic Force Microscopy (AFM)

AFM is a non-destructive method and a powerful tool to study the topography of a specimen. The crystal growth and crystal lattice defects of III-nitride semiconductors can be determined by AFM which helps to reveal dislocations within the grown GaN layers.

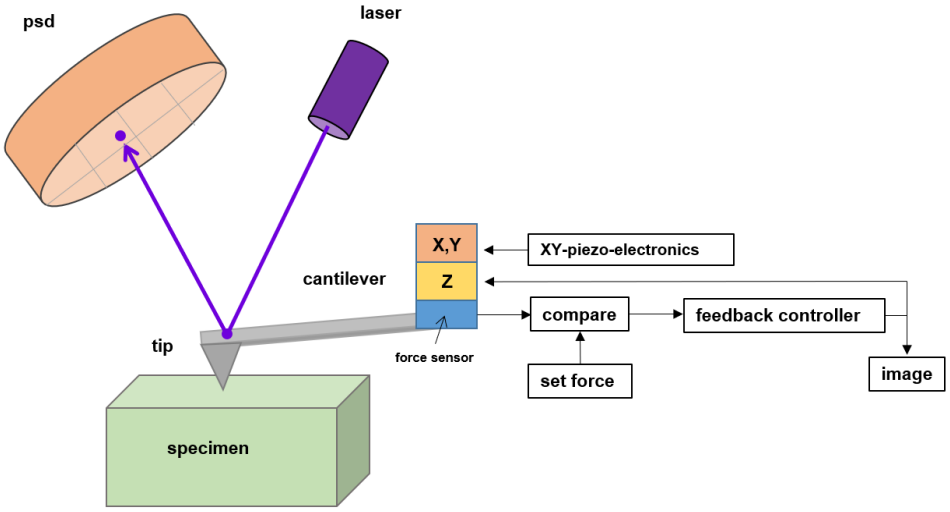

Fig. 8 Drawing of the major components needed for AFM measurements which illustrate the AFM working principle.

The basic principle of AFM imaging relies on optical feedback while a sharp tip scans the specimen surface in a raster pattern [53, 54]. A scheme of the basic components is illustrated in Figure 8. The sharp tip is located at the end of a cantilever which is illuminated by a laser on its back end. The laser deflection is detected via a position-sensitive photodetector (PSD) and changes depending on the surface height of the specimen. The position of the cantilever is controlled by a feedback loop to keep a constant interaction force between the specimens.

AFM microscopy can be carried out in three different modes (contact, non-contact, or tapping mode). The mode defines the force that is dominant between the tip and the specimen, as depicted in a Lennard Jones curve in Figure 9 [53]. The attracted forces are dominant when the tip is approaching the specimen surface and with a further approach, a mix of attractive and repulsive forces appear (tapping mode). In the tapping mode, the cantilever oscillates by a piezoelectric attenuator near its resonance frequency of several kHz. The tip is lowered until it slightly touches the surface, and the oscillation amplitude is dampened. A constant oscillation amplitude is maintained during the measurements. The non-contact mode is present if the tip locates in the minimum of the Lennard-Jones potential whereas, in contrast, the contact mode only represents the repulsive forces when the tip is in close contact with the sample surface [54, 55].

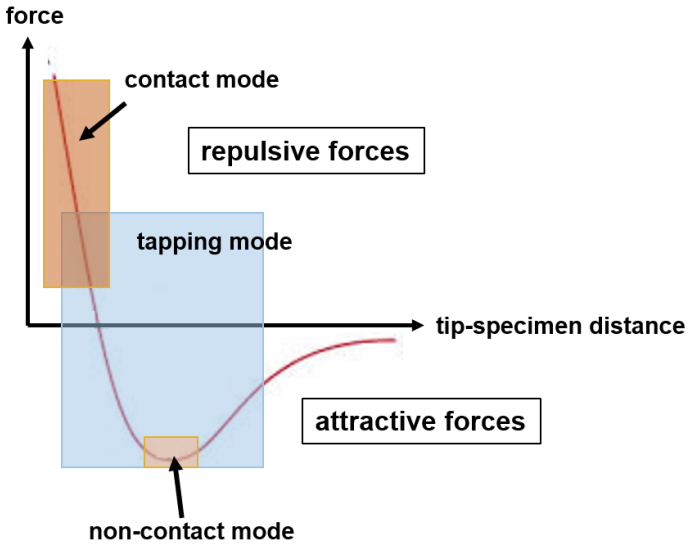

Fig. 9 Schematic of the three common AFM modes regarding to the interacting forces between the tip and the sample surface (Lennard-Jones potential).

The AFM technique relies on mechanical imaging which is untypical as other microscopes rely on electromagnetic radiation. As mentioned, the topography of a specimen is measured three-dimensionally with a sharp tip whereby the tip is positioned near the specimen's surface and moves across it. A reconstruction of the surface is rebuilt by the precise monitoring of the motion of the tip. Specimen areas of less than $100\,\mu m^2$ and less than $20\,\mu m$ in height can be measured precisely [55]. AFM is the method of choice for flat samples to study the surface's mechanical properties. Its resolution situates on that of the atomic scale. Artifacts, such as repeating patterns, vibrations, and scanner and probe artifacts might occur and disturb the resolution. The most common artifact is the probe artifact in which the surface features appear too large or too small because the tip is not able to raster the features precisely [53]. Hence, the tip must be as sharp as possible to avoid these types of artifacts. However, the AFM image always represents a mix of the tip and the real topography.

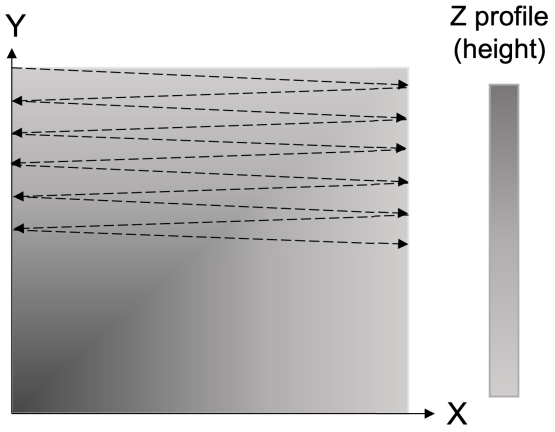

Fig. 10 Schematic of the cantilever movement with the tip to generate an AFM image.

For the generation of an image by AFM, a feedback controller with piezoelectric

elements controls the z-direction of the tip, as shown in Figure 10. The piezoelectric element sets the motion in the x and y directions but only allows a motion in the z-direction. When the force sensor detects a decreasing or increasing force, the piezoelectric element moves the tip up and down. In the tapping mode, the feedback loop maintains a constant oscillation amplitude and the detector measures the amplitude signal. If the amplitude or frequency is maintained constantly, the non-contact mode is preferred. The contact mode represents the extraordinary mode in which a constant cantilever deflection is maintained.

2.2.2 Scanning Electron Microscopy (SEM)

The fundamental principle of SEM is to create an image of a specimen surface while it is scanned with an electron beam of several keV. These microscopes use an electron-optical system of electromagnetic and electrostatic lenses to generate a fine electron beam on the sample, which is guided over the rectangular sample area to be examined [48]. The image is formed by the synchronous registration of electrons that interacted with the primary electron beam. During the scanning process, two main types of electrons are created due to interactions with the primary beam. The bulk of these electrons is secondary electrons (SE) with an energy lower than 50 eV, which are detected by an Everhart-Thornley detector [48, 53]. The SE are produced by interacting with the atoms of the sample and serve as the most frequently used source of information. Due to their low energy, they originate from the uppermost nanometers of the surface. Elements with a higher electron density interact more with the incident primary beam and thus more SE are created.

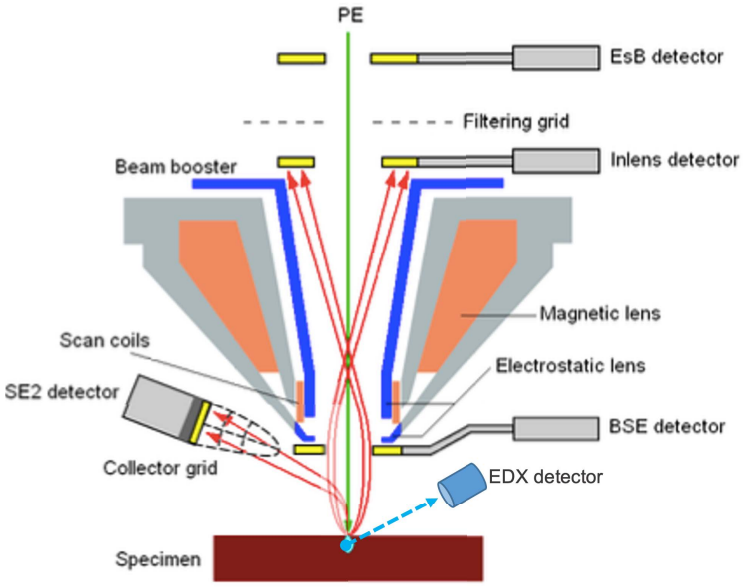

Fig. 11 Illustration of a typical SEM setup, showing the pathways of secondary electrons and backscattered electrons (red lines) compared to the pathway of X-rays for EDX detection (blue lines); the image was taken from [48].

The second type of electrons that are generated is backscattered secondary electrons (BSE), which are used for the second-most common imaging technique [48, 53]. These electrons are, as the name suggests, backscattered from the sample and carry energies of more than 50 eV. In Figure 12, the comparison between the SE

and BSE is illustrated more clearly. The intensity of the signal primarily depends on the average atomic number of the material, whereby heavy elements provide a stronger backscattering so that corresponding areas appear brighter. Areas with lighter elements, on the other hand, appear darker. The BSE image can be seen as a material contrast image and allows conclusions about the chemical nature of the sample material to be drawn [48]. The setup with both imaging methods is illustrated in Figure 11. The SE detector is located laterally to the chamber wall and thus the sample is always observed from the side. Due to this spatial arrangement, the images always yield good topographic information of the surface because the inelastic scattered electrons are detected. The SE detector is thus a good choice for measuring the chemical composition of the specimen surface.
The in-lens detector observes the sample from the top and thus the topographic information plays a minor role here. However, the in-lens detector is the detector of choice for the detection of material contrast as it registers the elastic BSE derived from the deeper layers inside the sample.

2.2.3 Energy Dispersive X-ray Spectroscopy (EDX)

EDX is a commonly and widely applied method that is used in combination with the SEM. Characteristic X-rays originating from fluorescence processes are used to characterize the elemental composition of a specific sample area. The characteristic X-rays derive from deeper bulk layers (up to 1 μm) and thus EDX does not represent a surface-sensitive method [48, 53].

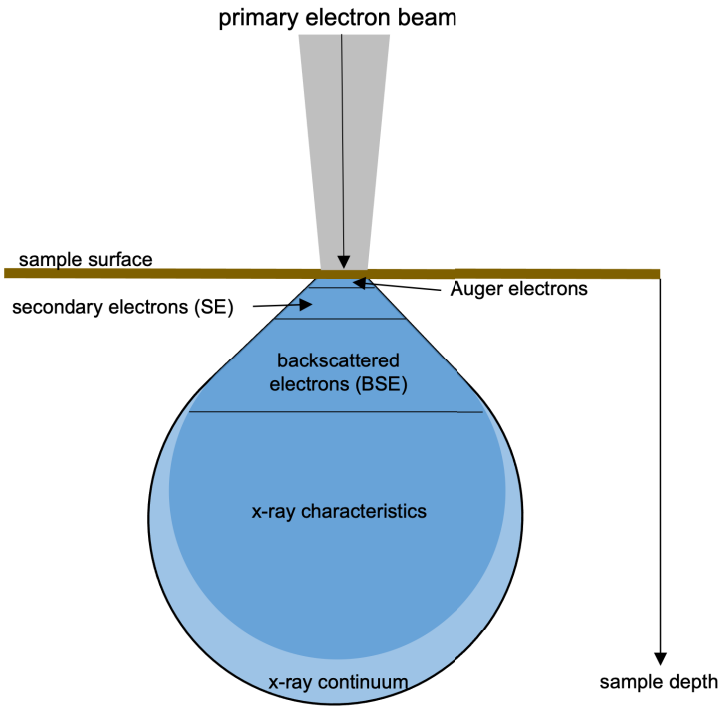

Fig. 12 Schematic of excitation depths of SE, BSE and X-rays inside a specimen.

Fluorescence is evoked when a primary electron knocks an electron close to the nucleus out of its position in the atom of the sample. This vacancy is immediately filled by a higher-energy electron from a higher orbital. The energy difference is released in the form of an X-ray quantum [44, 45]. The process is illustrated in

Figure 4 in Section 2.1.1. The X-ray radiation gained is element-specific and detected by suitable EDX detectors that are located at the side in the SEM specimen chamber next to the SE detector, as illustrated in Figure 11.

3 Theoretical Fundamentals II: Photocathodes

3.1 Definition of Photocathode Properties

3.1.1 Photoemission Model and Quantum Efficiency

The photoemission process can be described using two main theories. The one-step model represents a very basic theory model [56], whereas the three-step model is an extended version of it, as shown in Figure 13.

The one-step model uses an approximation where electrons are excited from a bound state into a free state out of the material. The model assumes a well-defined crystalline structure and is often used to study the band structure of materials. The one-step model is not practical for many photoemissive materials as it does not take electron scattering effects into account.

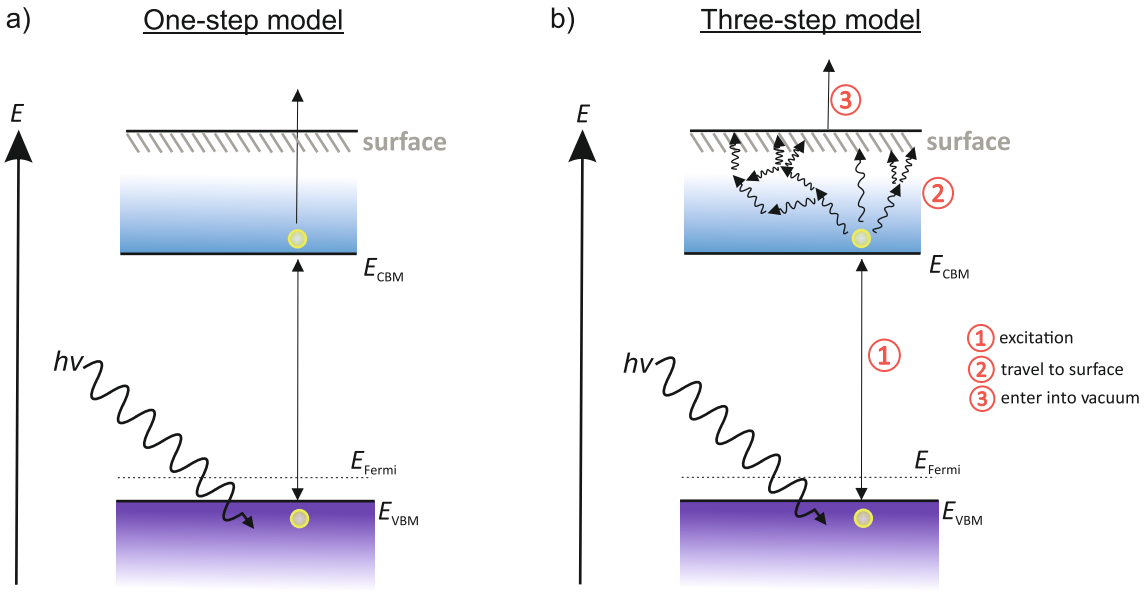

Fig. 13 Illustration of the comparison of the one-step model (left) and the three-step model (right).

The three-step photoemission model, shown in Figure 13 on the right side, was developed by Berglund and Spicer [57]. As the name suggests, this model explains the photoemission process in three independent steps, consisting of the optical excitation, the photoelectrons traveling toward the surface, and their escape into the vacuum. In this model, all three steps are treated separately from each other. In the first step, the excitation of an electron from the valence band (VB) into the conduction band (CB) occurs. The electrons of the VB absorb the incident photon energy and consequently the electrons are excited into the CB. This process is triggered if the incident photons provide sufficient energy to lift the electrons over the band gap barrier into the CB.

The second step describes the scattering events when the electrons travel toward the material surface. When the electrons are lifted into the CB, they diffuse or drift toward the cathode surface. A few of the electrons lose some energy on their way because they scatter and/or recombine with other atoms inside the material. The energy spread of the electrons is enlarged by this step.

The release of the photoelectrons into the vacuum represents the last step of this model. The photoelectrons reach the material's surface and have to pass an energy barrier prior to their escape into the vacuum. It is beneficial to reduce this vacuum energy level as much as possible to simplify the transition, e.g., through the deposition of a low work-function material, such as alkali-metals. As a consequence, the vacuum level (E_{vac}) is lowered close to the energy of the CB or in the optimal condition, it even situates below the conduction band minimum (CBM), which is called a negative NEA surface.

No band structure exists in metal photocathodes and thus photoelectrons have a high probability to scatter with each other. As a consequence, many electrons that are moving toward the surface lose nearly all of their energy and thus are not able to escape the cathode's surface, and only those electrons that have less than one electron mean free path can reach the surface and enter into the vacuum. Therefore, metal photocathodes provide a low QE due to their non-existent band gap and the scattering events that occur when the electrons are traveling.

In contrast, semiconductors provide much higher QE compared to metal photocathodes whereby incident photons with energy higher than the band gap excite electrons from the VB into the CB. Once the photoelectrons have entered into the CB, almost no scattering from electron-electron collisions can occur. The mean free path of photoelectrons in semiconductors is therefore much longer than that in metals and, as a result, more photoelectrons are able to escape the surface and contribute to the QE. Scattering processes in grain boundary or lattice scattering still occur, but the photoelectrons only lose a small part of their energy and – in most cases – still reach the surface [4].

Quantum Efficiency

QE is the most important factor when dealing with photocathodes and is defined as the ratio of the number of generated photoelectrons ($N_{\text{electrons}}$) divided by the number of incident photons (N_{photons}) [34], as shown in Equation 4. Thus, for photocathodes used in the injector, the QE depends on the incident photon beam energy and can be more practically calculated by the ratio of h (Planck constant), c (speed of light), and I (measured photocurrent from the photocathode) to q_{e} (elementary charge of an electron), λ (incident wavelength), and P_{light} (power of incident light).

$$QE = \frac{N_{\text{electrons}}}{N_{\text{photons}}} = \frac{h \cdot c}{q_{\text{e}}} \cdot \frac{I}{\lambda \cdot P_{\text{light}}} \tag{4}$$

The electronic structure of an emissive material and its relation to the outside environment is defined by some basic key terms, such as WF, electron affinity (EA), and Fermi level (E_{Fermi}). These key terms are summarized to convey a basic principle of a photocathode and its relationship to the environment [58] and are shown in Figure 14. The electronic structure of the material surface differs from sample to sample and is caused by internal and external factors such as the lattice structure, material defects, morphology, and surface composition and especially its surface cleanness.
The energy levels of electron transport are defined as CB and VB. The CBM represents the lowest energy level of the unoccupied state of uncorrelated electrons and

holes. In contrast, the valence band minimum (VBM) represents the highest energy level of occupied states with correlated electrons. The energy difference between these two levels is called the band gap (E_{gap}) while the highest occupied level where electrons are flexible and can move around freely is defined as the E_{Fermi} and marks the boundary between the occupied and unoccupied states in a continuum of states.

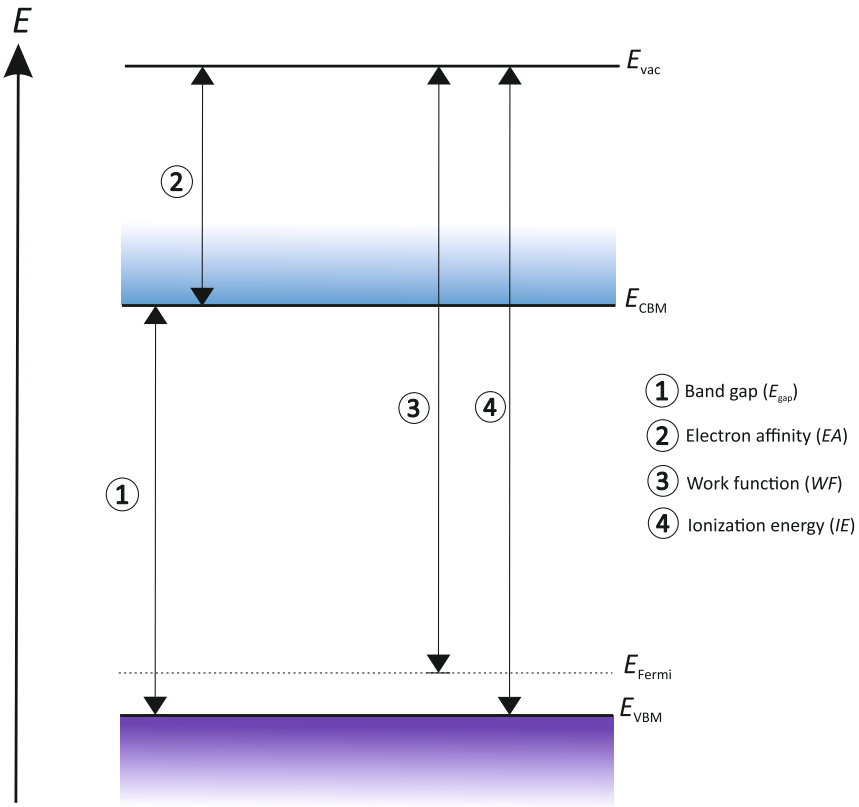

Fig. 14 Schematic representation of the fundamental key terms in photoemission processes.

An energy barrier such as the E_{vac} prevents flexible electrons from escaping from the material's surface. Thus, E_{vac} defines the potential energy of an electron positioned in a space outside of the solid. The E_{vac} location is strongly influenced by the nature of the material surface.
The energy difference between VBM and E_{vac} is called the ionization energy (IE) and refers to the minimum energy that is needed to remove an electron out of the material whereas the EA is defined by the energy difference between E_{vac}.
The WF is defined as the minimum energy needed to remove an electron from the E_{Fermi} and place it outside of the surface in free space.
The WF prevents a free electron at the E_{Fermi} from escaping from the solid into the outside space and is influenced by two main components, namely a bulk component (electronic density of states in the solid) and a surface component (redistribution of charges at the surface). As a consequence of coulomb repulsion and Pauli exclusion from adsorbates from the surface, the redistribution of the electron density can occur. Therefore, any deposition of an electronegative adsorbate on the surface results in an electron transfer that increases a surface dipole and influences the related surface terms [58]. For semiconductors, the WF depends on E_{Fermi} which is influenced by the density of states, temperature, and carrier concentration.

Metal Cathodes

Pure metal photocathodes such as Cu, Mg, or Pb have a high WF and require UV-light, which is the biggest disadvantage for high average current applications. However, metal photocathodes also display many advantages, the most important of which is their high robustness which enables them to provide a long operational lifetime [59, 60]. Mg is able to provide a QE of approximately 0.2 % when it underwent a proper surface cleaning in advance and is illuminated with UV-light (258 nm) [33]. Another big advantage is the simple preparation of metal photocathodes compared to semiconductor photocathodes. One possibility for metal cathodes is a soft chemical cleaning followed by a surface polishing until the cathode is polished to be mirror-like. The surface is de-oxidized and the cleaned, mirror-like metal cathode is stored under protection gas until it is installed in the UHV chamber.

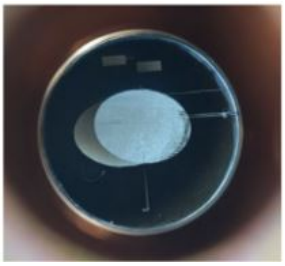

Fig. 15 Photo of a 10 mm Mg cathode inside the UHV chamber. The middle bluish part was cleaned with a laser of a spot size of 4 mm.

However, thermal vacuum cleaning is the most frequently used cleaning method for metal cathodes. After the cathode is installed in a UHV chamber, it undergoes a thermal cleaning step at a certain temperature with the aim to desorb adsorbates such as water (H_2O), molecular hydrogen (H_2), carbon monoxide (CO), and carbon dioxide (CO_2) from its metal surface. Typical temperatures are between 200 °C–300 °C for several hours up to one day. Besides the thermal cleaning in vacuum, UV ozon (O_3) laser cleaning, and hydrogen ion (H^+) or argon ion (Ar^+) irradiation as a sputter-cleaning can also be considered [59, 61, 62] and different cleaning methods are used in various laboratories. For the Mg photocathode used in ELBE, a UV laser cleaning is described in the following paragraph. The Mg cathode consists of a 10 mm, high purity (99.999 %) plug whose surface is cleaned by a UV laser with 258 nm, 100 kHz repetition rate, and 100 mW laser power. The cleaned area can be recognized as a 4 mm bluish spot in the middle of the 10 mm original Mg plug, as shown in Figure 15. This cleaning process is highly repeatable and thus the cathode can be re-used several times [33]. Even when the cathode was exposed to poisonous gases and its surface re-oxidized, the UV laser cleaning approach can be used to de-oxidize the surface to create a clean Mg surface once again.

Brief exposure to air is less hazardous for metal photocathodes than for cesiated photocathodes [33]. The QE of the metal cathode drops less by a short exposure than for semiconductor photocathodes. Of course, being exposed to gases for a longer time causes oxidation and leads to a change of the surface WF. Other metal photocathodes such as Cu [63] or Pb [64], which are used in Brookhaven National Laboratory (BNL) and Deutsches Elektronen-Synchrotron (DESY), are prepared in the same way.

Metal cathodes show low QE values between 10^{-4} to 10^{-1} compared to semiconductor photocathodes because of the energy loss due to scattering events and the low probability of electrons within one electron mean path of entering the vacuum.

3.1.2 Storage Lifetime of Photocathodes

A photocathode's lifetime and quality depend on many factors, especially on the vacuum conditions. All cathodes require a UHV environment to ensure sufficient QE and lifetime. Photocathodes have a naturally limited lifetime and thus their efficiency degrades exponentially as described by Equation 5. The time constant τ is the period of time that it takes for an exponentially decaying quantity to decay to a fraction e^{-1} of its initial value (QE_0), which means for 1 x τ it is 37 % of QE_0. The lifetime often shows a bi-exponential or a tri-exponential decay because, in most cases, the photocathode surface needs some equilibrium time after the preparation and is strongly influenced by the vacuum conditions and thus by the residual gases.

$$QE_t = QE_0 \cdot e^{-\left(\frac{t}{\tau}\right)} \tag{5}$$

The quality of the UHV system influences the photocathodes largely because the photoemissive layer is highly sensitive to any residual rest gases or molecules. The adsorption of residual gases is typically less significant for metal photocathodes than for semiconductor photocathodes. However, surface poisoning and the related QE losses were reported for metal cathodes that were exposed to gases for a longer time [61]. In contrast, semiconductors such as Cs_2Te or GaAs are immediately influenced by any vacuum instabilities [65, 66]. In this context, the photocathode's surface and thus the photosensitive layer is immediately contaminated by the adsorption of the residual gas. This poisoning leads to the increase of the EA and obstructs the ejection of photoelectrons into the vacuum. The photoemissive cathode might also react with the residual gas molecules, leading to a band structure change. It is thus necessary to maintain the integrity of the vacuum as well as possible with the help of vacuum pumps, especially for UHV applications, e.g., ion pumps and non-evaporable getter (NEG) pumps. The combination of these pump types can guarantee a vacuum between 10^{-10} and 10^{-11} mbar. GaAs is especially sensitive to any residual gases and require a 10^{-11} mbar (or better) vacuum. However, the incident photons of the laser also warm up the photocathode surface and therefore have a significant impact on the photocathodes' degradation. Thus, the photocathode has to be cooled to prevent any surface damage caused by laser irradiation.

3.1.3 Electrical Conductivity

Electrical conductivity plays a decisive role when dealing with photocathodes because electrons are permanently released from the material surface. As a logical consequence, the material's surface remains ionized until the material can receive new electrons from the contact with the cathode body and neutralize this ionization state. If the photocathode cannot receive new electrons from the contact with the cathode body, the surface remains ionized. Thus, the photocathode runs out of electrons and consequently loses its QE.
The electrical conductivity of semiconductors depends on many factors such as the temperature, pressure, and concentration of supplied impurities [4].

The conductivity can be increased and varied through the implantation of impurities, so-called dopants, into the intrinsic semiconductor crystal lattice. Dopant atoms replace native host atoms in the intrinsic crystal lattice and should have nearly the same size with one more or one fewer electron in the valence shell than the host atom.

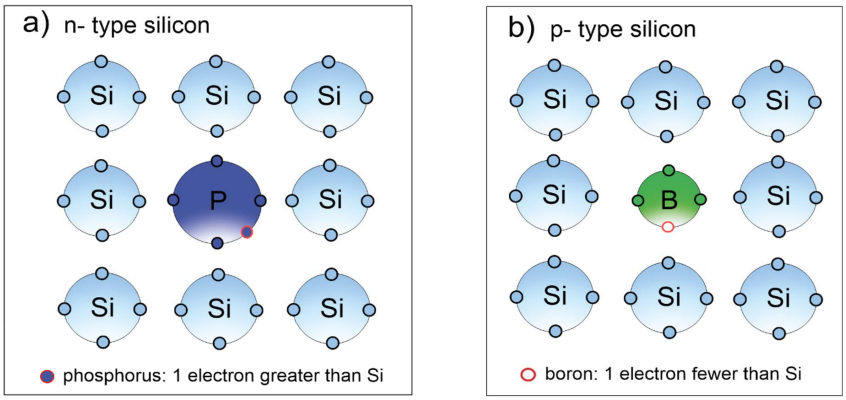

Fig. 16 Schematic drawing of n- and p-type doping, a) n-type Si with P as a dopant in the Si lattice and b) p-type Si with B as a dopant atom.

The p-type semiconductors carry dopant atoms that have one less electron than the host atom. Thus, these dopant atoms create holes (acceptor levels) in the intrinsic crystal structure [67, 68]. It takes only a little energy for electrons to be promoted into this acceptor level, leaving another hole in the VB. Other bound electrons are then able to jump and move into these holes and thus carry the electrical current. An example of a p-type semiconductor is given by Si, doped with boron (B), as shown in Figure 16. B has one less electron than Si, which has four valence electrons in its outer shell, and thus an electron vacancy at this position is created. The red circle in the outer B shell represents a hole in Figure 16.

For dopant atoms carrying an electron more than the host atom, a donor level at a higher energy level than the VB is created [67]. These semiconductors are called n-type semiconductors. Dopant electrons can easily overcome the small gap in the CB and become free carriers. In this case, the dopant electron leaving for the CB does not create a hole in the VB that is left behind. Figure 16 shows an example of an n-type semiconductor made of Si doped with phosphorous (P). The electron marked in red in the outer shell of P represents the additional electron compared to Si. In n-type semiconductors, an electron excess always exists in the crystal lattice, which can act as a free carrier.

The conductivity of semiconductors can be influenced by temperature. At 0 K, semiconductors show almost no conductivity because the VB is filled with electrons and the CB remains empty. There is no thermal energy available to lift an electron from the VB into the CB. With the adsorption of thermal energy at a higher temperature, the transition of an electron from VB to CB is possible. In contrast, the conductivity of metals decreases at a higher temperature because more lattice vibrations and atom-electron-scattering occur. However, semiconductors can compensate for these losses with their band gap and thus by the thermal transition of an electron from the VB to the CB.

3.2 Semiconductor Photocathodes

Semiconductor photocathodes are subdivided into positive electron affinity (PEA) cathodes and NEA cathodes based on the location of the E_{vac}, as shown in Figure 17. For PEA cathodes, the E_{vac} is above the CBM and for NEA the E_{vac} is below the CBM [5]. Cs_2Te and bi-/multi-alkali antimonide cathodes belong to the category of PEA cathodes, whereas GaAs and GaN belong to the NEA cathodes.

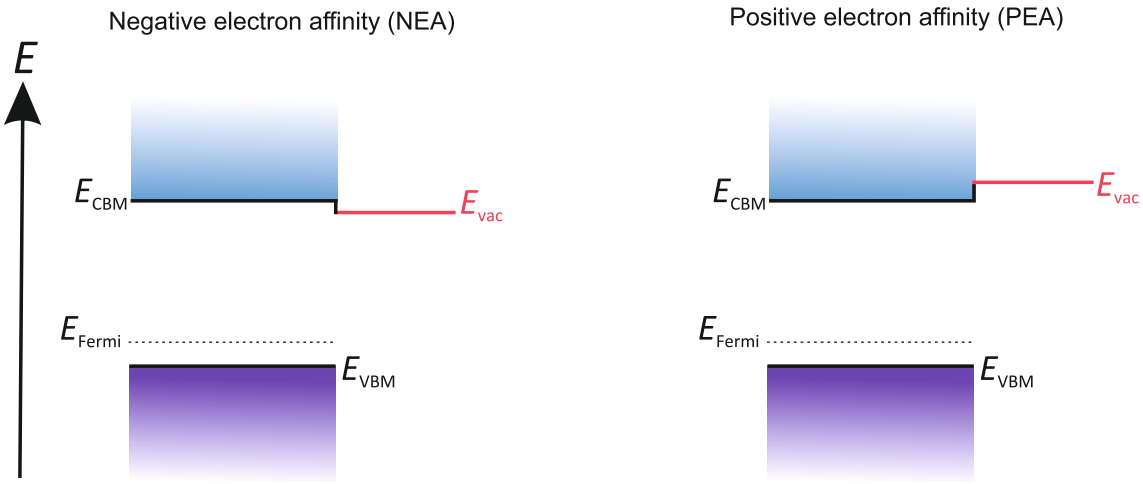

Fig. 17 Illustration of the difference between PEA and NEA surfaces regarding the location of the E_{vac}.

The semiconductor photocathodes can be further subdivided according to their production method: (i) crystals grown on a substrate or (ii) the surface activation with a deposition of Cs and O_2 on an as-received semiconductor. Cs_2Te is typically grown on a suitable substrate material, such as molybdenum (Mo) or Cu. A clean substrate is required prior to the Cs and tellurium (Te) deposition to deposit a pure crystal on it.

In contrast, semiconductors such as GaAs and GaN are commercially available and deposition with Cs and an electronegative partner such as O_2 is needed. Therefore, these semiconductor photocathodes belong to (ii).

3.2.1 p-type Gallium Nitride (GaN)

The family of III-nitride semiconductors consists of Al, gallium (Ga), and In compounds. They are widely used for blue, green, and UV-LEDs [69] and their wide and direct band gap makes these compound materials ideal for LEDs and detectors [70, 71]. Their adsorption range in UV and visible light indicates the potential of these compound materials for use as photocathodes [72]. The high thermal stability of GaN makes this nitride semiconductor attractive for use in high-power and high-temperature units [73, 74].

GaN as a photocathode seems to be more robust and achieves a higher QE than other photocathodes [23, 26, 34]. The potential application in particle accelerator injectors is quite new and has not been tested to date.

3.2.1.1 Crystal Structure of p-GaN

The cubic zinc blende crystal and hexagonal wurtzite structures are the two preferred crystal structures of GaN. The wurtzite structure is the thermo- dynamically more stable and energetically more favorable form. Each atom in the crystal lattice has four neighboring atoms with an sp^3 hybridization and the atoms are tetragonally arranged in the tightest sphere packing. The wurtzite type consists of two staggered hexagonal sub-lattices and has an ABABAB stacking sequence as shown in Figure 18. GaN is grown epitaxially along the c-axis, and the Ga or nitrogen (N) atoms can terminate the final layer. GaN is thus often referred to as N- or Ga-polar. Since the N atom is twice as electronegative as the Ga atom, strongly localized charges are formed in the crystal and cause polarization [75, 76].

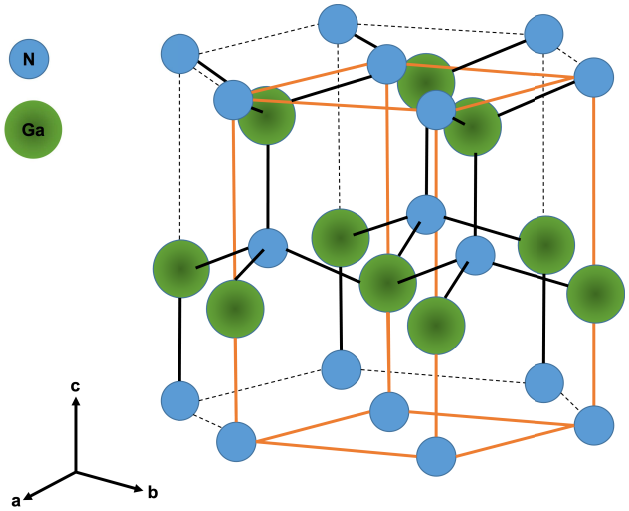

Fig. 18 Image of the hexagonal wurtzite crystal structure of GaN. Ga atoms are green and N atoms are blue. The smallest unit (basic cell) of the crystal lattice is marked in orange.

GaN is usually grown by MOCVD, molecular beam epitaxy (MBE), hydride vapor phase epitaxy (HVPE), or other physical deposition processes such as magnetron sputtering epitaxy (MSE) [67–69]. MOCVD is the most commonly applied method for industrial quantities where trimethylgallium (TMG), ammonia (NH_3), and biscyclopentadienyl magnesium (Cp_2Mg) are used as precursors for the crystal growth of p-GaN. A constant flow of molecular nitrogen (N_2) and H_2 is used as the carrier gas. The precursors decompose under high temperatures and are deposited as a p-GaN crystal onto a hot substrate. During the growth phase, impurities from O_2, H_2, carbon (C), or other unwanted inclusions are incorporated into the crystal lattice, which reduces the crystal quality or leads to a decrease in the carrier mobility. Cp_2Mg is used as a precursor for achieving the p-type in GaN. For this purpose, a Ga atom is replaced by a Mg atom in the intrinsic lattice. Due to the H_2-containing growth environment in MOCVD, the Mg atoms are often passivated by H_2 and together form a neutral Mg-H complex [67, 77]. An *ex-situ* annealing is subsequently used to remove the H atom and thus de-passivate the Mg-H complex. Depending on the temperatures used for the crystal growth or in the *ex-situ* annealing, crystal defects and facets are formed in the GaN lattice. Pyramidal facets that correspond to intersections of screw-component dislocations are revealed at the surface and are

formed when lower temperatures are used in the MOCVD process. These dislocations are also called V-Pits and create step terminations that appear as hillocks on the surface [78]. In contrast, when inverted V-Pits appear on the GaN surface, they are called etching pits and they exactly represent the hexagonal crystal structure of the GaN lattice. They mostly become visible when the surface is etched with oxidizing detergents [79–81]. These etching pits or hexagonal void holes result from poor coalescence during the initial stages of crystal growth.

3.2.1.2 Influence of the Substrate on the GaN Crystallinity

The choice of a suitable substrate is of great relevance for the crystal growth and its quality, and hence a substrate has to be chosen with lattice parameters, and chemical and physical properties that match the desired crystal layer. Although most optoelectronic GaN devices have sapphire as a substrate and therefore a high defect concentration, the devices do not display rapid degradation. While the lattice mismatch is the main criterion in the selection of the substrate, it is not the only relevant issue.The thermal expansion coefficient is relevant during the manufacturing process because high temperatures of approximately 1000 °C are often used which causes cracking in the deposited layers. A high crystal quality with low lattice mismatch is necessary to obtain a photocathode with a high QE. A poorly fitting thermal expansion coefficient causes strain in the epitaxial layer upon cooling. For thicker layers, this means that cracking might occur.

The dielectric properties represent another limitation e.g., sapphire is an isolator and thus an electrical contact should be mounted on the front side of the layer. In contrast, silicon carbide (SiC) has high conductivity and hence the contact could be mounted on the reverse side of the substrate.
Usually, a single crystalline or epitaxial film is grown on a substrate such as Si, sapphire (Al_2O_3), SiC, or spinel ($MgAl_2O_4$) [82, 83].

A high defect rate is caused by a high lattice mismatch between the GaN layer and its substrate. The most commonly used substrate is sapphire because of its availability and low cost. Unfortunately, sapphire is not an ideal substrate, because the lattice mismatch between sapphire and GaN crystal is between 16 and 17 %. The high lattice mismatch results in a high concentration of dislocations inside of the GaN crystal lattice that decreases the carrier mobility.
On the contrary, although SiC only has a lattice mismatch of 3 % [74, 82], the main limitation of using SiC lies in its high cost.
Si is a superior material due to its high quality, and large wafer sizes could be produced at a low cost. GaN layers grown on Si are of noticeably lower quality than those on sapphire because Si has the tendency to form amorphous silicon nitride (SiN) [74]. The biggest issue in applying GaN on Si substrates is their different thermal expansion coefficients as Si has a two times lower thermal expansion coefficient than GaN and this results in a potential cracking of GaN layers during the cooling step. Many techniques, such as introducing an aluminum nitride (AlN) buffer layer, a lower growth temperature, or Mg implantation, are implemented to try to optimize the crystal quality, improve the doping concentration, and reduce the lattice mismatch. As no ideal conditions have been found to date, these optimization attempts are ongoing at present.

3.2.1.3 Band Structure and Surface Requirements

Smith *et al.*. reported that wet chemical treatment on its own is not sufficient to remove C and oxygen (O) compounds from semiconductor surfaces. Therefore, the authors investigated additional thermal cleaning up to 800 °C where decomposition of the semiconductor material can occur [28].

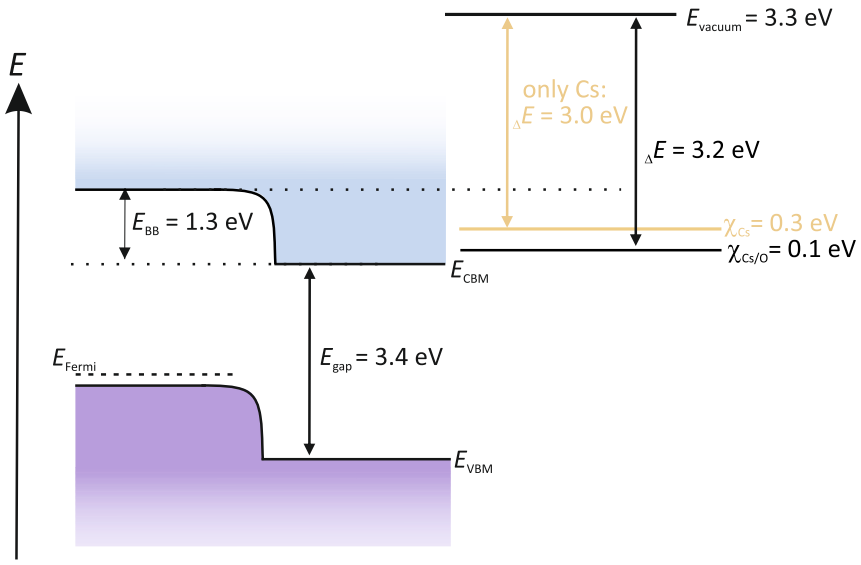

Fig. 19 Schematic representation of the band structure of p-GaN when activated with Cs and O_2.

An alkali metal such as Cs can reduce the GaN surface WF with the aim of forming an NEA surface. The photoemission of GaN and the role of O_2 in its activation process has been already discussed [84, 85]. It is widely accepted that the activation procedures applied to GaN and GaAs photocathodes should not necessarily be the same. Wang *et al.* reported on the activation of GaN with sequential Cs/O_2 and indicated that it does not lead to significant improvement compared to a simple activation with only Cs.
For photoemission, p-doping is also needed in GaN. The p-doping is responsible for the bend bending and producing a new reduced EA as shown in Figure 19. When Cs is now applied to the GaN surface, the E_{vac} is reduced by 3 eV and is located below the CB. O_2 on the p-GaN:Cs surface would only reduce the E_{vac} with a further 0.2 eV. Therefore, O_2 is not necessary and does not play any important role in obtaining an NEA surface on p-GaN. This means that the activation of GaN with Cs alone is more practicable and easier compared to other photocathodes, such as GaAs or Cs_2Te.

3.2.1.4 Performance as a Photocathode

Quantum efficiency (QE)

In 2000, Machuca *et al.* published their findings on Cs-activated GaN, which is more robust than other photocathodes and can achieve a QE of 53 % [23]. It is shown that the Cs-activated GaN photocathode has a lower susceptibility to O_2

when exposed to O_2. Therefore, the p-GaN photocathode is more robust and has a longer lifetime than GaAs photocathodes.
Depending on their p-dopant concentration, about 70 % QE could be achieved [24], which was the highest QE value ever reported for p-GaN. This means that an optimal Mg dopant concentration is required to support photoelectrons to travel toward the surface.

Lifetime

The degradation of NEA surfaces depending on the exposure to air and the adsorption of several gases, such as H_2, O_2, N_2, methane (CH_4), CO, and CO_2, was carried out by Chanlek *et al.* and Sato *et al.* [21, 86]. The studies showed that the NEA surface was strongly influenced by O_2 and CO_2, whereby the QE immediately dropped to almost 0 %. In contrast, CO only had a slight influence on the QE and thus on the photocathode degradation. Surprisingly, H_2, CH_4 and N_2 did not affect the photocathode quality at all. With an optimal temperature between 150–300 °C, desorption of CO and CO_2 from the poisoned NEA surface is possible [66] which means that a poisoned surface can be rejuvenated by applying a simple thermal treatment.
Additionally, the recovery of QE of Cs/O_2-activated p-GaN on sapphire by a thermal treatment process was studied [86]. In this study, GaN was thermally cleaned at 500 °C and 600 °C and activated by a YoYo process. In this research, the fresh photocathode was exposed to N_2 gas, which lowers the QE by three orders of magnitude. With a thermal treatment, the QE can recover 60 % of its initial value. Thus, it is evident that the re-activation of NEA cathodes is possible, although further studies are strongly recommended.

3.2.2 p-type Gallium Arsenide (GaAs)

In contrast to Cs_2Te, GaAs and GaN are already grown on a substrate and are commercially available. The fact that suppliers can guarantee the desired quality and the dopant concentrations is advantageous.
GaAs and its alloys found broad applications in photodetectors [87], electron microscopes [88], and photon-enhanced thermionic emission devices [89] since Scheer and Laar proposed GaAs as a photoemitter [90]. Its good spectral responses to near infrared (NIR) and low dark current meets the requirements for vacuum photodetectors. The possibility of reaching a high current density under excitation by visible lasers, spin-polarization, low thermal emittance, and a narrow energy distribution match the requirements of high brightness electron sources for FEL, energy recovery lines (ERL), and THz devices [91]. GaAs absorbs a broad wavelength spectrum in the visible range and has the ability to emit spin-polarized photoelectrons when illuminated with polarized NIR light [92]. In transmission electron microscopy, the spin-polarized electrons are also combined with accelerator technology by using a GaAs superlattice to dynamically observe magnetic field images with high resolutions [4].

Band Structure of the NEA Surface

GaAs is a semiconductor with a zinc blende structure and a direct band gap. This means the CBM is located above the VBM which is energetically more favorable compared to indirect band gap semiconductors.
For photoemission, p-doping is needed, which yields some holes in the lattice structure. The p-doping is responsible for lowering the CB to produce a new reduced EA energy, shown in Figure 20. By adding Cs only, the E_{vac} can be lowered to the same energy level as the CB. For the photoelectrons, it is therefore not possible to enter into the vacuum. By applying a strong electronegative oxidant such as O_2 or nitrogen tri-fluoride (NF_3) to the GaAs surface, the E_{vac} can be further reduced below the CBM and photoelectrons are able to leave the NEA surface [15, 93].

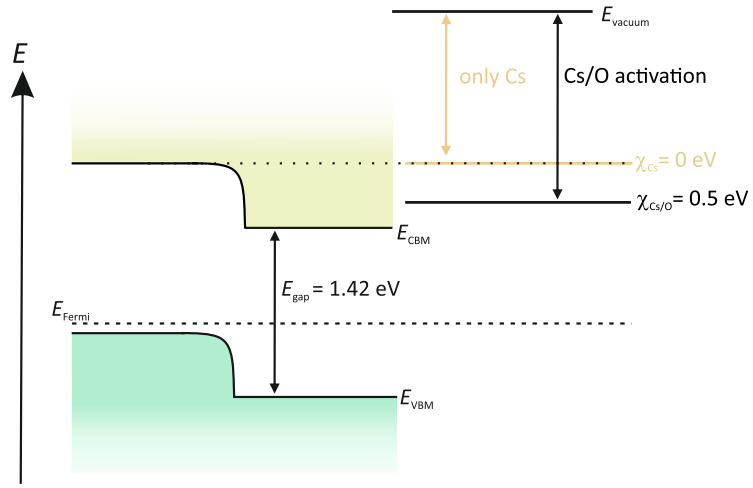

Fig. 20 Schematic drawing of the band structure of p-GaAs, activated in a YoYo process with Cs and O_2.

The as-received commercially available GaAs has to undergo a surface cleaning before it is activated with Cs and O_2. The wet chemical cleaning process applied for GaAs differs from lab to lab. Some labs prefer to use a simple solvent cleaning in acetone (C_3H_6O) or ethanol (EtOH), while others apply an etching in hydrochloric acid (HCl) solutions or a mixture of sulfuric acid (H_2SO_4) and hydrogen peroxide (H_2O_2) [94–97]. An alternative to wet chemical cleaning is ion-sputtering, which produces an atomically clean surface [98]. This technique uses energetic ions, such as Ar^+ or H^+, to bombard the semiconductor surface to remove adsorbates. The disadvantage of ion sputtering lies in the potential risk of surface damage and decomposition [99]. However, the more common and safer way is to thermally clean GaAs at 500–600 °C for a minimum of half an hour. As mentioned, the aim of thermal cleaning is to obtain a chemically clean and uniform GaAs surface, which can be examined by *ex-situ* or *in-situ* surface studies such as XPS.

Dipole Model of the NEA Surface

After GaAs is thermally cleaned, it is activated in a so-called YoYo process to obtain a GaAs photocathode. The YoYo process consists of the sequential deposition of Cs and O_2 to yield an NEA surface [100] as shown in Figure 21. The deposition

process is monitored by *in-situ* photocurrent measurements. At first, Cs is excessively deposited on the GaAs surface, as indicated by the descending photocurrent. Afterward, O_2 is added to the excessively cesiated surface. When the photocurrent increases again, first reaching a maximum and descending again, the deposition of O_2 is stopped. When this is repeated, the Cs deposition starts again. Each step is repeated several times until a final photocurrent is achieved. Other oxidative gases besides O_2, such as NF_3 could also be considered successful activation ingredients [101].

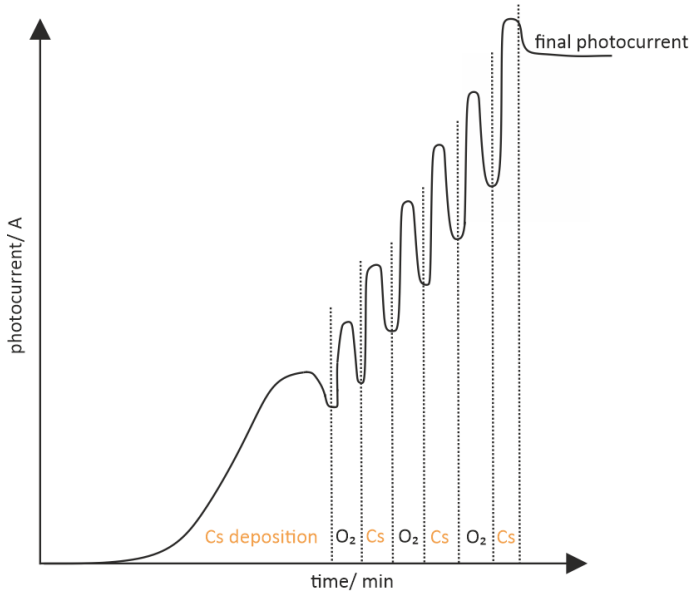

Fig. 21 Schematic drawing of a typical photocurrent evolution when a YoYo activation is used (alternately applying Cs and O_2).

There is no uniform recipe for GaAs preparation as different facilities follow different activation conditions. Some researchers also prefer to deposit Cs all the time and just occasionally turn on the O_2 to increase the photocurrent when it is needed [102]. This approach represents a co-deposition, rather than a sequential deposition. Recent research deals with the theory of a dipole model of Ga-O-Cs on the photocathode's surface and its importance for creating an NEA photocathode [20, 86, 103].

Spin-Polarization

As mentioned, GaAs can produce spin-polarized electrons. The nature of this polarization lies in the spin-orbit splitting of the valence band. The valence p band is split into fourfold $p_{3/2}$ levels and twofold $p_{1/2}$ levels, as shown in Figure 22.
The energy difference between these levels is 0.34 eV and the electron transition rule is $_{\Delta}m = \pm 1$. This means that for positive helicity light m is $+1$ and for negative helicity light it is -1. Some transitions are more favorable than others and thus the probability for positive helicity light is three times higher as more electrons are lifted into the $m = -1/2$ state than into the $m = +1/2$ state [92]. When electrons are excited from the spin-orbit-split-off band, no polarization occurs. In contrast, maximum polarization is obtained for photon energy exceeding the band gap energy

for less than 0.1 eV. A big advantage is the easily achievable polarization reversibility as the incident irradiation can be changed externally.

The main drawback of GaAs for high polarization is its reduced QE. However, usually, the electron spin-polarization yield (ESP) is between 30–50 %, depending on dopant concentration, temperature, and the operation mode for unstrained bulk GaAs [104, 105]. Demonstrations at Stanford Linear Accelerator Center (SLAC) showed that a polarization yield of up to 80 % was achieved with high-gradient doped strained GaAs [102]. However, the highest polarization yield of 84 % at 6.4 % QE was reported on superlattice structured GaAs with a distributed Bragg reflector (DBR) [106].

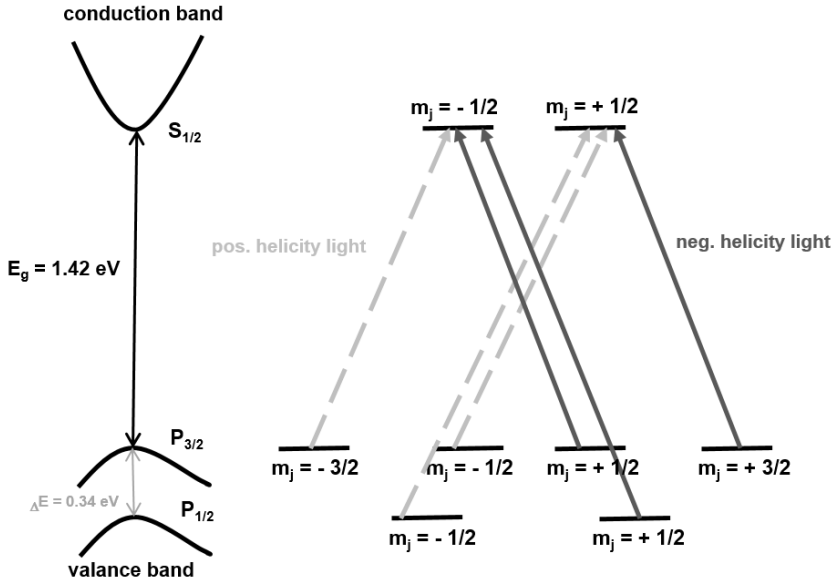

Fig. 22 Schematic representation of the electron transitions for the generation of spin-polarized electrons in GaAs photocathodes.

Performance as a Photocathode

GaAs photocathodes provide a high QE (over 10 %) in visible light and are often used to produce polarized electron beams when illuminated with NIR light [92]. The main advantage of this material is that it does not require UV-light to produce polarized electrons. Thus, using visible light or NIR is a great advantage for laser instrumentation. Studies dealing with GaAs-layered structures and superlattices show that they lead to higher polarization values but result in less QE [17].
The QE of GaAs is affected by many other factors than those discussed in the sections above. In addition to the vacuum, material quality, incident wavelength, cathode temperature, Schottky effect, and surface contaminations, the thickness of the GaAs layer, dopant concentration, and NEA conditions play a significant role in the successful operation of this material and its optimization is still a hot topic in modern research.

GaAs is successfully applied in DC Guns [20] and its potential application in RF injectors is still in the testing phase [107].

Reaching a long lifetime of GaAs photocathodes is still a challenging task because they degrade rapidly [66] as GaAs is very sensitive to any residual gases in the UHV regime and thus requires optimal UHV conditions. The main causes of degradation are ion back-bombardments, the application of a high-voltage, and the destructive heat load under intensive illumination. Ion back-bombardment and suboptimal vacuum conditions negatively influence the surface composition, resulting in a poisoned surface preventing the desired photoemission [21]. The lifetime can be improved if the activation process is optimized. Possible approaches for this optimization include the application of different novel oxidants as well as the elucidation of the role of N_2 [20, 101].
In recent years, research was carried out to protect the GaAs with a Cs_2Te [17, 94] or a multi-alkali antimonide protection layer [22]. The Cs_2Te protection layer is beneficial for the GaAs's lifetime, resulting in a five times slower QE decay than for a GaAs photocathode without a protection layer [108].

3.2.3 Cesium Telluride (Cs_2Te)

One of the most commonly used semiconductor photocathodes in photoinjectors is Cs_2Te, which provides a long operational lifetime and a high QE.
Many factors such as the quality of the evaporators, the thickness of the deposited layer, and gas impurities inside the UHV chamber influence the QE. Under ideal conditions, Cs_2Te can reach a QE of 10 % or more [6]. The Cs_2Te can be grown in a sequential deposition or in a co-deposition and the typical layer sequence is shown in Figure 23.
The standard process was established by Di Bona *et al.* [65] by using a sequential deposition in which Te and Cs are deposited on a mirror-like polished and 120 °C hot Cu or Mo substrate. The preparation of Cs_2Te photocathodes for ELBE SRF Gun II is described and discussed in Section 5.2 in detail.
Besides this sequential deposition process, a co-evaporation of Cs and Te is optional [109]. Both preparation techniques result in high QE of the Cs_2Te photocathodes, but it is assumed that Cu atoms diffuse into Te and cause some island growth. Therefore, these islands yield a lower QE compared to the Cs_2Te cathode on a Mo substrate [65]. However, the thickness of the grown Cs_2Te layers also plays a key role in the QE performance and is still under optimization at different facilities [110, 111].

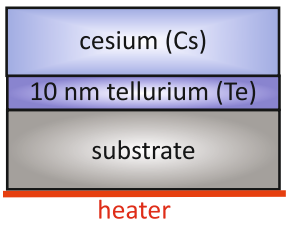

Fig. 23 Schematic overview of a typical layer sequence for a Cs_2Te photocathode, based on the original approach taken from [65].

High QEs of Cs_2Te can only be achieved under UV excitation, which is the biggest disadvantage of this photocathode compared to Sb-based photocathodes or GaAs photocathodes. Another disadvantage is the high sensitivity to any residual CO_2 or O_2 in the UHV system. The adsorption of any of these gas molecules changes

the surface WF in the way that the QE drops rapidly and hence the lifetime of the cathodes is strongly influenced by the vacuum conditions [112].

4 Technical Aspects of the Realization of *In-Situ* XPS Capability

4.1 Setup of Preparation Chamber and Challenges

4.1.1 Preparation Chamber with Ultra-High Vacuum

A visual representation of the preparation chamber as it was at the beginning of the project is shown in Figure 24. The spherical UHV chamber, with an average pressure of $5\,\mathrm{x}\,10^{-10}$ mbar, is connected to a loading chamber that has an average pressure of $1\,\mathrm{x}\,10^{-7}$ mbar, and the vacuum between the preparation chamber and loading chamber is separated by a metal gate valve. A manipulator picks up a Mo flag including a square-shaped sample and transports it from the loading chamber into the preparation chamber. The preparation chamber is equipped with a SRS® mass spectrometer to detect the rest gases inside the system. A SAES® NEG pump plus an Agilent® ion pump, placed at the bottom of the chamber, is required for achieving UHV conditions.

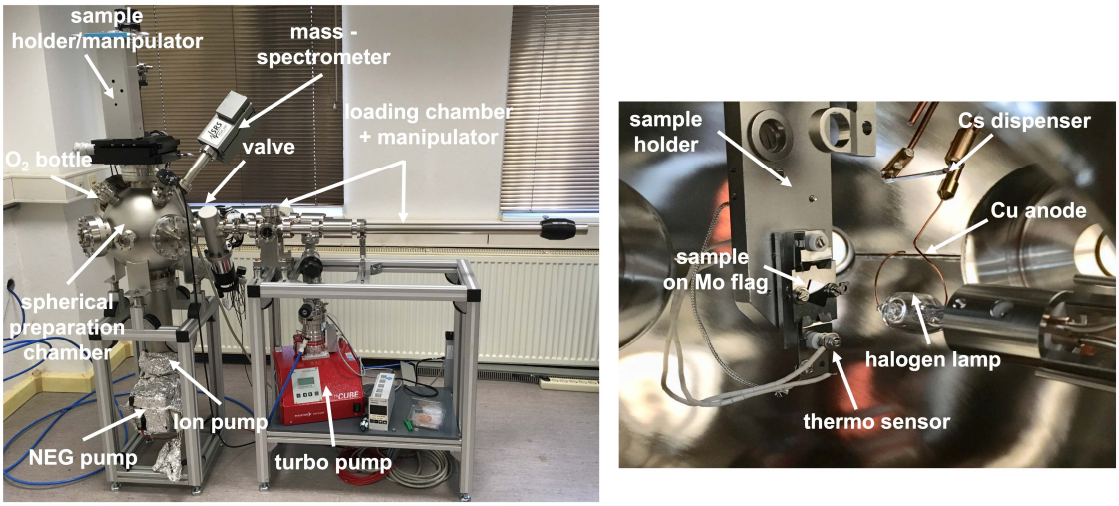

Fig. 24 Photos of the UHV preparation chamber (left) and the interior of the preparation chamber with all required parts for the photocathode preparation (right). Both photos show the initial status at the beginning of the project.

A rotatable and retractable sample holder is located in the middle inside the preparation chamber which has an integrated thermal sensor for temperature measurements (shown in Figure 24). Furthermore, a halogen lamp, a Cu anode, and a Cs dispenser are the main and necessary instruments for the preparation of III-V semiconductor photocathodes. An O_2 bottle is attached outside of the chamber which is mostly used for GaAs samples and thus needed in YoYo activations. All necessary parts were constructionally designed by HZDR and are shown in the photo in Figure 24. The preparation chamber for III-V semiconductors and its parts were systematically improved during the working period.

4.1.2 Thermal Cleaning and Temperature Measurement

The thermal cleaning with the halogen lamp and especially the temperature measurement of the heated sample posed a special challenge, which was solved within the scope of this thesis. For this thermal cleaning of the samples, a commercially available 400 W OSRAM® halogen lamp was used (see Figure 25). The glass bulb of the halogen lamp contained a small hole, which was necessary to prevent leaking due to rest gases inside the bulb. The glass bulb itself, which surrounded the tungsten filament, was kept to protect the sample from any tungsten traces that were potentially released during the thermal cleaning. The relevance of this glass bulb as a protection shield could be seen from a used halogen lamp that contained tungsten marks on the glass, as shown in Figure 25.

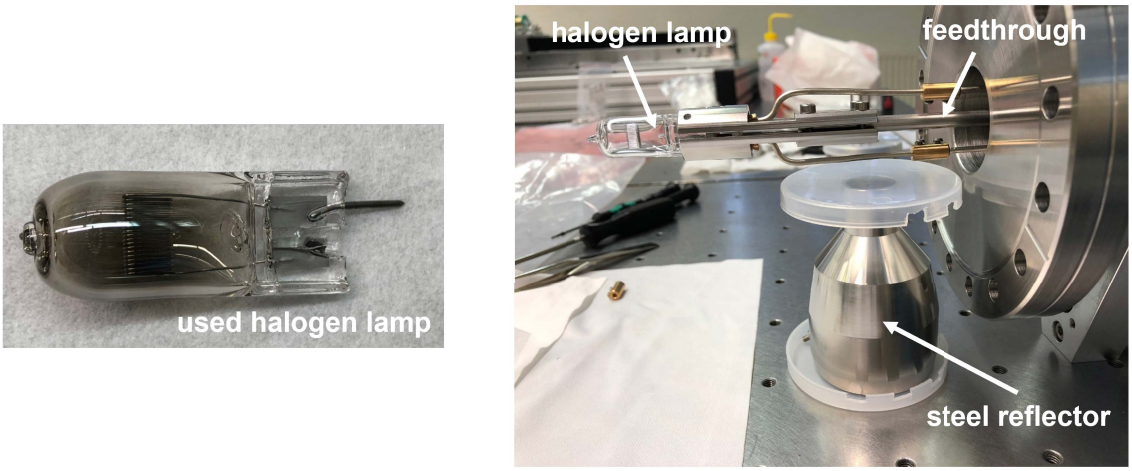

Fig. 25 Photo of a used halogen lamp (left), showing evaporated tungsten on its bulb, and a photo taken during the construction of the new halogen lamp with an advanced stainless steel reflector (right).

Another undesirable effect during the thermal cleaning was that the preparation chamber walls heated up, which could be observed by a deterioration of the vacuum. To counteract this, a steel reflector surrounding the halogen lamp was implemented. The assembly was performed in the cleanroom which is shown on the right side in Figure 25. The steel reflector is used to focus the irradiation of the halogen lamp onto the semiconductor surface to avoid additional heating of the UHV preparation chamber, as shown in Figure 26.

At the same time, the old Cs dispenser was replaced by two new Cs dispensers that were placed behind the ring anode (see Figure 26). Additionally, a mesh was installed at the bottom of the spherical chamber to prevent a sample drop into the ion getter pump and the potential risk of pump damage.
In the beginning, the temperature of the samples was measured by the internal thermo-sensor on the sample holder inside the preparation chamber shown in Figure 26. Because the sensor was located about 1 cm underneath the sample, it was out of focus of the halogen lamp irradiation and thus a little bit offset. The real temperature on the sample surface was therefore unknown. A calibration was attempted between the sample temperature and sensor by moving the sensor into the halogen lamp focus. A difference of 260 °C between the sensor temperature and

the "real" temperature on the sample was found, which is shown in the calibration curve for a p-GaN on a sapphire sample in Figure A 1 in the Appendix. Considering different thermal absorption coefficients, p-GaN on Si behaved differently than p-GaN on sapphire which is why the temperature measurements were inaccurate and the prediction of the real temperature was not clearly determined. Therefore, the chamber was equipped with an infrared (IR) sensor on the outside of the chamber at a window. The IR sensor is able to measure metal and semiconductor surfaces through the chamber window without absorption losses and was already calibrated by the supplier.

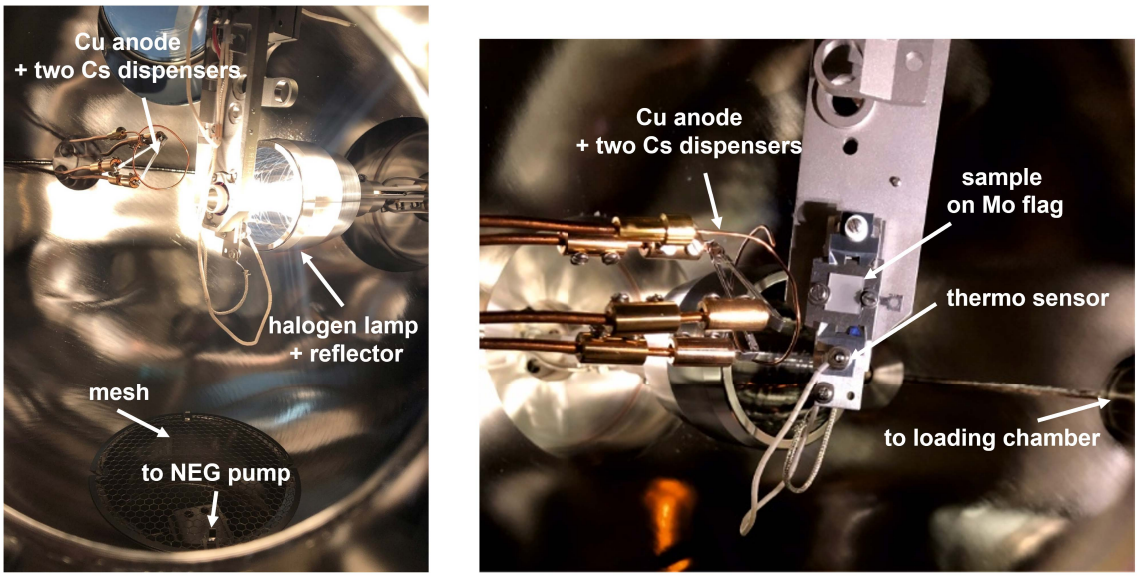

Fig. 26 Photo of the interior of the preparation chamber showing the new setup of the halogen lamp during a thermal cleaning (left) and the two new Cs dispensers from a side view (right).

4.1.3 Anode Drawbacks and Improvements

The Cu ring anode was replaced by a steel anode during the working period, as shown in Figure 27. The Cu anode always caused a small vacuum deterioration when it was turned on to track the photocathode current.
The partial vacuum deterioration was presumably caused by the generation of extra, undesired electrons, the release of adsorbed molecules, or other secondary processes when the photoelectrons hit the Cu surface of the anode because the Cu anode had no degas option. The vacuum conditions were improved by a steel anode that ensured better vacuum stability during the photocurrent measurement. Furthermore, the new steel anode has a degassing option through which a current of maximum 8 A can be applied through, shown in Figure 27. The outgassing has the aim to desorb any adsorbates and generate a contaminant-free anode surface and thus relieve the vacuum during photocurrent measurements. The outgassing of the anode is necessary after each bake-out of the preparation chamber.

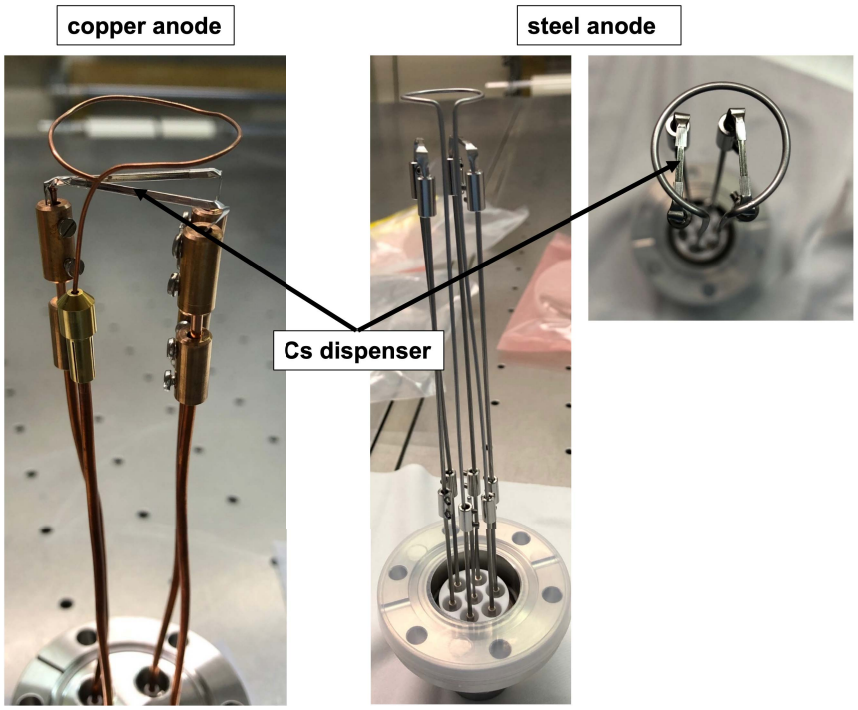

Fig. 27 Photo of the old Cu ring anode (left), including the Cs dispensers, and the improved stainless steel ring anode from a side view and top view (right).

4.1.4 Ultraviolet Light Sources for Photoelectron Excitation

The semiconductor sample has to be illuminated by UV-light at a wavelength of 310 nm during the activation to follow the deposition of Cs which is detected as an *in-situ* photocurrent. The photocathode was only partially illuminated afterward to measure its lifetime and its QE decay.
The UV-LED is placed outside of the chamber at a window (see Figure 28) and hence the incident light has to be guided from the outside of the chamber to the inside of the chamber and has to be focused on the square-shaped sample with the help of optical lenses and tubes, as shown in Figure 28. The focusing of the UV-light to a sample distance of 23 cm and the measurement of the UV-light output power was carried out outside of the chamber with a power meter.
The absorption of the UV-light from the window plays a significant role in the correct QE calculation, shown in Equation 4, and thus the UV absorption from the window has to be checked. The chamber was initially equipped with a boron-silicate window that absorbed approximately 90 % of the incident UV-light at 310 nm. The boron-silicate window was replaced by a quartz window that showed an 85 % transmission of UV-light at a wavelength of 310 nm. The incident power of the UV-light on the sample was measured at 50 μW.

An adjustable aperture in front of the UV-LED reduces the incident light power on the semiconductor sample to relieve the vacuum during the photocurrent measurements. The spectral response and width of the UV-LED used were determined by spectral response measurements in the range of 240–340 nm. The emitted wavelength of the UV-LED was measured at 310 nm with a spread of ±10 nm. The spectral width gained is shown in Figure A 2 in the Appendix.

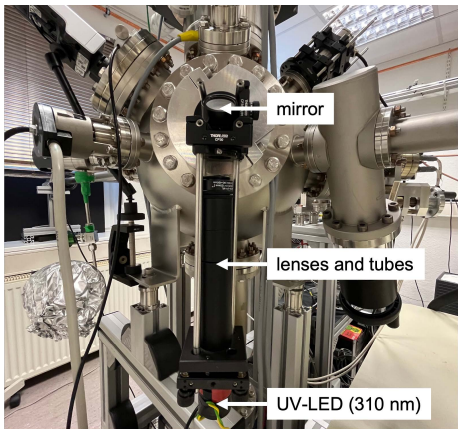

Fig. 28 Photo of the setup of the UV-LED outside of the preparation chamber which guides the UV-light through a quartz window onto the sample inside the chamber via lenses and a mirror.

Spectral Response Measurements

The spectral response measurement aims to specify the band gap of p-GaN:Cs photocathodes by illuminating them with different wavelengths in the UV range. For this purpose, a deuterium lamp was set up with a monochromator that covered a wavelength range of 200–500 nm. A focusing of the pathway of the incident light via lenses and mirrors was necessary to guide the light onto the p-GaN inside the preparation chamber. The setup and pathway of the guided light are shown in blue in Figure 29. The power of the incident light from the deuterium lamp depending on the wavelength was measured in advance and is shown in Figure A 3 in the Appendix.

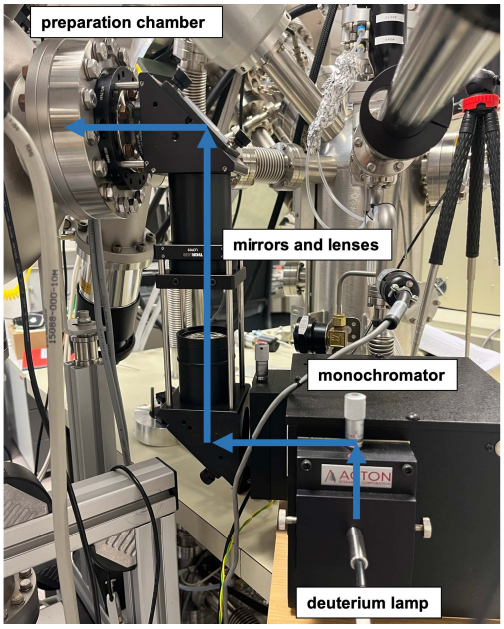

Fig. 29 Photo of the setup of the spectral response measurements, in which the blue arrows show the guided pathway from the deuterium lamp (UV-light source) into the preparation chamber.

4.1.5 Sample Holder and Manipulator

The sample holder consists of an OMICRON™ Mo flag, on which a square-shaped sample can be fixed (shown in Figure 30). The semiconductor dice was mounted onto the flag under dry N_2 atmosphere in a glovebox with the help of two steel screws and washers. The washers and screws hold the sample on the flag and thereby ensure that the sample does not drop. Furthermore, the washers provide electrical contact between the semiconductor p-GaN layer on top and the conductive flag.

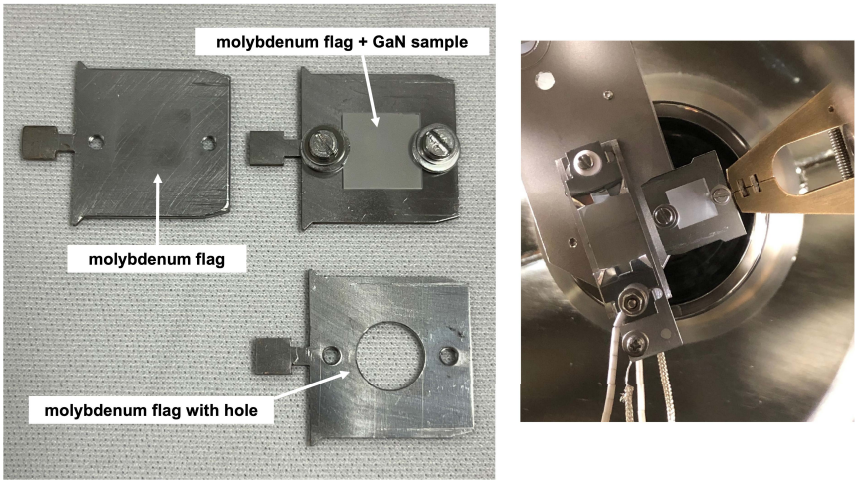

Fig. 30 Photos of the OMICRON™ sample flags, showing the original flag, the Mo flag with a p-GaN sample, and a modified Mo flag with a hole for the thermal cleaning of the sample from the backside which is shown on the left side. The sample transportation of the flag with the help of the manipulator is shown on the right side.

The p-GaN samples were transported into the loading chamber via a suitcase under a dry N_2 atmosphere. The manipulator can grasp the perturbation of the flag on the left side to ensure the sample transportation, as shown in Figure 30.

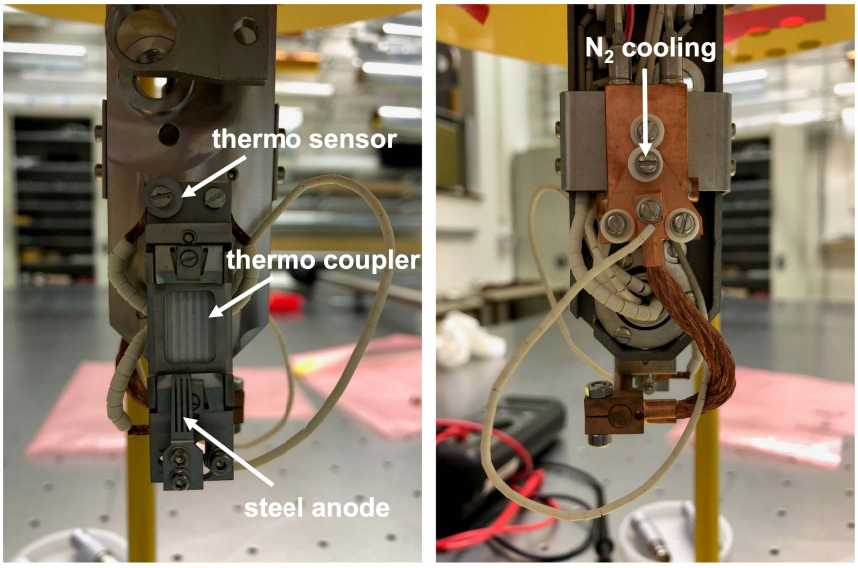

Fig. 31 Photo of the new sample holder inside the preparation chamber, showing the thermo elements and the N_2 cooling capability.

In later experiments, the sample holder inside the UHV preparation chamber was exchanged for a new one with an integrated thermo coupler that has the option to heat the sample from the backside. The thermo coupler is connected to the thermo sensor above the sample and a feedback loop controls the temperature which was set externally on a device. A special type of flag with a hole was developed for thermal cleaning from the backside, as shown in Figure 30.

The new sample holder has the additional option to cool the sample with a N_2 supply from the back of the holder, as shown in Figure 31.

4.1.6 Loading Chamber with Transportable Sample Suitcase

After the samples were wet chemically cleaned and mounted onto the Mo flag under a dry N_2 atmosphere, they were installed into a home-built suitcase that can be added to the loading chamber, as shown in Figure 32.

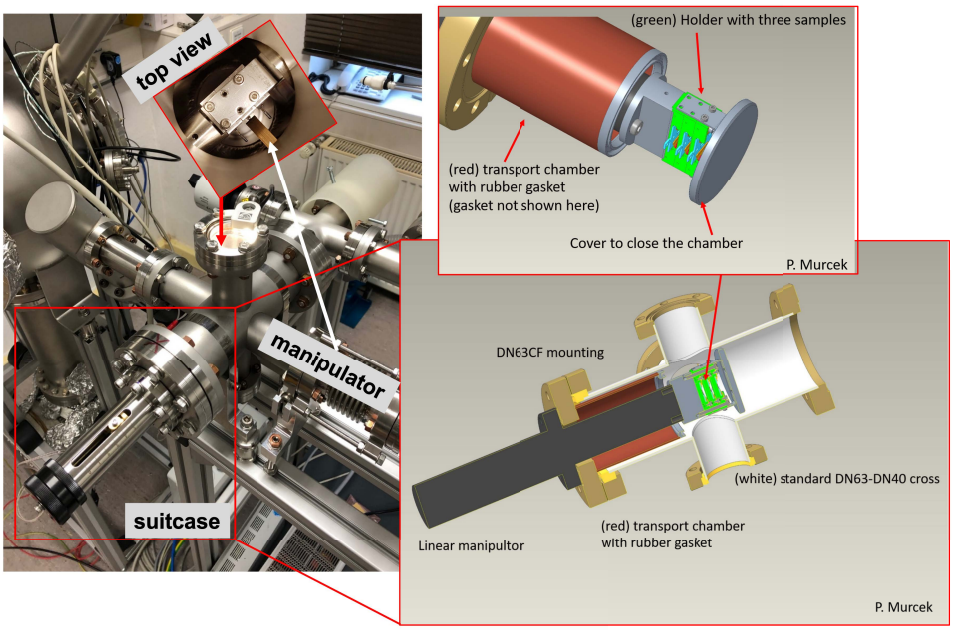

Fig. 32 Photo of the loading chamber part where the suitcase is adopted. 3D models show the retractable interior of the suitcase with the possibility to carry up to three samples under a dry N_2 atmosphere.

This suitcase was designed to avoid a re-oxidation of the sample surface after the wet chemical cleaning. The inner part of the suitcase can carry up to three Mo flags which are marked in green in Figure 32. The red part in Figure 32 is retractable and the suitcase is equipped with rubber sealing to hold the dry N_2 atmosphere during transportation. Adapted to the loading chamber, the inner part of the suitcase is extended and the samples are placed under the vacuum of the loading chamber (average pressure of 1×10^{-7} mbar). The advantage of this suitcase is that it allows collaborators from other labs to prepare, install, and transport samples to HZDR under a dry N_2 atmosphere.

4.1.7 Software for Controlling the Preparation Process

In-house software was developed to control all the necessary functionalities for the photocathode preparation. The software was developed by D. Bujdo (University of Applied Science, Dresden) within the framework of an internship and was written with LabView. A screenshot of the software user interface is depicted in Figure 33. On the left side, a file directory can be selected and the high voltage (HV) for the piezo-controller of the O_2 bottle is controlled in the same window. In the bottom corner of the window, a selection between different operation modes of the UV-LED can be made whereby the user can select between the operation mode "switched on, off or pulsed mode (A.O. = alternating operation)." For the pulsed mode, the LED is switched on and off every second. When the LED is off, the dark current is taken as a background value while vice versa, when the LED is on, the photocurrent from the photocathode is measured. The software calculates the photocurrent as the difference between the photocurrent of the photocathode subtracted from the dark current (background). The calculated photocurrent is displayed as an *in-situ* photocurrent as a function of time in the upper right corner of Figure 33.
The lower right corner in Figure 33 displays the vacuum measurement of the loading chamber or of the preparation chamber. In the upper right corner of the window, the voltage of the steel anode is chosen and the *in-situ* photocurrent can be illustrated as a function of time. A power supply controls the halogen lamp and regulates the applied current through the Cs dispensers as shown on the left side of the window in Figure 33. All devices used for the preparation of III-V photocathodes are listed in Table A 1 in the Appendix.

Fig. 33 Screenshot of the software user interface of the HZDR internally-developed software for the preparation of III-V semiconductor photocathodes.

4.2 Introduction of *In-Situ* XPS Analysis

The focus of this thesis was to extend the preparation chamber with a suitable analysis method that is able to characterize the sample surface without leaving the UHV environment. The challenge was to find a suitable method that operates under a UHV environment and can easily be adapted to the preparation chamber to ensure vacuum sample transportation.

An SEM with EDX analysis is an effective and cost-efficient choice but the SEM sample chamber only provides a vacuum at an average pressure of 5×10^{-7} mbar which would mean that all the sealing rings have to be replaced by Cu sealings to achieve UHV and there is no guarantee that the SEM electronics still work under these extreme UHV conditions.

Therefore, an XPS that already operates under UHV conditions represented the better choice although it is more expensive than an SEM. The difficulties and challenges that were faced during the connection of the XPS chamber to the preparation chamber, shown in Figure 34, are listed and discussed in the following subsections.

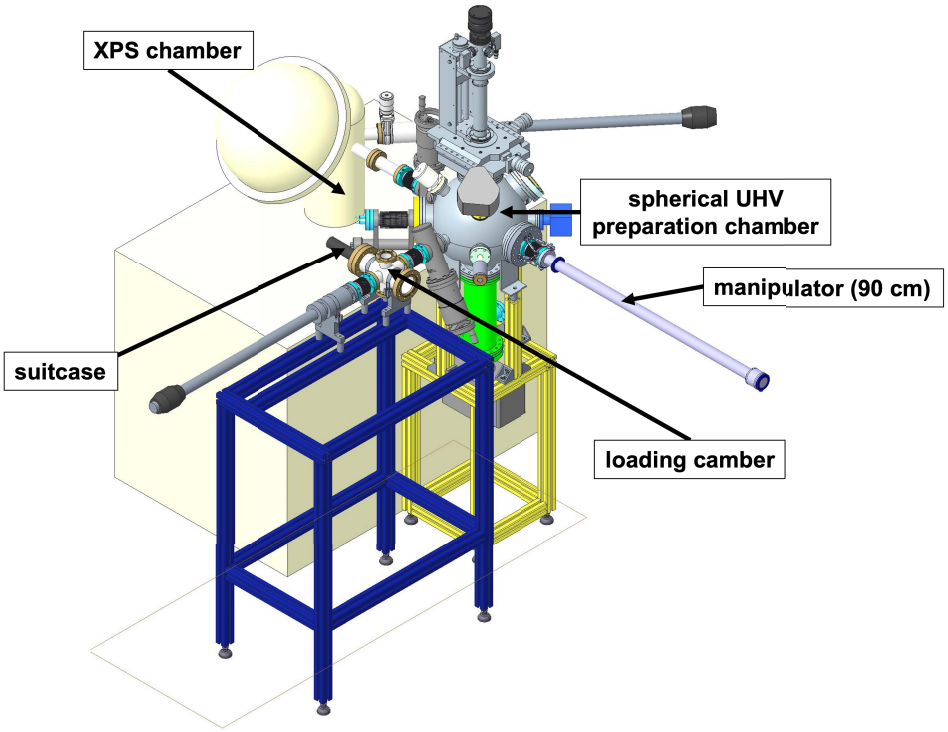

Fig. 34 3D model of the UHV preparation chamber including the loading chamber with the suitcase adaption and the connection of the XPS analysis chamber, which is represented by the white boxes (courtesy of P. Murcek).

4.2.1 Adaption Challenges between Preparation and XPS Chambers

Both chambers consist of a main spherical part where the sample is located in the chamber middle. Free flanges at the sides of both of the main spheres were used for the adaption and sample transportation between the chambers. A metal gate valve was placed between the two chambers to separate both UHV environments from each other, as shown in Figure 35. Additionally, the metal gate valve has the

aim to shield potential X-ray radiation from the X-ray dual anode of the XPS. A suitable X-ray irradiation safety and shielding protocol must be considered when the XPS chamber is opened and re-arranged for the extension of additional features such as a connection to another UHV chamber.
Both chambers should be equal in height to ensure that the connection tube and valve are aligned straight. This is necessary to prevent the bumping of the manipulator against the walls and thereby ensure safe sample transportation, as shown in Figure 35.

4.2.2 Sample Transportation under Ultra-High Vacuum

The *in-situ* transportation represented the most difficult part to ensure safe sample transportation under UHV conditions and avoid any complications such as sample dropping or bumping against the walls.
The sample is located vertically inside the preparation chamber, whereas in the XPS chamber the sample is located horizontally. Therefore, the preparation chamber was equipped with a 90 cm long manipulator with the ability to rotate the grasped sample vertically and horizontally, as shown schematically in Figure 34. When the long manipulator grasps the sample, the sample holder of the preparation chamber has to be retracted upwards to clear the way for the manipulator to move toward the XPS chamber.

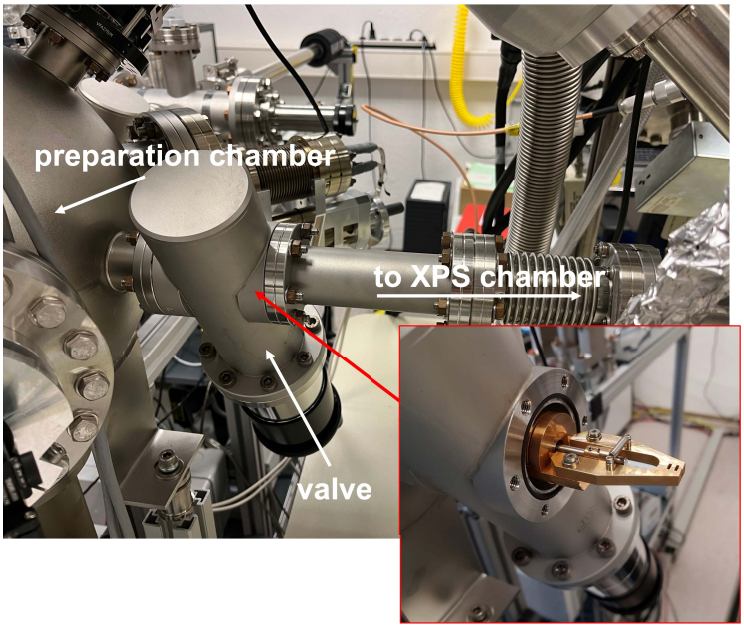

Fig. 35 Photos of the metal gate valve and adjustment of the manipulator (Cu jaws) between preparation and XPS chambers.

The valve between both chambers has to be opened and the manipulator including the sample can slowly be moved toward the XPS main chamber, as shown in Figure 35. It is necessary to move slowly to prevent any vacuum deterioration during transportation. The transportation can be followed by ethernet cameras to prevent blind driving. It is important to note that transportation along this long distance should not be carried out alone to prevent a sample bumping against the sample holders or other interior parts.

When the sample is inserted into the XPS sample holder, the manipulator is extracted back into the preparation chamber and the valve between both chambers is closed.

4.2.3 XPS Sample Puck Modification

Both chambers use different sample holders with different sample orientations. Therefore, the XPS sample holder had to be re-constructed to fit the Mo flag used in the preparation chamber. The original XPS sample holder had a discoidal shape (also called "puck") and was made of Mo on which samples can be fixed on the puck sites with Cu springs (shown in Figure 36).

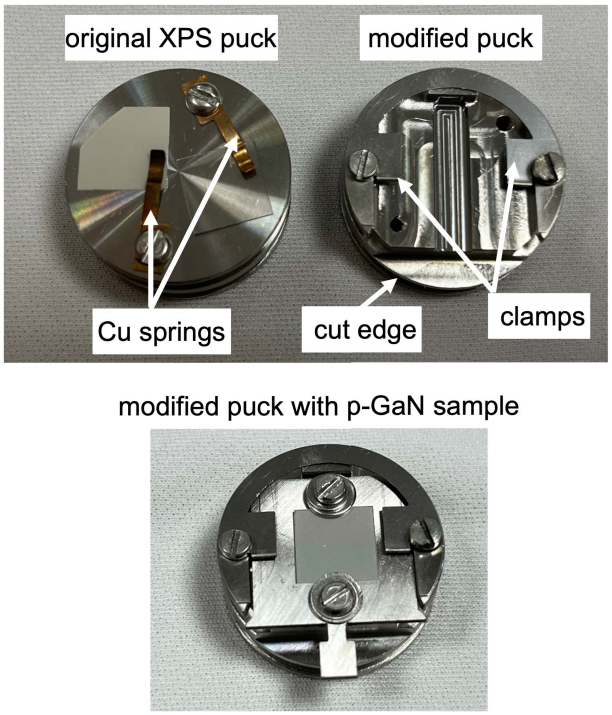

Fig. 36 Photos of the original XPS puck with GaN samples on it (left) and the modified puck with a cut edge and clamps (right) to fit the sample flag of the preparation chamber. The modified puck holding a p-GaN sample on the Mo flag is shown at the bottom.

The XPS puck was cut at an edge so that the manipulator can move far enough to put the sample flag onto the puck. Two clamps were attached to hold the flag in place and allow the manipulator to retract after the sample is placed onto the modified puck. The Mo flag is driven under these clamps and the sample flag is placed on the modified puck. The procedure of picking up the sample and placing it on the XPS puck is the most difficult part as the movements involved require high sensitivity and have to be trained.

It is essential to contact the sample properly because photoelectron spectroscopy is ion spectroscopy and the sample surface will be ionized if no proper contact is given whereby energy shifts in the spectrum or other artifacts occur from surface charging as a potential consequence.

4.3 Procedure for Ultra-High Vacuum Achievement

4.3.1 Preparation Chamber

The usage of turbo- and ion- pumps alone allow to achieve a vacuum of 10^{-9} mbar. Therefore, a so-called "bake-out" process was required to achieve UHV conditions at 10^{-10} mbar. This meant that the preparation and loading chamber had to undergo a bake-out procedure at 120–160 °C for several days. For this purpose, the activation and loading chambers were equipped with different layers consisting of Al foil, thermo-sensors, bake-out cables, a second layer of Al foil, and glass-fiber cloths to shield the hot chamber (see Figure 37). The Al foil had the aim to keep the heat from the bake-out cables onto the chamber.

Fig. 37 Photo of the preparation chamber during the bake-out procedure, wrapped with bake-out cables, layers of Al foil, and glass fiber cloths to achieve UHV conditions.

The bake-out cables were connected to a power supply and controlled by a feedback loop with thermo-sensors that were placed onto the chamber surface. The temperature was increased stepwise by applying a current through the cables. During the first day, the chamber was heated up to 120 °C to find an equilibrium at which H_2O was desorbed. On subsequent days, the system was baked-out at 160 °C, but the loading chamber part in which the suitcase was located was excluded from exposure to the 160 °C temperature because the rubber sealing of the suitcase cannot withstand higher temperatures. The manipulators were kept at 120 °C because the magnets were not made for temperatures above 80 °C. Dismounting the magnets prior to the bake-out would also be possible to prevent any magnet damage.
Figure 38 depicts the vacuum measurement against the time during the bake-out procedure. The vacuum deteriorated to 10^{-5} mbar and improved in the following days whereby the decreasing vacuum was an indicator of the successful removal of adsorbates inside the chamber. The manipulators in the loading and preparation chambers were moved slightly to ensure the complete removal of H_2O in these locations.

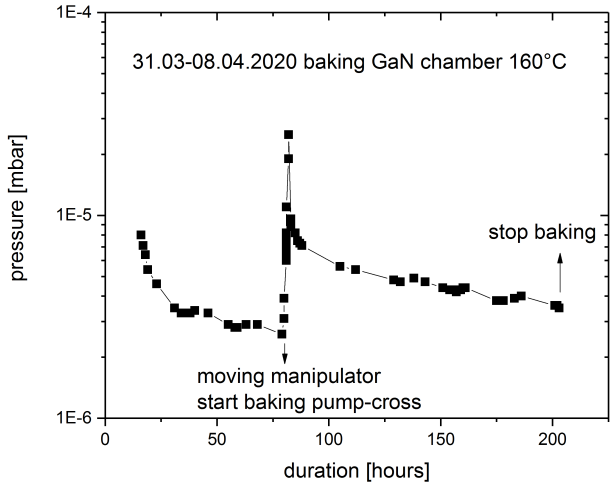

Fig. 38 Vacuum curve as a function of time during the bake-out procedure of the preparation chamber.

The bake-out was stopped after 200 hours and the NEG pump was regenerated. NEG pumps contain a mixture of different metals and metal alloys (Al, Zn, iron (Fe)) that have to be activated once in an activation process at a high temperature which meant that the NEG pump has to be heated to approximately 400 °C for 1 h. Afterward, the pump is able to absorb gases and molecules and provide a UHV environment.
The halogen lamp, steel anode, and Cs dispensers were outgassed by applying a current through them for a few minutes.

4.3.2 XPS Chamber

The bake-out procedure for the XPS chamber was easier compared to that of the preparation chamber as the XPS chamber had a bake-out tent and integrated heating tubes and fences. The tent had to be thrown over the main parts of the XPS chamber, as shown in Figure 39. The bake-out button was subsequently switched on which started the heating and its distribution through the fences. Integrated thermo-sensors regulated the temperature with a feedback loop and the external load-lock of the XPS was excluded from the bake-out altogether.

4.4 Status-Quo

The current status of the preparation and XPS chambers is shown in Figure 40. The swiveling sample holder including a p-GaN sample on the Mo flag is located in the middle of the preparation chamber and the sample holder is retractable upwards to clear the way for the 90 cm long manipulator to drive forward into the XPS chamber. The sample holder also provides a heating option and an optional N_2 cooling from the backside.

The improved steel ring anode and two Cs dispensers are shown on the right side in Figure 40. The steel anode could be outgassed after each bake-out to keep the anode surface contaminant-free and prevent a vacuum deterioration during pho-

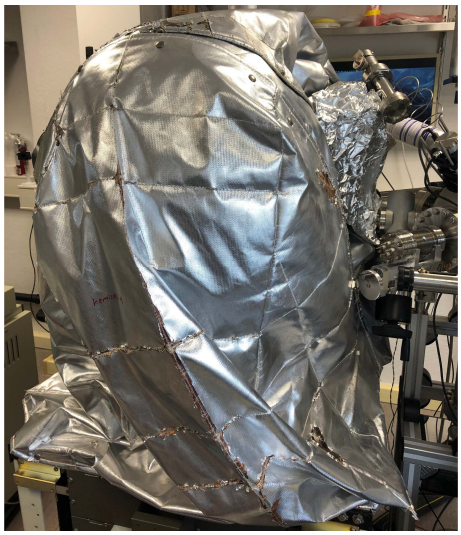

Fig. 39 Photo of the XPS chamber with its bake-out tent for the achievement of UHV conditions.

tocurrent measurements. The halogen lamp, surrounded by the steel reflector, is located behind the sample. The reflector is used to focus the heat onto the sample without warming up the chamber walls. The Cu head of the 90 cm long manipulator which grasps the sample flag and transports it into the XPS chamber is shown on the left side in Figure 40.
In the XPS chamber, the sample flag is placed onto the modified XPS sample puck and the manipulator is retracted after which the sample is ready for XPS analysis.

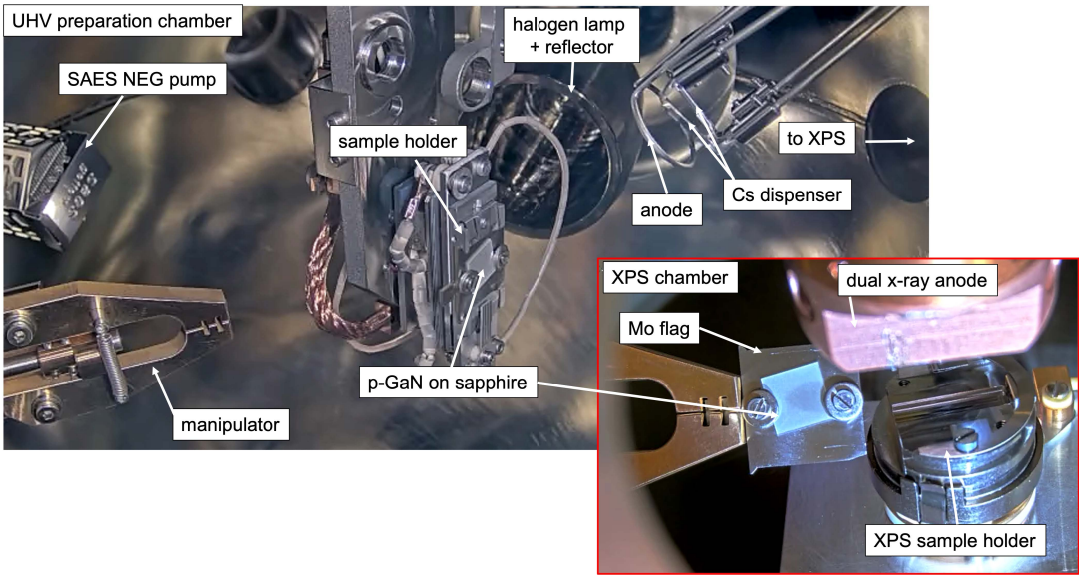

Fig. 40 The interior of the UHV preparation chamber (showing a sample holder, a halogen lamp with a reflector, a steel ring anode, and Cs dispensers) and the XPS analysis chamber connected to the preparation chamber via a manipulator.

5 Materials and Experimental Parameters

5.1 p-GaN

5.1.1 Specifications of the Samples Used

Several commercially available p-GaN samples were grown by MOCVD on different substrates such as sapphire, Si, and TiN [113]. All samples contained a different Mg concentration and thus had a different carrier concentration. They also vary in their layer structures, as shown in detail in Table 1. A GaAs sample that contained a Zn doping for its p-type was also measured. For GaAs and some GaN samples, no specifications were provided by the supplier and thus no values can be given here.

Tab. 1 p-GaN samples used with their properties (if known).

p-GaN thickness (μm)	substrate (μm)	buffer layer (μm)	Mg conc. (cm^{-3})	carrier conc. (cm^{-3})
5 μm	625 μm sapphire	-	N/A	6 x 10^{16} - 1 x 10^{17}
2 μm	430 μm Si	0.8 μm AlGaN	2 x 10^{19}	-
N/A	TiN	n-GaN	N/A	2 x 10^{17}

The cleaning process consisted of several steps, starting with a wet chemical cleaning, followed by a vacuum thermal cleaning at various temperatures, going to the activation with Cs and ended with the measurement of the storage lifetime.

5.1.2 Wet Chemical Cleaning

The p-GaN samples were processed by a wet chemical cleaning step to ensure successful activation. The purpose of wet chemical cleaning was to remove residual attached contaminants such as air molecules or dust particles from the surface. Several solvents such as methanol (CH_3OH), iso-propanol (C_3H_8O), C_3H_6O, and EtOH were studied to determine their effect on the p-GaN surface. Additionally, the effect on the semiconductor surface of etchant solutions, such as hydrofluoric acid (HF) and "piranha" solution (H_2SO_4:H_2O_2) was studied, because these etchants are commonly applied in the semiconductor industry.
The p-GaN samples were cleaned in 99 % pure EtOH in an ultrasonic bath for 15 min. Afterward, the samples were treated with a mixture of H_2SO_4 (98 %) and H_2O_2 (30 %) (1:1 by volume), a so-called "piranha" solution, at 140 °C for 15 min before the semiconductors were etched in a 0.5 % or 40 % HF solution for two minutes and subsequently rinsed in a H_2O bath for a minimum of 10 min. In the last step, the samples were dipped into EtOH and a mixture of benzol (C_6H_6)/C_3H_8O (1:3 by volume).
An alternative cleaning process with only "piranha" solution was carried out to avoid handling of hazardous HF acid. Therefore, the p-GaN samples were cleaned in 99 % pure EtOH in an ultrasonic bath for 15 min. Afterward, the samples were

treated with a "piranha" solution at 140 °C for 15 min. In the last step, the samples were dipped into HCl (36 %) and rinsed with deionized H_2O and 99 % EtOH.
The "piranha" solution is a strong oxidizing agent and can remove most organic contaminants, whereas HCl removes metal ions from the surface.
Not all samples and substrates were acid resistant, such as GaAs and p-GaN on TiN, and thus these samples were only cleaned in an ultrasonic bath with 99 % EtOH. The effect of the wet chemical etching process was studied by AFM, XPS, and SEM measurements.

5.1.3 Thermal Cleaning

The wet chemically cleaned samples were mounted with steel washers on the Mo flag and were transported under a dry N_2 atmosphere into a UHV chamber. In the UHV chamber, a thermal cleaning was carried out using a 400 W halogen lamp with a metal reflector. The temperature on the p-GaN surface was measured with an IR sensor.
Alternatively, some samples were thermally cleaned through their substrate via a thermo element from the backside.
The thermal cleaning process could be followed by monitoring the vacuum. Prior to the thermal cleaning process, the pressure of the UHV chamber is 3×10^{-10} mbar on average. Depending on the applied current to the halogen lamp or thermo element, an increase in the vacuum indicated a release of desorbed gases or molecules. The thermal cleaning was carried out at a minimum of 30 min for each sample and at different temperatures. The samples were analyzed concerning their surface quality and compared according to the applied thermal cleaning temperature and the QE values obtained.

5.1.4 Activation Process with Cesium

After the wet chemical and thermal cleaning, the sample was activated with Cs to obtain an NEA surface to produce a p-GaN:Cs photocathode. The p-GaN was activated with a thin layer of Cs when it was cooled down to room temperature. The thermal cleaning was repeated in every activation cycle. The current applied through the Cs dispenser caused a partial vacuum deterioration which stabilized again after several minutes. The current was increased stepwise until no gases were desorbed anymore and a constant Cs flux was guaranteed. The typical Cs dispenser currents were between 3–4 A and the deposition process was monitored by *in-situ* photocurrent measurements. In the beginning, no photocurrent was detected after the Cs deposition had been started. After 10–20 min, the photocurrent started to rise slowly and steadily until it reached a maximum. An aperture reduced the UV-light power and consequently the photocurrent during the Cs deposition, which was a relief for the vacuum. In the end, when the photocurrent reached a maximum, the aperture was opened to take the maximum photocurrent value.

YoYo Activation

The YoYo activation represented a special requirement for achieving an NEA surface of GaAs. Furthermore, this process was tested on p-GaN samples although O_2 was not required for a successful activation of p-GaN. The YoYo process consisted of the sequential deposition of Cs and O_2, shown as an example in Figure 21. The deposition of Cs and O_2 was monitored by *in-situ* photocurrent measurements. At first, Cs was deposited which was followed by a deposition of O_2. Afterward, the Cs and O_2 deposition was repeated several times until a final photocurrent was achieved.

5.1.5 Re-activation Process

After the photocathode was measured in its degradation, meaning the lifetime and thus the QE decay, the photocathode was thermally cleaned again and once more activated with Cs, and optional O_2 was applied. The procedure of thermal cleaning, activation, and lifetime measurement was defined as one cycle. Therefore, one sample can be re-used several times and was studied in its photocathode quality compared to its first activation cycle.

5.2 Crystal Growth of Cs_2Te

5.2.1 Preparation Chamber of Cs_2Te without Analytical Capabilities

The Cs_2Te preparation chamber was located in the cleanroom to ensure a particle-free environment and thus to prevent any dust particles from being released in the particle accelerator. An image of the main parts inside the Cs_2Te chamber is shown in Figure 41.

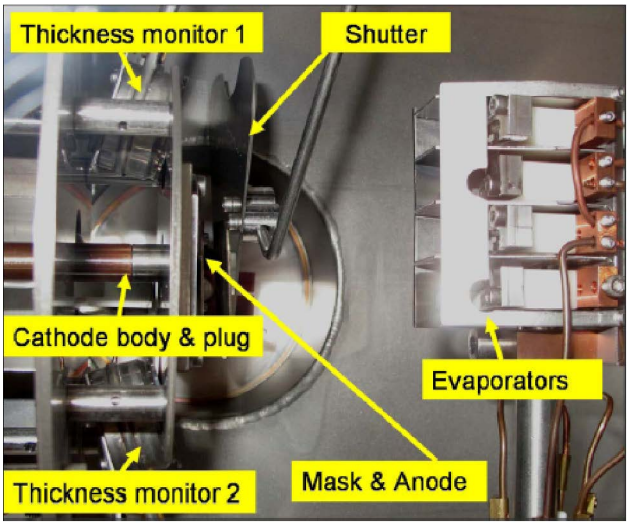

Fig. 41 The interior of the Cs_2Te preparation chamber, showing a cathode body with a plug, shutter, a mask which is also an anode, two thickness monitors, and Cs and Te evaporators.

The chamber contained a 15 cm long Cu cathode body on which a substrate plug was screwed at the front. In front of the cathode body, there was a ring anode which

was also used as a mask. A shutter protected the cathode from laser irradiation and the evaporator flux. Six evaporators from SAES® were placed in front of the cathode body with a plug on it, as shown in Figure 41. Two of them contained Te and the other four contained Cs. Twice as much Cs as Te was needed for the production of Cs_2Te. Two monitors detect the Te and Cs layer thickness by a quartz crystal microbalance.
A transport chamber was adapted to the preparation chamber and separated in the vacuum by a metal gate valve. The transport chamber can store up to six cathodes simultaneously and was used to store the photocathodes after production because it provided a better vacuum than the preparation chamber. Furthermore, the chamber transported the Cs_2Te cathodes into the SRF Gun II.

5.2.2 Substrate Preparation

Prior to the Cs_2Te deposition, a clean and smooth substrate surface was required to ensure a high photocathode quality. Cu and Mo are both suitable substrates for Cs_2Te. At HZDR, Cu was used as a substrate which consisted of a 7–8 mm long Cu plug which had a diameter of 10 mm.

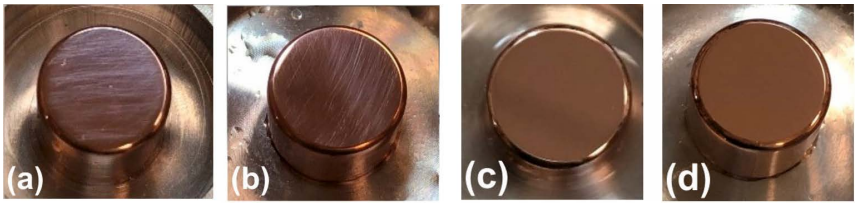

Fig. 42 Photos of the polishing results on the Cu surface after each polishing step.

The Cu needs to be polished to a mirror-like surface prior to the Cs_2Te deposition. Different polishing cloths and SiC suspensions were used on the Cu surface in a TEGRAMIN polishing machine. The surface roughness after the final polishing step is about 20 nm. The optical result of the polishing steps is shown in Figure 42 while the detailed polishing steps are summarized in Table A 6 in the Appendix.

5.2.3 Preparation of Cs_2Te

The preparation process of Cs_2Te at HZDR was oriented according to the original approach developed by Istituto Nazionale di Fisica Nucleare (INFN) from Di Bona [65]. The mirror-like polished Cu plug was screwed on the cathode body and loaded into the UHV preparation chamber. Prior to the Cs_2Te deposition, the Cu plug was heated up to 250 °C for several hours to desorb any residual gases or molecules from the Cu surface. Afterward, the Cu temperature was kept at 120 °C.
Outgassing of the evaporators was necessary to degas the adsorbed gases whereby rest molecules might be incorporated as impurities into the grown Cs_2Te film and change the photoemissive properties if no outgassing was applied.
The relevant parameters that were observed during the Cs_2Te preparation process are shown in Figure 43. The green line shows the monitored thickness of the deposited layer while the power applied to the evaporator (Te or Cs) is shown in magenta. The temperature of the Cu substrate is shown in orange and the black line represents the measured vacuum inside the preparation chamber. The vacuum

was kept below 6×10^{-9} mbar during the whole preparation process. A Te layer of 8 nm thickness was first deposited on the Cu substrate at a temperature of 120 °C. A voltage of 100 V was applied to the anode, and the Cu plug including its Te layer was illuminated by a UV-LED at a wavelength of 260 nm and 340 nm to measure the *in-situ* photocurrent during the Cs deposition, as shown in Figure 44.

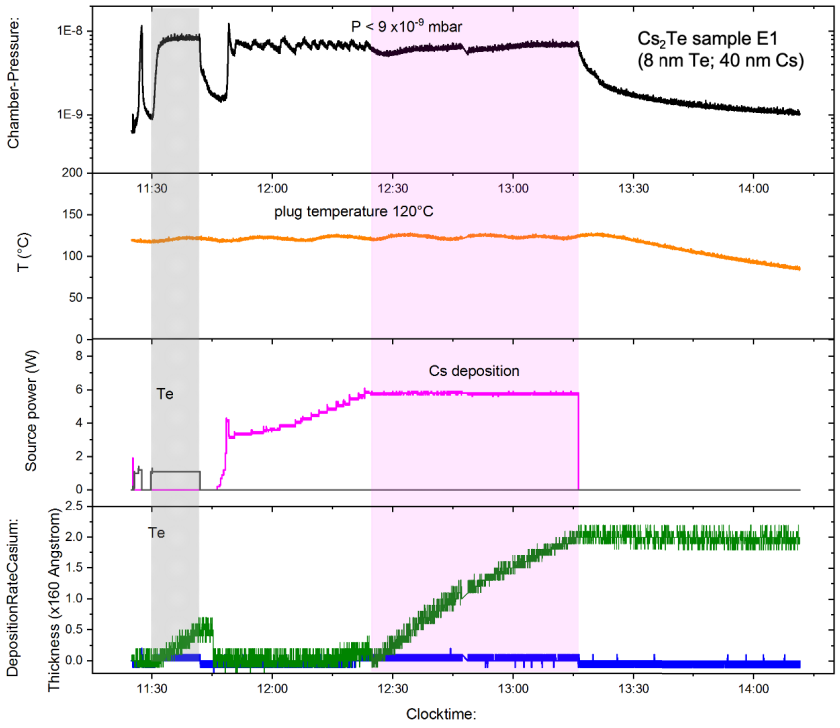

Fig. 43 Monitored parameters during the preparation of a Cs_2Te photocathode (sample E1), measured Cs and Te thickness (green), dispenser power (magenta), Cu temperature (orange), and vacuum curve (black).

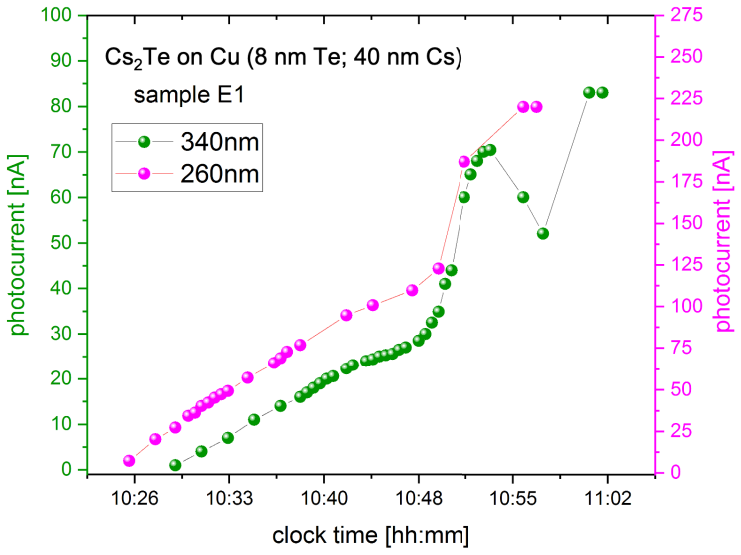

Fig. 44 *In-situ* photocurrent curves of Cs_2Te (sample E1) during the deposition of Cs when illuminated with UV-light at a wavelength of 340 nm (green) and at 260 nm (magenta).

The photocurrent increased slowly at the beginning of the Cs deposition, for both wavelengths. After reaching a maximum, the photocurrent decreased whereby the maximum in the photocurrent was observed more clearly at a wavelength of 340 nm than 260 nm. However, the maximum indicated that the cathode was saturated with Cs and thus the Cs deposition was stopped. A 40 nm thick Cs layer was applied to the 8 nm thick Te layer. It should be noted that the thicknesses did not correlate with the chemical composition of the Cs_2Te film.
The freshly prepared Cs_2Te photocathode was subsequently stored in the transport chamber. Figure 45 shows a photo of the freshly deposited Cs_2Te layer on the Cu substrate. The Cs_2Te film was observed as a 4 mm spot in the middle of the 10 mm Cu plug. The borders of the 4 mm spot appeared darker because the deposited layers (Te and Cs) did not overlap exactly and were slightly offset. Thus, these border areas had a locally different thickness. The surface morphology of these offset border areas was assumed to have a different QE than the cathode center and was later studied in detail with SEM and EDX in Section 8.2.3.

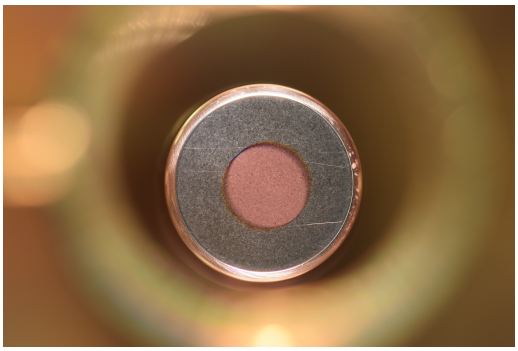

Fig. 45 Photo of a freshly deposited Cs_2Te layer (4 mm in diameter) on a Cu plug (10 mm in diameter).

5.3 Instrumental Parameters of the Analytical Methods

5.3.1 *In-Situ* XPS

The UHV preparation chamber was directly connected to an XPS, as shown in Figure 34 and Figure 40, and the sample surface was studied after each treatment step. The sample was transported under UHV conditions from the preparation chamber into the XPS chamber via a manipulator. The XPS sample holder was a home-built construction fitting the Mo flag with the sample on top.

XPS experiments were performed using an X-ray photoelectron spectrometer (PHI 5600) at an average pressure of 5×10^{-9} mbar. The XPS spectra were conducted using an Al K_α line ($hv = 1486$ eV) and a Mg K_α line ($hv = 1254$ eV) from a non-monochromatized dual X-ray source with a 4 mm aperture. The XPS spectra were collected using a commercial system equipped with a hemispherical energy analyzer. Survey spectra were taken with a pass energy of 117.4 eV and a step energy of 1.0 eV while detailed spectra were taken with a pass energy of 58.8 eV and an energy step of 0.25 eV. The energy scale was calibrated to the peak positions of Cu $2p_{3/2}$ and gold (Au) $4f_{7/2}$. The fitting of the experimental data was obtained using Casa XPS© and a Gaussian–Lorentzian shape with a fixed area ratio of 1.5. A Shirley background was applied to all spectra.

5.3.2 *Ex-Situ* AFM

The AFM images were taken on an Asylum Research Cypher AFM Microscope in AC mode (tapping mode) with an AC-160 cantilever (Si with an silver (Ag) coating, tip radius of 10 nm). The measured area of the sample surface was 0.2 to 30 μm with a resolution of 256 or 512 points whereby 1 Hz was used for the tip frequency and 285–287 kHz for the drive frequency. All AFM images have different set points and drive amplitudes.
Gwyddion (Version 2.53) was used for the evaluation of the AFM images and for the prediction of the surface root mean square (RMS) roughness.

5.3.3 *Ex-Situ* SEM/EDX

The SEM images were captured using a Zeiss NVision 40 FIB/SEM microscope with an electron beam energy of 10–20 kV and an SE or Inlens (BSE) detector. The semiconductor samples were grounded with Cu tape on the SEM sample holder to ensure the conductivity of the samples.

The EDX measurements were performed at a working distance below 10 mm and carried out with a Bruker QUANTAX EDS spectrometer.

6 Surface Characterization of p-GaN on Sapphire

This section is the main chapter of the thesis and deals with the intensive study and surface characterization of p-GaN on sapphire. A detailed study was carried out on p-GaN grown on sapphire because of its low costs and widespread availability.

The sample treatment in this work consisted of several steps, starting with a wet chemical cleaning, followed by a vacuum thermal cleaning, going to the activation, and subsequently the measurement of the degradation of the p-GaN:Cs photocathode. Each treatment step is discussed separately in the following sections and all sample series are compared regarding the QE values achieved and the storage lifetimes.

Special attention was paid to the degradation mechanism of the p-GaN:Cs photocathodes influenced by remaining surface C contaminations. Furthermore, the influence of X-ray irradiation on photocathode performance was determined in lengthy X-ray experiments.

6.1 Surface Analysis of As-received p-GaN Wafer

Figure 46 shows the surface of an untreated as-received p-GaN on a sapphire sample. The p-GaN sample exhibited a smooth, well-defined, uniform surface with an average RMS roughness of 1.7 nm for the examined area (see Figure 46 on the left side). Bright spots that correspond to intersections of screw-component dislocations were found all over the surface. These dislocations create step terminations and cause lattice defects, which were the reason for hillock formations [78]. The AFM measurements were carried out at different surface areas and on several samples to improve the statistical accuracy.

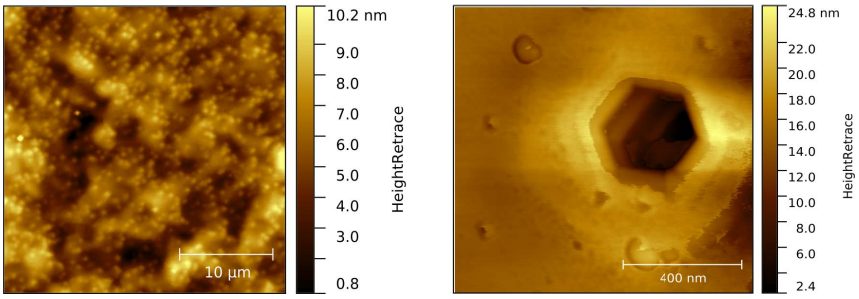

Fig. 46 AFM images of original p-GaN surface grown on sapphire by MOCVD, as received from Xiamen [113].

Additionally, dark spots were detected on the p-GaN surface. These correspond to dislocations within the crystal growth (see Figure 46 on the right side). This so-called etching pit exactly represented the hexagonal crystal structure of the GaN lattice and became visible when the surface was etched with oxidizing detergents [79–81]. The observed pit had a width of 360 nm and a depth of several μm, which indicated that these hexagonal void holes result from poor coalescence at the beginning of the crystal growth.

In addition, SEM was used to study the original p- GaN surface. In the SEM image (see Figure 47), the original p-GaN surface exhibited a smooth and uniform surface. Etch pits were also observed in SEM, confirming the hexagonal shape of these pits.

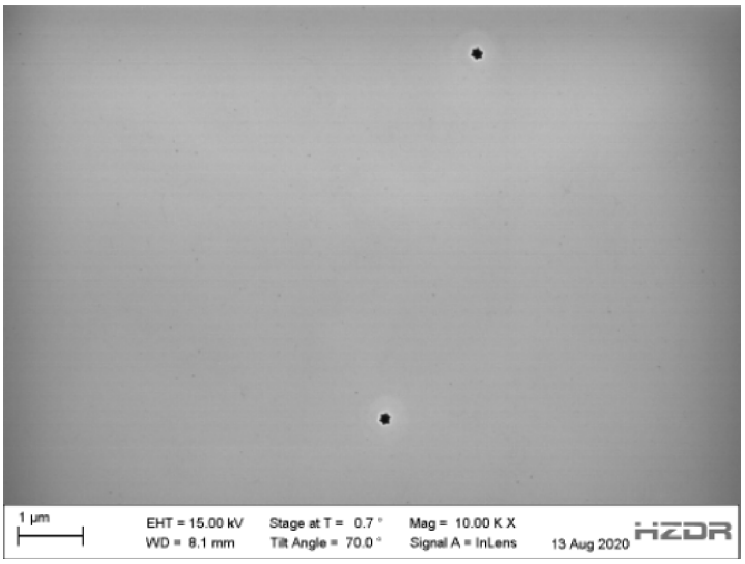

Fig. 47 SEM images of the original p-GaN surface that was grown on sapphire.

6.2 Influence of the Wet Chemical Cleaning

The p-GaN samples were processed by a wet chemical cleaning to ensure successful activation. The purpose of wet chemical cleaning was to remove residual attached contaminants, such as air molecules or dust particles, from the surface. Several different cleaning processes of the GaN on the sapphire surface were carried out and studied by AFM and SEM. It was essential to remove almost all adsorbed gases such as O_2 and other particles that were attached to the surface before the sample was transported into the preparation chamber.

6.2.1 Surface Analysis after Solvent Cleaning

The p-GaN samples were cleaned with different solvents such as CH_3OH, C_3H_8O, C_3H_6O, and EtOH in an ultrasonic bath for 15 min and were studied immediately using AFM to follow the cleaning effect on the surface. AFM images from the cleaned p-GaN on sapphire surfaces treated with these simple solvents are summarized in Figure 48.
The AFM images revealed that, in most cases, after cleaning with such solvents the p-GaN surface did not yield a sufficient result. The surface was inhomogeneous and showed many round irregularities when it was cleaned with CH_3OH, C_3H_8O, and C_3H_6O. These inhomogeneities led to an increase in the surface roughness and it seemed that even more molecules were attached to the p-GaN surface after this cleaning than before. An SEM image of a p-GaN surface cleaned with C_3H_6O is shown in Figure 49. The SEM image revealed several dark spots on the surface that confirmed the AFM measurements.
In contrast, the p-GaN surface showed a different effect when it was cleaned with 99 % pure EtOH as a smooth surface with typical hillocks was observed. The p-GaN surface looked almost the same as the original surface after cleaning with EtOH, shown in Figure 46. Cleaning with EtOH was shown to be the optimal approach.

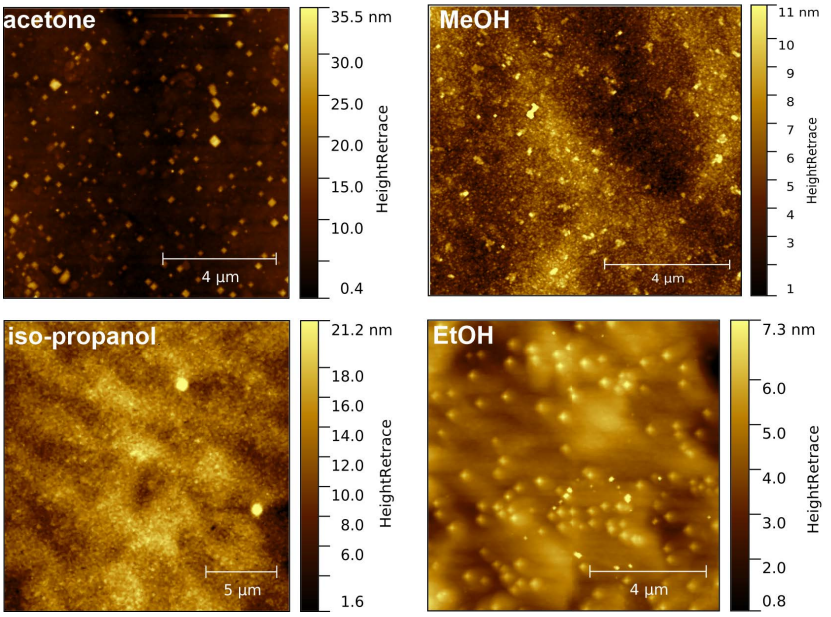

Fig. 48 AFM images of the p-GaN, grown on sapphire, surface cleaned with C_3H_8O, CH_3OH, C_3H_6O, and EtOH.

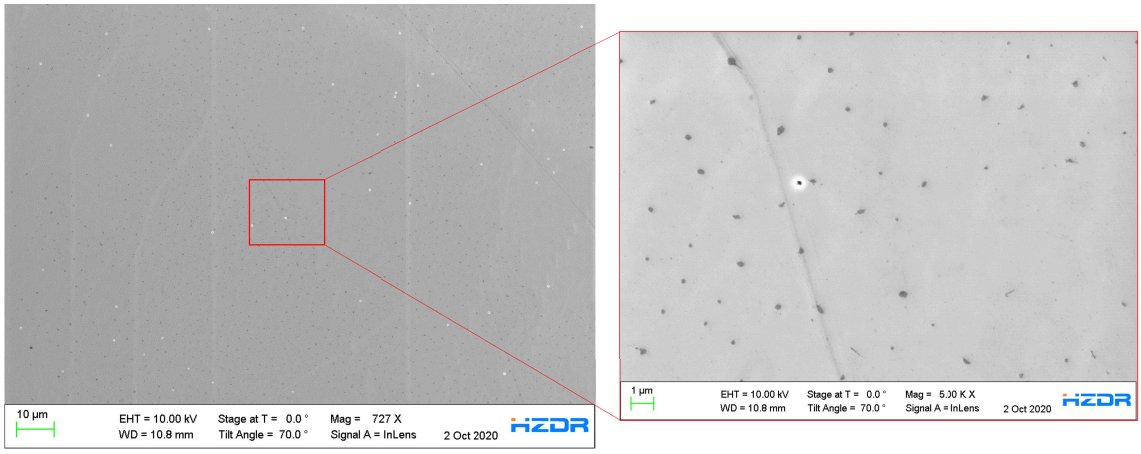

Fig. 49 SEM images of p-GaN on sapphire after cleaning in C_3H_6O in an ultrasonic bath.

6.2.2 Hydrofluoric Acid (HF) Cleaning

An etching process using HF was tried, which is a common and widely used cleaning process in the semiconductor industry, to develop a suitable wet chemical cleaning approach for the p-GaN surface.This cleaning procedure is described in Section 5.

The p-GaN surface was significantly influenced by the HF solutions used with different concentrations, namely 0.5 % and 40 % (see Figure 50). The p-GaN surface was very smooth and less rough when 0.5 % HF was used. In contrast, the surface roughness increased and the smooth surface disappeared when 40 % HF was used to clean the p-GaN surface.

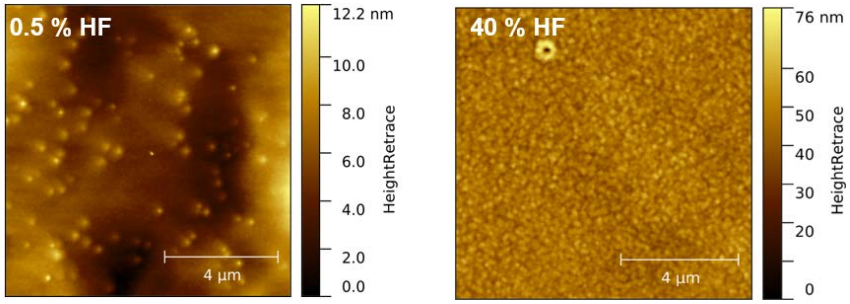

Fig. 50 AFM images of the p-GaN surface after cleaning in 0.5 % and 40 %HF solution.

With SEM, large crystals of several μm in size were found on the p-GaN surface after cleaning with 0.5 % HF (see Figure 51). A treatment with HF solution led to an etching of the first top p-GaN layers, causing an increase in the surface roughness. Additionally, it seemed to cause the formation of surface crystals when the etched surface is exposed to air. The cleaning with HF solution might be a good choice when air can be excluded to avoid the growth of such surface crystals. However, a wet chemical cleaning approach without using highly toxic HF acid is desirable.

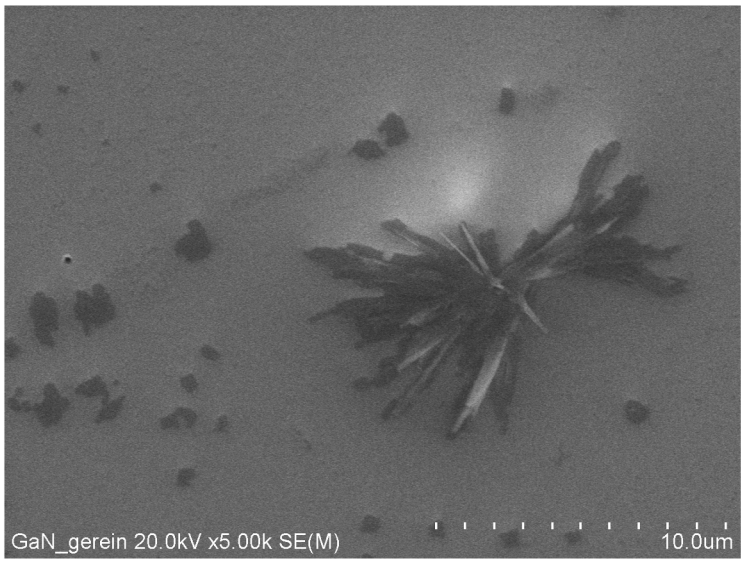

Fig. 51 SEM images of a p-GaN surface after a cleaning in 0.5 % HF solution and exposure to air.

6.2.3 "Piranha" Cleaning

A wet chemical cleaning was carried out in which "piranha" solution was used instead of HF. The effect of the wet chemical etching process with the "piranha" solution was studied using AFM measurements that were processed under a normal air environment. After cleaning with the "piranha" solution, the samples were dipped into HCl and rinsed in H_2O and EtOH, as described in Section 5.1.2.

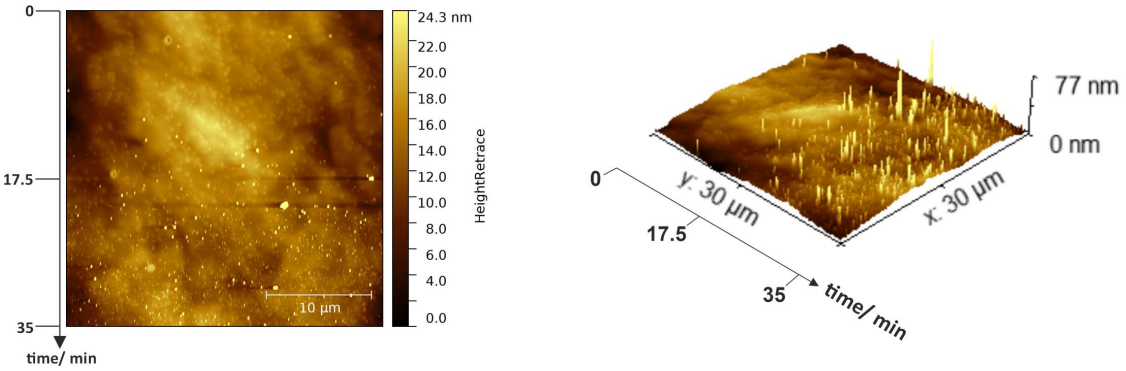

Fig. 52 *In-situ* AFM images of a cleaned p-GaN surface showing the appearance of surface peaks with ongoing exposure time under an air environment.

At the beginning (on the left of the AFM image in Figure 52), the surface was still smooth and had many hillocks that represented screw dislocations in the hexagonal crystal structure. At this stage, the surface had an average RMS roughness of 1.7 nm, which is similar to that of the untreated sample (Figure 46). During the ongoing measurement, some additional bright peaks became visible, whose appearance was even more pronounced with the measurement time. At the end of the measurement, at the bottom of the image, the surface was completely covered with bright peaks. These bright peaks contain a maximum height of approximately 77 nm and are illustrated more clearly in the 3D AFM image (see Figure 52, right side). It was assumed that the wet chemical cleaning uncovers free, unbound Ga atoms on the p-GaN surface. With exposure to O_2, these free Ga atoms start to form gallium oxide (Ga_xO_y) on the surface. With increasing time, these islands were converted into a homogeneous oxide layer that covered the complete p-GaN surface. As a result, the importance of O_2 exclusion was clearly observed in these experiments.

In the following experiments, all samples were immediately prepared and transported under a dry N_2 environment after the wet chemical cleaning with "piranha" solution to prevent this oxidation process.

Surface Composition (XPS)

The XPS spectra of O 1s, C 1s, and Ga $2p_{3/2}$ are shown in Figure 53 as a comparison between the original and wet chemically cleaned surfaces. The spectra were normalized to their backgrounds to be comparable in the intensities of the related photoemission peaks.

The original p-GaN surface represented the p-GaN surface prior to any treatment. The XPS spectra of the original p-GaN surface were deconvoluted into three sub-peaks. In the O 1s photoemission spectrum, the main peak was located at a BE of 532 eV and accompanied by a small shoulder at 529 eV, which was derived from a less intense photoemission peak of Ga_xO_y. The third sub peak was located at a BE of approximately 534 eV, which was caused by adsorbed H_2O or a carbonyl (C=O) compound.

A C peak at 284.9 eV was found in the C 1s spectra, which was derived from adventitious C. At a higher BE, a small shoulder at 286.4 eV was observed, which corresponded to a hydroxyl (C–OH) compound.

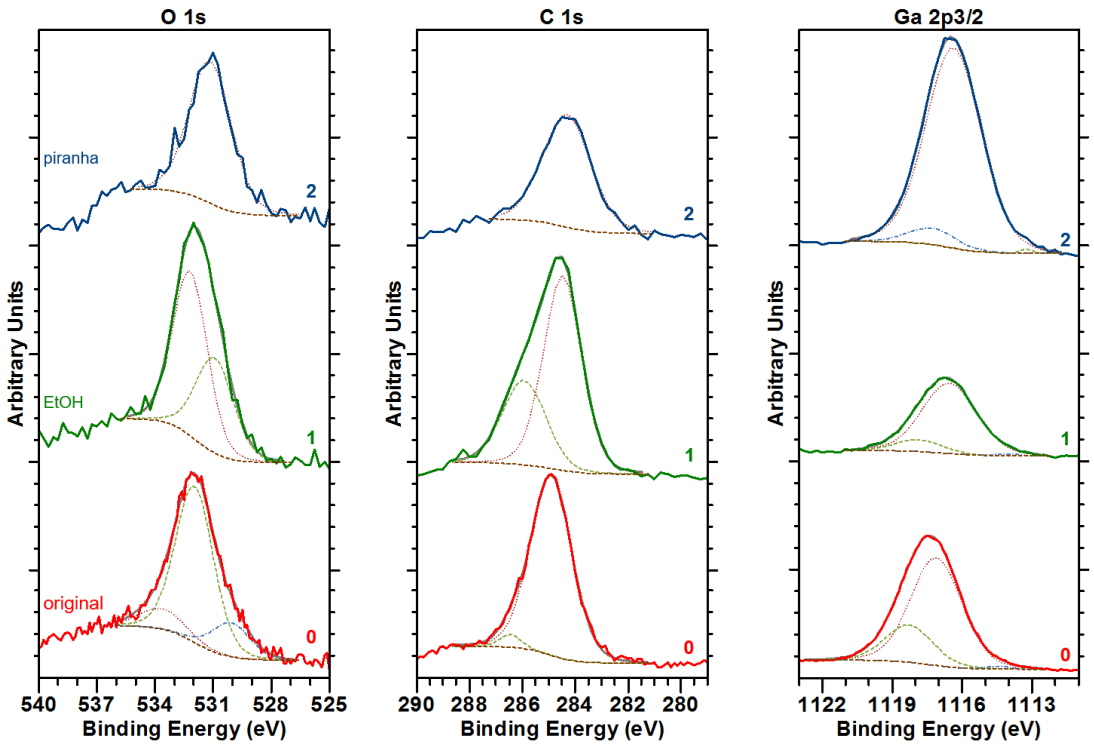

Fig. 53 O 1s, C 1s, and Ga $3d_{3/2}$ photoelectron spectra for the original p-GaN surface (line 0), cleaned with EtOH only (line 1) and after a "piranha" cleaning procedure (line 2).

The Ga $2p_{3/2}$ peak showed a deconvolution into two components. The main peak was located at approximately 1117 eV and caused by the GaN component, while the sub peak at 1118.5 eV was derived from a Ga_xO_y component.
The N 1s spectra were not shown because the Al excitation was inconvenient, as it led to the superposition of the photoemission N 1s peak and the Auger Ga electron transition between L- and M- shells (LMM). Therefore, it was difficult to predict a proper fitting for the N 1s photoemission peak.
Compared to the original p-GaN surface, the O 1s and C 1s photoemission peaks increased when the p-GaN was cleaned with 99 % pure EtOH whereby especially the C component at 284.5 eV increased (line 1 in Figure 53). A broad shoulder at 286 eV derived from C–OH components of EtOH was observed. The O 1s peak showed a splitting into two components. One of the sub peaks arose from adsorbed molecular O_2 (530.9 eV), while the other sub peak was derived from a C–OH compound (532.2 eV) in the 99 % pure EtOH solution. The decrease of the Ga $2p_{3/2}$ peak intensity was therefore caused by the C and O contamination layer of the solvent residuals from the EtOH solution on the p-GaN surface.
Less O and C were yielded when the p-GaN surface was treated with “piranha” solution and the C–OH compound at 286 eV, which appeared for the EtOH-cleaned surface, disappeared almost completely.
The Ga $2p_{3/2}$ peak at a BE of 1118.5 eV disappeared almost completely which meant that the Ga_xO_y compound was also reduced due to the “piranha” cleaning. Additionally, the O concentration was also reduced because the O 1s peak intensity decreased after the cleaning with the “piranha” solution. Therefore, the “piranha” cleaning was able to reduce the C and O contamination layer on the p-GaN surface

and consequently, the Ga $2p_{3/2}$ intensity increased.
After the "piranha" treatment, a shift toward lower BEs in all XPS photoemission peaks was observed, which was an effect of the reduction of C and O compounds on the p-GaN surface.

The wet chemical cleaning using the "piranha" procedure was an efficient pre-cleaning step to reduce the C and O concentration on the p-GaN surface. In contrast, using EtOH only led to an increase of O and C as solvent residuals remaining on the p-GaN surface.

6.3 Influence of the Thermal Cleaning

6.3.1 Surface Analysis after Halogen Lamp Irradiation

Because an atomically clean surface was not achieved by a wet chemical cleaning, the p-GaN sample underwent a subsequential thermal cleaning. The temperature was measured on the p-GaN sample surface via an IR sensor, which was calibrated for semiconductor surfaces.

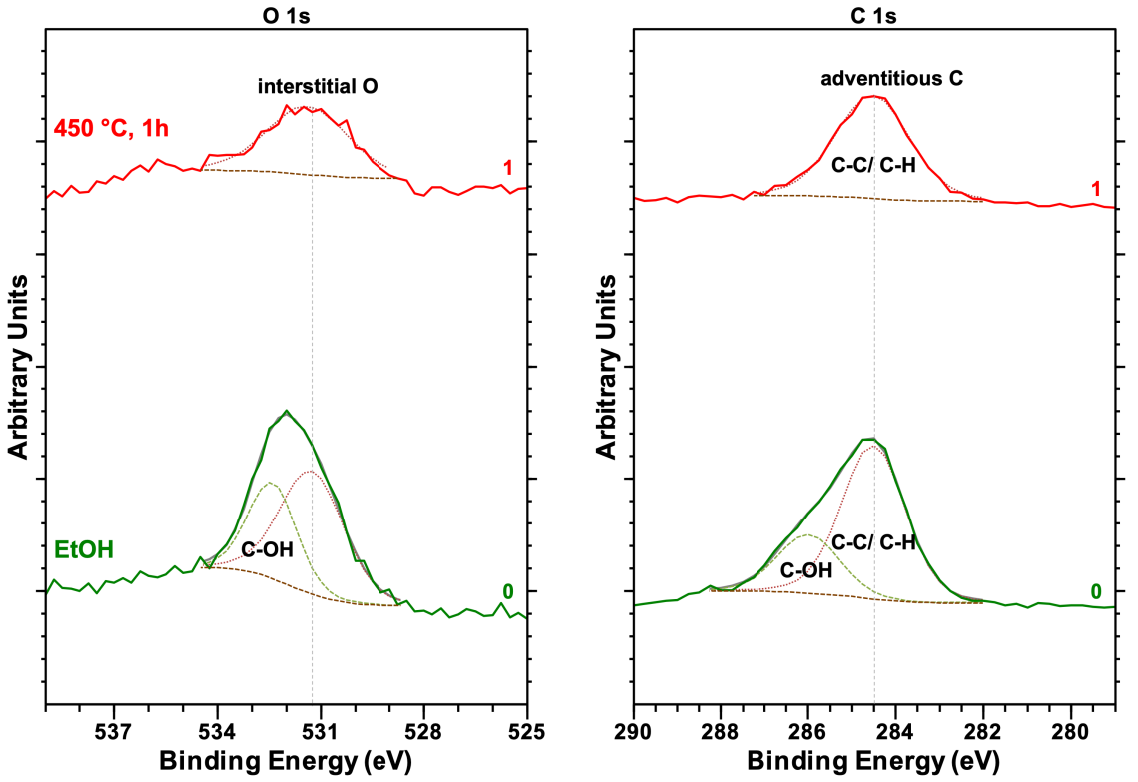

Fig. 54 O 1s and C 1s photoelectron spectra for the p-GaN surface cleaned with EtOH (line 0) and after thermal cleaning at 450 °C (line 1).

Detailed XPS spectra of O 1s and C 1s spectra of the p-GaN surface cleaned with 99 % EtOH (line 0) and of the p-GaN surface, thermally cleaned at 450 °C (line 1) are compared in Figure 54. The O 1s photoemission peak showed a splitting into two components for the EtOH-cleaned p-GaN surface. The sub-peak at 531.4 eV was assigned to adsorbed O_2 and other O compounds, and that at a BE of 532.2 eV to a C–OH compound.
The C 1s peak displayed the main C component at 284.5 eV, which is derived from

adventitious C. Besides this main C peak, a broad shoulder at 285.9 eV resulting from C–OH components of EtOH was observed. The contaminations were reduced in their peak intensities, when the p-GaN surface was thermally treated at 450 °C for 1 hour (see line 1 in Figure 54). The C–OH compound disappeared completely in both spectra, in the O 1s and C 1s, respectively, and only a small O peak remained on the p-GaN surface. It was assumed that this O peak originated from interstitial O in the sublayers of the crystal lattice as an unwanted impurity from the growth by using MOCVD. Furthermore, the C was not removed completely, but the C 1s peak was reduced in its peak intensity by the thermal cleaning. Therefore, an atomically clean surface was also not achieved by a vacuum thermal cleaning. However, the thermal cleaning reduced the C and O contaminations in their peak intensities which meant that they must be lowered in their relative concentrations on the p-GaN surface.

6.3.2 Surface Analysis after Backside Heating

The p-GaN layer was furthermore studied by a vacuum thermal cleaning at different temperatures through the sapphire substrate by using a thermo element from the backside.

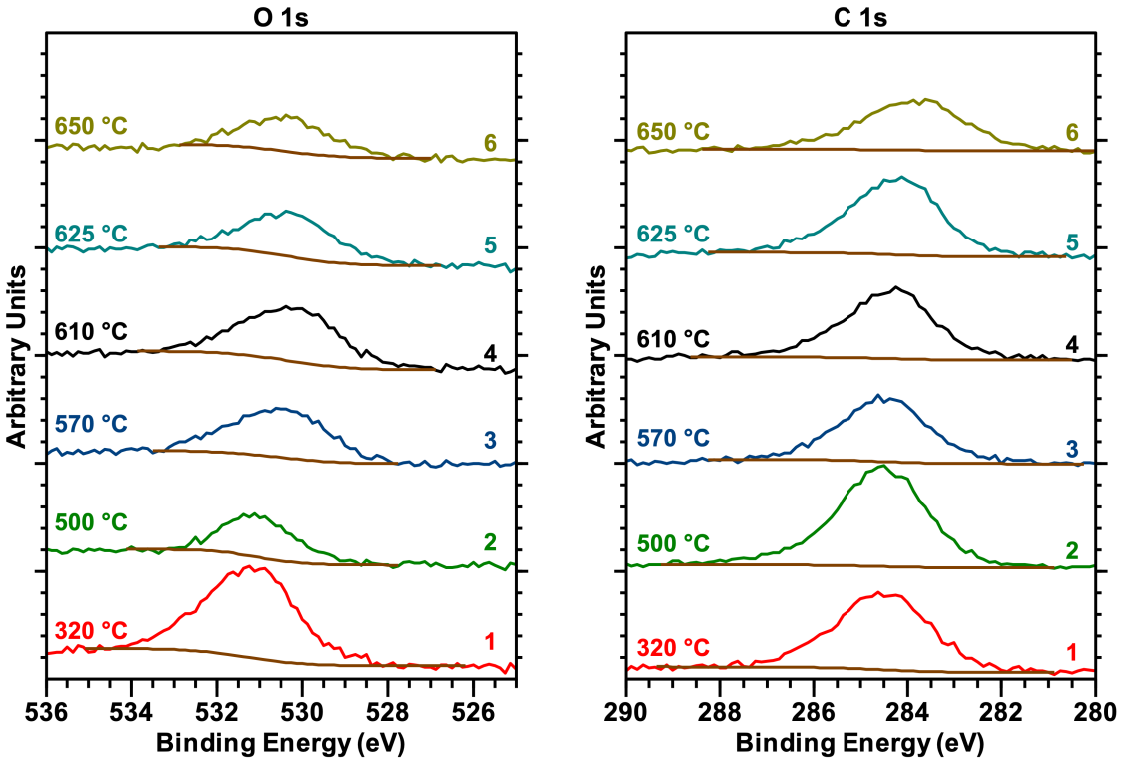

Fig. 55 O 1s and C 1s photoelectron spectra for the p-GaN surface (sample A9) cleaned at several temperatures (lines 0–6) from the backside.

The changes in the O and C photoemission peak intensities, which depended on the applied temperature, are shown in lines 1 to 6 in Figure 55. Several temperatures between 320–650 °C were applied to the p-GaN sample to remove surface O and C. The XPS measurements were carried out when the sample was cooled down to room temperature, but after the thermal cleaning the presence of O and C was always observed on the p-GaN surface and only a partial reduction of the C and O

concentration was achieved. Even at a temperature of 650 °C, it was not possible to remove the C and O completely as a residual amount of O and C remained on the surface, resulting in a small, broad peak that was still detectable. It is well known that C, O, and other impurities were incorporated into the crystal lattice as unwanted impurities and that C remained on the surface when a semiconductor is manufactured by MOCVD [114–116]. The crystal quality and carrier mobility can suffer due to these unwanted impurities that also have an undesirable effect on the photocathode performance.

6.3.3 QE Performance Depending on Surface Quality

After the wet chemical cleaning and the thermal cleaning, the samples were activated with Cs to obtain an NEA surface and thereby produce p-GaN:Cs photocathodes. The colors that are used in the following diagrams represent different temperatures used in the thermal cleanings and follow a logical ordering as shown in Figure 56. All QE values obtained, including the activation conditions, are summarized in Table A 2 in the Appendix.

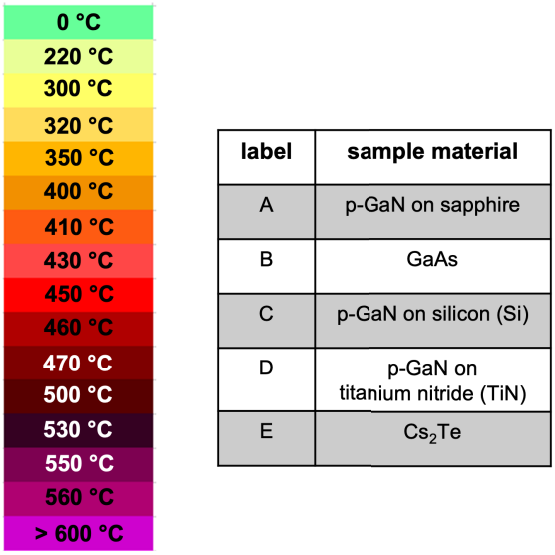

Fig. 56 Color labels for the temperatures used in the thermal cleaning (left), and an extra label for the different sample materials (right).

Figure 57 shows a comparison of the QE values obtained for different p-GaN:Cs on sapphire photocathodes, depending on the applied cleaning temperature. All samples shown in Figure 57 were thermally cleaned by using the halogen lamp and the cycles of heating and activation were repeated several times for each sample to improve the statistical accuracy.

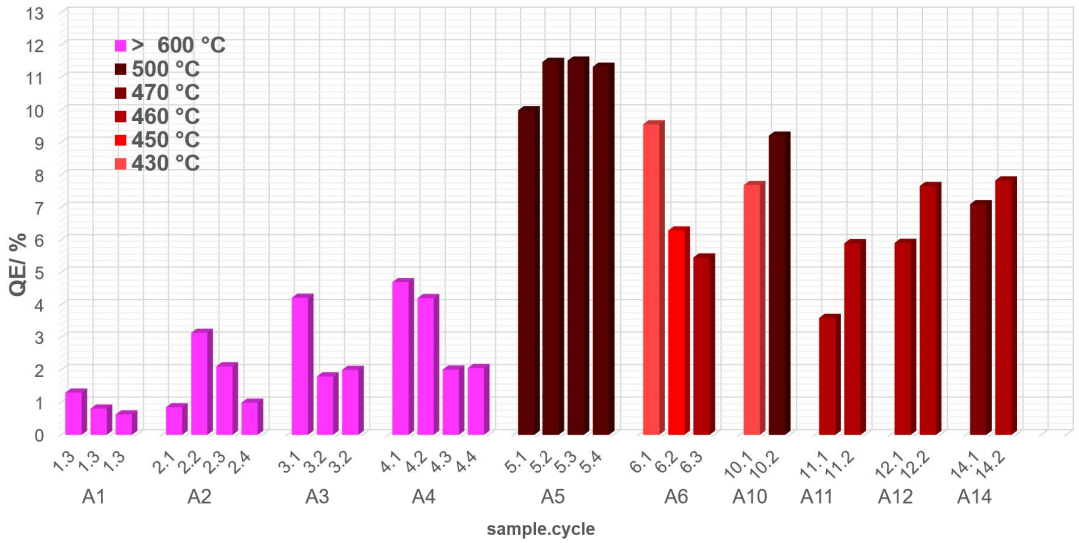

Fig. 57 QE values obtained for a series of p-GaN:Cs photocathodes that were thermally cleaned with a halogen lamp.

The ordinate in Figure 57 shows the QE of the freshly activated p-GaN:Cs photocathodes, whereas the x-axis shows the sample number, followed by its cycle number. The p-GaN samples examined show different QE values depending on the applied temperature. Low QE values were obtained for samples where a temperature over 600 °C was applied, while samples that were thermally cleaned at lower temperatures showed higher QE values. The highest QE (> 10 %) was achieved for sample A5 when the p-GaN was cleaned at 500 °C. Thermally cleaned at a temperature above 600 °C, samples A1–A4 yielded lower QE values than those obtained from a lower thermal cleaning temperature (400–500 °C). The remaining C and O concentration on the semiconductor surface influenced the semiconductor surface quality, especially its ability to form an NEA surface. To determine the reason for the low QE after the thermal cleaning at high temperatures, surface studies with XPS and SEM were carried out as described in Sections 6.7.1 and 6.7.3.

The QE values obtained for samples A7 and A8 are shown separately in Figure 58. The two samples were thermally cleaned through their sapphire substrates from the backside. The temperature was measured on the p-GaN layer at the frontside with the IR sensor. Figure 58 thus shows a comparison of the QE values obtained for these two p-GaN:Cs on sapphire photocathodes, depending on the cleaning temperature applied from the backside. The two p-GaN samples showed different QE values and no QE value was obtained for sample A7 where no thermal cleaning was applied prior to the activation. Higher QE values were obtained for sample A7 when thermally cleaned at higher temperatures (220–600 °C). For sample A8 which was thermally cleaned above 600 °C, lower QE values were obtained compared to those for sample A7. The highest QE (nearly 10 %) was obtained for sample A7 in the third cycle, when p-GaN was cleaned at 320 °C. The results confirmed the statements that temperatures above 300 °C were required for NEA surfaces to effectively remove C and O contaminations and to rejuvenate an NEA surface [66]. However, no higher QE values were obtained for samples A7 and A8, thermally cleaned from the backside, compared to those QE values from samples A1–A14, cleaned using the halogen lamp.

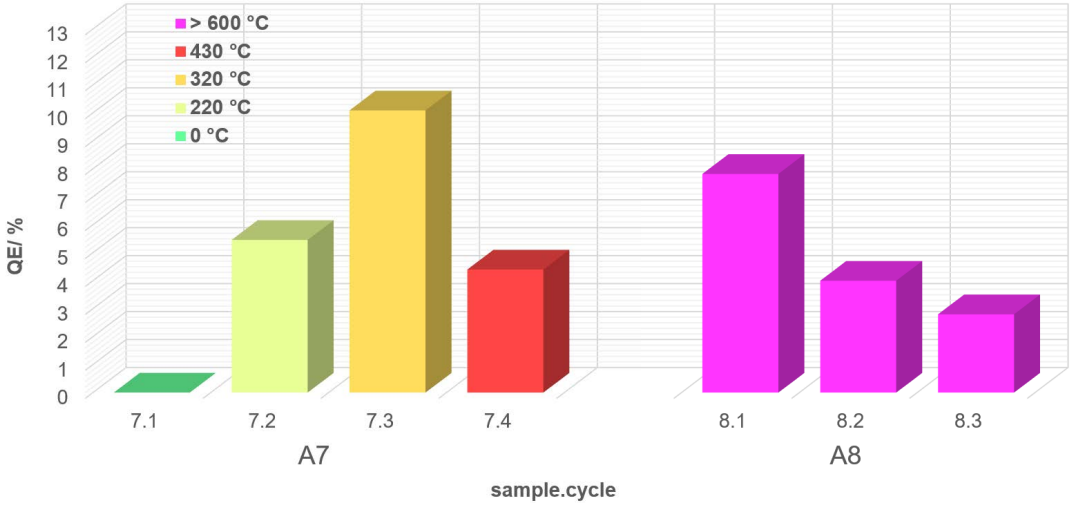

Fig. 58 QE values obtained for a series of p-GaN:Cs photocathodes that were thermally cleaned through the sapphire substrate from the backside.

6.3.4 Storage Lifetime vs. Thermal Cleaning Temperature

A comparison between the measured storage lifetimes of the p-GaN:Cs photocathodes is shown in Figure 59. In the experiments conducted, the storage lifetime is defined as the time interval from the completion of the activation to the time when the QE drops down to 1 %. For a reasonable comparison, the QE was tracked for several days, and a prediction of the lifetime was made from its exponential decay fitted by a suitable tri-exponential model shown in Equation 6 [117].

$$y = y_0 + A_1 \cdot e^{(-(x-x_0)/t_1)} + A_2 \cdot e^{(-(x-x_0)/t_2)} + A_3 \cdot e^{(-(x-x_0)/t_3)} \tag{6}$$

The activated p-GaN:Cs photocathodes were stored under a stable UHV environment during the lifetime measurement. The p-GaN:Cs on sapphire samples A3 and A4, cleaned above 600 °C, showed storage lifetimes of less than 50 h. This meant that after the Cs deposition, the QE decayed rapidly to 1 % within 50 h. These photocathodes survived longer after the first activation than after their reactivation, where significantly shorter lifetimes of less than 50 h were measured. The storage lifetime could be increased for the p-GaN:Cs photocathode A5, which was thermally cleaned at 500 °C. For the p-GaN:Cs photocathode A6, cleaned at a temperature between 400–450 °C, the lifetime was also increased. The storage lifetime was extrapolated to over 5000 h for the first cycle in the experiment. For all other photocathodes (A7–A14) no lifetimes can be provided because too few points were measured to provide a reliable extrapolation of the storage lifetimes. Additionally, some of these samples (A10–A14) were negatively influenced by the X-ray irradiation of the XPS measurements which caused a significant QE loss.

In summary, the p-GaN:Cs photocathode A5, thermally cleaned at 500 °C, showed the highest QE (> 10 %), while the GaN:Cs photocathode A6, cleaned at 400–450 °C, showed the longest lifetime (> 5000 h). The first activation cycle of sample A6 resulted in 9.5 % QE and the longest lifetime, and thus treating the p-GaN thermally at 400–450 °C represented the best compromise to obtain the required QE and storage lifetime result.

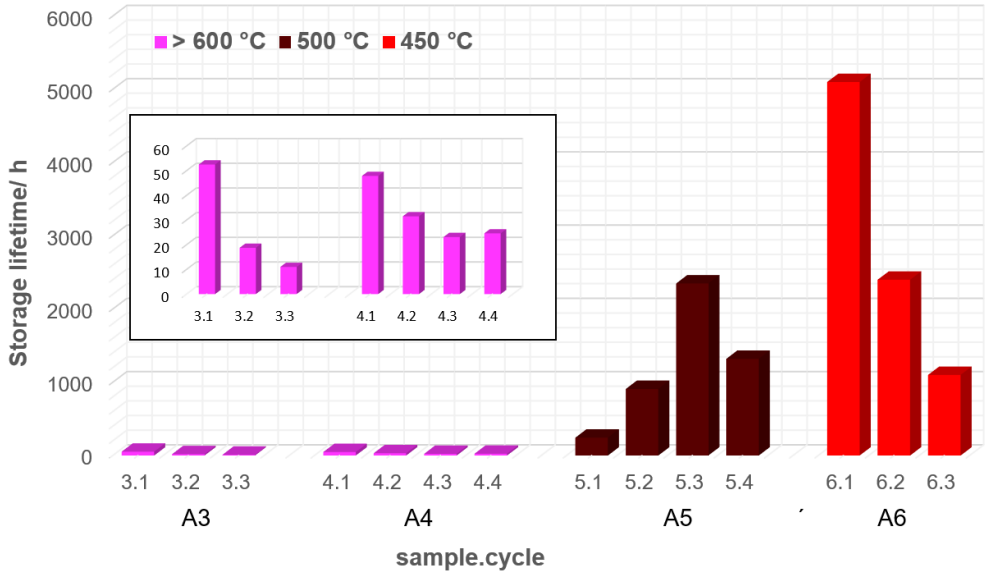

Fig. 59 Storage lifetimes and extrapolated lifetimes for a series of p-GaN:Cs photocathodes thermally cleaned with a halogen lamp.

6.4 Influence of Argon Ion Irradiation

6.4.1 On p-GaN Surface

C and O remained on the p-GaN surface and were not removed completely by a thermal cleaning. The p-GaN surface was therefore irradiated by Ar^+ with 1.5 keV energy for 10 min. Figure 60 shows a comparison of detailed XPS spectra of O 1s, C 1s, and Ga $2p_{3/2}$ of a thermally cleaned p-GaN surface at 650 °C and an Ar^+ irradiated surface. After the Ar^+ irradiation, neither O nor C was detectable on the p-GaN surface. This indicated that the C and O were located at the surface or in the sub-surface of p-GaN because the Ar^+ were able to remove those contaminants. A shift toward a lower BE in the Ga $2p_{3/2}$ photoemission peak occurred after the p-GaN surface underwent the Ar^+ bombardment. This shifting might indicate a charging effect from the remaining Ar^+ of the p-GaN surface or be caused by the removal of the C and O contaminations.

6.4.2 On p-GaN:Cs Photocathode Surface

The effect of Ar^+ on a p-GaN:Cs photocathode surface was also studied using XPS. For this purpose, a p-GaN:Cs photocathode (sample A13) with 2 % QE was irradiated with Ar^+ of an energy of 1.5 kV for 10 min. The same sample was irradiated again with Ar^+ at higher energy than the previous Ar^+ bombardment. The Ar^+ had an energy of 2.5 kV in the second Ar^+ bombardment that was applied for 5 min to the p-GaN surface. The Ga $3d_{3/2}$ and N 1s photoemission peaks from the survey spectra were used for the quantification and the calculation of the Ga:N ratio that changed in response to the Ar^+ bombardment. The XPS survey spectra are shown in Figures A 4–A 6 in the Appendix.

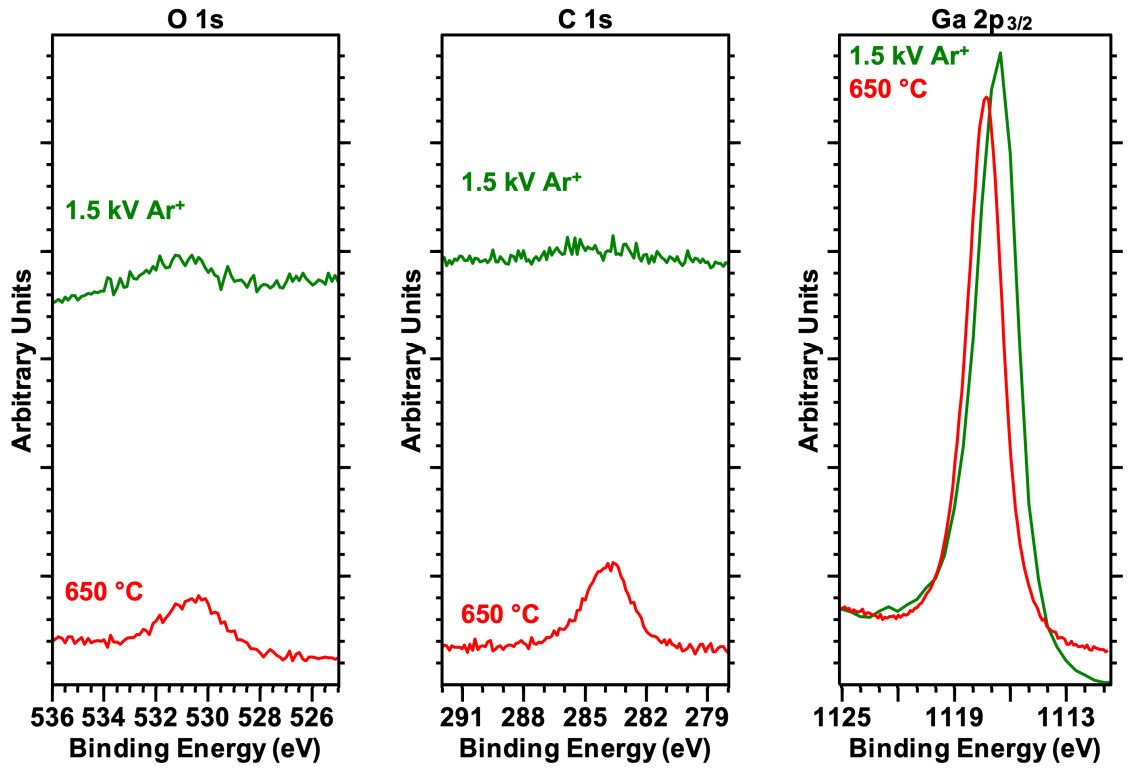

Fig. 60 O 1s, C 1s, and Ga $2p_{3/2}$ photoemission spectra for the p-GaN surface after thermal cleaning at 650 °C from the backside (red line), and after Ar^+ irradiation at an energy of 1.5 kV for 10 min (green line).

Table 2 summarizes the quantitative values that were obtained from the survey spectra. A Ga:N ratio of 1 was measured for the initial p-GaN:Cs photocathode with 2 % QE. The original GaN ratio began to change and turned into 1:4 when the surface was irradiated with Ar^+ of an energy of 1.5 kV. Irradiated with Ar^+ of a higher energy at 2.5 kV, the Ga:N ratio changed to 1:8 and thus the surface was enriched with Ga atoms, thereby indicating that a depletion in the N atoms occurred.

Tab. 2 Atomic concentrations derived from the survey spectra for a p-GaN surface with 2 % QE and after Ar^+ sputtering.

treatment	Ga 3d (at.-%)	N 1s (at.-%)	Cs $3d_{5/2}$ (at.-%)	O 1s (at.-%)	Ga:N ratio
2 % QE	21.08	20.85	48.53	9.74	1.01
1.5 keV	59.37	40.63	-	-	1.4
2.5 keV	64.83	35.17	-	-	1.8

Cs and O were present before the sputtering but disappeared under the Ar^+ bombardment on the p-GaN surface.

6.4.3 Surface Morphology after Thermal Cleaning, Argon Ion Irradiation and Activation

SEM and EDX measurements were carried out to study the p-GaN surface morphology after the p-GaN underwent a wet chemical cleaning, several thermal cleanings, Ar^+ sputtering, and an activation cycle.

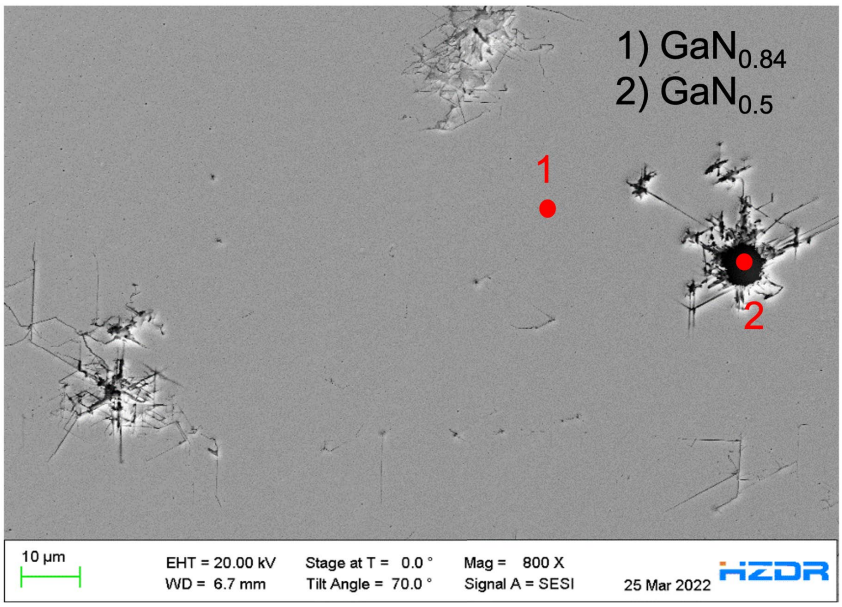

Fig. 61 SEM image of a p-GaN:Cs surface (sample A9) that underwent thermal cleaning at 650 °C, Ar^+ sputtering and a Cs activation. The EDX measurements showed depletion in N atoms at positions 1 and 2 at the surface.

Figure 61 shows an SEM image of a p-GaN surface (sample A9) that underwent a wet chemical cleaning, a thermal cleaning at different temperatures, Ar^+ ion irradiation, and a Cs activation. The extensively treated p-GaN surface showed irregularities in the surface morphology and large black holes were found. The excessive thermal cleaning might have caused the appearance of these holes, where the original p-GaN layer was destroyed. EDX measurements confirmed that the composition of N and Ga atoms changed in this area. The N atomic concentration inside the black holes was half of that of the Ga atoms when EDX was measured at position 2 in Figure 61. Furthermore, the p-GaN surface showed an unequal GaN ratio of 1:0.84 at position 1 in Figure 61 in which depletion of N atoms must also have occurred.

Round crates were found at the surface (see Figure 62). The appearance of these round crates was associated with a damaging effect due to Ar^+ irradiation. The crates were consistent and had almost the same diameter. Therefore, it is assumed that the Ar^+ irradiation caused an unwanted change in the surface morphology.
These sputtering results showed that a depletion in N atoms occurred and thus the examined p-GaN surfaces showed a preferential sputtering of N atoms when irradiated with Ar^+.

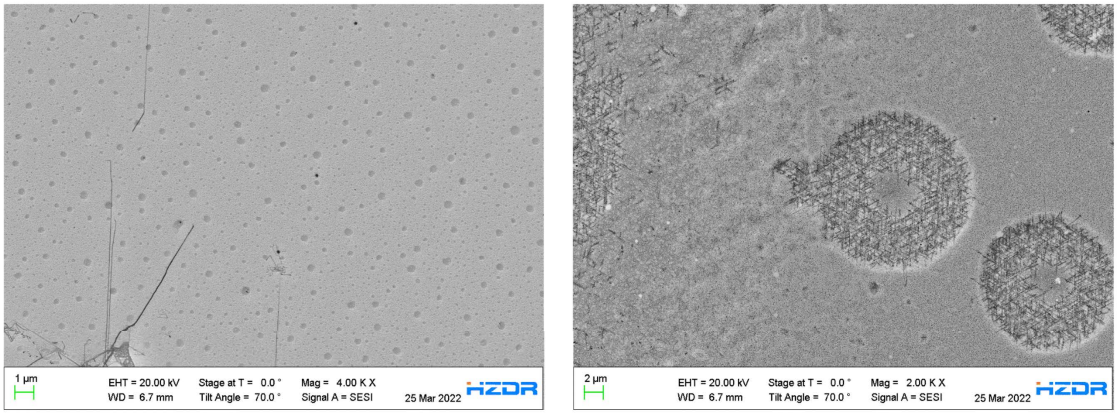

Fig. 62 SEM images of a p-GaN:Cs surface (sample A9) that underwent a thermal cleaning at 650 °C and Ar^+ sputtering that resulted into surface crates and destroyed the p-GaN surface.

6.5 Surface Analysis of the p-GaN Surface after Cesium Activation

A successful activation by applying Cs to the p-GaN surface was possible, although some C and O remained on the p-GaN surface after the thermal cleaning. p-GaN on sapphire (sample A5) was wet chemically cleaned and then thermally cleaned at 500 °C. It was activated with a thin layer of Cs when it was cooled down to room temperature. The same thermal cleaning was repeated in every activation cycle. Typical photocurrent curves during the activation are shown in Figure 63 for sample A5 as an example. An aperture reduced the UV-light power and consequently the photocurrent, which provided relief for the vacuum. In the beginning, no photocurrent could be detected after the Cs deposition started. After 10–20 min, the photocurrent slowly and steadily started to increase until it reached a maximum. Finally, when the photocurrent reached this maximum, the aperture was opened to take the maximum photocurrent value. The starting points and speed of growth depend on the current applied to the Cs dispenser. The maximum achieved QE values for all samples are summarized in Table A 2 in the Appendix.
The QE decay curves after a successful activation are also shown for sample A5 in Figure 63. The QE dropped exponentially during the hours following the activation and stabilized after a certain time. The same sample was thermally cleaned again when the QE reached 1 %. After the thermal cleaning, before the sample was activated with Cs again, some photocurrent was observed. This indicated that the thermal cleaning did not remove all of the Cs from the p-GaN surface and this phenomenon was observed for samples A5 and A6, but not for sample A4, which was treated at a higher temperature. For samples A7–A14, XPS measurements confirmed that in some cases Cs indeed remained on the p-GaN surface after the thermal cleaning.

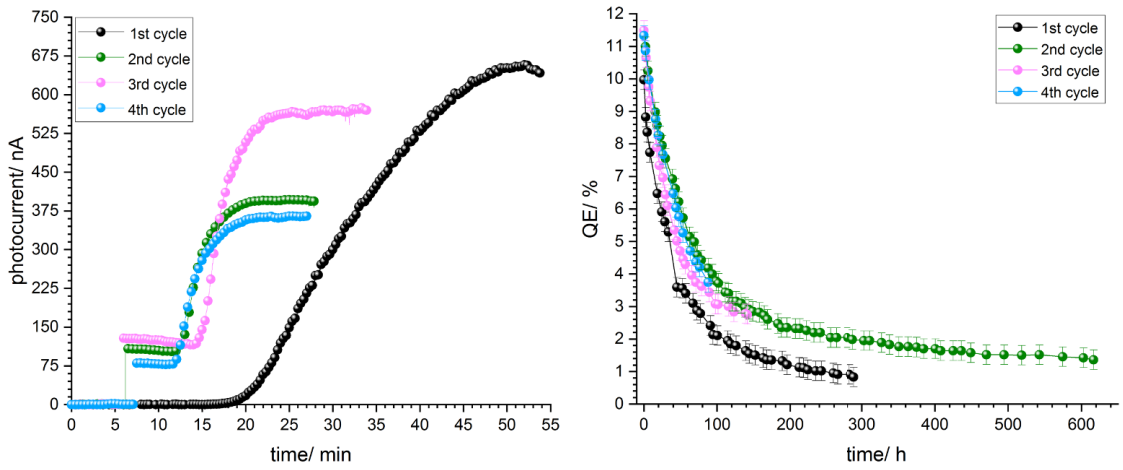

Fig. 63 Photocurrent curves of p-GaN (sample A5), which was thermally cleaned at 500 °C and activated with Cs for four cycles (left), and QE decay curves of the same p-GaN:Cs photocathode after activation (right).

XPS analysis was used to study the effect of the Cs deposition on the chemical composition of the p-GaN surface. The N 1s, O 1s, C 1s, and Ga $3d_{3/2}$ photoemission peaks are depicted in Figure 64 to compare the p-GaN surface (sample A10) before (line 0) and after (line 1) the Cs activation was applied. For the N 1s and Ga $3d_{3/2}$ peaks, a shift of approximately 0.50 eV to a higher BE was observed. The electron density of these photoemission peaks changed due to the high electron input from the Cs on the p-GaN's surface. This shift indicated the successful adsorption of the Cs on the p-GaN surface. No shift in the BE for O 1s was observed, which means that the detected O was not influenced by the Cs deposition and was located in deeper surface sublayers. The C 1s photoemission peak was mainly influenced by the deposition of Cs. As shown in the previous section, adventitious C was still present after the thermal cleaning and could not entirely be removed from the p-GaN surface. It is well known that undesirable O and C impurities, in particular, are incorporated into the p-GaN crystal lattice during MOCVD growth [114–116]. However, a new C component appeared at a BE of approximately 286 eV when the Cs was deposited. A small sub-peak, originating from adventitious C, was still detectable but decreased in intensity. The component at a higher BE (286 eV) must have been C surrounded by a higher electron density. Thus, this new component showed the formation of a cesium carbide (Cs_xC_y) species. The freshly deposited Cs appeared more attracted to the residual C than to the p-GaN surface. A similar effect of the C photoemission peak shifting toward a higher BE depending on the Cs amount was reported for the adsorption of Cs on graphite [118, 119]. Significantly, there are few studies on alkali metal carbides.

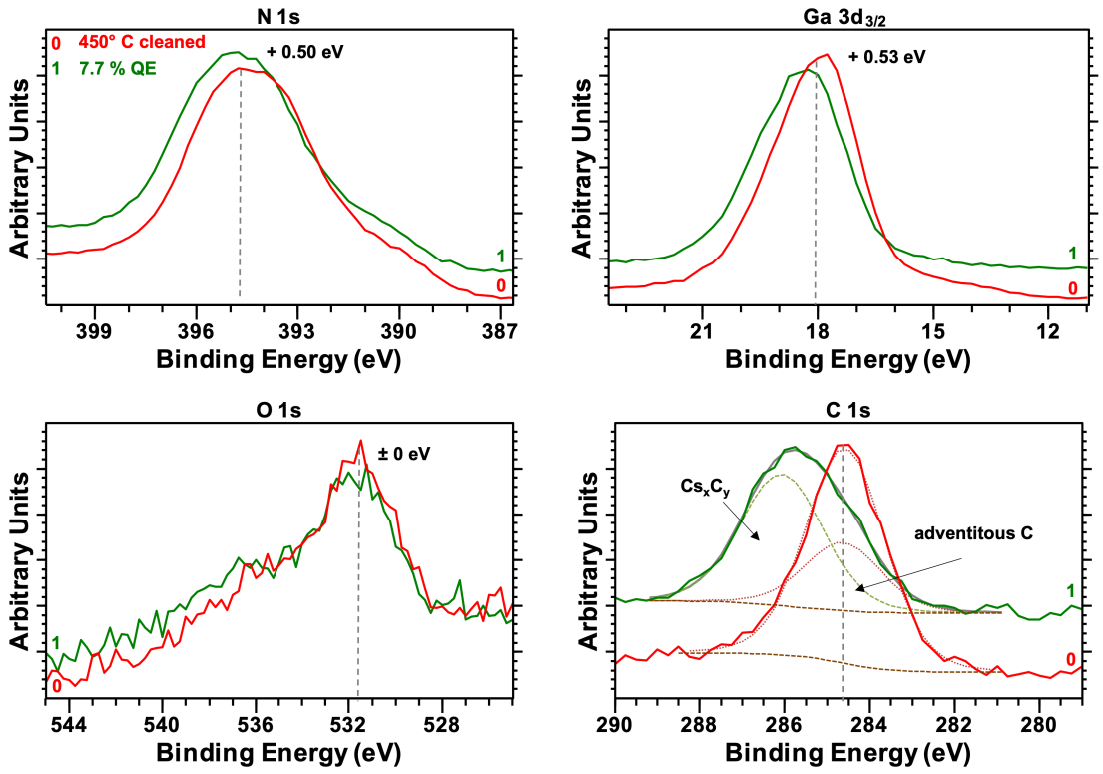

Fig. 64 Ga $3d_{3/2}$, N 1s, O 1s, and C 1s photoelectron spectra for the p-GaN surface (sample A10) after thermal cleaning at 450 °C (line 0) and after Cs activation with 7.7 % QE (line 1).

Detailed XPS spectra were also taken in the Cs 3d core level region. They exhibited a typical paired structure due to spin-orbit splitting (739.75 eV for $3d_{3/2}$ and 725.75 eV for $3d_{5/2}$), as shown in the survey spectrum in Figure A 7 in the Appendix. The resulting spin-orbit shifted exactly 14 eV between corresponding peaks. Only the Cs $3d_{5/2}$ photoemission peak was considered for further evaluation and thus showed a detailed Cs $3d_{5/2}$ photoemission spectrum. The $3d_{5/2}$ photoemission peak shifted toward a lower BE with respect to the metallic Cs^0 (Cs $3d_{5/2}$ = 726.4 eV), as shown in Figure 65. The main Cs peak of 725.75 eV represented the adsorbed Cs on the p-GaN surface. The surface Cs was expected to be positively charged (Cs^{+1}) in relation to the bulk Cs^0. This shift toward a lower BE for Cs adsorbates on metal substrates has previously been observed and discussed [120]. Furthermore, a few publications have noted oxidation states of Cs oxides and the Cs peak shifting toward lower BE when the oxidation state changed to +1 (Cs^{+1}) [121–123].
The O 1s photoemission peak usually appears at a BE of approximately 530 eV, within the typical BE range of an alkali metal oxide [124, 125]. In contrast, the O 1s peak was not influenced by the Cs and hence it was assumed that the Cs was attached to the p-GaN surface in a Cs^{+1} chemical state or as a Cs_xC_y, which must also be in a Cs^{+1} state.
A broad peak at approximately 729 eV was identified from Cs plasmons [43] while a further sub-peak at 722.6 eV could have originated from a charging artifact [126], although its appearance is rarely reported.

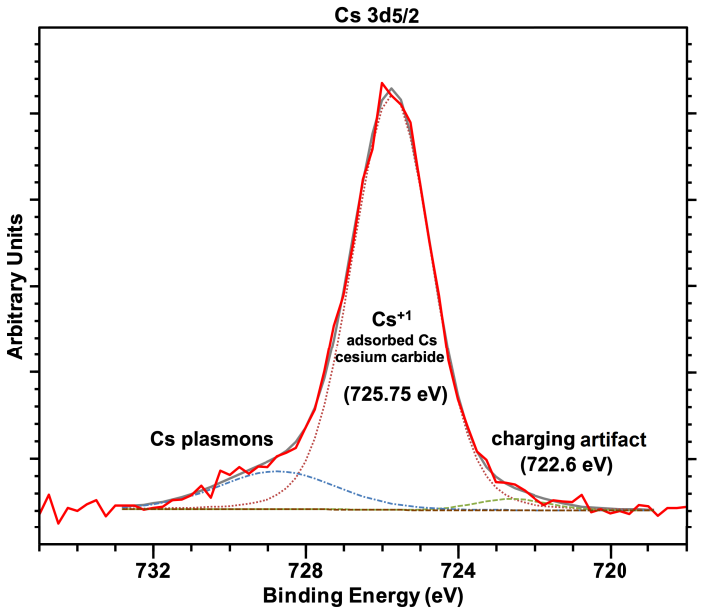

Fig. 65 Cs $3d_{5/2}$ photoemission spectrum of the adsorbed Cs on the p-GaN surface, with the peak fitting showing three components.

6.5.1 Spectral Response of the p-GaN:Cs Photocathode

The spectral response was measured for the p-GaN:Cs photocathode (sample A12) to determine its cut-off wavelength.

The QE showed an almost negative linear dependency with increasing wavelength,

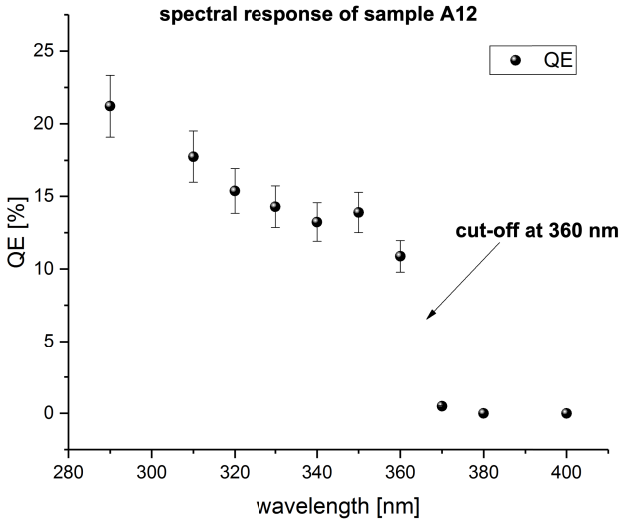

Fig. 66 Spectral response of a p-GaN:Cs photocathode (sample A12) showing its cut-off edge at 360 nm, which is related to a band gap of 3.4 eV.

as shown in Figure 66. The cut-off wavelength for sample A12 was found at 360 nm where the QE dropped significantly to zero. The QE remained zero at wavelengths longer than 360 nm because photoelectrons were no longer able to overcome the band gap.

The QE value increased at shorter wavelengths due to the effect that the photoelectrons gained more E_{kin} and thus these electrons had a higher probability to reach the surface. The photoelectrons thus had a longer IMFP. Sample A12 showed a maximum QE value of 21 % at a wavelength of 290 nm.
The spectral response experiment was repeated with another p-GaN:Cs photocathode (sample A11) that showed the same cut-off wavelength at 360 nm. The spectral response curve for sample A11 is shown in Figure A 8 in the Appendix.

The cut-off wavelength for the p-GaN photocathodes was reported at 360 nm [127] which aligned with the experimental results obtained in this work. Therefore, a slight relief of the UV-laser system can be ensured when using p-GaN:Cs photocathodes in photoinjectors.

6.5.2 Surface Composition after YoYo Activation

A YoYo activation (with Cs and O_2) and its potential benefit for the p-GaN photocathode performance was studied, although O_2 was not required for achieving a p-GaN photocathode. Figure 67 depicts an example of the photocurrent curve of a p-GaN surface (sample A14), alternately activated with Cs and O_2 during the YoYo activation.

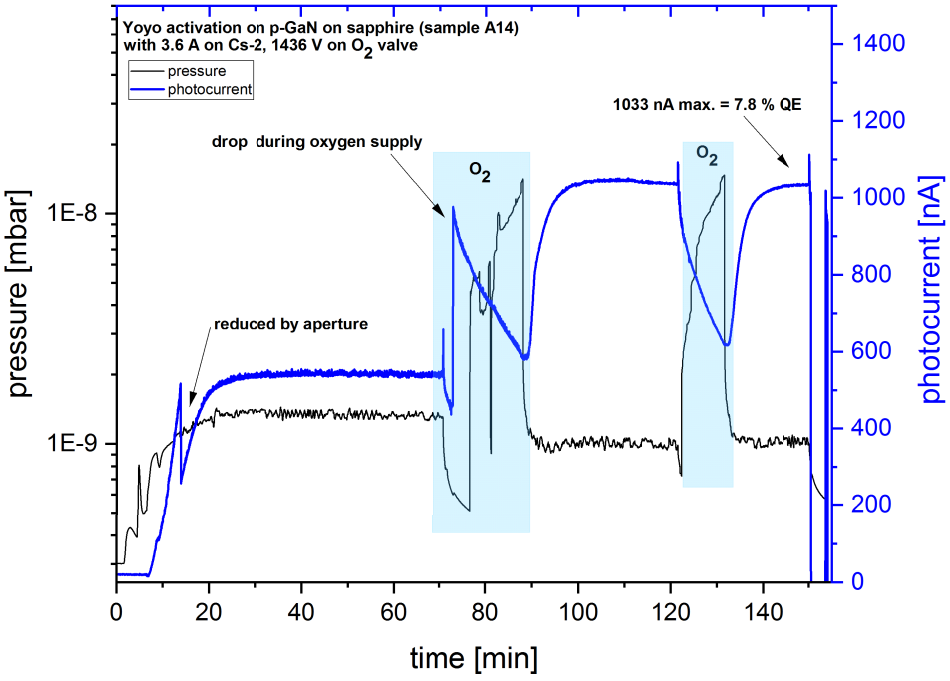

Fig. 67 Photocurrent curve during a YoYo activation of p-GaN (sample A14), in which Cs and O_2 are alternately applied.

Sample A14 was exclusively activated with Cs in the previous cycle, and thus this YoYo activation represented the second cycle. As usual, the p-GaN surface of sample A14 was thermally cleaned at 450 °C with the halogen lamp prior to the application of the YoYo activation.
Cs was then deposited first until the photocurrent saturated to a plateau (see Figure 67) and O_2 was subsequently applied to the cesiated p-GaN surface so that the

pressure was raised to 10^{-8} mbar. Typically, the photocurrent should have been increased by the O_2 as shown in other YoYo activations for p-GaN [20, 128, 129]. However, in this YoYo activation, the photocurrent dropped during the application of O_2, as shown in Figure 67. After an O_2 application of about 10 min, Cs was deposited until a saturation plateau was reached again. This time, the photocurrent reached a higher value compared to the previous photocurrent plateau. Another deposition of O_2 and Cs was applied until a maximum photocurrent of 1033 nA (7.8 % QE) was achieved.

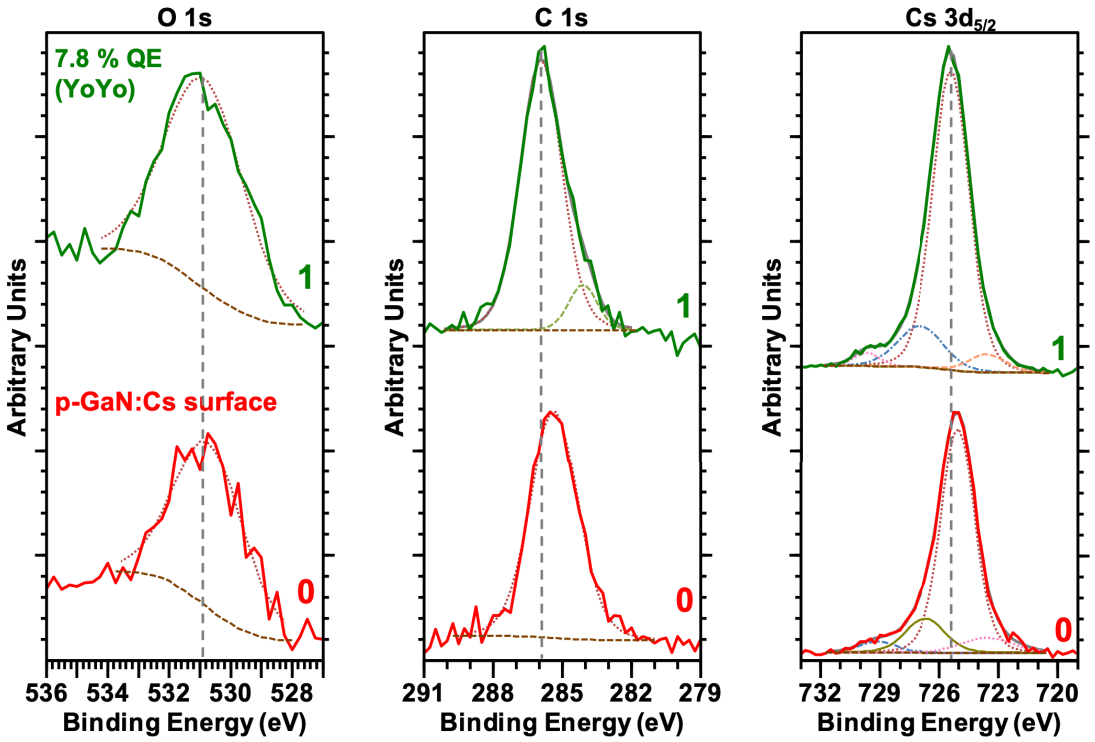

Fig. 68 O 1s, C 1s, and Cs $3d_{5/2}$ photoemission spectra of the p-GaN:Cs surface before YoYo activation was carried out (line 0) and after the p-GaN surface was YoYo activated (line 1).

The YoYo-activated photocathode was transported into the XPS chamber to study its chemical surface composition. As indicated previously, this YoYo activation represented the second activation cycle for sample A14. After the first cycle, the p-GaN surface was thermally cleaned at 460 °C but Cs remained on the p-GaN surface. The remaining Cs did not hinder the freshly deposited Cs of the following cycle to form an NEA surface. In contrast, if some Cs was left on the surface from the previous thermal cleaning, it mostly was beneficial for achieving a higher QE value. Therefore, Cs was present in the XPS spectra before the YoYo activation was carried out. The survey spectra are shown in Figure A 9 in the Appendix.
Figure 68 shows the detailed XPS spectra of O 1s, C 1s, and Cs $3d_{5/2}$ as a comparison between the p-GaN:Cs surface after the thermal cleaning (line 0) and the p-GaN surface after the YoYo activation with 7.8 % QE. The O 1s spectrum showed one O component at approximately 530.80 eV for the p-GaN surface after the thermal cleaning (line 0) which was not influenced by the YoYo activation (line 1).

A C component was found at 285.35 eV after the thermal cleaning that turned into two components after the YoYo activation. One component was found at a BE of 284.08 eV and the second component at a BE of 285.89 eV. The C component at a higher BE indicated a formation of a Cs_xC_y species. The C component at the BE of 284 eV was associated with adventitious C.
Several components appeared in the Cs $3d_{5/2}$ spectra and the main component was found at a BE of 725.05 eV (line 0). Besides this main component, sub-peaks at a BE of 723.57 eV, 726.71 eV and 729.14 eV were found. The sub-peak at 729.14 eV was derived from Cs plasmons.
When the p-GaN surface was YoYo activated, the main Cs peak shifted 0.34 eV toward a BE at 725.39 eV. Additionally, the BE of the sub-peak at 726.71 eV shifted 0.2 eV toward a BE at 723.57 eV. The component at 726.95 eV remained in its position and did not shift at all.
The main Cs peak was located at a lower BE (at approximately 725 eV) compared to the bulk metallic Cs^0 (at 726.4 eV). This meant that the Cs inside the Cs–O layer contained a positive charge. This result aligns with the reported results of a Cs^{+1}-O^{2-}-Cs^{+1} dipole layer [130–132]. The component at approximately 726 eV might derive from metallic Cs because Cs was used excessively in the YoYo activation. The component with the lower peak intensity at a BE of approximately 723 eV was derived from a charging artifact.

Figure 69 shows the QE values obtained for YoYo-activated p-GaN samples (samples A6, A7, and A14). The photocurrent curves for the YoYo activations for samples A6 and A7 are also shown in Figures A 10 and A 11 in the Appendix.
All YoYo activations were carried out as a re-activation which meant that a small amount of Cs was present in the XPS spectra before the YoYo activation was applied.

For the YoYo-activated p-GaN surfaces, QE values between 6–8 % were achieved whereby the QE values did not significantly differ from those values in which exclusively Cs was used. Samples A6 and A7 could be re-activated again without additional thermal cleaning, while sample A14 showed a higher QE when it was thermally cleaned at 450 °C prior to the YoYo activation. The photocurrent was increased when O_2 was also applied in the activation process, as shown as an example in the photocurrent curve in Figure 69.

The YoYo process was more challenging compared to activation with only Cs and has the potential risk to release a large amount of O_2 into the UHV chamber. One thus has to be careful when using O_2 inside the UHV chamber and avoid any uncontrolled oxidation.

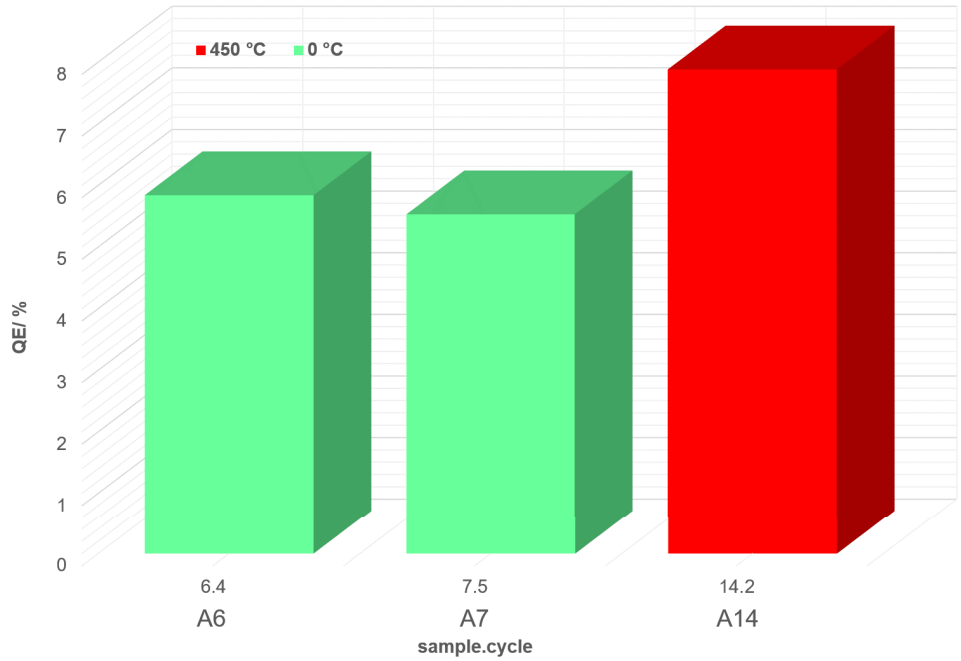

Fig. 69 QE values obtained for two p-GaN:Cs photocathodes that were activated with a YoYo process (Cs and O_2).

6.6 Degradation of p-GaN:Cs Photocathodes

6.6.1 Influence of Surface Carbon on the QE Decay

Photocathodes undergo natural degradation caused by residual gases in a vacuum environment [34]. Even in an ideal UHV environment, photocathodes loose QE. Thus, the surface chemical state under UHV conditions at different times during storage was studied to investigate the correlation between the mechanism of cathode degradation and the surface chemical state change. A detailed XPS analysis allowed to identify and quantify the relative elemental composition of the surface and distinguish between the chemical bonding states of the main elements. Different photoemission peaks from the p-GaN:Cs photocathode were acquired at different stages of QE decay, as shown in Figure 70. The freshly prepared photocathode initially had a 7.7 % QE. A QE drop accompanied each XPS measurement due to X-ray damage, which is discussed in Section 6.4. Between the XPS measurements, the QE decayed exponentially, as it is typical of this material. Figure 70 indicates that a shift of 0.35 eV toward a lower BE was measured for Ga $3d_{3/2}$, Cs $3d_{5/2}$, C 1s, and O 1s along with the QE decay. The N 1s spectra are not shown here because Al excitation is ineffective for N analysis due to the superposition of the photoemission N 1s line and the Auger Ga (the LMM Auger process) transition [43, 49, 126].
In general, a shift toward a lower BE means that the electronic structure of the observed element changes, and its oxidation state subsequently changes. The BE is, therefore, often regarded as a "chemical shift" [43, 49].

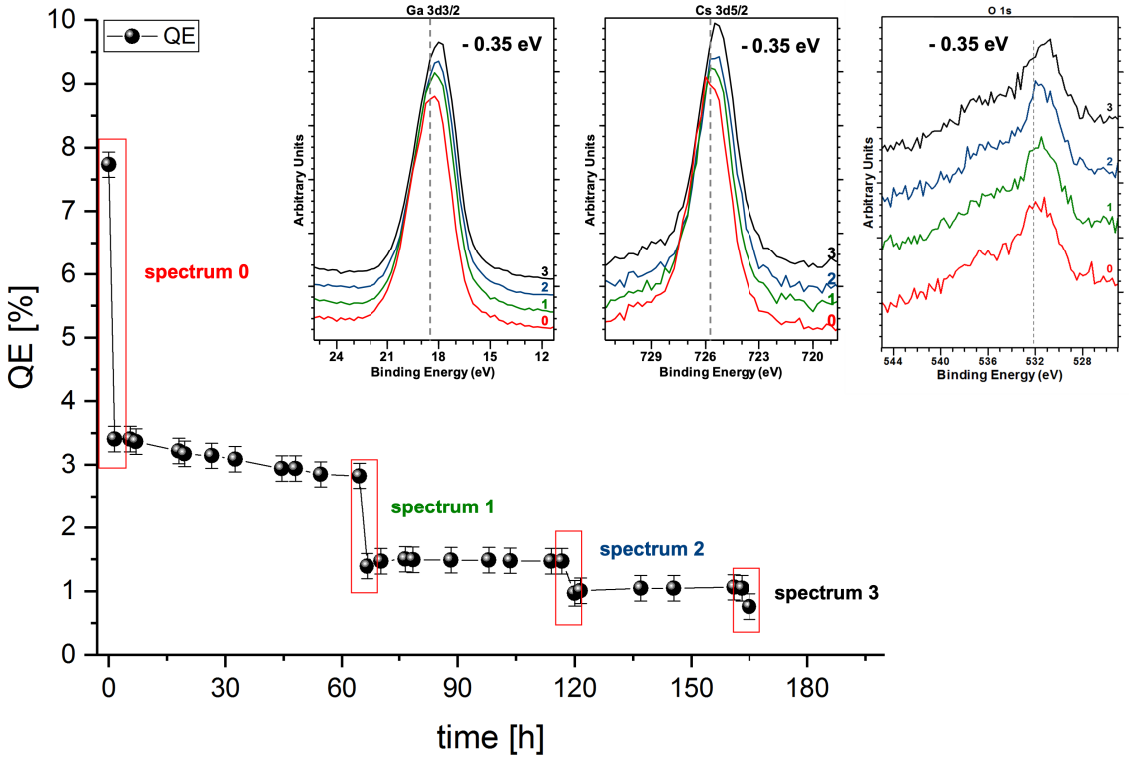

Fig. 70 The QE decay of the p-GaN:Cs photocathode (sample A10) and the Ga $3d_{3/2}$, Cs $3d_{5/2}$, and O 1s photoemission spectra at different times during their decay.

The relative concentration and the peak intensity of Cs did not change during the photocathode degradation and thus a loss of Cs was excluded. No additional Cs compound was found, which implied that the Cs had not changed its chemical state. At the C 1s photoemission peak, the intensity of the Cs_xC_y species, at a BE of 286 eV, increased significantly, and its peak width became narrower during QE decay, as shown in Figure 71.
It was thus assumed that the adhesion between Cs and the p-GaN surface became weaker, which was reflected by the shift toward lower BEs. This shift also indicated that the surface might be positively charged and that charging effects might occur [133]. Consequently, the GaN-Cs bonding became less pronounced, and the EA increased until Cs_xC_y islands dominated the p-GaN:Cs photocathode surface, thereby disturbing the NEA surface which subsequently disappeared. The possible reasons for changing an XPS's peak intensity are typically (i) a change in the number of atoms associated with the respective oxidative state of the surface or (ii) a change in the depth distribution of such atoms caused by diffusion processes [43, 49]. It was thus concluded that the number of Cs_xC_y species was increasing during this degradation and that the additional diffusion of the C atoms from the bulk toward the surface could have contributed to the formation of Cs_xC_y. The formation of Cs_xC_y and such islands during the operation of Cs-activated photocathodes has not previously been reported. Accordingly, the previously mentioned explanations must be viewed with caution and encourage other researchers working on improving the p-GaN photocathodes to note this phenomenon, as it may be one of the critical factors for determining the QE and these systems' lifetimes.

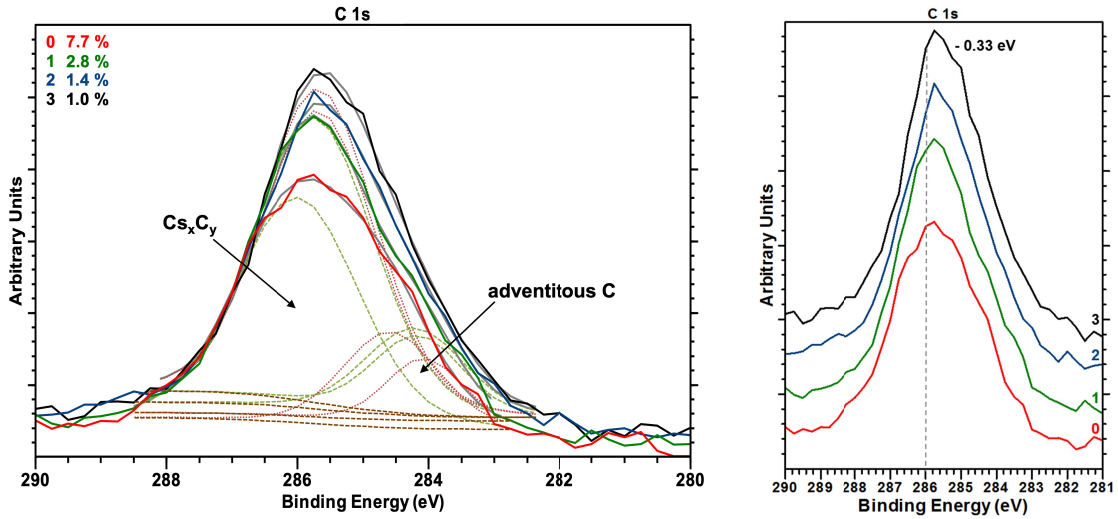

Fig. 71 The C 1s photoemission spectrum showing the evolution of the Cs_xC_y species and the degradation of the p-GaN:Cs photocathode (sample A10) on the left side and the shift to a lower BE along with the degradation of the p-GaN:Cs photocathode (right side).

6.6.2 Surface Model of Cesium-Carbide Island Growth

A surface model of a freshly prepared p-GaN:Cs photocathode is schematically illustrated in Figure 72.

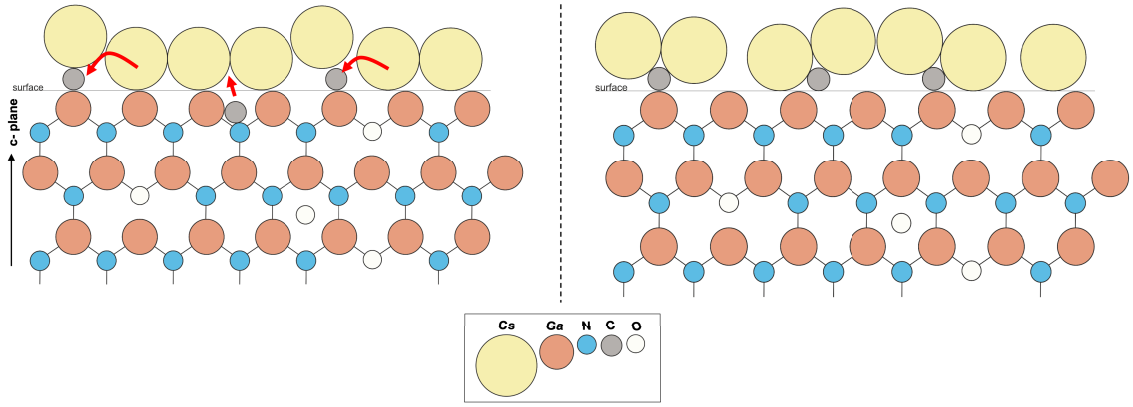

Fig. 72 The surface model of a freshly prepared p-GaN:Cs photocathode, in which the surface C attracts a part of the Cs (left). The surface model of an aged p-GaN:Cs photocathode showing the formation of Cs_xC_y islands (right).

This model indicates that the formation and growth of Cs_xC_y species caused QE degradation. The p-GaN has a hexagonal crystal lattice that grows along the c-plane (0001), and the surface is mostly Ga terminated. In addition, O may have been present in the crystal lattice and C in the surface layers, both as unwanted impurities from the MOCVD process [115, 116]. TMG is used as a precursor for Ga in the MOCVD process, and high temperatures are necessary for its decomposition. Lee *et al.* showed that the decomposition of TMG depended on the applied temperature and that a low C concentration could be detected in semiconductor sublayers [114]. While the residual C concentration reduction could be controlled during

crystal growth, the C could not entirely be removed. In contrast to the O, the concentration of C associated with the surface was always higher than in the bulk [115, 116]. Thus, an atomically clean surface was not obtained, as some residual C from the growth process was always present. When the Cs was applied, it was deposited on the p-GaN surface next to and on top of those contaminants. With increasing storage time, the Cs atoms began moving toward the C atoms, and the adhesion between Cs and p-GaN became weaker, as illustrated in Figure 72 on the right side. The C began to form a bond with Cs, that is, a Cs_xC_y species. It was assumed that in this process some Cs_xC_y islands were formed, which caused the photocathode to age.

6.6.3 Influence of X-ray Irradiation

The p-GaN:Cs photocathodes lost QE after every transport into the XPS analysis chamber. The QE decay curve for sample A10 is shown as an example in Figure 70. The QE dropped significantly during the hours following activation, especially after the sample was analyzed using XPS. Typically, the QE decays exponentially for p-GaN:Cs photocathodes, as indicated in another publication [26]. The QE stabilized when the sample was returned to the UHV preparation chamber. It was shown that the rapid QE loss after the XPS analysis was not the result of transportation but was most likely caused by the X-ray's influence from the dual anode.
The studies on the effects of X-rays during XPS analysis were conducted using a lengthy irradiation experiment. For this purpose, p-GaN (sample A14) was treated the same way as samples A10–A12: it was cleaned with 99 % pure EtOH, thermal cleaned for 1 h, and activated with Cs. The resulting p-GaN:Cs photocathode showed 7 % QE after the Cs deposition. Sample A14 was subsequently irradiated for 5.5 h with X-rays from the Mg source at a beam power of 100 W and 11 keV. The photocathode was neither transported nor moved. Thus, transportation did not influence these experiments. The Cs $3d_{5/2}$ and Cs $3d_{3/2}$ spin-orbit photoemission peaks with suitable fittings, in relation to the X-ray exposure time, are shown in Figure 73. A shift of 0.25 eV toward a lower BE with increasing irradiation time was observed. The Cs 3d peak shape and the Cs concentration remained constant during this experiment.
The main peak at 725.5 eV was derived from adsorbed Cs with a positive charge (Cs^{+1}) on the p-GaN surface, while the sub-peak at 723 eV belonged to a charge artifact, as noted in the previous Section 6.6.1. When the irradiation time increased in lines 1–3, a Cs component of approximately 726 eV appeared in the photoemission spectra that was not observed for the freshly prepared photocathode (line 0). This photoemission peak of 726 eV originated from metallic Cs^0. The X-ray irradiation caused surface melting and unwanted heating, which resulted in a change in the surface composition. Thus, the bulk Cs^0 component was not observable at the beginning of the experiment when the photocathode was freshly prepared. The X-ray beam thermalized the sample and caused external aging of the photocathode. Furthermore, the Cs concentration did not change during an X-ray exposure of 5.5 h and it was assumed that redistribution in the sample strongly influenced the adhesion between GaN and Cs as it is well known that X-ray irradiation significantly impacts semiconductors and their surfaces [49]. Consequently, the adsorbed Cs on p-GaN could be redistributed under X-ray heating conditions, thereby building metallic Cs. However, the sample was neither cooled nor measured in its temperature. The

X-ray beam power reduction or the sample cooling down could prevent, or at least decrease the X-ray damage. Sample A14 had 7 % QE before XPS analysis and yielded only 1.2 % QE after being treated by X-ray irradiation for 5.5 h. It was assumed that the X-ray damage also caused the QE losses observed in all other samples measured with XPS. Transportation effects that might negatively influence QE decay in these experiments were excluded. It is recommended considering this X-ray damage risk when working with cesiated semiconductor photocathodes with X-ray-based analytical devices (XPS or X-ray diffraction (XRD)).

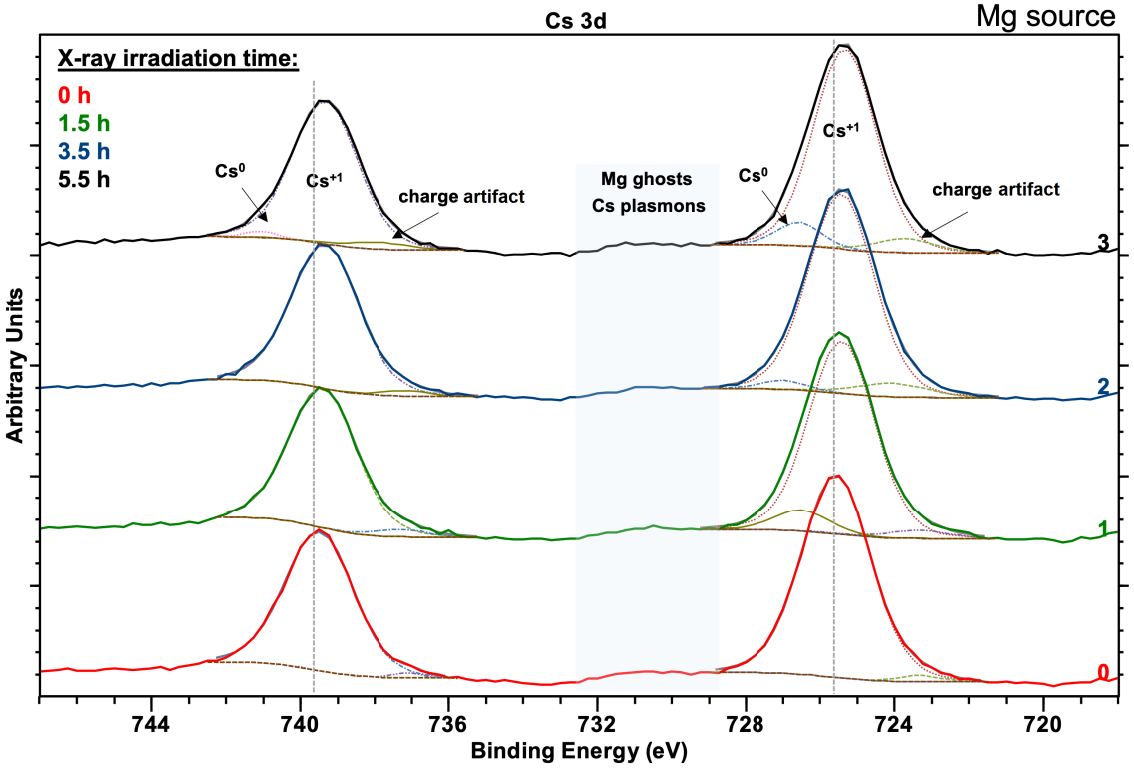

Fig. 73 Cs 3d spectra of a p-GaN:Cs photocathode (sample A14) influenced by the X-ray irradiation time.

6.7 Influence of Re-activations on the p-GaN Surface

6.7.1 After Thermal Cleaning

When the QE had a value below 1 %, sample A10 was thermally cleaned before the subsequent Cs activation. After the new thermal cleaning, the photocurrent was partially restored even before the subsequent Cs activation was conducted. In a previous publication, it was noted that this phenomenon occurred during re-activation, but it could only occur if Cs remained on the p-GaN's surface [26]. As shown in Figure 74, the XPS data confirmed that the Cs was not entirely removed from the p-GaN surface after thermal cleaning.

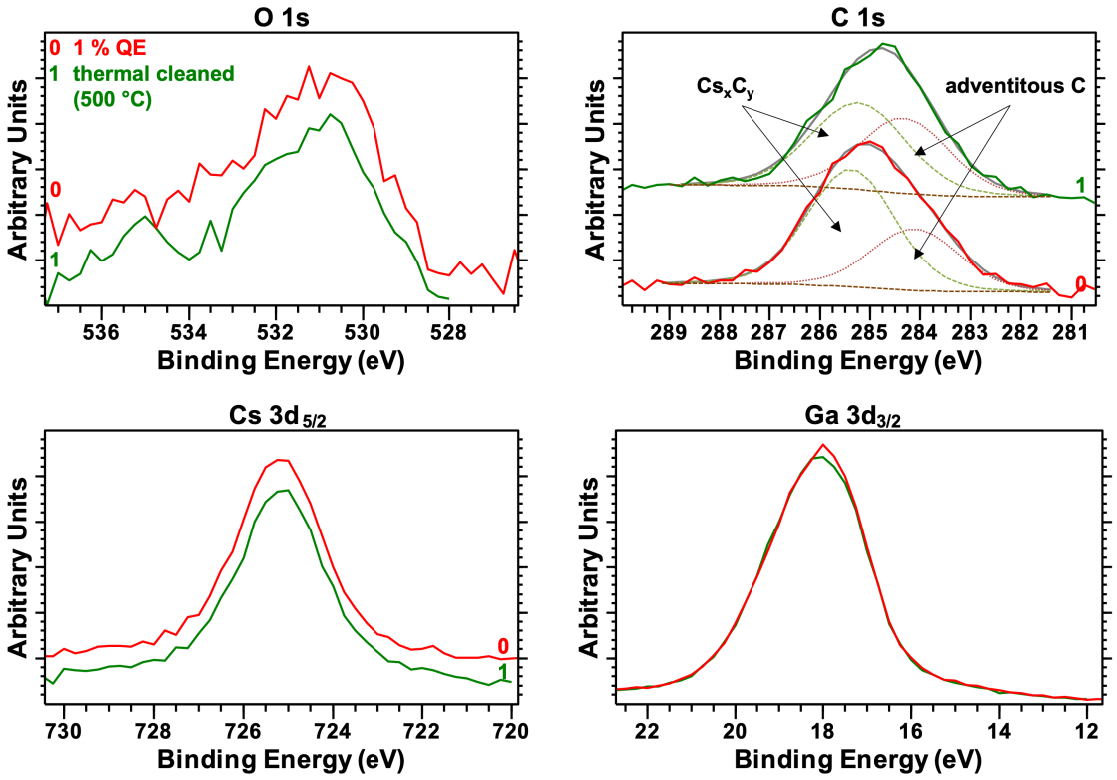

Fig. 74 The Ga $3d_{3/2}$, Cs $3d_{5/2}$, O 1s, and C 1s photoelectron spectra of the p-GaN:Cs surface before (line 0) and after (line 1) renewed thermal cleaning at 500 °C.

A comparison of the photoemission peaks from sample A10 (with 1 % remaining QE) before (line 0) and after (line 1) the thermal cleaning at 500 °C is shown in Figure 74. For O 1s and Ga $3p_{3/2}$, no difference before and after the thermal treatment was observed. The thermal cleaning also did not affect the Cs peak because it remained on the p-GaN surface and did not decrease in intensity or atomic concentration. The most substantial effect of the thermal cleaning was again observed at the C 1s peak, especially for the Cs_xC_y species. The intensity of the Cs_xC_y species decreased after the thermal cleaning and, vice versa the intensity of adventitious C increased. The sample was thermally cleaned at 500 °C for 120 min without successfully removing all the Cs and the Cs_xC_y species. It was assumed that during the thermal cleaning of the p-GaN:Cs photocathode, the Cs_xC_y species decomposed into metallic Cs and adventitious C.
To ensure the reproducibility of the results, two more p-GaN on sapphire samples

(samples A11 and A12) underwent similar treatments, and their XPS spectra are shown in Figures A 12–A 15 in the Appendix. Similar behaviors for these samples were also observed during activation, degradation, and re-activation.

6.7.2 Influence of Cesium after the Re-activation

The p-GaN was re-activated with the deposition of freshly applied Cs, although some remaining Cs from the previous activation remained on the p-GaN's surface. This time, the p-GaN:Cs photocathodes reached a QE of 9.2 %, which was slightly higher than in the first activation. Thus, the Cs that had remained on the p-GaN surface did not negatively impact the re-activation process and it was even beneficial and led to a higher QE.

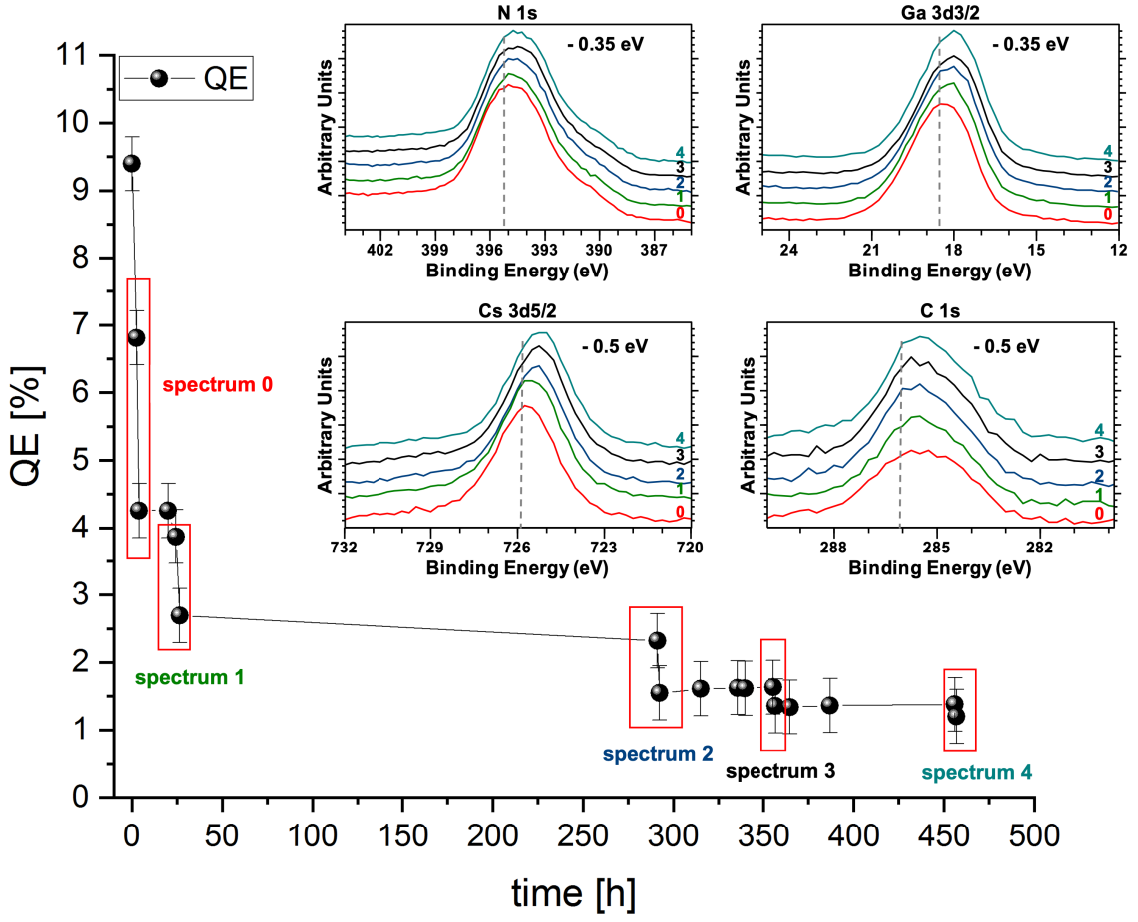

Fig. 75 The QE decay curve of the re-activated p-GaN:Cs photocathode (sample A10) with the corresponding Ga $3d_{3/2}$, Cs $3d_{5/2}$, and O 1s photoemission spectra, taken at different points in the decay curve.

The degradation of the re-activated p-GaN:Cs photocathode, followed by XPS analysis, is shown in Figure 75. The same effect in the degradation was observed as explained in the previous section. The N 1s and Ga $3d_{3/2}$ peaks shifted 0.35 eV, whereas the Cs $3d_{5/2}$ and C 1s peaks shifted 0.5 eV toward a lower BE. These significant shifts indicated that the Cs and C amounts might correlate and that their behavior primarily caused the degradation.

6.7.3 Surface Morphology

The cleaned and activated p-GaN:Cs photocathodes were studied with SEM to examine their surface morphology. Additionally, the surface composition was characterized by EDX spectroscopy whereby the p-GaN:Cs samples were taken out of the UHV chamber. Hence, the resulting EDX spectra might not show the original surface conditions because the p-GaN:Cs photocathodes were exposed to air. In particular, the Cs oxidized into a cesium peroxide (Cs_2O_2) or cesium hydroxide (CsOH) compound, and thus the original surface composition changed.

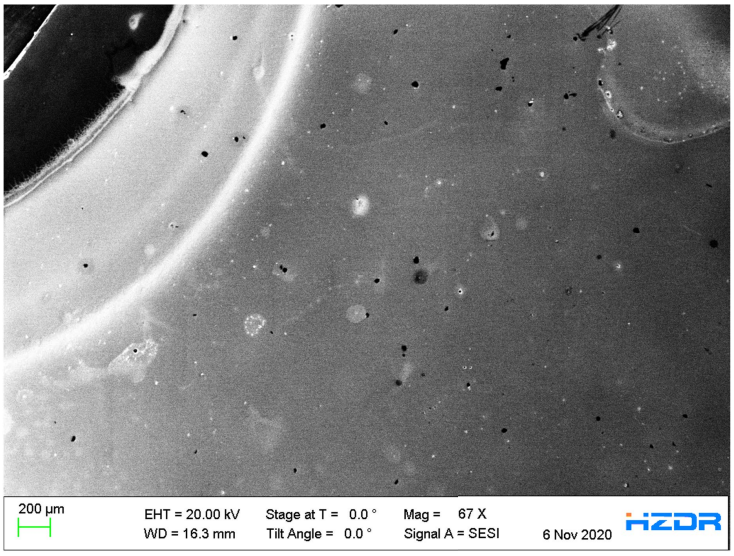

Fig. 76 SEM image of a p-GaN:Cs photocathode (sample A1), treated several times above 600 °C followed by numerous Cs activations.

Figure 76 shows an SEM image of a part of the $9 \times 9\,\mathrm{mm}^2$ p-GaN:Cs photocathode (sample A1). Sample A1 underwent four cycles of thermal cleaning above 600 °C, each followed by Cs activations. The different brightness values in the SEM image indicated an inhomogeneous p-GaN:Cs surface. The half-round, bright area on the left side in Figure 76 is derived from a round steel washer, which was used to fix the p-GaN sample on the sample holder. The original p-GaN:Cs surface on the right side in Figure 76 appeared darker. Therefore, the brighter area on the left side contained heavier elements compared to the rest of the p-GaN:Cs surface.
Fe was found in the bright area where the washer was located, as confirmed by EDX measurements, and shown in Figures A 16 and A 17 in the Appendix.
In contrast, the p-GaN:Cs photocathode (sample A5) was thermally cleaned at 500 °C and then activated for four cycles. A part of the sample A5 surface is shown in the SEM image in Figure 77. This image was taken additionally to compare the influence of the thermal cleaning on the surface morphology to sample A1, as shown in Figure 76. Therefore, both SEM images were taken in the area where the samples were fixed with the steel washer.
In Figure 77, the surface of sample A5 appeared homogeneous. In addition, other parts of sample A5 were examined by SEM, and no discrepancies were observed. The surface composition was proven by an EDX measurement showing an expected ratio of 1:1 for Ga:N, which is shown in Figure A 18 in the Appendix. Thus, the SEM/EDX measurements have reinforced the statement that the thermal clean-

ing at temperatures up to 500 °C neither changed the original p-GaN surface nor destroyed the original p-GaN composition.

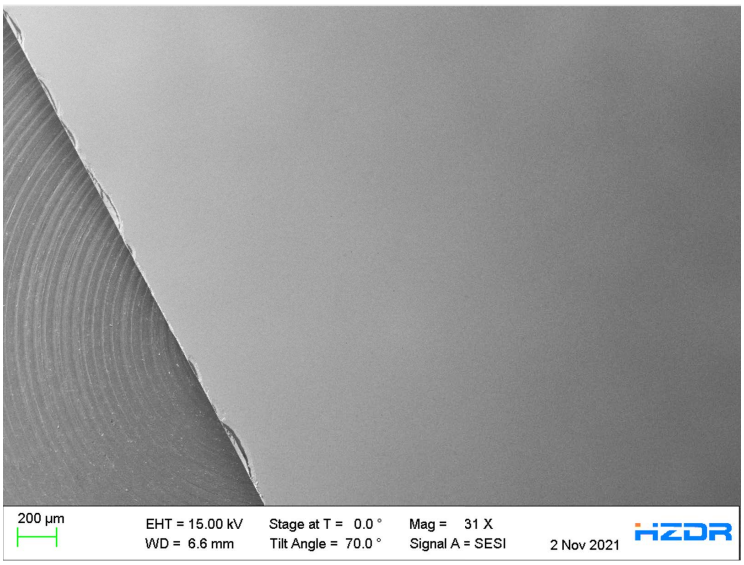

Fig. 77 SEM image of a p-GaN:Cs photocathode (sample A5), several times treated above 500 °C, followed by several Cs activations.

The surface of sample A5 additionally showed several round particles when it was measured using AFM (see Figure 78). These small particles sometimes appeared on the surface of a p-GaN:Cs photocathode that was activated several times. The particles are also observed under SEM for sample C2 (see Figure 85) and were identified as CsOH or Cs compounds by EDX measurements (see Figure A 19 in the Appendix).

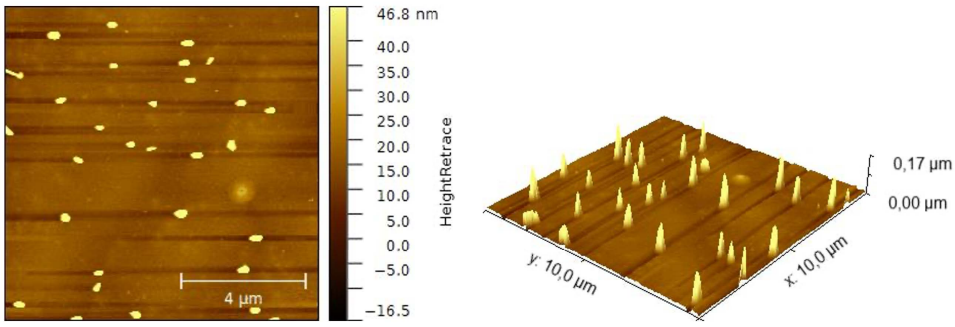

Fig. 78 2D and 3D AFM images of a p-GaN:Cs photocathode (sample A5) which was treated several times above 500 °C and Cs activated.

7 p-GaN:Cs Photocathode Performance on other Substrates

The main focus of the thesis was the intensive study of p-GaN surfaces grown on sapphire and their potential to function as photocathodes with high QE. As mentioned, p-GaN on sapphire is cheap and easily commercially available but, due to some factors such as its isolation properties, it is not the best choice for the GaN layer. Apart from p-GaN grown on sapphire, p-GaN layers grown on Si and TiN were also studied with *in-situ* and *ex-situ* analytical methods to determine their potential to be photocathodes. This Section 7 serves as a minor side-study supplementing the detailed study of p-GaN grown on sapphire (Section 6).

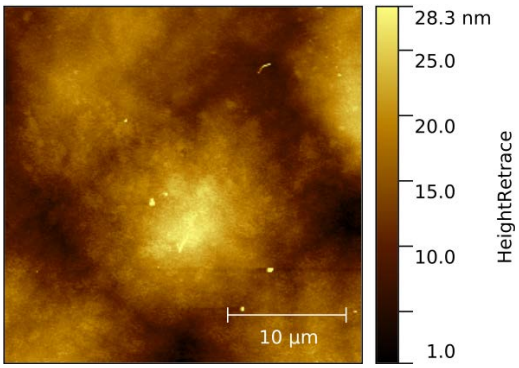

Fig. 79 AFM image of the original p-GaN surface on Si, as received from Xiamen [113].

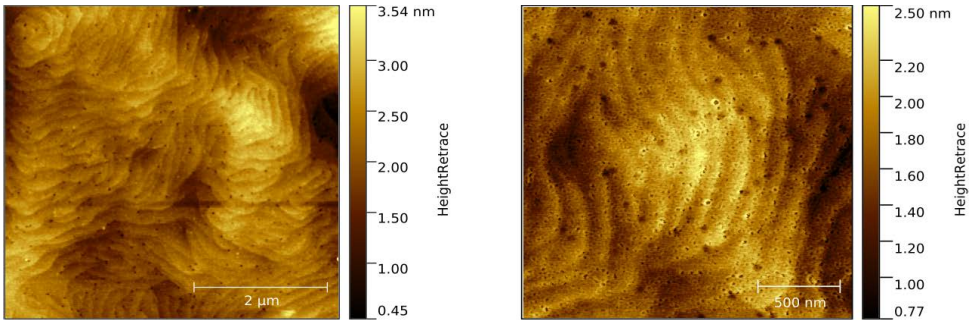

Fig. 80 AFM images of the p-GaN on Si surface after cleaning with the "piranha" procedure.

An AFM image of the original, untreated p-GaN on a Si surface is shown in Figure 79. The original p-GaN on Si exhibited a smooth and uniform surface and only a few particles and dust contaminations were found, resulting in an RMS roughness of approximately 3.0 nm. The p-GaN on Si samples were wet chemically cleaned with the "piranha" procedure, and the etched surface topography is shown in Figure 80. The wet chemical cleaning resulted in the removal of contaminants and oxide layers from the sample surface. Consequently, the terrace-like structure of p-GaN on Si was observed (see Figure 80). This structure was derived from the different rates of crystal growth on the AlN buffer layer. Therefore, the p-GaN on Si showed a different structure than p-GaN on sapphire [74].

The black spots (see Figure 80)were identified as etching pits, exactly representing the hexagonal structure of the grown p-GaN crystal. It is well known that

the lattice mismatch between p-GaN and Si is similar to the lattice mismatch of sapphire. The p-GaN on Si showed significantly more etching pits than p-GaN on sapphire, which indicated a higher defect rate in the crystal lattice that was not fully compensated by the AlN buffer [74, 82, 134]. Owing to the wet chemical cleaning, the RMS roughness of p-GaN on Si could be reduced to 0.5 nm, which was a significant improvement and beneficial for future applications in the injector system.

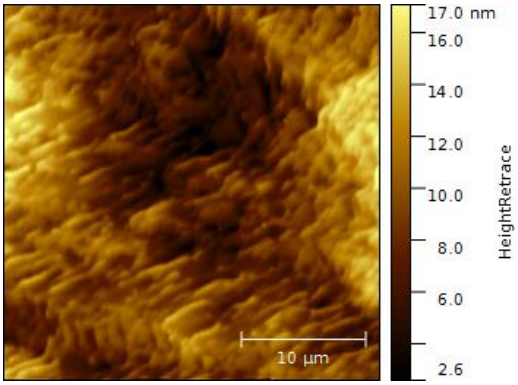

Fig. 81 AFM image of the original p-GaN surface on TiN.

An AFM image of the untreated p-GaN on the TiN surface is shown in Figure 81. The original p-GaN on the TiN surface also showed a terrace-like structure, similar to the one of the p-GaN on Si in Figure 80. In general, it exhibited a uniform surface. The p-GaN on TiN was not cleaned with "piranha" or any other etchant solutions and only a cleaning with 99 % pure EtOH in an ultrasonic bath was applied.

7.1 QE vs. Thermal Cleaning Temperature

After the p-GaNs on Si samples were wet chemically cleaned, the samples were transported under a N_2 atmosphere into the UHV chamber, where they underwent a thermal cleaning process prior to the Cs activation. The QE values obtained from different p-GaN:Cs on Si photocathodes, thermally cleaned at various temperatures, are summarized in Figure 82. The thermal cleaning followed by the activation was repeated several times for each sample. Sample C1 displayed the lowest QE and was destroyed by thermal cleaning above 600 °C. As a result, no re-activation could be carried out for C1. Sample C2, cleaned at a temperature of 500 °C, demonstrated a slightly higher QE (2.5 %) which was reproduced for five activation cycles.
QE values of approximately 4 % were obtained with sample C3 and were reproduced in three cycles. The best QE (4.3 %) was obtained in the third cycle with sample C4, which was thermally cleaned at 500 °C.
Sample C4 showed a low QE when thermally treated at only 300 °C. This QE value could be improved when the same sample was thermally cleaned at higher temperatures.

p-GaN:Cs photocathodes on Si showed significantly lower QE values than p-GaN:Cs photocathodes on sapphire. This is assumed to be due to the higher etching pit rate on the p-GaN on Si surface.

p-GaN on TiN showed similar QE values (see Figure 83) to those of p-GaN on Si (see Figure 82). Sample D1 showed no QE in its first cycle, which was thermally cleaned at 450 °C and it was assumed that residual C and O remained on the surface that hindered the formation of an NEA surface. The QE could be improved when the same sample was thermally cleaned at higher temperatures.

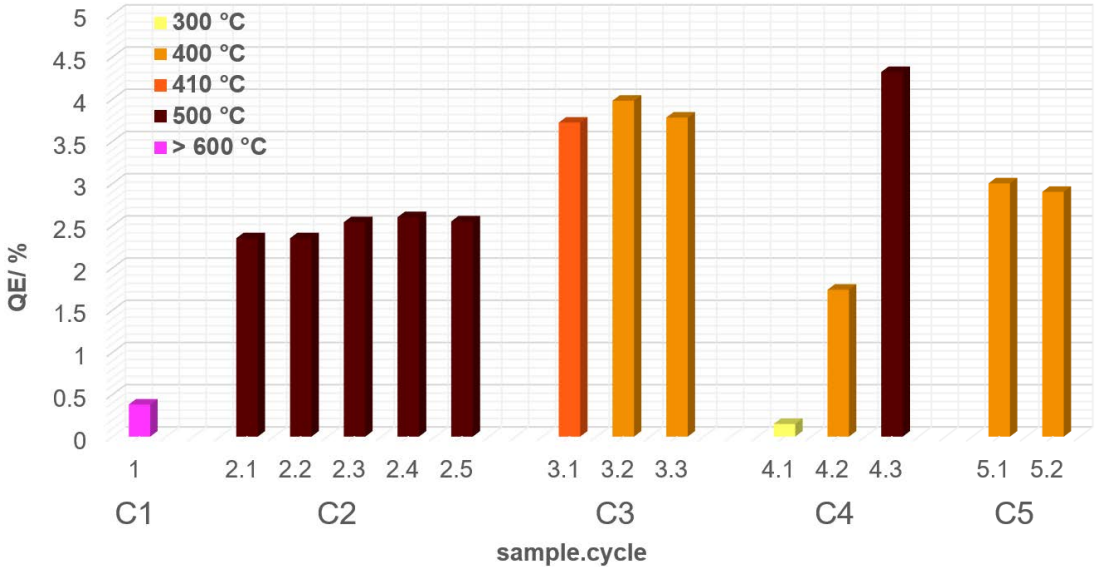

Fig. 82 QE values obtained for a series of p-GaN:Cs photocathodes that were grown on Si and thermally cleaned with a halogen lamp.

The highest QE was measured in the third cycle for sample D1. A QE of approximately 4 % was obtained in the fourth cycle in which D1 was not thermally cleaned but activated by a YoYo activation.
Similar QE values were derived from sample D2, which was thermally cleaned from the backside at 600 °C in each cycle. However, no improvement in the QE value was observed from the thermal cleaning at the backside.

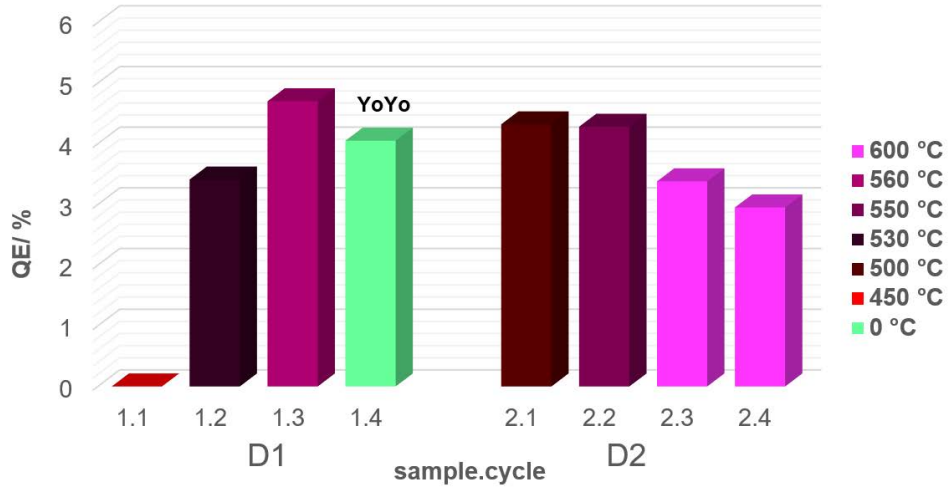

Fig. 83 QE values obtained for two p-GaN:Cs photocathodes that were grown on TiN. Sample D1 was thermally cleaned with a halogen lamp, and sample D2 was thermally cleaned from the backside through the TiN substrate.

7.2 Storage Lifetime of p-GaN:Cs Photocathodes on Si

The storage lifetimes of the p-GaN:Cs on Si samples were also examined and are shown in Figure 84. For sample C1, no lifetime could be determined because the sample was destroyed after the thermal cleaning and the activation. The thermal cleaning at this high temperature caused crystal tension, and hence the sample burst after Cs was deposited to the surface.

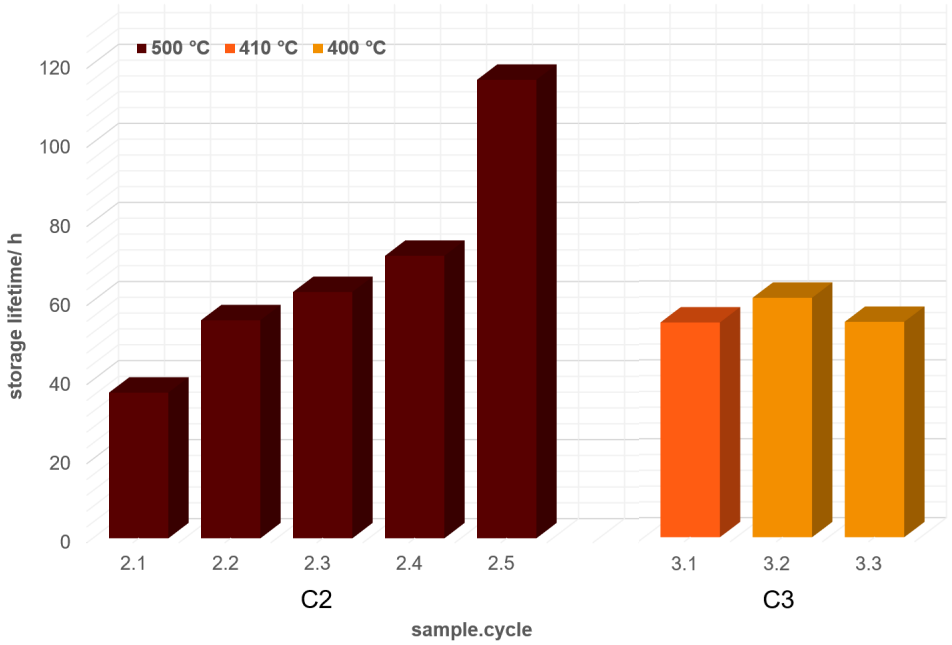

Fig. 84 Storage lifetimes obtained for a series of p-GaN:Cs photocathodes on Si.

Samples C2 and C3 displayed much shorter lifetimes compared to those of p-GaN:Cs on sapphire, shown in Figure 59.
The QE decay of samples C2 and C3 was followed for several hours and days. Sample C2, which was cleaned at 500 °C, showed lifetimes between 30 and 120 h whereby its lifetime increased with every activation cycle. Therefore, the longest lifetime of almost 120 h was achieved in the fifth cycle.
In contrast, the storage lifetime of sample C3, which was cleaned at 400 °C, was between 50 and 60 h and similar for each activation cycle. For samples C4–C5 no lifetimes can be given because these samples were influenced by X-ray irradiation in XPS measurements or were measured at too few points to provide a reasonable extrapolation concerning their storage lifetime.

In summary, sample C2, cleaned at 500 °C, showed a lower QE but a longer lifetime than sample C3, thermally cleaned at 400 °C. Sample C1, cleaned above 600 °C, showed the lowest QE and was destroyed at this temperature. In accordance with the results obtained for p-GaN:Cs on sapphire photocathodes, a thermal cleaning at temperatures of 400–500 °C is more beneficial for the QE and the lifetime of p-GaN:Cs on Si photocathodes.

7.3 Surface Morphology after Cleaning and Activation

The surface morphology of the p-GaN:Cs on a Si photocathode (sample C2), which was thermally cleaned at 500 °C and activated five times, was examined by SEM, as shown in Figure 85.

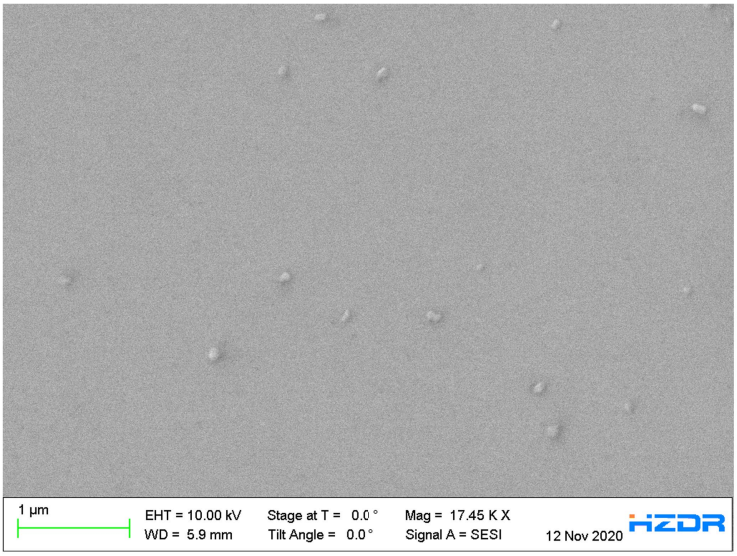

Fig. 85 SEM image of a p-GaN:Cs on Si photocathode (sample C2), thermally cleaned at 500 °C and activated with Cs for five cycles.

The examined p-GaN:Cs photocathode (sample C2) was taken out of the UHV chamber and exposed to air. Its surface components, such as Cs, were probably oxidized as, in general, Figure 85 shows a smooth and uniform p-GaN:Cs surface. The Cs appeared as round and small particles and was found all over the surface. The Cs was oxidized to a Cs_2O_2 or a CsOH compound due to exposure to natural air and moisture. Although it is difficult to examine monolayer thin films by EDX, Cs as an oxide compound could be detected here as evidenced by EDX spectroscopy in Figure A 19 in the Appendix.

The p-GaN:Cs on the Si surface of sample C2 appeared homogeneous, and no significant irregularities were observed. The thermal cleaning at 500 °C was proven to be safe for the p-GaN surface and led to the effective production of a p-GaN:Cs photocathode.

8 Analytical Methods applied on other Photocathodes

This section deals with surface studies of other semiconductor photocathodes such as GaAs and Cs_2Te. Both photocathodes should be regarded as comparative materials to p-GaN and therefore play a minor role in this thesis. *Ex-situ* and *in-situ* methods were used for GaAs to compare its surface conditions to the p-GaN surface in the same way.

Only *ex-situ* methods were available for the surface characterization of Cs_2Te. The Cs_2Te photocathodes were taken out of the UHV chamber because the Cs_2Te preparation chamber was not equipped with an *in-situ* analytical capability.

8.1 Surface Characterization of GaAs Photocathodes

8.1.1 Surface Composition Depending on Cleaning Process

Solvent-Cleaned Surface

The original GaAs surface was examined by AFM and XPS prior to the vacuum thermal cleaning. AFM displayed a smooth surface providing an average RMS roughness of 0.85 nm (see Figure 86). In addition, the surface displayed several scratches and inhomogeneities at a height of approximately 31 nm. The scratches might have resulted from the polishing process by the supplier because a diamond suspension is mostly used to polish semiconductor surfaces. Furthermore, the GaAs surface showed a granular structure with some peaks on it which might represent the adsorbed O_2 on the GaAs surface. The adsorption of O_2 under the air environment was observed for p-GaN by *in-situ* AFM measurements in Section 6.2.3.

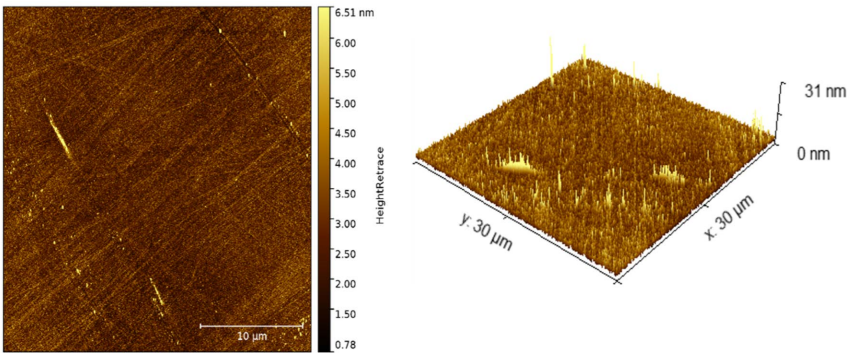

Fig. 86 2D and 3D AFM images of the GaAs surface, cleaned with EtOH only.

Detailed XPS spectra of the photoemission peaks of O 1s, C 1s, Ga $2p_{3/2}$, and arsen (As) 3d are shown for a GaAs surface, cleaned with 99 % pure EtOH, in Figure 87. The spectra were normalized to their backgrounds to be comparable in the intensities of the related photoemission peaks.

The O 1s photoemission spectrum displayed one broad peak, shown in the upper left corner in Figure 87. This O peak (531.9 eV) could derive from a C–OH compound of EtOH or from O_2 that were weakly adsorbed on the GaAs surface and it was thus challenging to predict the number of components from this broad O peak.

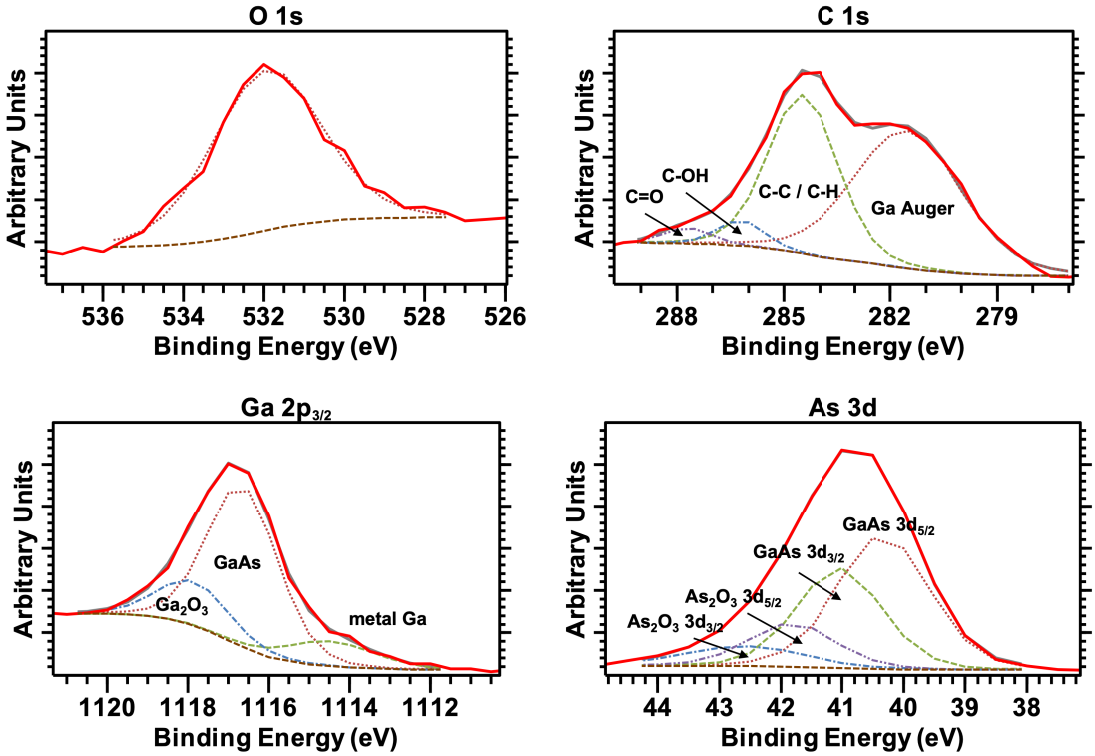

Fig. 87 O 1s, C 1s, Ga $2p_{3/2}$, and As 3d photoemission spectra of the EtOH-cleaned GaAs surface.

The excitation with the Mg X-ray source was inconvenient because a Ga Auger LMM peak at a BE of 281.52 eV overlapped with the C 1s photoemission peaks. However, although this broad Ga Auger peak appeared in the C 1s spectrum, the main C peak at 284.46 eV was found which derived from adventitious C (C–C or C–H bonds). Besides this main C peak, a broad shoulder at a BE of 286.2 eV from a C–OH compound and a smaller peak at 287.68 eV from a C=O compound were observed. This supported the presence of a C–OH compound, observed in the O 1s photoemission spectrum.

The main photoemission peak appeared at 1116.8 eV in the Ga $2p_{3/2}$ spectrum that derived from the GaAs compound. The main Ga $2p_{3/2}$ peak was accompanied by a small sub peak at 1113.9 eV from metal Ga, while a Ga_xO_y component appeared at a higher BE of 1118.2 eV. The spin-orbit splitting of the corresponding Ga $2p_{5/2}$ at 1143 eV was not shown here.

The As 3d photoemission peak showed a spin-orbit splitting of 0.68 eV between its two spin states, As $3d_{5/2}$ and As $3d_{3/2}$, respectively. The main peak was found at 40.3 eV that derived from As $3d_{5/2}$, whereas the As $3d_{3/2}$ appeared at 41.04 eV. Both As components were derived from the GaAs compound. Two additional peaks were observed at a higher BE, at 41.8 and 42.6 eV, that must belong to a higher oxidation state of $3d_{3/2}$ and $3d_{5/2}$ of the As compounds and they potentially belonged to an

arsen oxide (As_2O_3) compound.

Thermal Cleaned Surface

The GaAs sample was vacuum thermally cleaned at 550 °C (2 h), followed by a thermal cleaning at 600 °C (30 min) from the backside. The related detailed XPS spectra are shown in Figure 88. O was removed almost completely after the thermal cleaning, while the C remained on the surface (see Figure 88). No proper fitting can be given for C 1s because the Ga LMM Auger peak overlapped with those peaks of the C 1s. However, it is assumed that there was a peak at a BE of approximately 284 eV caused by adventitious C.

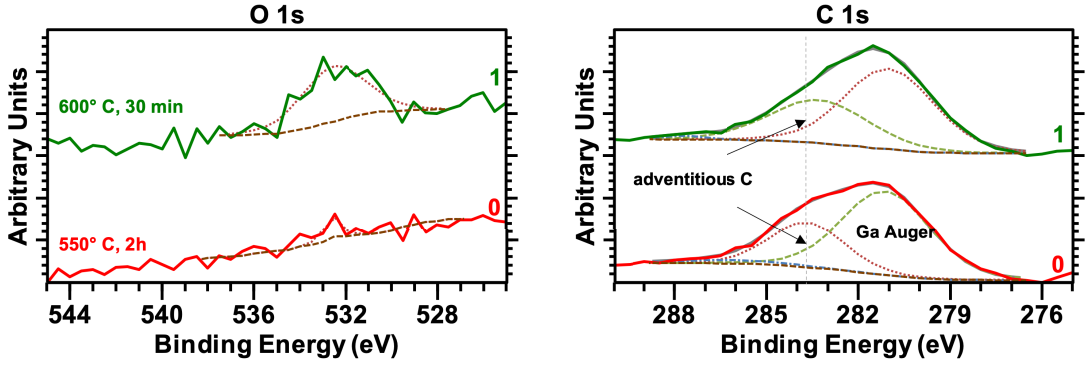

Fig. 88 O 1s and C 1s photoemission spectra of the GaAs surface, thermally cleaned at 550 °C (line 0) and 600 °C (line 1).

The thermal cleaning was not able to remove the C completely but reduced its peak intensity. The O was removed completely after 550 °C but appeared again after a thermal cleaning at 600 °C. This effect might be caused by diffusion processes of incorporated O from sublayers that travel toward the surface during annealing. However, an atomically clean surface was not achieved.

8.1.2 QE vs. Surface Conditions

Cs and O_2 were required to achieve an NEA surface on GaAs. The YoYo process was carried out for two GaAs samples which were compared regarding their QE values. The photocurrent activation curves and the QE decay curves are shown in Figures A 20–A 23 in the Appendix for both samples and all cycles.

Sample B1 was thermally cleaned at 350 °C by the halogen lamp and showed no photoemission at all after the YoYo activation. When the same sample was thermally cleaned at 450 °C and YoYo activated again, a QE of 0.8 % was obtained. XPS measurements were not available at this time to study the sample surface of B1, but it is assumed that a high concentration of C and O remained on the GaAs surface after the thermal cleaning. The contaminations prevented a successful formation of an NEA surface and thus no QE or only a low QE was obtained.

In contrast, sample B2 was thermally cleaned at higher temperatures than sample B1 (550 °C and at 600 °C) from the backside. A reduction of C and O, that built a surface contamination layer, was traceable by XPS measurements. Therefore, the surface quality influenced the maximum achievable QE. For sample B2, QE values

of 7.7 and 8.2 % were obtained because the O and C concentrations were lowered. Figure 89 shows a comparison between the QE values of the two samples B1 and B2, depending on the applied thermal cleaning temperature. The first activation of sample B2 was not successful and thus no QE can be shown.

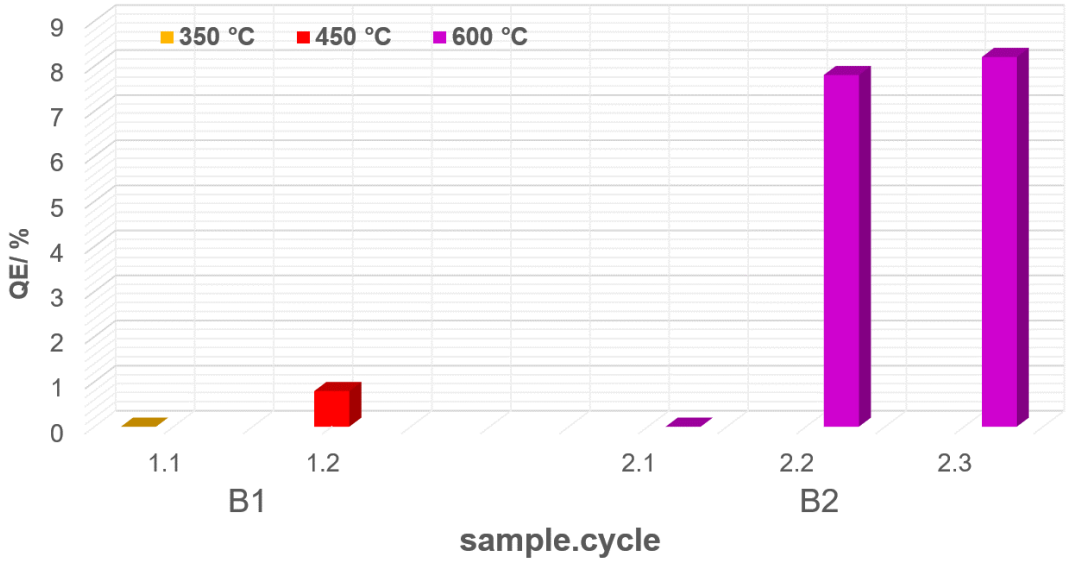

Fig. 89 The QE values that were obtained for two GaAs samples for which different thermal cleaning temperatures were used.

8.1.3 Influence of Carbon Impurities on QE Decay

The surface composition was studied by *in-situ* XPS after the GaAs surface was activated by the YoYo process in its second activation cycle. The first activation of sample B2 yielded no QE value and thus XPS spectra of the second activation cycle are shown.

As mentioned, the thermal cleaning did not completely remove the C from the surface and thus an atomically clean surface was not obtained prior to the deposition of Cs and O_2. After the YoYo activation, Cs and O were observed in the photoemission spectra shown in Figure 90. The Cs 3d displayed a spin-orbit splitting of 14 eV between the Cs $3d_{3/2}$ and $3d_{5/2}$ peaks. For further evaluation, only the spin state of Cs $3d_{5/2}$ was considered.

The main Cs peak was located at a BE of 725.3 eV, accompanied by a smaller sub-peak at 722.8 eV. The main peak at 725.3 eV is derived from the Cs inside the Cs–O dipole layer (Cs^+-O^{2-}-Cs^+) [132] whereas the sub-peak at 722.8 eV is derived from a charging artifact [126]. A ghost signal from the Mg excitation source at a BE of 728 eV and Cs plasmons at 730 eV were also observed [43]. Both peaks also appeared at higher BE in the $3d_{3/2}$ state, respectively.

The deposition of Cs had the greatest influence on the C 1s peak, especially on the C peak at a BE of approximately 284 eV that was derived from adventitious C. After the YoYo activation, a shift toward a higher BE at 286 eV and an increase in the peak intensity in the C 1s peak was observed. The appearance of the C 1s peak at a higher BE than before indicated the formation of a so-called Cs_xC_y species. Additionally, the formation of a Cs–O compound, probably a CsOH or a Cs_2O_2 at a BE

at approximately 533 eV and weakly absorbed O_2 or peroxide ion (O_2^{2-}) at approximately 531 eV were observed in the O 1s spectrum [119–121, 135]. However, the Ga $2p_{3/2}$ and the As 3d photoemission peaks remained in their positions at 1116 eV and 41 eV, respectively, and thus were unaffected by the Cs and O_2 deposition.

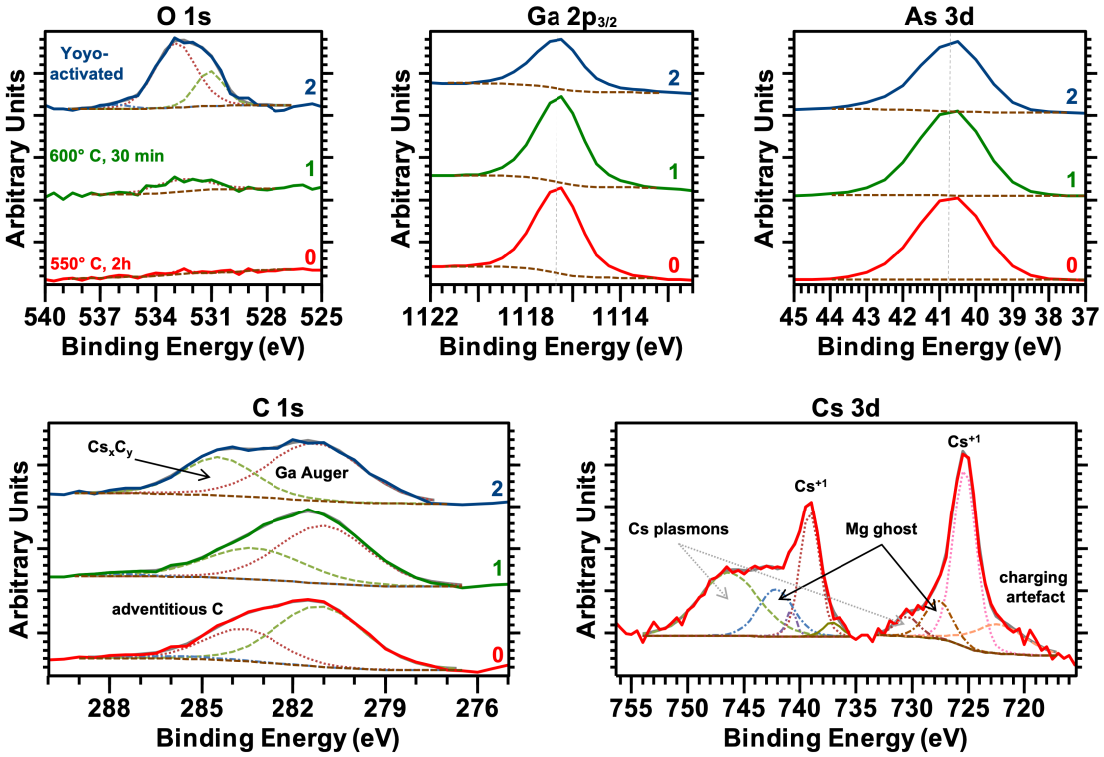

Fig. 90 O 1s, C 1s, Cs 3d, Ga $2p_{3/2}$ and As 3d photoemission spectra of the GaAs surface, after a thermal cleaning at 550 °C (line 0) and 600 °C (line 1), and after YoYo activation (line 2).

The QE value obtained for sample B2 was 7.7 % in the second activation cycle, which decayed exponentially as a function of time as shown in Figure A 22 in the Appendix. A significant QE loss was observed after each XPS measurement which was an undesirable side effect of the X-ray irradiation (see Section 6.4). Furthermore, the XPS spectra shed light on the behavior of the Cs_xC_y compound. Figure 91 shows detailed XPS spectra depending on the QE decay (at 7.7, 2.0, and 0.8 % QE). With ongoing degradation, a shift of 0.27 eV toward a lower BE in the Ga and As peaks was observed. The Cs $3d_{5/2}$ peaks also shifted 0.2 eV toward a lower BE. In contrast, the O and C photoemission peaks showed a completely different behavior.
The peak intensity of the Cs_xC_y increased with ongoing degradation, which is shown in Figure 91 in the C 1s photoemission spectra. It is assumed that the residual surface C attracted the freshly deposited Cs to form a Cs_xC_y species. The peak intensity is directly linked to the number of atoms with the respective oxidation state. This would mean that a formation of these Cs_xC_y islands is preferred and causes an increase in intensity. The change in intensity can also be caused by diffusive processes because the intensity depends on the depth distribution of the atoms [43, 49]. In this case, it would mean that C atoms diffused toward the surface, bonded to the Cs, and were observed as an increase in the intensity of the Cs_xC_y species. Interestingly, no literature concerning the formation of Cs_xC_y

and such island formation exists, and hence the observations and interpretations in this section must be treated with caution. The adhesion between Cs and the GaAs surface became weaker and an NEA surface was no longer obtained when Cs formed a Cs_xC_y species.
Only a small amount of O was detectable after the YoYo activation which must have been derived from O in sublayers of the Cs–O dipole layer. Cs was deposited last and therefore represented the end termination layer.

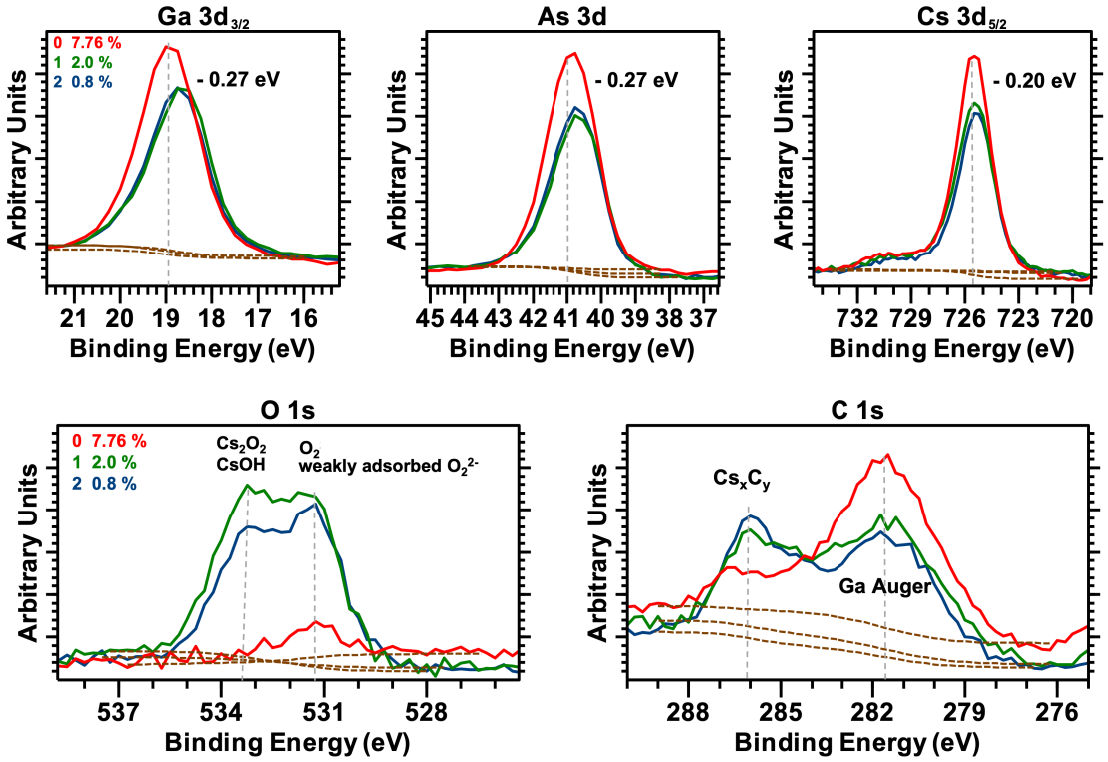

Fig. 91 O 1s, C 1s, Cs $3d_{5/2}$, Ga $2p_{3/2}$, and As 3d photoemission spectra of the GaAs surface during its degradation, showing 7.7 % QE (line 0), 2.0 % QE (line 1), and 0.8 % QE (line 2).

During the degradation, the O peak increased in its peak intensity and was deconvoluted into two main components. The main peak at approximately 533 eV was accompanied by a smaller sub-peak at a lower BE (approximately 531 eV) that derived from weakly adsorbed O_2 or O_2^{2-} and was already observed on the freshly prepared surface. However, the existence of these O peaks indicated that there were a minimum of two O components with different chemical states on the GaAs surface. The O component at a higher BE might be derived from a Cs_2O_2 or a CsOH compound. The effect of OH^- to form a Cs–OH species inside of the Cs–O dipole layer has been discussed in previous studies [132].
The O and C peaks increased in their intensity while the photocathode lost its QE. In contrast, the Ga $3d_{3/2}$, As 3d, and Cs $3d_{5/2}$ photoemission peaks decreased in their intensities during the degradation. This meant that the surface was covered with an O or R–OH compound layer including an additional Cs_xC_y compound.
After the second activation cycle, a white spot was observed on the GaAs sample and the sample cracked between the washers, as shown in Figure 92. In the O 1s spectrum, almost no O was observed after the thermal cleaning, thereby indicating

that the thermal cleaning must have been successful. It also indicated that the heat might be localized on the GaAs surface and the heat dissipation inside the GaAs was inhomogeneous. Consequently, the sample burst between the washers because of different temperatures during the cooldown that caused strain forces in the GaAs lattice.

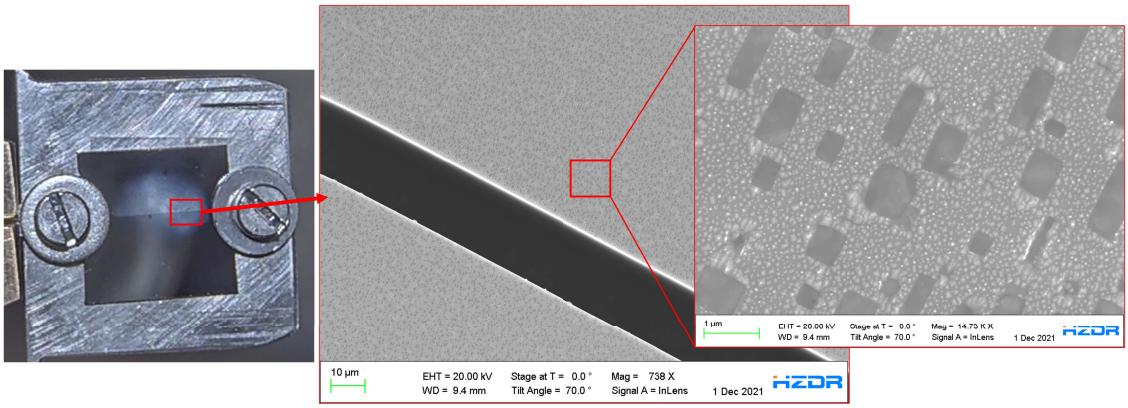

Fig. 92 Photo of the GaAs sample B2 (left) and *ex-situ* SEM images for the same sample after it was taken out of the UHV preparation chamber, showing two different crystal structures on the GaAs surface.

SEM and EDX measurements showed that two different crystal structures existed in this area, including a tetrahedral structure in which the Ga:As ratio was found to be 1 and an orthorhombic structure in which two times more Ga than As was detected. The related EDX spectra are shown in Figure A 24 in the Appendix.
Apart from this area, where the sample cracked, the surface was more homogeneous, as shown in Figure 93.

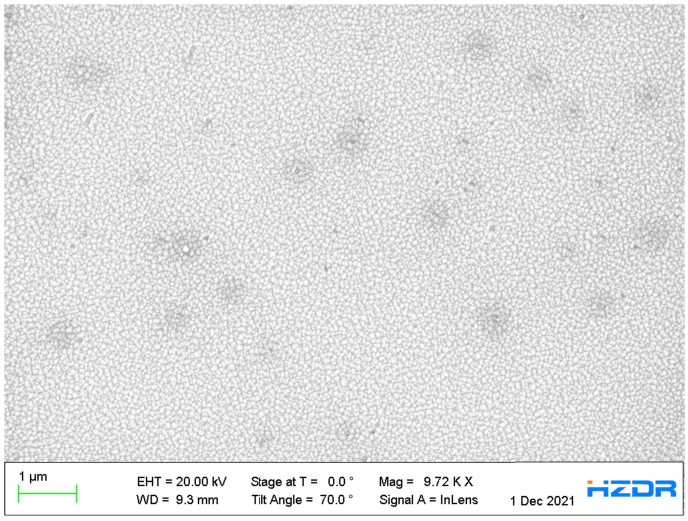

Fig. 93 *Ex-situ* SEM image of the GaAs photocathode surface measured in other areas than shown in Figure 92.

Since the GaAs was taken out of the UHV chamber, as a result of which the surface composition changed, no clear statement about the surface under UHV conditions can be made.

8.1.4 Surface Behavior in Re-activations

Sample B2 was thermally cleaned again at 600 °C when the QE decayed below 1 % in its second activation cycle. The results that are shown in Figure 95 thus represent the third activation cycle for sample B2.
The thermal cleaning was successful in the removal of Cs but not of C and O. It is assumed that the thermal cleaning at 600 °C led to a decomposition of the Cs_xC_y into C and Cs. The Cs was subsequently removed completely by the thermal cleaning and Cs atoms left the GaAs surface, and were no longer detectable. After the thermal cleaning, a C peak at a BE of 284.5 eV was found in the C 1s spectra that derived from adventitious C. Furthermore, the O components were also not removed and both O components (at approximately 533 and 531 eV) remained on the surface. After an additional thermal cleaning at 600 °C, the C and O peaks remained and even increased in their intensity. C and O might thus have diffused from deeper layers to the GaAs surface.
However, when Cs and O_2 were applied to the GaAs surface in a new YoYo activation, the same effect as already seen in the previous activations was observed. Cs had the strongest influence on the C and built a Cs_xC_y species that increased in its intensity with the ongoing degradation of the photocathode. A shift of 0.2 eV toward a higher BE at 533 eV for the O peak was recognized. This meant that the O component located near the surface was significantly influenced by the deposition of Cs.

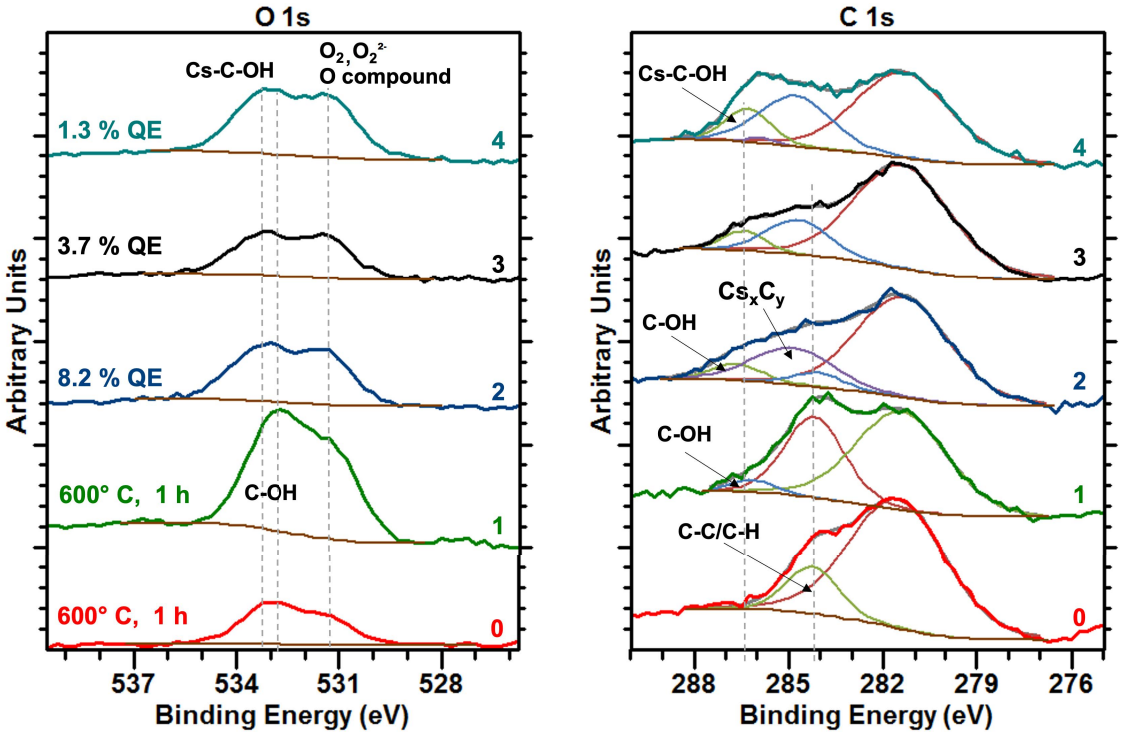

Fig. 94 O 1s and C 1s photoemission spectra for the GaAs surface after a renewed thermal cleaning at 600 °C (line 0), and again 600 °C (line 1), and after YoYo activation with 8.2 % QE (line 2), and degrading with 3.7 % QE (line 3), and 1.3 % QE (line 4).

In the third activation cycle, a maximum QE of 8.2 % was obtained. This QE value was higher than for the second cycle activation in which a QE of 7.7 % was

achieved. Therefore, the O and C remaining after the thermal cleaning did not hinder a successful formation of an NEA surface and seemed even more beneficial for the photocathode performance in the following activation cycle.

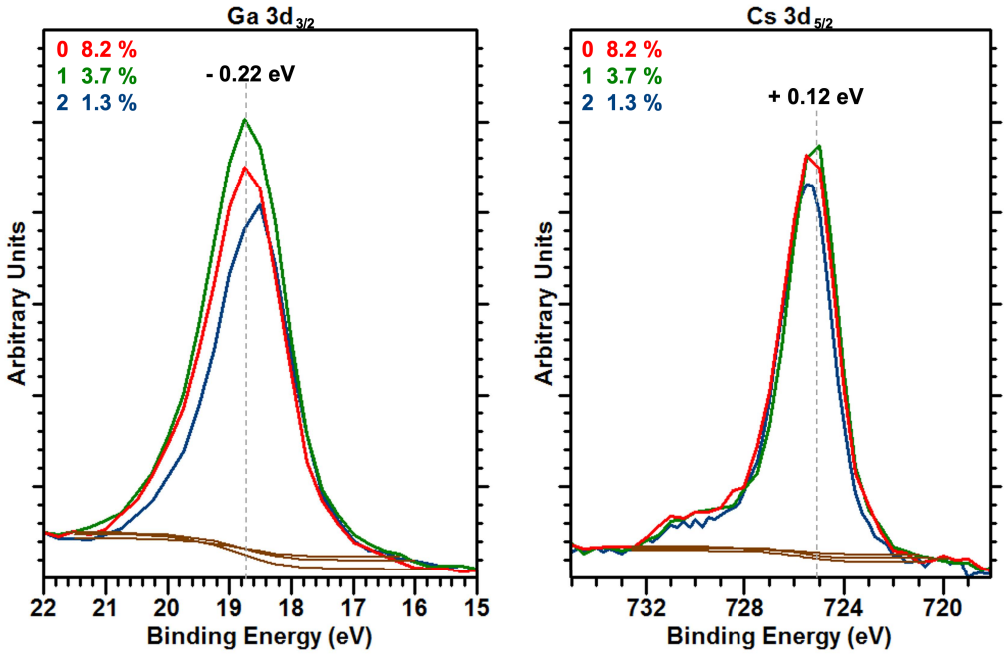

Fig. 95 Ga $3d_{3/2}$ and Cs $3d_{5/2}$ photoemission spectra for the GaAs surface, studied in its degradation after a renewed (3rd time) YoYo activation with 8.2 % QE (line 0), with 3.7 % QE (line 1), and 1.3 % QE (line 2). The Ga $3d_{3/2}$ spectra show a shift toward a lower BE, while the Cs $3d_{5/2}$ spectra show a shift toward a higher BE.

However, with ongoing degradation, a shift of 0.22 eV toward a lower BE in the Ga $3d_{3/2}$ was observed, as shown in Figure 95. The main reason for the degradation was the formation of Cs_xC_y which negatively influenced the GaAs photocathode's performance. Furthermore, an additional component at a higher BE of around 286.5 eV was observed which represented a C component with a strong electronegative partner [43]. It might be a C–OH or C=O component. Additionally, a shift of 0.12 eV toward a higher BE was observed in the Cs $3d_{5/2}$ spectrum. The Cs might also have bonded to a strong electronegative partner such as O_2 whereby one possible component would be a C–OH in combination with a Cs compound.

8.2 Surface Characterization of Cs_2Te Photocathodes

8.2.1 Surface Analysis of Cu Substrates

The surface topography and morphology of the unpolished and the mirror-like polished Cu surface were studied using AFM and SEM measurements before Cs_2Te was deposited on the Cu surface.

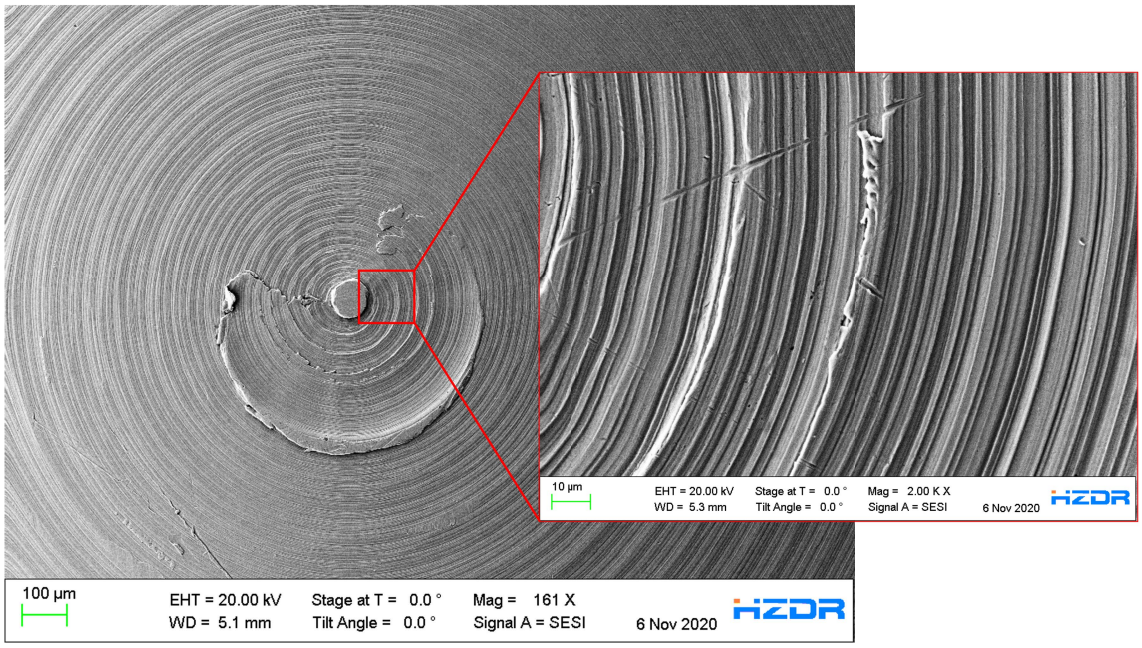

Fig. 96 SEM images of the unpolished Cu plug surface.

An SEM image of a non-polished Cu plug surface is shown in Figure 96, revealing a concentric Cu surface. Many grooves and notches were found which built a concentric structure from the middle of the plug center. The grooves were generated by the drilling machine of the workshop.
The AFM images shown in Figure 97 confirmed the concentric structure observed in the SEM. The non-polished Cu had an average roughness of approximately 106 nm which indicated a non-smooth, rough surface.

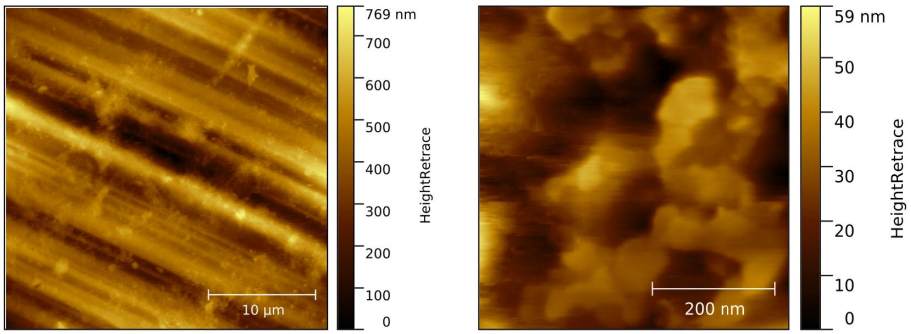

Fig. 97 AFM images of the unpolished Cu plug, drilled by the workshop.

After the polishing (described in Section 5.2.2) the Cu surface appeared optically as a mirror-like surface. An SEM image of a polished Cu surface is shown in Figure 98. The concentric structure disappeared and no grooves were found anymore. The polished surface exhibited a smooth surface and showed a RMS roughness of 20 nm according to AFM.

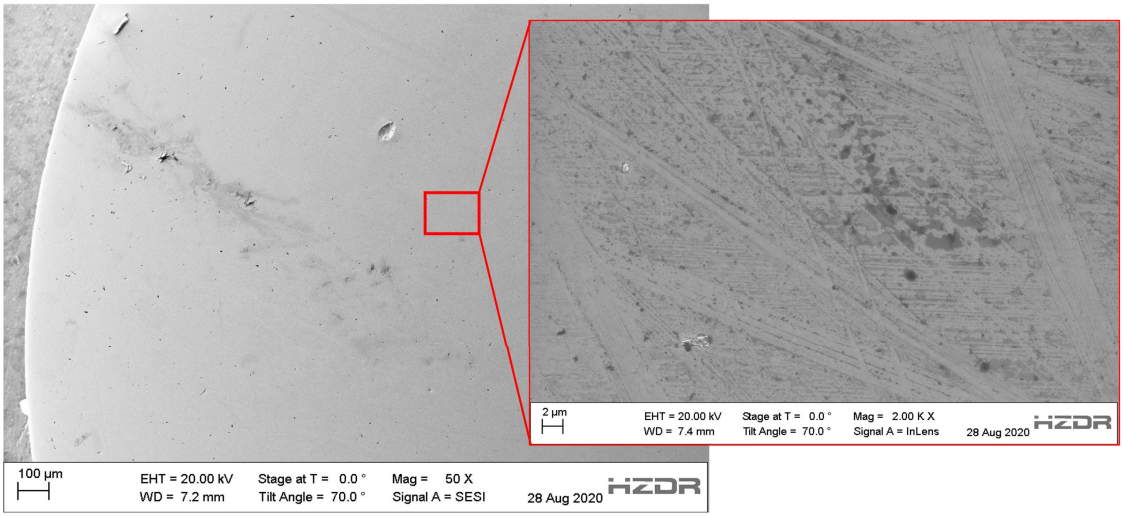

Fig. 98 SEM images of the polishing result on the polished Cu plug surface.

The Cu surface contained several scratches, which might be an undesirable side effect of the polishing suspension. These scratches might originate from the Cu structure itself, from deeper layers, or they might be caused externally by the polishing using SiC suspensions. Some SiC particles, which were identified as residuals from the polishing suspension, were found at the surface and were identified with EDX, as shown in Figure A 25 in the Appendix.
The initial grain size of the Cu was furthermore revealed by the polishing and was observed by AFM measurements that are shown in Figure 99.

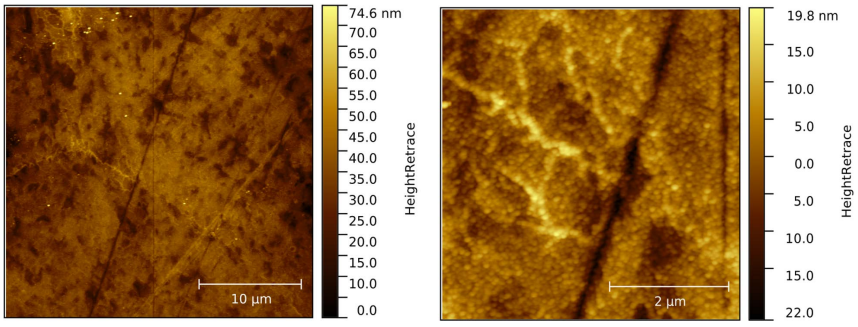

Fig. 99 AFM images of the polished Cu plug surface.

The improvement of the polishing of the Cu surface and the comparison between the unpolished and polished Cu surface was noticeable and was highly significant for the Cs_2Te quality. The mirror-like Cu was subsequently transported to the cleanroom and rinsed with C_3H_8O, 5 % citric acid ($C_6H_8O_7$) solution, and C_6H_6.

8.2.2 QE Performance of Cs_2Te during Operation in SRF Gun II

The survivability under RF fields is one of the requirements for a robust photocathode. The Cs_2Te photocathodes generally show good survivability under RF fields compared to other semiconductor photocathodes such as GaAs. Nevertheless, the Cs_2Te at HZDR was always affected by the applied RF field and all photocathodes showed a typical QE loss during their operational lifetime. A QE decay curve and the QE maps for a Cs_2Te photocathode (sample E1), used in ELBE SRF Gun II, are shown in Figure 100.

A QE map is a 3D image of the QE distribution of the photoemissive layer generated by scanning the surface with a laser. The photocathode surface is scanned area by area and measured in terms of its QE. It thus shows a specific QE value for a given surface. An inhomogeneous QE distribution of the photocathode thus indicates inhomogeneities and surface changes within the Cs_2Te layer.

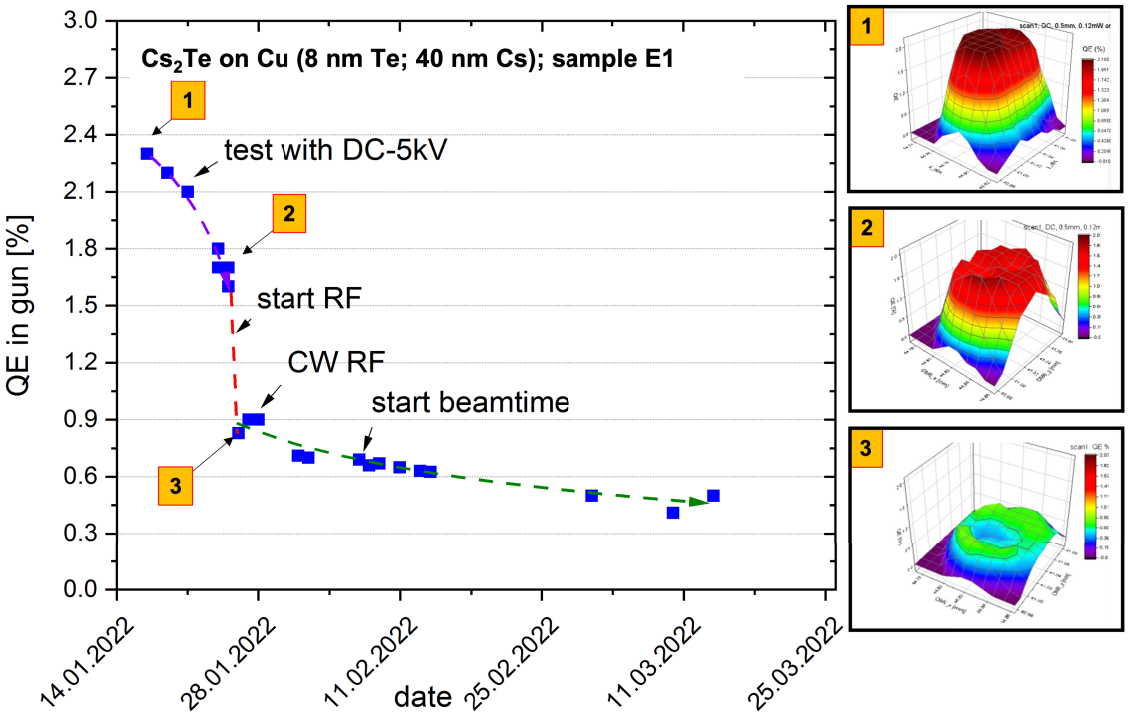

Fig. 100 QE decay curve of Cs_2Te (sample E1) during its operational lifetime in the SRF Gun II with corresponding QE maps, taken at three different points in the decay curve.

The QE map with number 1 in Figure 100 was taken when the cathode was freshly inserted into the SRF Gun II. The QE map indicated a homogenous Cs_2Te layer because the same QE value was measured in the photoemissive area of 4 mm. With ongoing operation in the SRF Gun II, the photocathode lost QE as shown in the QE decay curve in Figure 100. QE map number 2 showed less QE in the middle of the photocathode compared to QE map number 1. The QE became even more inhomogeneous when the RF field was applied to the photocathode, as shown in QE map number 3. The QE especially decreased in the middle of the photoemissive layer compared to the border regions. One reason for this might be ion back-bombardment which happens when residual gases are ionized and are accelerated backward onto the cathode surface, damaging the Cs_2Te photoemissive

layer. Another reason might be that photoelectrons hit the cavity wall and release attached gases, which contaminate the cathode surface. However, it is evident that the QE was negatively influenced during the RF operation with the consequence of significant QE losses in the middle of the photoemissive Cs_2Te layer.

The chemical composition in the middle of the Cs_2Te layer was assumed to be different from the chemical composition at the border region, where the Cs and Te layers were deposited slightly offset from each other. Further investigations of the chemical composition before and after SRF operation were discussed in Section 8.2.3. However, the high impact of the RF field on the photoemissive layer and its influence on the surface area, especially localized in the central region, was illustrated by the QE map.

8.2.3 Analysis of the Degraded Cs_2Te Surface

The QE decay of the Cs_2Te photocathode (sample E1) is shown in Figure 101. The photocathode lifetime was measured at a wavelength of 260 nm with a power of 140 μW whereby a voltage of 350 V was applied to the anode. The freshly prepared photocathode showed a QE of 6.1 % but it lost approximately half of its initial QE during its transportation into the transport chamber. This QE drop signalized that the photoemissive layer was sensitive to the motion in vacuum and thus to any vacuum instabilities which caused the release of gases or molecules. The transport chamber was moved from the cleanroom to the ELBE SRF Gun II. During this transportation, the Cs_2Te did not lose much QE and its QE value stayed almost constant. The photocathode showed a residual QE of 2.3 % when it was inserted into the SRF Gun II. During the operation, the cathode was influenced by the applied RF field and lost the QE further.

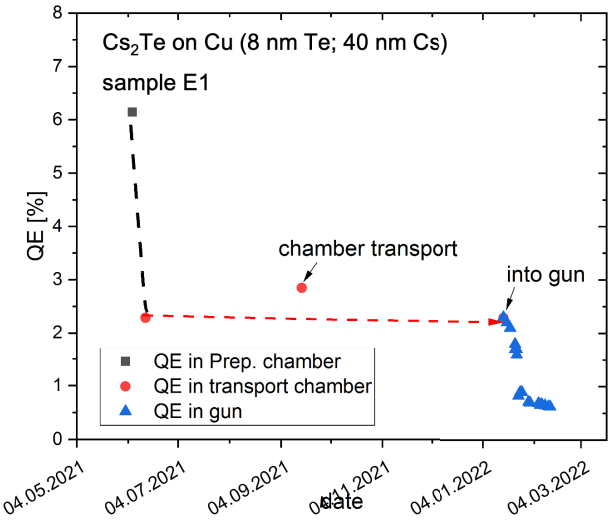

Fig. 101 QE decay of sample E1 after the preparation, storage in the transport chamber and transportation to the SRF Gun II, measured at a λ of 260 nm and with a bias of 350 V on the anode.

After the use in the SRF Gun II, the photocathode was stored in the transport chamber for several months and the used photocathode was subsequently taken out for *ex-situ* surface measurements.

Chemical Composition with XPS

Two Cs_2Te photocathodes (samples E1 and E2) were compared in their chemical compositions using XPS measurements.

Sample E2 contained a 6 nm Te layer and a 32 nm Cs layer, while sample E1 had a 8 nm Te layer and a 40 nm Cs layer. Sample E1 was used in the SRF Gun II while sample E2 was not. Both Cs_2Te layers of the samples were deposited on Cu.
The two photocathodes were taken out of the UHV preparation chamber and therefore the resulting XPS spectra might not show the original surface conditions because the Cs_2Te photocathodes were exposed to air. Nevertheless, a comparison of Te and Cs photoemission peaks reflecting the chemical composition of two samples allowed to receive an information about the influence of the RF field.

The XPS survey spectra of both samples were normalized to their backgrounds and showed a large amount of O and C that was derived from the air environment (see Figure 102).

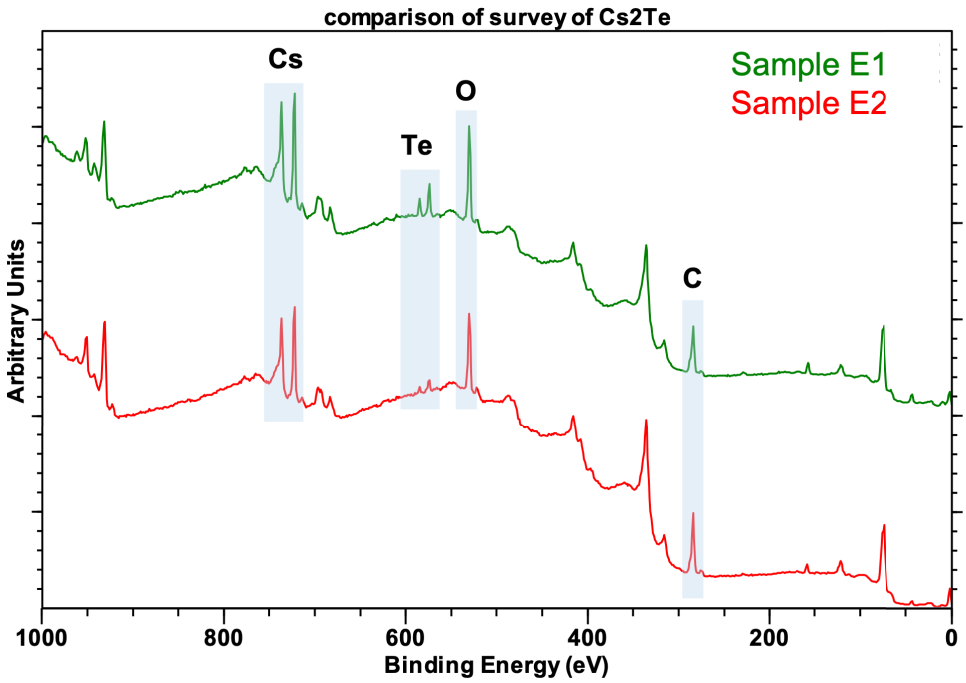

Fig. 102 Photoemission survey spectra of Cs_2Te surfaces for sample E1 (green line) and sample E2 (red line), showing a large amount of C and O for both Cs_2Te surfaces because the samples were taken out of the Cs_2Te UHV preparation chamber.

Figure 103 shows the detailed spectra of the Cs $3d_{5/2}$ photoemission peaks from samples E1 and E2 as a comparison. The Cs $3d_{5/2}$ peaks showed a shift toward a lower BE compared to the Cs^0 (726.4 eV) [43]. The main photoemission peak was therefore observed at a BE of 724.1 eV for both samples. The location of this Cs peak at a lower BE than for the bulk Cs indicated that the Cs component might have been derived from a Cs compound in which the Cs contained an oxidation state of +1. The Cs probably turned into a Cs_2O_2 or a CsOH on exposure to the air environment [132]. Furthermore, a sub peak at approximately 725.5 eV appeared, which might be derived from Cs_2O_2 [118]. A third sub peak showed up at approximately 722 eV which was a charging artifact and occurred in almost all of the XPS spectra [126]. The oxidation of Cs into a Cs_2O_2 or CsOH was further supported by the location

of the O 1s photoemission peak in the BE as the O peak was found at a BE of 530 eV in the survey spectra for both samples. At this BE, metal or alkali-metal oxides typically appear in the spectra [43, 124, 125] Additionally, a large amount of C at a BE of 284.15 eV was found that represented adventitious C. The detailed XPS spectra of the O and C peaks are shown in Figure A 26 in the Appendix.

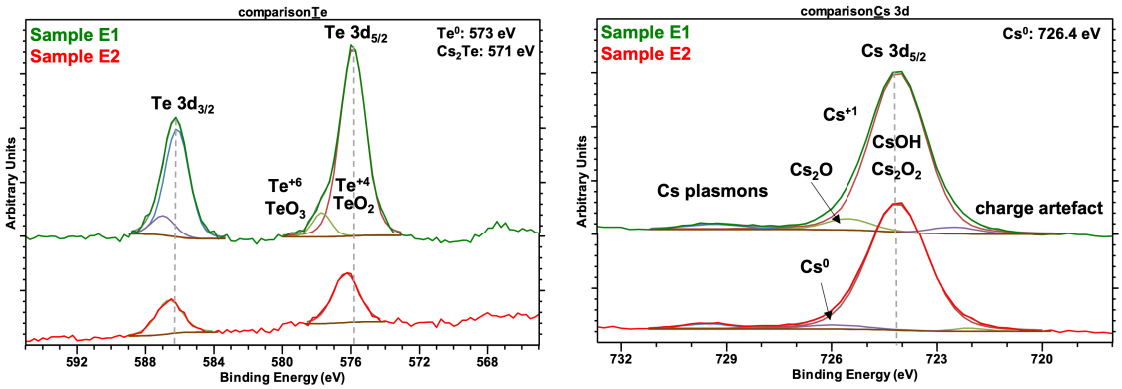

Fig. 103 Te 3d and Cs $3d_{5/2}$ photoemission spectra for the Cs_2Te photocathode surface, used in SRF Gun II (sample E1, green), and as a prepared Cs_2Te photocathode surface (sample E2, red).

Interestingly, the Te photoemission peak showed a significant difference between the two samples, as indicated in Figure 103. The Te peak for sample E2, which was not used in the SRF Gun II, showed a lower peak intensity compared to the Te peak of sample E1, which was used in the SRF Gun II. One reason might be that sample E2 generally contained a lower amount of Te, resulting in a less intensive peak. In contrast, sample E1 contained a slightly higher amount of Te with a 2 nm thicker layer than that of sample E2. Another reason for the difference in the peak intensities was that the Cs layer of sample E1 was influenced by the RF field during its operation in the SRF Gun II. This meant that the Cs layer is thin enough to detect a higher amount of Te in sample E1 because a part of the Cs atoms might have left the Cs_2Te surface under the RF field.

Additionally, the Te 3d peak of sample E1 showed a decomposition into two components, while in sample E2 only one Te component was observed. The main Te peak was measured at a BE of 575.88 eV, accompanied by a small sub peak at 577.71 eV. In general, higher oxidation states are found at higher BE. Thus, this shift toward a higher BE meant that the Te must have a higher oxidation state compared to the bulk tellurium (Te^0) at 573 eV [43]. The Te probably turned into tellurium oxide (TeO_2) or tellurium trioxide (TeO_3), in which the Te ion has an oxidation state of +4 and +6. Apart from the difference in their peak intensities, the Te peak showed different BE values for the two samples. For sample E2, the main Te 3d peak was found at a BE of 576.63 eV as a single component. As a Cs_2Te compound, Te is located at a BE of 571 eV, where the Te has an oxidation state of -2 [65, 136]. For both samples, no Te^{-2} state and thus no Cs_2Te compound was found in the Te 3d spectra.

The XPS measurements showed that sample E1 differed significantly in the Te signal, especially in the Te chemical state and intensity, when compared to the Te signal of sample E2. This implied that the RF field and thus an operation in the SRF Gun II had an influence on the Cs_2Te photoemissive layer. However, no clear

statement concerning the original chemical composition can be made because the samples were taken out of the vacuum environment. It is worth mentioning that *in-situ* analysis is essential to avoid surface oxidation and to analyze the original composition under UHV conditions.

Surface Morphology with SEM and EDX

A Cs_2Te photocathode (sample E3), which had a 10 nm Te layer and a 45 nm Cs layer, was taken to the SEM. The SEM measurements of this sample aimed to study the surface morphology in the surface regions in which the Cs and Te layers were deposited slightly offset from each other.
As sample E3 was taken out of the UHV chamber, the resulting EDX spectra might not show the original surface conditions because the Cs_2Te photocathodes were exposed to air. In particular, the Cs oxidized into a Cs_2O_2 or CsOH compound, and thus the original surface composition changed.

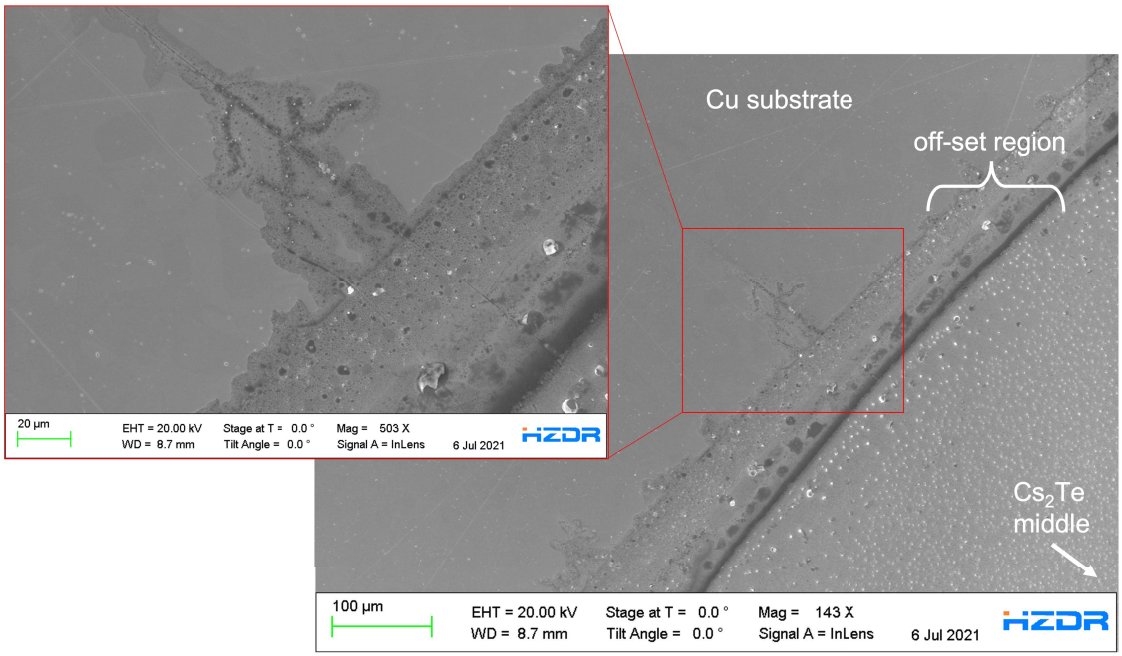

Fig. 104 *Ex-situ* SEM image of the Cs_2Te surface in its border region, where Cs and Te were deposited off-set to each other, and an SEM image at higher magnification of the off-set region.

An SEM image of the border region of sample E3 is shown in Figure 104. The Cs_2Te photocathode showed inhomogeneities in the border region of the deposited layer as the border region was different in its morphology compared to the middle region. The area at the bottom right belonged to the middle of the photocathode, where the Cs_2Te layer was deposited. Next to the middle area, a circle with a different morphology was observed, representing the off-set region. Cu from the Cu substrate was found in the outer part of this circular region. An SEM image at higher magnification from the outer border region is also shown on the left side in Figure 104. At this magnification, the crystal growth of Cs_2Te along the Cu grains and surface scratches were observed which meant that no clear boundary existed for the deposited Cs_2Te. EDX was used to identify whether the different borders differ

in their chemical composition or were homogenous.
EDX is not a surface-sensitive method because the detected X-rays were generated from about 1 μm depth of the material as mentioned in Section 2.2.3. Therefore, Te within a 45 nm thick Cs_2Te layer was hard to detect. More Cs was detectable in the middle region of the photocathode than in the outer areas. Additionally, in the middle area, Cs particles were found all over the surface, as shown in detail in Figure 105. The Cs particles were not observed in the circular border region.

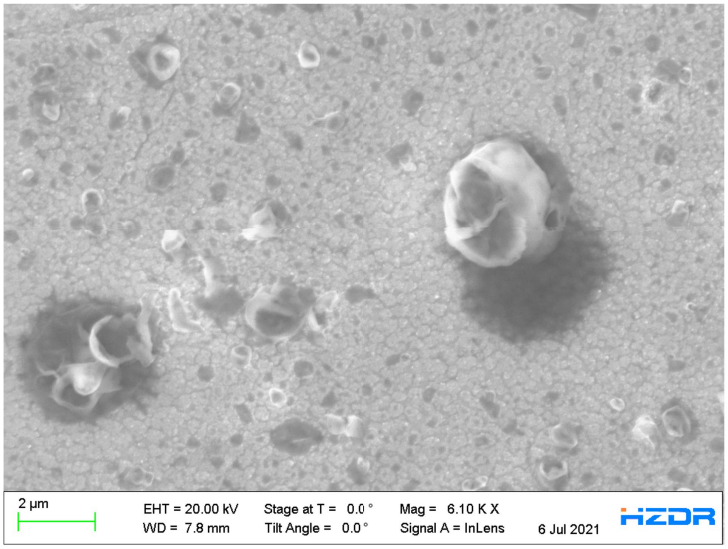

Fig. 105 *Ex-situ* SEM images of surface particles found in the middle area of sample E3. EDX identified the particles as a Cs–O compound, which probably is a CsOH compound.

EDX measurements identified these particles as a Cs oxide compound, probably a CsOH, and a small amount of Te was also detectable. The EDX spectrum of the CsOH particle is shown in Figure A 27 in the Appendix.

9 Conclusions

The cleaning and activation of commercially available p-doped gallium nitride (p-GaN) samples, grown on sapphire by MOCVD was successfully demonstrated in lengthy experiments. A III-V semiconductor photocathode preparation chamber with an average UHV pressure of 5×10^{-10} mbar and all the necessary functionalities was successfully commissioned. The different functionalities inside the preparation chamber, such as the anode, the sample holder with a heating and cooling option from the backside, and a halogen lamp, were developed and continuously improved in the last few years.
The adaption of an *in-situ* XPS to the preparation chamber, which represented one of the main goals of this thesis, was furthermore successfully realized. The surface chemical composition and the surface changes of the p-GaN:Cs photocathodes were studied without leaving the UHV environment, which opened up a new opportunity to trace chemical surface states and thus the surface quality. Many technical challenges such as the equalization of the different sample holders, the alignment of the chamber heights, the adjustment of the connection tubes, and the sample transportation were addressed and discussed in this work.

The thesis focussed on the detailed surface study of p-GaN grown on sapphire. Different wet chemical cleaning processes were validated via *ex-situ* AFM measurements, showing that the cleaned surface possesses an average RMS roughness of 1.7 nm for p-GaN samples grown on sapphire. Etching pits were observed on the surface that represented the hexagonal crystal structure.

Furthermore, AFM measurements confirmed the adsorption of O_2 on the p-GaN surface when the freshly cleaned samples were exposed to air. Consequently, it is crucial to protect the p-GaN sample from the air environment to avoid oxidation. The cleaning process was carried out under dry N_2 in a glovebox, and the p-GaN samples were subsequently transported into the UHV preparation chamber under this dry N_2 atmosphere. A suitcase that ensured the exclosure of air gases after the wet chemical cleaning and provided for sample transportation under a dry N_2 atmosphere was developed and successfully used.
Although a wet chemical cleaning with "piranha" solution (H_2SO_4:H_2O_2) was found to be the best choice because low C and O concentrations were found on the cleaned p-GaN surface, a cleaning with 99 % EtOH followed by a subsequential vacuum thermal cleaning at 450 °C represented a simple cleaning procedure that is manageable for all laboratories.

After the wet chemical cleaning, the p-GaN samples underwent a subsequential vacuum thermal cleaning. The presence of O during the sample handling, as well as the temperature applied during the thermal cleaning, significantly influenced the surface morphology and affected the QE and lifetime. Moderate temperatures of 400–500 °C were found to be more beneficial for the p-GaN surface quality, which was reflected by achieving higher QE values. SEM investigations showed that the surface morphology of p-GaN was changed at temperatures above 600 °C.
In-situ XPS measurements showed that the vacuum thermal treatment was not able to remove C and O entirely but the thermal cleaning reduced the peak intensities and thus their relative concentrations on the surface. The remaining O and C contaminations were assumed to be residuals from the MOCVD process.
The complete removal of these contaminants can only be achieved by Ar^+ irradiation

on the p-GaN surface, which was accompanied by a strong depletion of the N atoms. The excessive thermal cleaning and Ar^+ irradiation consequently caused a large number of defects on the semiconductor surface, which could be validated by SEM and EDX.

After the thermal cleaning, the samples were activated with a thin layer of Cs at an average pressure of approximately 1×10^{-9} mbar. The activation method with Cs alone was feasible and practically reliable. With p-GaN:Cs on sapphire photocathodes, a high QE of over 10 % and an extrapolated storage lifetime of over 5000 h were demonstrated.

The XPS measurements shed light on the surface composition after the deposition of Cs and helped to study the degradation mechanism of p-GaN:Cs photocathodes. A shift toward a higher BE was observed in the XPS spectra of the N 1s and Ga $3d_{3/2}$ photoemission peaks. This shift indicated that the electron-rich Cs was successfully adsorbed onto the p-GaN surface.
Before the Cs activation, adventitious C at a BE of 284 eV was found, which was also present after the Cs activation but did not shift in terms of its BE. The presence of this remaining C had a significant effect on photocathode degradation. After the activation with Cs, a new C compound at a higher BE (approximately 286 eV) in the C 1s spectrum appeared, which was identified as a Cs_xC_y species. With ongoing degradation of the photocathode, the photoemission peak intensity of the Cs_xC_y species increased. The formation and continuous growth of the Cs_xC_y species on the p-GaN surface were assumed to cause a shift of the related photoemission peaks back toward a lower BE.
Cs showed an oxidation state of Cs^{+1} which was observable at a lower BE than for the metal Cs^0. This meant that the Cs was positively charged after it was deposited on the p-GaN surface and also kept this oxidation state during its transformation into a Cs_xC_y species.

The re-activation of p-GaN:Cs photocathodes was practical and reproducible. Some remaining photocurrent was measured after the samples were thermally cleaned prior to the next Cs activation and the *in-situ* XPS measurements revealed that Cs was not removed completely from the surface. However, the remained Cs seemed beneficial for the re-activations because higher QE values were achieved compared to those QE values achieved in the first activations.

The QE of the photocathodes decayed exponentially and an extrapolation helped to predict the photocathode's total storage lifetime without measuring the "real" lifetime until the QE vanished completely.
However, significant QE losses were always measured after the p-GaN:Cs photocathodes were studied by XPS. The origin of the QE loss derived from the incident X-rays as an external influence. Cs and its adhesion on the p-GaN surface were strongly influenced by the incident X-ray irradiation, which led to accelerated external aging of p-GaN photocathodes, which was observed by a shifting of the Cs photoemission peaks toward a lower BE. It is therefore recommended to use a lower X-ray beam power or to cool the samples to prevent X-ray damage to cesiated photocathodes.

The surface morphology was studied *ex-situ* with SEM and EDX after the samples were thermally cleaned and activated with Cs. The results showed that the surface appeared inhomogeneous when the sample was thermally cleaned at a high temperature above 600 °C. A thermal cleaning from the backside through the sapphire substrate represented an alternative to thermal cleaning with a halogen lamp.

However, the thermal cleaning from the backside resulted in nearly the same QE values and thus no benefit was gained from using this thermal cleaning method.

In addition to the intensive study of p-GaN grown on sapphire, extensive experiments were also conducted on p-GaN grown on other substrates such as Si and TiN. The QE values and storage lifetimes of p-GaN:Cs on Si were significantly lower than those achieved for p-GaN:Cs on sapphire, which was related to the p-GaN crystal quality that was influenced by the substrate. However, the p-GaN photocathodes grown on these substrates also showed a high potential to be future electron sources for accelerators.

A few experiments were conducted on GaAs photocathodes in which the surface quality was characterized with *in-situ* and *ex-situ* methods. The studies on GaAs were intended to show that p-GaN and its activation are more practical and more feasible.
The *in-situ* XPS measurements helped to explain the surface changes of YoYo-activated GaAs. A successful reduction of O and C on the GaAs surface was achieved after the thermal cleaning at temperatures of 600 °C. As a result, higher QE values of 7–8 % were obtained. The main reason for the GaAs photocathode degradation was found to be the formation of a Cs_xC_y species that increased in its peak intensity with ongoing QE decay.

In this work, YoYo-activated p-GaN was studied in addition to the p-GaN activated with Cs alone. QE values between 6–8 % were obtained for p-GaN surfaces in which the YoYo activation was applied. Because the YoYo activation required molecular O_2, the activation was more complex compared to the activation with Cs alone because the O_2 partial pressure has to be controlled and set precisely to avoid O_2 overdosing of the sample. An activation with solely Cs was the better choice for p-GaN because it is more practical and comparable QE values were obtained.

Less extensive studies were also carried out on Cs_2Te photocathodes to highlight the necessity of *in-situ* analytical capabilities.
Cs_2Te photocathodes are the preferred photocathodes for the ELBE SRF Gun II at the moment. The elaborate preparation of the grown crystal of Cs_2Te on Cu was demonstrated in which a maximum QE value of approximately 6 % was achieved. During the transportation into the SRF Gun II, and due to the operation in the SRF Gun II, the Cs_2Te photocathode lost approximately half of its initial QE. The reason for this QE loss and the surface conditions under vacuum could not be studied because no analytical capabilities were available in the Cs_2Te preparation chamber. *Ex-situ* analysis of the Cs_2Te photocathodes was not able to show the "real" surface because the Cs and Te oxidized into hydroxide and/or oxide compounds on exposure to air.

Overall, twice as high QE values were achievable for p-GaN:Cs on sapphire photocathodes than for Cs_2Te photocathodes. Furthermore, p-GaN:Cs photocathodes showed higher QE values than GaAs whose activation is more complex because it requires O_2 and Cs. *In-situ* XPS measurements revealed that C and O were incorporated as unwanted impurities into the p-GaN lattice, which resulted from the growth of MOCVD. The remaining surface C contamination was found to be the main reason for the photocathode degradation. The *in-situ* XPS showed that an undesired formation of a Cs_xC_y species on the surface increased in its intensity which caused the degradation of the p-GaN:Cs photocathodes.

In this thesis, the chemical composition of p-GaN as a III-V semiconductor pho-

tocathode was studied because an adaption of an XPS system to a UHV preparation chamber has been successfully realized. The *in-situ* XPS measurements allowed for studying surface changes of the photocathodes without leaving the UHV environment. The capability to study samples with an *in-situ* method helped to shed light on different treatments, especially in the cleaning and activation, to examine the photocathode performance regarding the surface quality. Special attention was paid to elucidating the photocathode degradation mechanism more clearly.

10 Outlook

p-GaN is a promising candidate for a future novel electron source in particle accelerators [26, 137]. Although p-GaN requires UV-light, its spectral response is adjustable by the manipulation of the band gap with suitable dopant atoms [70, 73]. These dopants, e.g. In, are able to shift the band gap into the wavelength range of visible light. Furthermore, p-GaN can be more easily prepared compared to other semiconductor photocathodes such as Cs_2Te or GaAs. Another advantage is the possibility to juvenile this cathode with subsequent thermal treatment, followed by a Cs activation when the photocathode is degraded. A detailed study of the p-GaN:Cs photocathode degradation under the exposure of several gases such as CH_4, CO, CO_2, H_2, and O_2 is required to study the lifetime and hence the robustness of the photocathode.

Other substrate materials besides sapphire such as Si, SiC, or TiN can be also considered as suitable substrates for p-GaN. While p-GaN on other substrates might not be easily available and more expensive, the photocathode performance, especially the QE, might be improved by a higher p-GaN crystallinity in which no C and O is incorporated into the crystal lattice and fewer crystal defects arise. The proposal of using a conductive substrate (such as Cu) for p-GaN would be ideal to dissipate the heat inside the SRF Gun II and is extensively studied [10].

Commercially available p-GaN, grown by MBE or HVPE represents another alternative with a higher crystallinity compared to p-GaN grown with MOCVD.

The remaining surface impurities, especially C and O, could potentially be removable by an ion bombardment of He, H_2, or argon (Ar) clusters at low energies. To date, no sufficient ion bombardment was reported in which a p-GaN surface was irradiated with helium ion (He^+) or H^+ and examined on its surface with XPS. A suitable sputtering method might yield a C-free p-GaN surface without damaging it which consequently would lead to higher QE and thus to a better photocathode performance.
Due to time constraints, no reference materials were measured and thus no quantifications were provided for the examined samples. Hence, suitable reference substances are needed to provide an XPS quantification.

The Mg dopant concentration – and thus its carrier concentration – is important for photocathode performance. If the concentration is too low, no photoemission takes place because the photoelectrons cannot travel toward the surface. Hence, a sufficient concentration of 1×10^{18}–$1 \times 10^{19}\,cm^{-1}$ would be desirable but is hardly achievable in the growth mechanism. Further studies on highly Mg-doped p-GaN samples are desirable.

One goal of this work was the study of p-GaN on sapphire from the material point of view. The potential application in the ELBE SRF Gun II needs intensive

pre-studies of the operational performance of this material before it can be used as an electron source. Information concerning the operational parameters and the behavior in the injector system is not available at the moment but is essential for future work. Measurements of a cooled p-GaN:Cs photocathode and its QE performance during the application of an RF field have not been tested to date. Furthermore, a QE map would be helpful for determining whether the QE distribution is homogenous on the cesiated p-GaN surface.

The lifetime of GaAs photocathodes is improved by a protecting Cs_2Te layer [94], which might be also a good choice for p-GaN:Cs photocathodes. HZDR is already experienced in the growth of Cs_2Te and the activation of p-GaN and GaAs. The approach of combining both semiconductor materials and creating a new photocathode (p-GaN:Cs_2Te) might pave the way for the next generation of photocathodes with high QE. The production and surface behavior of new potential photocathodes and their surface qualities are now traceable with *in-situ* XPS studies which will help to achieve better photocathode properties for the ELBE SRF Gun II in the future.

References

[1] Krysztof, Michał. "Field-emission electron gun for a MEMS electron microscope". In: *Microsystems Nanoeng.* 7.1 (2021). ISSN: 20557434. DOI: 10.1038/s41378-021-00268-9.

[2] Hawkes, Peter W. and Spence, John C.H. *Science of Microscopy*. Volume 1. Springer, 2007. ISBN: 0-387-25296-7.

[3] Zhao, Lingrong et al. "Noninvasive time-sorting in radio frequency-compressed ultrafast electron diffraction". In: *Struct. Dyn.* 8.4 (2021). ISSN: 23297778. DOI: 10.1063/4.0000113. arXiv: 2105.03563.

[4] Gaertner, Georg et al. *Modern Developments in Vacuum Electron Sources*. Ed. by Springer. Volume 135. 2020. ISBN: 9783030472900.

[5] Dowell, D. H. et al. "Cathode R&D for future light sources". In: *Nucl. Instruments Methods Phys. Res. Sect. A Accel. Spectrometers, Detect. Assoc. Equip.* 622.3 (2010), pp. 685–697. ISSN: 01689002. DOI: 10.1016/j.nima.2010.03.104. URL: http://dx.doi.org/10.1016/j.nima.2010.03.104.

[6] Kong, S. H. et al. "Cesium telluride photocathodes". In: *J. Appl. Phys.* 77.11 (1995), pp. 6031–6038. ISSN: 00218979. DOI: 10.1063/1.359188.

[7] Qian, H. J. et al. "Surface photoemission in a high-brightness electron beam radio frequency gun". In: *Appl. Phys. Lett.* 97.25 (2010), pp. 1–4. ISSN: 00036951. DOI: 10.1063/1.3531561.

[8] Cultrera, Luca et al. "Thermal emittance and response time of a cesium antimonide photocathode". In: *Appl. Phys. Lett.* 99.15 (2011), pp. 1–4. ISSN: 00036951. DOI: 10.1063/1.3652758.

[9] Bazarov, Ivan V. et al. "Thermal emittance and response time measurements of a GaN photocathode". In: *J. Appl. Phys.* 105.8 (2009). ISSN: 00218979. DOI: 10.1063/1.3110075.

[10] Vogel, M et al. "GaN Thin Film Photocathodes for High Brightness Electron Beams; GaN Thin Film Photocathodes for High Brightness Electron Beams". In: *9th Int. Part. Accel. Conf. Vancouver,BC, Canada*. JaCoW Publishing, 2018, pp. 4594–4597. ISBN: 9783954501847. DOI: 10.18429/JACoW-IPAC2018-THPMK118.

[11] Akasaki, I., Amano, H., and Nakamura, S. *Efficient blue light-emitting diodes leading to bright and energy-saving white light sources*. Tech. rep. 2014.

[12] Xiang, R. and Teichert, J. "Photocathodes for High Brightness Photo Injectors". In: *Phys. Procedia, Int. Conf. Laser Appl. Accel. LA3NET 2015*. Vol. 77. Elsevier B.V., 2015, pp. 58–65. ISBN: 4935126035. DOI: 10.1016/j.phpro.2015.11.010. URL: http://dx.doi.org/10.1016/j.phpro.2015.11.010.

[13] Spicer, W. E. "Negative affinity 3-5 photocathodes: Their physics and technology". In: *Appl. Phys.* 12.2 (1977), pp. 115–130. ISSN: 03403793. DOI: 10.1007/BF00896137.

[14] Wu, C. I. and Kahn, A. "Electronic states and effective negative electron affinity at cesiated p-GaN surfaces". In: *J. Appl. Phys.* 86.6 (1999), pp. 3209–3212. ISSN: 00218979. DOI: 10.1063/1.371191.

[15] Wang, Xiaohui et al. "[GaN(Mg)-Cs]:[O-Cs] model for the Negative Electron Affinity GaN (0001) surface". In: *Optik (Stuttg).* 127 (2016), pp. 7611–7624. DOI: 10.1016/j.ijleo.2016.05.140.

[16] Bae, J et al. "Long Lifetime Spin-Polarized GaAs Photocathode Activated by Cs2TeLong Lifetime Spin-Polarized GaAs Photocathode Activated by Cs2Te". In: *9th Int. Part. Accel. Conf.* JACoW Publishing, 2018, pp. 1–4. ISBN: 9783954501847. DOI: 10.18429/JACoW-IPAC2018-TUPML025.

[17] Bae, Jai Kwan et al. "Improved lifetime of a high spin polarization superlattice photocathode". In: *J. Appl. Phys.* 127.12 (2020). ISSN: 10897550. DOI: 10.1063/1.5139674. arXiv: 1911.09609.

[18] Yamamoto, Naoto et al. "Thermal emittance measurements for electron beams produced from bulk and superlattice negative electron affinity photocathodes". In: *J. Appl. Phys.* 102.2 (2007). ISSN: 00218979. DOI: 10.1063/1.2756376.

[19] Chubenko, Oksana et al. "Monte Carlo modeling of spin-polarized photoemission from p -doped bulk GaAs". In: *J. Appl. Phys.* 130.6 (2021). ISSN: 10897550. DOI: 10.1063/5.0060151.

[20] Pastuszka, S. et al. "Preparation and performance of transmission-mode GaAs photocathodes as sources for cold dc electron beams". In: *J. Appl. Phys.* 88.11 (2000), pp. 6788–6800. ISSN: 00218979. DOI: 10.1063/1.1311307.

[21] Chanlek, N. et al. "High stability of negative electron affinity gallium arsenide photocathodes activated with Cs and NF3". In: *J. Phys. D. Appl. Phys.* 48.37 (2015), pp. 1–6. ISSN: 13616463. DOI: 10.1088/0022-3727/48/37/375102.

[22] Cultrera, Luca et al. "Long lifetime polarized electron beam production from negative electron affinity GaAs activated with Sb-Cs-O: Trade-offs between efficiency, spin polarization, and lifetime". In: *Phys. Rev. Accel. Beams* 23.2 (2020), p. 23401. ISSN: 24699888. DOI: 10.1103/PhysRevAccelBeams.23.023401. URL: https://doi.org/10.1103/PhysRevAccelBeams.23.023401.

[23] Machuca, Francisco et al. "Prospect for high brightness III–nitride electron emitter". In: *J. Vac. Sci. Technol. B Microelectron. Nanom. Struct.* 18.6 (2000), p. 3042. ISSN: 0734211X. DOI: 10.1116/1.1321270.

[24] Uchiyama, Shoichi et al. "GaN-based photocathodes with extremely high quantum efficiency". In: *Appl. Phys. Lett.* 86.10 (2005), pp. 1–3. ISSN: 00036951. DOI: 10.1063/1.1883707.

[25] Rozhkov, S. A. et al. "Surface photovoltage in a p-GaN(Cs) photocathode". In: *J. Phys. Conf. Ser.* 1199.1 (2019). ISSN: 17426596. DOI: 10.1088/1742-6596/1199/1/012031.

[26] Schaber, Jana et al. "Influence of Surface Cleaning on Quantum Efficiency , Lifetime and Surface Morphology of p-GaN : Cs Photocathodes". In: *Micromashines* 13.849 (2022), pp. 1–14. URL: https://doi.org/10.3390/mi13060849.

[27] Machuca, Francisco et al. “Simple method for cleaning gallium nitride (0001)”. In: *J. Vac. Sci. Technol. A Vacuum, Surfaces, Film.* 20.5 (2002), pp. 1784–1786. ISSN: 0734-2101. DOI: 10.1116/1.1503782.

[28] Smith, L. L. et al. “Cleaning of GaN surfaces”. In: *J. Electron. Mater.* 25.5 (1996), pp. 805–810. ISSN: 03615235. DOI: 10.1007/BF02666640.

[29] Tereshchenko, O E et al. “Low-Temperature Method of Cleaning p -GaN(0001) Surfaces for Photoemitters with Effective Negative Electron Affinity”. In: *Phys. Solid State* 46.10 (2004), pp. 1949–1953.

[30] Lu, Pengnan. “Optimization of an SRF Gun for High Bunch Charge Applications at ELBE”. PhD thesis. 2017. URL: https://nbn-resolving.org/urn:nbn:de:bsz:14-qucosa-223386.

[31] Xiang, R. “Review of superconducting radio frequency gun”. In: *Proc. IPAC2021* (2021), pp. 2556–2561. DOI: 10.18429/JACoW-IPAC2021-WEXC03. URL: https://www.jacow.org/IPAC2021/papers/WEXC03.pdf.

[32] Xiang, R et al. “SRF Gun and SRF Linac driven THz at ELBE successfully in User Operation”. In: *19th Int. Conf. RF Supercond. SRF2019, Dresden, Ger.* JACoW Publishing, 2019, pp. 915–917. ISBN: 9783954502110. DOI: 10.18429/JACoW-SRF2019-THP032.

[33] Teichert, J. et al. “Successful user operation of the superconducting radio-frequency photo electron gun with Mg cathodes at ELBE”. In: *Phys. Rev. Accel. Beams* 24.033401 (2021), pp. 1–30. DOI: 10.1103/PhysRevAccelBeams.24.033401.

[34] Dowell, D. H. and Rao, T. *An Engineering Guide to Photoinjectors*. Ed. by Triveni Rao, David H. Dowell. arXiv.org, 2014. ISBN: 978-1481943222. URL: https://arxiv.org/abs/1403.7539.

[35] Baryshev, Sergey V. et al. “Cryogenic operation of planar ultrananocrystalline diamond field emission source in SRF injector”. In: *Appl. Phys. Lett.* 118.5 (2021). ISSN: 00036951. DOI: 10.1063/5.0013172.

[36] Cultrera, L. et al. “Photoemission characterization of N-polar III-Nitride photocathodes as bright electron beam source for accelerator applications”. In: 2021, pp. 1–18. arXiv: 2110.01533. URL: http://arxiv.org/abs/2110.01533.

[37] Tripathi, Prabhakar et al. “Design and Simulation of the Thermionic Emission-Based Reltron Oscillator”. In: *IEEE Trans. Plasma Sci.* 48.2 (2020), pp. 438–445. ISSN: 19399375. DOI: 10.1109/TPS.2020.2966408.

[38] Arnold, A et al. “Commissioning Results of the 2nd 3.5 Cell SRF Gun For ELBE”. In: *Proc. LINAC2014, Geneva, Switz.* 2014, pp. 578–580. ISBN: 9783954501427.

[39] Arnold, Andre et al. “RF Performance Results of the 2nd ELBE SRF Gun”. In: *Proc. SRF2015* (2015), pp. 1227–1230.

[40] Xiang, Rong and Schaber, Jana. “Review of Recent Progress on Advanced Photocathodes for Superconducting RF Guns”. In: *Micromachines* 13.8 (2022), p. 1241. ISSN: 2072-666X. DOI: 10.3390/mi13081241. URL: https://www.mdpi.com/2072-666X/13/8/1241.

[41] Xiang, R. et al. “Cs2Te normal conducting photocathodes in the superconducting rf gun”. In: *Phys. Rev. Spec. Top. - Accel. Beams* 13.4 (2010), pp. 1–7. ISSN: 10984402. DOI: 10.1103/PhysRevSTAB.13.043501.

[42] Xiang, R. et al. “Recent improvement of Cs2Te photocathodes at HZDR”. In: *IPAC 2014 Proc. 5th Int. Part. Accel. Conf.* 2014, pp. 642–644. ISBN: 9783954501328.

[43] Moulder, J.F. and Chastain, J. *Handbook of X-ray Photoelectron Spectroscopy: A Reference Book of Standard Spectra for Identification and Interpretation of XPS Data*. Physical Electronics Division, Perkin-Elmer Corporation, 1992. ISBN: 9780962702624.

[44] Stevie, Fred A. and Donley, Carrie L. “Introduction to x-ray photoelectron spectroscopy”. In: *J. Vac. Sci. Technol. A* 38.6 (2020), p. 063204. ISSN: 0734-2101. DOI: 10.1116/6.0000412.

[45] Briggs, D. and Grant, J.T. *Surface Analysis by Auger and X-Ray Photoelectron Spectroscopy*. IM Publications and SurfaceSpectra Limited, 2003. ISBN: 1901019047.

[46] Powell, Cedric J. “Practical guide for inelastic mean free paths, effective attenuation lengths, mean escape depths, and information depths in x-ray photoelectron spectroscopy”. In: *J. Vac. Sci. Technol. A* 38.2 (2020), p. 023209. ISSN: 0734-2101. DOI: 10.1116/1.5141079.

[47] Reichelt, Manuela. *Vorlesungskript zum 2. Kurs (Röntgen- und Elektronenspektroskopie) im Aufbaustudium Analytik und Spectroscopie*. 2020.

[48] Ackermann, J. “Handbuch für die Rasterelektronenmikroskope SUPRA (VP) und ULTRA”. 2004.

[49] Watts, John F. and Wolstenholme, John. *An Introduction to Surface Analysis by XPS and AES*. Vol. 3. John Wiley & Sons, 2019. ISBN: 0470847123. DOI: 10.1002/9781119417651.

[50] Engelhard, Mark H. et al. “Introductory guide to backgrounds in XPS spectra and their impact on determining peak intensities”. In: *J. Vac. Sci. Technol. A* 38.6 (2020), p. 063203. ISSN: 0734-2101. DOI: 10.1116/6.0000359.

[51] Tougaard, Sven. “Practical guide to the use of backgrounds in quantitative XPS”. In: *J. Vac. Sci. Technol. A* 39.1 (2021), p. 011201. ISSN: 0734-2101. DOI: 10.1116/6.0000661.

[52] Major, George H. et al. “Practical guide for curve fitting in x-ray photoelectron spectroscopy”. In: *J. Vac. Sci. Technol. A* 38.6 (2020), p. 061203. ISSN: 0734-2101. DOI: 10.1116/6.0000377.

[53] Bauer, J. *Vorlesungskript zum 2. Kurs (Oberflächenanalytik) im Aufbaustudium Analytik und Spectroscopy*. 2020.

[54] Tsukruk, Vladimir V. “Section 2: Scanning Probe Microscopy Basics”. In: *Scanning Probe Microsc. Soft Matter*. John Wiley & Sons, 2011, pp. 8–10.

[55] Cypher User Guide. “Cypher SPM User Guide, USER GUIDE 2”. 2013. URL: https://courses.physics.illinois.edu/phys598BP/sp2015/Files%5CCypherGUIDE.pdf.

[56] Zhou, Yang and Zhang, Peng. "A quantum model for photoemission from metal surfaces and its comparison with the three-step model and Fowler-DuBridge model". In: *J. Appl. Phys.* 127.16 (2020), pp. 0–11. ISSN: 10897550. DOI: 10.1063/5.0004140.

[57] Spicer, W. E. "Photoemissive, Photoconductive, and Optical Absorption Studies of Alakli-Antimony Compunds". In: *Phys. Rev.* 112.1 (1958), p. 114. ISSN: 0031-899X. DOI: 10.1103/PhysRev.112.114.

[58] Kahn, Antoine. "Fermi level, work function and vacuum level". In: *Mater. Horizons* 3.1 (2016), pp. 7–10. ISSN: 20516355. DOI: 10.1039/c5mh00160a. URL: http://dx.doi.org/10.1039/C5MH00160A.

[59] Xiang, R et al. "Study of Magnesium Photocathodes for Superconducting RF Photoinjectors". In: *Proc. IPAC 2018*. 13. 2018, pp. 4142–4144. ISBN: 9783954501847.

[60] Dowell, David H. and Schmerge, John F. "Quantum efficiency and thermal emittance of metal photocathodes". In: *Phys. Rev. Spec. Top. - Accel. Beams* 12.7 (2009), pp. 1–10. ISSN: 10984402. DOI: 10.1103/PhysRevSTAB.12.074201.

[61] Dowell, D. H. et al. "In situ cleaning of metal cathodes using a hydrogen ion beam". In: *Phys. Rev. Spec. Top. - Accel. Beams* 9.6 (2006), pp. 1–8. ISSN: 10984402. DOI: 10.1103/PhysRevSTAB.9.063502.

[62] Kühn, J. et al. "A Cu Photocathode for the Superconducting RF Photoinjector of BERLinPro". In: *Proc. IPAC2018, Vancouver, BC, Canada*. 2018, pp. 1247–1250. ISBN: 978-3-95450-184-7. DOI: 10.18429/JACOW-IPAC2018-TUPMF002.

[63] Jones, L B et al. "Transverse Energy Distribution Measurements for Polycrystalline and (100) Copper Photocathodes with Known Levels of Surface Roughness; Transverse Energy Distribution Measurements for Polycrystalline and (100) Copper Photocathodes with Known Levels of Surf". In: *Proc. IPAC2018* (2018), pp. 4438–4441. DOI: 10.18429/JACoW-IPAC2018-THPMK062.

[64] Smedley, J. et al. "Lead photocathodes". In: *Phys. Rev. Spec. Top.- Accel. Beams* 11.1 (2008), pp. 1–9. ISSN: 10984402. DOI: 10.1103/PhysRevSTAB.11.013502.

[65] Bona, A. di et al. "Auger and x-ray photoemission spectroscopy study on Cs 2 Te photocathodes". In: *J. Appl. Phys.* 80.5 (1998). DOI: https://doi.org/10.1063/1.363161.

[66] Iijima, H. et al. "Surface analysis of a degraded NEA-GaAs photocathode by temperature programmed desorption technique". In: *IPAC 2011 - 2nd Int. Part. Accel. Conf.* 2011, pp. 3158–3160. ISBN: 9789290833666.

[67] Ruterana, Pierre and Albrecht, Martin. *Nitride Semiconductors: Handbook on Materials and Devices*. Wiley-VCH Weinheim, 2003. ISBN: 3527403876.

[68] Quay, Rüdiger. *Gallium Nitride Electronics*. Springer, 2008. ISBN: 978-3-540-71890-1. DOI: 10.1007/978-3-540-71892-5.

[69] Prabaswara, Aditya et al. “Review of GaN thin film and nanorod growth using magnetron sputter epitaxy”. In: *Appl. Sci.* 10.9 (2020). ISSN: 20763417. DOI: 10.3390/app10093050.

[70] Pearton, S. J. et al. “Fabrication and performance of GaN electronic devices”. In: *Mater. Sci. Eng. R Reports* 30.3-6 (2000), pp. 55–212. ISSN: 0927796X. DOI: 10.1016/S0927-796X(00)00028-0.

[71] Pankove, Jacques I. “GaN: From fundamentals to applications”. In: *Mater. Sci. Eng. B* 61-62 (1999), pp. 305–309. ISSN: 09215107. DOI: 10.1016/S0921-5107(98)00523-6.

[72] Siegmund, Oswald H. W. et al. “GaN photocathodes for UV detection and imaging”. In: *UV/EUV Visible Sp. Instrum. Astron. II* 5164 (2003), p. 134. ISSN: 0277786X. DOI: 10.1117/12.510429.

[73] Pearton, S. J. et al. “GaN electronics for high power, high temperature applications”. In: *Electrochem. Soc. Interface* 9.2 (2000), pp. 34–39. ISSN: 10648208. DOI: 10.1149/2.f06002if.

[74] Kukushkin, S. A. et al. “Substrates for epitaxy of gallium nitride: New materials and techniques”. In: *Rev. Adv. Mater. Sci.* 17.1-2 (2008), pp. 1–32. ISSN: 16065131.

[75] Lukin, G. “Entwicklung einer Hochtemperatur-Gasphasenepitaxie (HTVPE) für die Herstellung von GaN”. PhD thesis. 2018.

[76] Reiher, Fabian et al. “Wachstum von Galliumnitrid - basierten Bauelementen auf Silizium (001) - Substraten mittels metallorganischer Gasphasenepitaxie”. PhD thesis. 2009.

[77] Liu, S.T. et al. “Different annealing temperature suitable for different Mg doped P-GaN”. In: *Superlattices and Microstructures* 104 (2017), pp. 63–68. ISSN: 0749-6036. DOI: https://doi.org/10.1016/j.spmi.2017.02.016. URL: https://www.sciencedirect.com/science/article/pii/S074960361730099X.

[78] Bogenschütz, A.F. *Ätzpraxis für Halbleiter*. Hanser-Verlag: Munich, Germany, 1967.

[79] Lu, L. et al. “Microstructure and origin of dislocation etch pits in GaN epilayers grown by metal organic chemical vapor deposition”. In: *J. Appl. Phys.* 104.12 (2008). ISSN: 00218979. DOI: 10.1063/1.3042230.

[80] Lee, Moonsang et al. “Nearly perfect GaN crystal via pit-assisted growth by HVPE”. In: *CrystEngComm* 19.15 (2017), pp. 2036–2041. ISSN: 14668033. DOI: 10.1039/C7CE00246G.

[81] Min, Lu et al. “Etch Pits and Threading Dislocations in GaN Films Grown by Metal-Organic Chemical Vapour Deposition”. In: *Chinese Phys. Lett.* 20.3 (2003), p. 398. DOI: 10.1088/0256-307X/20/3/324.

[82] Jarndal, Anwar et al. “On the performance of GaN-on-Silicon, Silicon-Carbide, and Diamond substrates”. In: *Int. J. RF Microw. Comput. Eng.* 30.6 (2020), pp. 1–10. ISSN: 1099047X. DOI: 10.1002/mmce.22196.

[83] Wang, Wenliang et al. “Epitaxial growth of GaN films on lattice-matched ScAlMgO4 substrates”. In: *CrystEngComm* 18.25 (2016), pp. 4688–4694. ISSN: 14668033. DOI: 10.1039/c6ce01071g. URL: http://dx.doi.org/10.1039/C6CE01071G.

[84] Wang, Shengzhao et al. “The evolution of GaN photocathode surface barrier before and after activation”. In: *Proc. SPIE*. February 2019. 2019, p. 21. ISBN: 9781510623286. DOI: 10.1117/12.2505545.

[85] Ma, Jun et al. “Photoemission mechanism of GaN photocathode:a first-principle study”. In: *Proc. 2019 IEEE 4th Adv. Inf. Technol. Electron. Autom. Control Conf. IAEAC 2019*. 2019, pp. 1451–1455. ISBN: 9781728119076. DOI: 10.1109/IAEAC47372.2019.8997809.

[86] Sato, Daiki et al. “Recovery of quantum efficiency on Cs/O-activated GaN and GaAs photocathodes by thermal annealing in vacuum”. In: *J. Vac. Sci. Technol. B* 38.1 (2020), p. 012603. ISSN: 2166-2746. DOI: 10.1116/1.5120417.

[87] Zhu, X. et al. “Enhancing Performance of a GaAs/AlGaAs/GaAs Nanowire Photodetector Based on the Two-Dimensional Electron-Hole Tube Structure”. In: *ACS Appl. Mater. Interfaces* (2020). ISSN: 19448252. DOI: 10.1021/acs.nanolett.0c00232.

[88] Kuwahara, Makoto et al. “Coherence of a spin-polarized electron beam emitted from a semiconductor photocathode in a transmission electron microscope”. In: *Appl. Phys. Lett.* 105.19 (2014). ISSN: 00036951. DOI: 10.1063/1.4901745. URL: http://dx.doi.org/10.1063/1.4901745.

[89] Liu, Lei et al. “High-performance GaAs nanowire cathode for photon-enhanced thermionic emission solar converters”. In: *J. Mater. Sci.* 54.7 (2019), pp. 5605–5614. ISSN: 15734803. DOI: 10.1007/s10853-018-03231-8. URL: https://doi.org/10.1007/s10853-018-03231-8.

[90] Scheer, J J and Laar, J Van. “quantum part spectrum,” in: *Solid State Commun.* 3 (1965), pp. 189–193.

[91] Carr, G. L. et al. “High-power terahertz radiation from relativistic electrons”. In: *Nature* 420.6912 (2002), pp. 153–156. ISSN: 00280836. DOI: 10.1038/nature01175.

[92] Pierce, D. T. et al. “The GaAs spin polarized electron source”. In: *Rev. Sci. Instrum.* 51.4 (1980), pp. 478–499. ISSN: 00346748. DOI: 10.1063/1.1136250.

[93] Zhang, Junju et al. “Photoemission stability of negative electron affinity GaN photocathode”. In: *Optoelectron. Devices Integr. IV*. Ed. by Zhang, Xuping et al. 8555. 2012, p. 85551C. DOI: 10.1117/12.2001125. URL: http://proceedings.spiedigitallibrary.org/proceeding.aspx?doi=10.1117/12.2001125.

[94] Biswas, Jyoti et al. “High quantum efficiency GaAs photocathodes activated with Cs, O2, and Te”. In: *AIP Adv.* 11.2 (2021). ISSN: 21583226. DOI: 10.1063/5.0026839. URL: https://doi.org/10.1063/5.0026839.

[95] Özkartal, Abdullah and Noori, Dheyab Thaer. “Effects of thermal annealing on the characterization of p-NiO/n-GaAs heterojunctions produced by thermal evaporation”. In: *J. Mater. Sci. Mater. Electron.* 32.10 (2021), pp. 13462–13471. ISSN: 1573482X. DOI: 10.1007/s10854-021-05924-4.

[96] Levchenko, Iryna et al. “Improvement the InAs, InSb, GaAs and GaSb surface state by nanoscale wet etching”. In: *Appl. Nanosci.* 0123456789 (2021). ISSN: 21905517. DOI: 10.1007/s13204-021-01784-w. URL: https://doi.org/10.1007/s13204-021-01784-w.

[97] Zhang, Yijun et al. “Application of scanning focused X-ray imaging positioning technique in preparation of GaAs photocathodes”. In: *Proc. SPIE.* SPIE Photonics Europe. 2020, p. 54. ISBN: 9781510635067. DOI: 10.1117/12.2556086.

[98] Razek, N. et al. “GaAs surface cleaning by low energy hydrogen ion beam treatment”. In: *J. Vac. Sci. Technol. A Vacuum, Surfaces, Film.* 20.4 (2002), pp. 1492–1497. ISSN: 0734-2101. DOI: 10.1116/1.1488949.

[99] Greczynski, G. and Hultman, L. “Towards reliable X-ray photoelectron spectroscopy: Sputter-damage effects in transition metal borides, carbides, nitrides, and oxides”. In: *Appl. Surf. Sci.* 542.November 2020 (2021), p. 148599. ISSN: 01694332. DOI: 10.1016/j.apsusc.2020.148599. URL: https://doi.org/10.1016/j.apsusc.2020.148599.

[100] Togawa, K et al. “Surface charge limit in NEA superlattice photocathodes of polarized electron source”. In: *Nucl. Instruments Methods Phys. Res. A* 414 (1998), pp. 431–445.

[101] Henderson, Brian S. *Study of Negative Electron Affinity GaAs Photocathodes.* Tech. rep. 1. 2009, pp. 1–18.

[102] Zhang, Yijun et al. “Effect of excessive Cs and O on activation of GaAs(100) surface: From experiment to theory”. In: *J. Appl. Phys.* 128.17 (2020). ISSN: 10897550. DOI: 10.1063/5.0028042. URL: https://doi.org/10.1063/5.0028042.

[103] Fisher, D. G. et al. “Photoelectron surface escape probability of (Ga,In)As: CsSingle Bond signO in the 0.9 to [inverted lazy s] 1.6 μm range”. In: *J. Appl. Phys.* 43.9 (1972), pp. 3815–3823. ISSN: 00218979. DOI: 10.1063/1.1661817.

[104] McCarter, James L. et al. “Two novel approaches for electron beam polarization from unstrained GaAs”. In: *Proc. Sci. - XVth Int. Work. Polariz. Sources, Targets, Polarim.* Vol. 060. PoS. 2013, pp. 1–7. DOI: 10.22323/1.182.0060.

[105] Liu, Wei et al. “A comprehensive evaluation of factors that influence the spin polarization of electrons emitted from bulk GaAs photocathodes”. In: *J. Appl. Phys.* 122.3 (2017). ISSN: 10897550. DOI: 10.1063/1.4994306. URL: http://dx.doi.org/10.1063/1.4994306.

[106] Liu, Wei et al. “Record-level quantum efficiency from a high polarization strained GaAs/GaAsP superlattice photocathode with distributed Bragg reflector”. In: *Appl. Phys. Lett.* 109.25 (2016). ISSN: 00036951. DOI: 10.1063/1.4972180. URL: http://dx.doi.org/10.1063/1.4972180.

[107] Wang, E et al. “Testing a GaAs cathode in SRF gun”. In: *Part. Accel. Conf. (PAC 2011), New York, NY.* Ed. by Wang, E et al. 2011.

[108] Bae, Jai Kwan et al. “Rugged spin-polarized electron sources based on negative electron affinity GaAs photocathode with robust Cs2Te coating”. In: *Appl. Phys. Lett.* 112.15 (2018), pp. 1–6. ISSN: 00036951. DOI: 10.1063/1.5026701. URL: http://dx.doi.org/10.1063/1.5026701.

[109] Suberlucq, G and Suberlucq, G. “Technological challenges for high-brightness photo-injectors”. In: *Eur. Organ. Nucl. Res. Cern - AB Dep. EPAC 2004, Lucerne, Switz.* RII3-CT-2003-506395. 2004, pp. 64–68.

[110] Monaco, L. et al. “Growing and characterization of CS2Te photocatodes with different thicknesses at InFN LaSA”. In: *Proc. 39th Int. Free. Laser Conf. FEL 2019*. 2019, pp. 297–300. ISBN: 9783954502103. DOI: 10.18429/JACoW-FEL2019-WEA04.

[111] Huang, P. et al. “Test of CS2Te thickness on cathode performance at Pitz”. In: *Proc. 39th Int. Free. Laser Conf. FEL 2019*. 2019, pp. 473–476. ISBN: 9783954502103. DOI: 10.18429/JACoW-FEL2019-WEP062.

[112] Zhou, F. et al. “Commissioning of the SLAC Linac Coherent Light Source II electron source”. In: *Phys. Rev. Accel. Beams* 24.7 (2021), p. 73401. ISSN: 24699888. DOI: 10.1103/PhysRevAccelBeams.24.073401. URL: https://doi.org/10.1103/PhysRevAccelBeams.24.073401.

[113] Xiamen, Co. Ltd. *Xiamen*. 2018. URL: https://www.powerwaywafer.com.

[114] Lee, F. et al. “The Decomposition of Trimethylgallium and Trimethylaluminum on Si(100)”. In: *MRS Proc.* 131.951 (1988), pp. 951–954. ISSN: 0272-9172. DOI: 10.1557/proc-131-339.

[115] Chen, Jr Tai et al. “Impact of residual carbon on two-dimensional electron gas properties in AlxGa1-xN/GaN heterostructure”. In: *Appl. Phys. Lett.* 102.19 (2013). ISSN: 00036951. DOI: 10.1063/1.4804600.

[116] Cao, Zikun et al. “The influence of temperature and TMGa flow rate on the quality of p -GaN”. In: *AIP Adv.* 11.3 (2021). ISSN: 21583226. DOI: 10.1063/5.0045393. URL: https://doi.org/10.1063/5.0045393.

[117] OriginLab Corporation, Northampton, MA, USA. *Origin(Pro), Version2020*. 2020.

[118] Larichev, Yu V. et al. “An XPS study of the promotion of Ru-Cs/Sibunit catalysts for ammonia synthesis”. In: *Kinet. Catal.* 46.4 (2005), pp. 597–602. ISSN: 00231584. DOI: 10.1007/s10975-005-0113-9.

[119] Kelty, Stephen P. et al. “Core-level binding energies of Cs-doped C60 and graphite”. In: *J. Phys. Chem.* 95.18 (1991), pp. 6754–6756. ISSN: 00223654. DOI: 10.1021/j100171a004.

[120] Hamlyn, Rebecca C.E. et al. *Structure and Chemical State of Cesium on Well-Defined Cu(111) and Cu2O/Cu(111) Surfaces*. Vol. 124. 5. 2020, pp. 3107–3121. ISBN: 2136932020. DOI: 10.1021/acs.jpcc.9b10608.

[121] Ebbinghaus, G and Simon, A. “Electronic strucutre of Rb, Cs, and some of their metallic oxides studied by photoelectron spectroscopy”. In: *Chem. Phys.* 43.1970 (1979), pp. 117–133.

[122] Yang, Sheng Jenn and Bates, Clayton W. "The role of cesium suboxides in low-work-function surface layers studied by x-ray photoelectron spectroscopy: Ag-O-Cs". In: *Appl. Phys. Lett.* 36.8 (1980), pp. 675–677. ISSN: 00036951. DOI: 10.1063/1.91620.

[123] Bates, C. W. et al. "X-ray photoemission studies of superficially oxidized cesium antimonide photoemitters". In: *Appl. Phys. Lett.* 38.5 (1981), pp. 387–389. ISSN: 00036951. DOI: 10.1063/1.92348.

[124] Dupin, Jean Charles et al. "Systematic XPS studies of metal oxides, hydroxides and peroxides". In: *Phys. Chem. Chem. Phys.* 2.6 (2000), pp. 1319–1324. ISSN: 14639076. DOI: 10.1039/a908800h.

[125] Biesinger, Mark C. et al. "Resolving surface chemical states in XPS analysis of first row transition metals, oxides and hydroxides: Cr, Mn, Fe, Co and Ni". In: *Appl. Surf. Sci.* 257.7 (2011), pp. 2717–2730. ISSN: 01694332. DOI: 10.1016/j.apsusc.2010.10.051. URL: http://dx.doi.org/10.1016/j.apsusc.2010.10.051.

[126] *XPS database*. URL: https://xpsdatabase.com/cesium-cs-z55/.

[127] Zhang, Xingyue et al. "Theoretical study on 2D photoelectric emission of GaN nanorod array and nanocone array photocathode". In: *Int. J. Energy Res.* 45.2 (2021), pp. 2265–2276. ISSN: 1099114X. DOI: 10.1002/er.5918.

[128] Norton, Timothy J. et al. "Results from Cs activated GaN photocathode development for MCP detector systems at NASA GSFC". In: *UV/EUV Visible Sp. Instrum. Astron. II* 5164.February (2003), p. 155. ISSN: 0277786X. DOI: 10.1117/12.507528.

[129] Zhang, Yijun et al. "Improved activation technique for preparing high-efficiency GaAs photocathodes". In: *Opt. Mater. Express* 7.9 (2017), p. 3456. ISSN: 2159-3930. DOI: 10.1364/ome.7.003456.

[130] Wu, J. X. et al. "The annealing behaviour of a Cs2O/GaAs(110) surface studied by electron spectroscopy". In: *J. Phys. Condens. Matter* 13.39 (2001), pp. 8725–8731. ISSN: 09538984. DOI: 10.1088/0953-8984/13/39/301.

[131] Wu, J. X. et al. "Annealing behavior of a Cs2O/Cs2O2/GaAs(110) surface studied by electron spectroscopy". In: *J. Vac. Sci. Technol. A Vacuum, Surfaces, Film.* 20.5 (2002), pp. 1532–1535. ISSN: 0734-2101. DOI: 10.1116/1.1494817.

[132] Su, C. Y. et al. "Photoelectron spectroscopic determination of the structure of (Cs,O) activated GaAs (110) surfaces". In: *J. Appl. Phys.* 54.3 (1983), pp. 1413–1422. ISSN: 00218979. DOI: 10.1063/1.332166.

[133] Baer, Donald R. et al. "XPS guide: Charge neutralization and binding energy referencing for insulating samples". In: *J. Vac. Sci. Technol. A* 38.3 (2020), p. 031204. ISSN: 0734-2101. DOI: 10.1116/6.0000057.

[134] Paszkiewicz, R. et al. "MOVPE GaN grown on alternative substrates". In: *Cryst. Res. Technol.* 36.8-10 (2001), pp. 971–977. ISSN: 02321300.

[135] Band, A. et al. "Characterization of oxides of cesium". In: *J. Phys. Chem. B* 108.33 (2004), pp. 12360–12367. ISSN: 15206106. DOI: 10.1021/jp036432o.

[136] Lederer, S. et al. “XPS Studies of Cs2Te Photocathodes”. In: *Proc. FEL 2007, Novosib. Russ.* 2007, pp. 457–460. ISBN: 2004506008.

[137] Wang, Xiaohui et al. “Negative electron affinity of the GaN photocathode: A review on the basic theory, structure design, fabrication, and performance characterization.” In: *J. Mater. Chem. C* 9.38 (2021), pp. 13013–13040. ISSN: 20507526. DOI: 10.1039/d1tc03244e.

List of Figures

1 3D model of the ELBE SRF Gun II at HZDR showing the incident UV laser pathway (violet) hitting the photocathode in the back wall that ejects electrons. The electrons are subsequently accelerated downstream (blue). . . . 3
2 3D model of the photocathode inside the SRF Gun II, showing its cooling system with a LN supply [33]. . . . 4
3 Specialized 3D model for the adaption of p-GaN semiconductor photocathodes onto the SRF Gun II Cu body with the help of a Cu support, pierce cone and In sheet. . . . 4
4 Schematic of different processes including a) X-ray photoemission, and subsequent relaxation by b) Auger electron emission, and c) fluorescence. . . . 9
5 Drawing of a PHI 5600 XPS spectrometer taken from [43] but without X-ray monochromator (left side). A photo of the adapted XPS chamber, connected to the UHV preparation chamber at HZDR (right side). . . . 10
6 X-ray photoelectron spectrum (survey spectrum) of silver (Ag) showing an increasing background (left) and an X-ray photoelectron spectrum (detailed spectrum) of the carbon (C) 1s peak of a polymer (right), showing the influence of electronegativity on the BE ("chemical shift") [45]. . . . 11
7 Illustration of the IMFP of photoelectrons as a function of E_{kin} (also known as "universal curve"). . . . 12
8 Drawing of the major components needed for AFM measurements which illustrate the AFM working principle. . . . 13
9 Schematic of the three common AFM modes regarding to the interacting forces between the tip and the sample surface (Lennard-Jones potential). . . . 14
10 Schematic of the cantilever movement with the tip to generate an AFM image. . . . 14
11 Illustration of a typical SEM setup, showing the pathways of secondary electrons and backscattered electrons (red lines) compared to the pathway of X-rays for EDX detection (blue lines); the image was taken from [48]. . . . 15
12 Schematic of excitation depths of SE, BSE and X-rays inside a specimen. 16
13 Illustration of the comparison of the one-step model (left) and the three-step model (right). . . . 19
14 Schematic representation of the fundamental key terms in photoemission processes. . . . 21
15 Photo of a 10 mm Mg cathode inside the UHV chamber. The middle bluish part was cleaned with a laser of a spot size of 4 mm. . . . 22
16 Schematic drawing of n- and p-type doping, a) n-type Si with P as a dopant in the Si lattice and b) p-type Si with B as a dopant atom. . . 24
17 Illustration of the difference between PEA and NEA surfaces regarding the location of the E_{vac}. . . . 25

18 Image of the hexagonal wurtzite crystal structure of GaN. Ga atoms are green and N atoms are blue. The smallest unit (basic cell) of the crystal lattice is marked in orange. 26
19 Schematic representation of the band structure of p-GaN when activated with Cs and O_2. 28
20 Schematic drawing of the band structure of p-GaAs, activated in a YoYo process with Cs and O_2. 30
21 Schematic drawing of a typical photocurrent evolution when a YoYo activation is used (alternately applying Cs and O_2). 31
22 Schematic representation of the electron transitions for the generation of spin-polarized electrons in GaAs photocathodes. 32
23 Schematic overview of a typical layer sequence for a Cs_2Te photocathode, based on the original approach taken from [65]. 33
24 Photos of the UHV preparation chamber (left) and the interior of the preparation chamber with all required parts for the photocathode preparation (right). Both photos show the initial status at the beginning of the project. 35
25 Photo of a used halogen lamp (left), showing evaporated tungsten on its bulb, and a photo taken during the construction of the new halogen lamp with an advanced stainless steel reflector (right). 36
26 Photo of the interior of the preparation chamber showing the new setup of the halogen lamp during a thermal cleaning (left) and the two new Cs dispensers from a side view (right). 37
27 Photo of the old Cu ring anode (left), including the Cs dispensers, and the improved stainless steel ring anode from a side view and top view (right). 38
28 Photo of the setup of the UV-LED outside of the preparation chamber which guides the UV-light through a quartz window onto the sample inside the chamber via lenses and a mirror. 39
29 Photo of the setup of the spectral response measurements, in which the blue arrows show the guided pathway from the deuterium lamp (UV-light source) into the preparation chamber. 39
30 Photos of the OMICRON™ sample flags, showing the original flag, the Mo flag with a p-GaN sample, and a modified Mo flag with a hole for the thermal cleaning of the sample from the backside which is shown on the left side. The sample transportation of the flag with the help of the manipulator is shown on the right side. 40
31 Photo of the new sample holder inside the preparation chamber, showing the thermo elements and the N_2 cooling capability. 40
32 Photo of the loading chamber part where the suitcase is adopted. 3D models show the retractable interior of the suitcase with the possibility to carry up to three samples under a dry N_2 atmosphere. 41
33 Screenshot of the software user interface of the HZDR internally-developed software for the preparation of III-V semiconductor photocathodes. 42

34 3D model of the UHV preparation chamber including the loading chamber with the suitcase adaption and the connection of the XPS analysis chamber, which is represented by the white boxes (courtesy of P. Murcek). . . . 43
35 Photos of the metal gate valve and adjustment of the manipulator (Cu jaws) between preparation and XPS chambers. . . . 44
36 Photos of the original XPS puck with GaN samples on it (left) and the modified puck with a cut edge and clamps (right) to fit the sample flag of the preparation chamber. The modified puck holding a p-GaN sample on the Mo flag is shown at the bottom. . . . 45
37 Photo of the preparation chamber during the bake-out procedure, wrapped with bake-out cables, layers of Al foil, and glass fiber cloths to achieve UHV conditions. . . . 46
38 Vacuum curve as a function of time during the bake-out procedure of the preparation chamber. . . . 47
39 Photo of the XPS chamber with its bake-out tent for the achievement of UHV conditions. . . . 48
40 The interior of the UHV preparation chamber (showing a sample holder, a halogen lamp with a reflector, a steel ring anode, and Cs dispensers) and the XPS analysis chamber connected to the preparation chamber via a manipulator. . . . 48
41 The interior of the Cs_2Te preparation chamber, showing a cathode body with a plug, shutter, a mask which is also an anode, two thickness monitors, and Cs and Te evaporators. . . . 51
42 Photos of the polishing results on the Cu surface after each polishing step. . . . 52
43 Monitored parameters during the preparation of a Cs_2Te photocathode (sample E1), measured Cs and Te thickness (green), dispenser power (magenta), Cu temperature (orange), and vacuum curve (black). 53
44 *In-situ* photocurrent curves of Cs_2Te (sample E1) during the deposition of Cs when illuminated with UV-light at a wavelength of 340 nm (green) and at 260 nm (magenta). . . . 53
45 Photo of a freshly deposited Cs_2Te layer (4 mm in diameter) on a Cu plug (10 mm in diameter). . . . 54
46 AFM images of original p-GaN surface grown on sapphire by MOCVD, as received from Xiamen [113]. . . . 57
47 SEM images of the original p-GaN surface that was grown on sapphire. 58
48 AFM images of the p-GaN, grown on sapphire, surface cleaned with C_3H_8O, CH_3OH, C_3H_6O, and EtOH. . . . 59
49 SEM images of p-GaN on sapphire after cleaning in C_3H_6O in an ultrasonic bath. . . . 59
50 AFM images of the p-GaN surface after cleaning in 0.5 % and 40 %HF solution. . . . 60
51 SEM images of a p-GaN surface after a cleaning in 0.5 % HF solution and exposure to air. . . . 60
52 *In-situ* AFM images of a cleaned p-GaN surface showing the appearance of surface peaks with ongoing exposure time under an air environment. . . . 61

53 O 1s, C 1s, and Ga $3d_{3/2}$ photoelectron spectra for the original p-GaN surface (line 0), cleaned with EtOH only (line 1) and after a "piranha" cleaning procedure (line 2). 62
54 O 1s and C 1s photoelectron spectra for the p-GaN surface cleaned with EtOH (line 0) and after thermal cleaning at 450 °C (line 1). . . . 63
55 O 1s and C 1s photoelectron spectra for the p-GaN surface (sample A9) cleaned at several temperatures (lines 0–6) from the backside. . . 64
56 Color labels for the temperatures used in the thermal cleaning (left), and an extra label for the different sample materials (right). 65
57 QE values obtained for a series of p-GaN:Cs photocathodes that were thermally cleaned with a halogen lamp. 66
58 QE values obtained for a series of p-GaN:Cs photocathodes that were thermally cleaned through the sapphire substrate from the backside. . 67
59 Storage lifetimes and extrapolated lifetimes for a series of p-GaN:Cs photocathodes thermally cleaned with a halogen lamp. 68
60 O 1s, C 1s, and Ga $2p_{3/2}$ photoemission spectra for the p-GaN surface after thermal cleaning at 650 °C from the backside (red line), and after Ar^+ irradiation at an energy of 1.5 kV for 10 min (green line). 69
61 SEM image of a p-GaN:Cs surface (sample A9) that underwent thermal cleaning at 650 °C, Ar^+ sputtering and a Cs activation. The EDX measurements showed depletion in N atoms at positions 1 and 2 at the surface. 70
62 SEM images of a p-GaN:Cs surface (sample A9) that underwent a thermal cleaning at 650 °C and Ar^+ sputtering that resulted into surface crates and destroyed the p-GaN surface. 71
63 Photocurrent curves of p-GaN (sample A5), which was thermally cleaned at 500 °C and activated with Cs for four cycles (left), and QE decay curves of the same p-GaN:Cs photocathode after activation (right). 72
64 Ga $3d_{3/2}$, N 1s, O 1s, and C 1s photoelectron spectra for the p-GaN surface (sample A10) after thermal cleaning at 450 °C (line 0) and after Cs activation with 7.7 % QE (line 1). 73
65 Cs $3d_{5/2}$ photoemission spectrum of the adsorbed Cs on the p-GaN surface, with the peak fitting showing three components. 74
66 Spectral response of a p-GaN:Cs photocathode (sample A12) showing its cut-off edge at 360 nm, which is related to a band gap of 3.4 eV. . 74
67 Photocurrent curve during a YoYo activation of p-GaN (sample A14), in which Cs and O_2 are alternately applied. 75
68 O 1s, C 1s, and Cs $3d_{5/2}$ photoemission spectra of the p-GaN:Cs surface before YoYo activation was carried out (line 0) and after the p-GaN surface was YoYo activated (line 1). 76
69 QE values obtained for two p-GaN:Cs photocathodes that were activated with a YoYo process (Cs and O_2). 78
70 The QE decay of the p-GaN:Cs photocathode (sample A10) and the Ga $3d_{3/2}$, Cs $3d_{5/2}$, and O 1s photoemission spectra at different times during their decay. 79

71 The C 1s photoemission spectrum showing the evolution of the Cs_xC_y species and the degradation of the p-GaN:Cs photocathode (sample A10) on the left side and the shift to a lower BE along with the degradation of the p-GaN:Cs photocathode (right side). 80
72 The surface model of a freshly prepared p-GaN:Cs photocathode, in which the surface C attracts a part of the Cs (left). The surface model of an aged p-GaN:Cs photocathode showing the formation of Cs_xC_y islands (right). 80
73 Cs 3d spectra of a p-GaN:Cs photocathode (sample A14) influenced by the X-ray irradiation time. 82
74 The Ga $3d_{3/2}$, Cs $3d_{5/2}$, O 1s, and C 1s photoelectron spectra of the p-GaN:Cs surface before (line 0) and after (line 1) renewed thermal cleaning at 500 °C. 83
75 The QE decay curve of the re-activated p-GaN:Cs photocathode (sample A10) with the corresponding Ga $3d_{3/2}$, Cs $3d_{5/2}$, and O 1s photoemission spectra, taken at different points in the decay curve. . . . 84
76 SEM image of a p-GaN:Cs photocathode (sample A1), treated several times above 600 °C followed by numerous Cs activations. 85
77 SEM image of a p-GaN:Cs photocathode (sample A5), several times treated above 500 °C, followed by several Cs activations. 86
78 2D and 3D AFM images of a p-GaN:Cs photocathode (sample A5) which was treated several times above 500 °C and Cs activated. . . . 86
79 AFM image of the original p-GaN surface on Si, as received from Xiamen [113]. 87
80 AFM images of the p-GaN on Si surface after cleaning with the "piranha" procedure. 87
81 AFM image of the original p-GaN surface on TiN. 88
82 QE values obtained for a series of p-GaN:Cs photocathodes that were grown on Si and thermally cleaned with a halogen lamp. 89
83 QE values obtained for two p-GaN:Cs photocathodes that were grown on TiN. Sample D1 was thermally cleaned with a halogen lamp, and sample D2 was thermally cleaned from the backside through the TiN substrate. 89
84 Storage lifetimes obtained for a series of p-GaN:Cs photocathodes on Si. 90
85 SEM image of a p-GaN:Cs on Si photocathode (sample C2), thermally cleaned at 500 °C and activated with Cs for five cycles. 91
86 2D and 3D AFM images of the GaAs surface, cleaned with EtOH only. 93
87 O 1s, C 1s, Ga $2p_{3/2}$, and As 3d photoemission spectra of the EtOH-cleaned GaAs surface. 94
88 O 1s and C 1s photoemission spectra of the GaAs surface, thermally cleaned at 550 °C (line 0) and 600 °C (line 1). 95
89 The QE values that were obtained for two GaAs samples for which different thermal cleaning temperatures were used. 96
90 O 1s, C 1s, Cs 3d, Ga $2p_{3/2}$ and As 3d photoemission spectra of the GaAs surface, after a thermal cleaning at 550 °C (line 0) and 600 °C (line 1), and after YoYo activation (line 2). 97

91 O 1s, C 1s, Cs $3d_{5/2}$, Ga $2p_{3/2}$, and As 3d photoemission spectra of the GaAs surface during its degradation, showing 7.7 % QE (line 0), 2.0 % QE (line 1), and 0.8 % QE (line 2). 98
92 Photo of the GaAs sample B2 (left) and *ex-situ* SEM images for the same sample after it was taken out of the UHV preparation chamber, showing two different crystal structures on the GaAs surface. 99
93 *Ex-situ* SEM image of the GaAs photocathode surface measured in other areas than shown in Figure 92. 99
94 O 1s and C 1s photoemission spectra for the GaAs surface after a renewed thermal cleaning at 600 °C (line 0), and again 600 °C (line 1), and after YoYo activation with 8.2 % QE (line 2), and degrading with 3.7 % QE (line 3), and 1.3 % QE (line 4). 100
95 Ga $3d_{3/2}$ and Cs $3d_{5/2}$ photoemission spectra for the GaAs surface, studied in its degradation after a renewed (3rd time) YoYo activation with 8.2 % QE (line 0), with 3.7 % QE (line 1), and 1.3 % QE (line 2). The Ga $3d_{3/2}$ spectra show a shift toward a lower BE, while the Cs $3d_{5/2}$ spectra show a shift toward a higher BE. 101
96 SEM images of the unpolished Cu plug surface. 102
97 AFM images of the unpolished Cu plug, drilled by the workshop. . . 102
98 SEM images of the polishing result on the polished Cu plug surface. . 103
99 AFM images of the polished Cu plug surface. 103
100 QE decay curve of Cs_2Te (sample E1) during its operational lifetime in the SRF Gun II with corresponding QE maps, taken at three different points in the decay curve. 104
101 QE decay of sample E1 after the preparation, storage in the transport chamber and transportation to the SRF Gun II, measured at a λ of 260 nm and with a bias of 350 V on the anode. 105
102 Photoemission survey spectra of Cs_2Te surfaces for sample E1 (green line) and sample E2 (red line), showing a large amount of C and O for both Cs_2Te surfaces because the samples were taken out of the Cs_2Te UHV preparation chamber. 106
103 Te 3d and Cs $3d_{5/2}$ photoemission spectra for the Cs_2Te photocathode surface, used in SRF Gun II (sample E1, green), and as a prepared Cs_2Te photocathode surface (sample E2, red). 107
104 *Ex-situ* SEM image of the Cs_2Te surface in its border region, where Cs and Te were deposited off-set to each other, and an SEM image at higher magnification of the off-set region. 108
105 *Ex-situ* SEM images of surface particles found in the middle area of sample E3. EDX identified the particles as a Cs–O compound, which probably is a CsOH compound. 109
1 Temperature calibration of the thermo sensor when the sample (red) was in focus of the halogen lamp and when the thermo sensor (blue) was set in focus. V
2 Measured spectral width of the commercially available UV-LED with a maximum λ at 310 nm. V
3 Measured output power of the deuterium lamp according to the used wavelength. VI

4 XPS survey spectrum of sample A13 with 2 % QE, before A13 underwent an Ar^+ irradiation. . . . VI
5 XPS survey spectrum of the surface of sample A13 after Ar^+ irradiation at an energy of 1.5 keV. . . . VII
6 XPS survey spectrum of the surface of sample A13 after Ar^+ irradiation at an energy of 2.5 keV. . . . VII
7 Cs 3d photoemission spectrum of the activated p-GaN surface, showing an Cs 3d spin–orbit splitting of exactly 14 eV between the $3d_{3/2}$ and $3d_{5/2}$ spin state. . . . VIII
8 Spectral response of a p-GaN:Cs photocathode (sample A11) showing its cut-off edge at 360 nm, which is related to a band gap of 3.4 eV. . . . VIII
9 XPS survey spectra of the surface of sample A14 after thermally cleaned at 450 °C (red) and after YoYo activated (green). . . . IX
10 *In-situ* photocurrent curve of sample A6 during a YoYo activation; showing a photocurrent increase when Cs was applied and a decrease when O_2 was applied. . . . IX
11 *In-situ* photocurrent curve of sample A7 during a YoYo activation; showing the influence of the alternating application of Cs and O_2 on the photocurrent of sample A7. . . . X
12 The Ga $3d_{3/2}$, Cs $3d_{5/2}$, O 1s, and C 1s photoelectron spectra of the p-GaN:Cs surface (sample A11) before (line 0) and after (line 1) renewed thermal cleaning at 500 °C . . . X
13 The Ga $3d_{3/2}$, Cs $3d_{5/2}$, O 1s, and C 1s photoelectron spectra of the p-GaN:Cs surface (sample A11) with 3.6 % QE (line 0, red) and with 1.3 % QE (line 1, green). . . . XI
14 The Ga $3d_{3/2}$, Cs $3d_{5/2}$, O 1s, and C 1s photoelectron spectra of the p-GaN:Cs surface (sample A12) after thermal cleaning at 460 °C (line 0) and after Cs activation (line 1). . . . XI
15 The Ga $3d_{3/2}$, Cs $3d_{5/2}$, O 1s, and C 1s photoelectron spectra of the p-GaN:Cs surface (sample A12) with 5.9 % QE (line 0) and with 1.6 % QE (line 1). . . . XII
16 *Ex-situ* SEM images of the p-GaN:Cs on sapphire photocathode (sample A1) taken in the area where the steel washer fixed the sample on the sample holder and a higher magnification where the chemical composition by EDX (see Figure A 17) was measured. . . . XII
17 *Ex-situ* EDX measurement of p-GaN:Cs on sapphire photocathode (sample A1) showing the difference between the bright (steel washer area, blue dots) and dark area (p-GaN:Cs photocathode surface, black line); EDX was taken from SEM image (see Figure A 16). . . . XIII
18 *Ex-situ* EDX measurement of p-GaN:Cs on sapphire photocathode (sample A5), showing a Ga:N ratio of approximately 1. . . . XIII
19 *Ex-situ* EDX measurement on the p-GaN:Cs on Si photocathode (sample C2), thermally cleaned at 500 °C and activated with Cs for five cycles; showing the EDX spectra of the original p-GaN surface (black line) and the Cs particle (blue dots), which was probably an CsOH particle. . . . XIV

20 *In-situ* photocurrent curve of sample B1 during two YoYo activation cycles; the first cycle (left) resulted in no photocurrent while the second cycle (right side) shows the Cs application in orange and the O_2 application in blue; the *In-situ* photocurrent reached 120 nA. . . . XIV
21 *In-situ* photocurrent curve of sample B2 during the first YoYo activation cycle. . . . XV
22 *In-situ* photocurrent curve of sample B2 during the second YoYo activation cycle (left); the Cs application is marked in orange, while the O_2 application is marked in blue; QE decay curve of the GaAs photocathode (right) with the QE points where the XPS measurements were taken (marked in red). . . . XV
23 *In-situ* photocurrent curve of sample B2 during the third YoYo activation cycle (left); the Cs application is marked in orange, while the O_2 application is marked in blue; the QE decay curve of the GaAs photocathode (right) where the QE dropped significantly when XPS measurements were taken. . . . XVI
24 *Ex-situ* SEM of GaAs (sample B2) in the middle area, showing different crystal structures (left); EDX measurements (right) showed different Ga:As ratios inside the different crystal structures. . . . XVI
25 SEM Image of the surface of mirror-like polished Cu with a particle on the surface; EDX measurements identified the particle as a SiC particle from the polishing suspension. . . . XVII
26 O 1s and C 1s photoemission spectra of sample E1 (green line) and sample E2 (red line); taken from the survey spectrum as a zoom of the sample E1 and E2. . . . XVII
27 *Ex-situ* EDX measurement; focussed on the particle on the Cs_2Te surface of sample E3; identifying the particle as a CsOH. . . . XVII

List of Tables

1 p-GaN samples used with their properties (if known). 49
2 Atomic concentrations derived from the survey spectra for a p-GaN surface with 2 % QE and after Ar^+ sputtering. 69
1 Used electronic devices for the preparation chamber that were controlled by the internal software. I
2 Measured p-GaN samples with activation parameters; applied Cs dispenser current, photocurrent of p-GaN:Cs photocathode, used UV-light power, and QE from Equation 4. Sample A9 was thermally cleaned stepwise, beginning at 320 °C, 500 °C, 570 °C, 610 °C, 625 °C and ending with 650 °C. Afterwards A9 was irradiated with Ar^+ at 1.5 keV and unsuccessfully Cs activated. Sample A13 was used for preferential sputtering of Ar^+ at 1.5 keV and at 2.5 keV energy. II
3 Activation parameters of GaAs samples. III
4 Activation parameters of p-GaN on Si samples. III
5 Activation parameters of p-GaN on TiN samples. III
6 Polishing steps that were used for achieving a mirror-like surface of the Cu plugs, used afterwards as a substrate for Cs_2Te. IV
7 Studied Cs_2Te photocathodes on Cu substrate with the thickness of deposited Cs and Te layer and initial QE value. IV

11 Acknowledgments

In diesem letzten Abschnitt der Arbeit möchte ich mich bei all denjenigen bedanken ohne deren Hilfe ich diese Arbeit hätte nicht beenden können.

Mein erster Dank gilt **Prof. Gaponik**, für seine Bereitschaft diese Dissertation ohne Zweifel zu betreuen und mich in seine Arbeitsgruppe aufzunehmen. Darüber hinaus möchte ich mich für sein Vertrauen in meine wissenschaftlichen Fähigkeiten, vor allem auch in die als lehrtätige Person, aber auch für die vielen Konsultationen, Gespräche und das zeitintensive Korrekturlesen herzlichst bedanken.

Mein zweiter Dank gilt **Prof. Jiang** für die Bereitschaft diese Dissertation als Zweitgutachter anzunehmen und mich für die gute Zusammenarbeit mit seiner Arbeitsgruppe der Universität Siegen bedanken, die mir auch interessante Einblicke in deren p-GaN Herstellung ermöglichte.

Ein herzliches Dankeschön gilt ebenso **Prof. Brunner** für seine Bereitschaft als Drittgutachter zu fungieren und ich möchte mich auch bei ihm für seine Unterstützung bedanken.

Den allermeiste Dank gebührt allerdings Frau **Dr. Xiang**, ohne die diese Arbeit überhaupt nicht möglich gewesen wäre. Sie war mir in den letzten 4,5 Jahren die bestmögliche Betreuerin, die mir ebenso viel Freiraum als auch die notwendige Anleitung und Anreize gegeben hat, die ich gebraucht habe. Bei ihr möchte ich mich ebenfalls für ihr Vertrauen in meine wissenschaftlichen Fähigkeiten bedanken und für die zahlreichen Diskussionen, Gespräche und auch die vielen Dienstreisen, die mir ermöglicht wurden, bedanken. Ich habe sehr viel von ihr in den letzten Jahren gelernt und konnte meine Fähigkeiten, über die der Chemie ausbauen. Es ist etwas ganz Besonderes als Doktorand den Auf- und Ausbau eines Fotokathodenlabors mit dem Kauf eines XPS-Gerätes zu betreuen. Vielen Dank für diese Erfahrung!
Frau Dr. Xiang ist nicht nur Betreuerin dieser Promotion, sondern auch eine Freundin und eine wertgeschätzte Kollegin geworden, was essenzielle Bestandteile einer außerordentlichen Betreuung ausmachen. Sie hatte sowohl für fachliche Diskussionen als auch für private Angelegenheiten ein offenes Ohr und ich wünsche ihr, dass sie in Zukunft weitere zahlreiche Doktoranden: innen erfolgreich betreuen darf und wird.

Ebenso möchte ich mich bei Herrn **Dr. Teichert** für seine Unterstützung bedanken. Die Zusammenarbeit und Diskussionen habe ich ebenso genossen wie auch die vielen privaten Gespräche. Ihm wünsche ich für die Zukunft eine wohlverdienten und erholsamen Ruhestand, der jetzt wieder entspannter angegangen werden kann, da alle Doktoranden ihre Arbeiten beendet haben.

Dank gebührt ebenso **Prof. Michel** und dem gesamten **ELBE-Team**, mich als Chemikerin unter all den Physikern herzlichst aufgenommen zu haben. Auch wenn wir manchmal unterschiedliche Sprachen sprechen, haben wir viel miteinander erlebt und zusammen gelacht. In den ganzen Jahren habe ich mich nie alleine oder fehl am Platz in der Abteilung gefühlt. Ohne die tatkräftige Unterstützung von **Enno**, **Arndt** und **Matthias** wäre das Labor in der 119 nicht das, was es jetzt ist.
Besonderer Dank gilt auch meinen lieben **Petr** und **Paul**, die doch sehr, sehr viele Nerven durch mich verloren haben, wenn mal wieder etwas „von allein“ oder auf magische Weise kaputt gegangen ist. Ohne eure Unterstützung und die ganz besondere Motivation durch zahlreiche Schokolade wäre ich jetzt definitiv nicht fertig geworden.

Bei **Prof. Stumpf** möchte ich mich für die Bereitstellung des Laborplatzes im Institut für Ressourcenökologie bedanken. Insbesondere bei Frau **Dr. Vogel** und Frau **K. Flemming**, die mir jahrelang Zugang zu ihren Laboren und AFM gewährt haben und deren Chemikalien ich einfach mitbenutzen durfte. Vielen lieben Dank auch für Ihr Vertrauen!

Bei **Prof. Facsko** möchte ich mich für die Benutzung vom SEM im Ionenstrahlzentrum bedanken. Ebenso beim Herrn **Dr. Bischoff** für seine geduldige Art, seine Einweisung, Ratschläge und sein Vertrauen in meine Fähigkeiten.
Das Arbeiten in diesen beiden Abteilungen hat mir immer sehr viel Freude bereitet und ich möchte mich daher bei allen Beteiligten für Ihre ausserordentliche Hilfsbereitschaft bedanken.

Ebenso möchte ich mich bei Frau **L. Heinrich** bedanken, die das ständige Arbeiten in der 119 tatkräftig unterstützt hat, mich mit Spezialitäten aus ihrem heimischen Garten versorgt hat und durch deren Anwesenheit das ganze Arbeiten dort oben nicht ganz so einsam geblieben ist. Ohne Sie und Ihre Unterstützung wäre das Labor in der 119 auch nicht in diesen optimalen Zustand gekommen.

Ein besonderer Dank gilt auch meinem Leidensgenossen **Shuai**, der sehr oft bereit war mich bei Laborarbeiten (die natürlich immer in den offiziellen Arbeitszeiten stattgefunden haben) mit einer helfenden Hand zu unterstützen und mich mit chinesischen Spezialitäten zu versorgen. Herzlichen Dank für die zahlreichen lustigen Abende mit Hotpot und viel flüssiger Motivation um die Doktorandenzeit gut zu überstehen. Wir haben viele lustige Abende zusammen erlebt, die stressige Phasen reduziert haben und die uns lange in Erinnerung bleiben werden.

Ein besonderer Dank gebührt meinem lieben **Kai**, der mich überhaupt dazu ermutigte zum Bewerbungsgespräch ans HZDR zu gehen. Ohne ihn wäre ich da gar nicht erst erschienen. Danke dafür, dass du mir immer mit Rat und Tat zur Seite gestanden hast und mit mir über viel Fachliches diskutiert hast. Für die besondere Unterstützung in all den Jahren und das ständige Korrekturlesen meiner Paper, Poster, Unisachen usw. möchte ich mich herzlichst bedanken. Ein besonderer Dank gilt ihm dafür, mich bedingungslos zu unterstützen und alle meinen Launen ertragen zu müssen. Durch seine ruhige Art gelingt es ihm mich durchatmen zu lassen und dass ich zurück zur Ruhe finde, sonst wären in den letzten Jahren bestimmt einige Köpfe gerollt.
Dank gilt auch seinen Eltern, **Kathrin** und **Dieter**, die mich in all den Jahren auch tatkräftig unterstützt haben.

Ein herzliches Dank gilt allen meinen Freunden und besonders meiner Familie (**Iris**, **Paul** und meinem Bruder **Tim**), ebenso meiner ganzen Verwandtschaft, besonders meinen zahlreichen Cousinen und Cousins, die mich in den letzten Jahren unterstützt haben und mir immer positiv zugeredet haben. Ohne die positiven Worte von euch hätte ich bestimmt nicht so lange durchgehalten.

Die Arbeit widme ich meinen Großeltern **Ursela** und **Kornelius** von denen ich wohl die naturwissenschaftliche Begabung geerbt habe und die mich immer unterstützt haben. Auch wenn sie nicht mehr an diesen besonderen Ereignis teilhaben können, bleiben sie immer in Erinnerung und immer ein Teil von mir.

In diesem Sinne möchte ich mich bei allen von ganzem Herzen für Rat, Tat und Ihre Unterstützung bedanken, denn letztendlich ist und bleibt eine Forschungsarbeit eine Teamarbeit.

A Appendix

Tab. A 1 Used electronic devices for the preparation chamber that were controlled by the internal software.

device	**specification**	**function**
Keithley	1024 1100 V source meter	photocurrent
Heinziger	LNC 300-20 pos	O_2 flow
Delta Electronica	SM 70-AR-24	power supply for Cs and halogen lamp
RHC VG Scienta	Eurotherm 2408	power supply for backside heating
Ionivac	IM 540	vacuum gauge
Varian	Midivac	Ion pump controller
Roithner UV-LED	DUV310-HL5N	UV-light source
SAES Getter	CS/MNF/4.1/12 FT10+10	Cs dispenser
OSRAM	400 W	halogen lamp
National Instruments	cRIO9074	software controller
OPTRIS IR sensor	CT 3MH1-CF3-CB3	temperature measurement
OCEAN Optics	DH-2000	deuterium lamp
Princeton Instruments	Acton SP2150	monochromator

Tab. A 2 Measured p-GaN samples with activation parameters; applied Cs dispenser current, photocurrent of p-GaN:Cs photocathode, used UV-light power, and QE from Equation 4. Sample A9 was thermally cleaned stepwise, beginning at 320 °C, 500 °C, 570 °C, 610 °C, 625 °C and ending with 650 °C. Afterwards A9 was irradiated with Ar^+ at 1.5 keV and unsuccessfully Cs activated. Sample A13 was used for preferential sputtering of Ar^+ at 1.5 keV and at 2.5 keV energy.

sample	T (°C)	Cs current (A)	photocurrent (nA)	$P_{UV-light}$ (μW)	QE (%)
A1	> 600	3.3	373	110	1.31
		3.4	230	110	0.81
		3.5	178	110	0.63
A2	> 600	3.6	242	110	0.85
		3.7	895	110	3.15
		3.0	600	110	2.11
		3.3	283	110	0.99
A3	> 600	3.4	1200	110	4.22
		3.45	510	110	1.79
		3.55	580	110	2.04
A4	> 600	3.5	1335	110	4.69
		3.4	1198	110	4.21
		3.3	572	110	2.01
		3.4	586	110	2.06
A5	500	3.3	3228	125	9.99
		3.3	3710	125	11.48
	> 600	3.3	3720	125	11.52
	> 600	3.3	3660	125	11.33
A6	430	3.3	1260	51	9.56
	450	3.3	830	51	6.30
	460	3.3	720	51	5.46
YoYo	0	3.3	770	51	5.84
A7	0	3.3	0	51	0.00
	220	3.3	720	51	5.46
	320	3.4	1330	51	10.09
	430	3.5	580	51	4.40
YoYo	0	3.5	730	51	5.54
A8	600	3.8	1031	51	7.82
	650	3.8	530	51	4.02
	700	3.7	375	51	2.85
A10	420	3.4	1014	51	7.69
	500	3.3	1214	51	9.21
	0	3.2	1039	51	7.88
A11	460	3.5	480	51	3.64
	460	3.3	780	51	5.92
A12	420	3.3	780	51	5.92
	500	3.3	1010	51	7.66
A14	470	3.8	935	51	7.10
YoYo	455	3.6	1033	51	7.84

Tab. A 3 Activation parameters of GaAs samples.

sample	T (°C)	Cs current (A)	photocurrent (nA)	$P_{UV-Light}$ (μW)	QE (%)
B1	350	3.6	0	51	0
	450	3.7	103	51	0.78
B2	600	3.4	0	51	0
	600	3.9	1023	51	7.76
	600	3.8	1083	51	8.21

Tab. A 4 Activation parameters of p-GaN on Si samples.

sample	T (°C)	Cs current (A)	photocurrent (nA)	$P_{UV-Light}$ (μW)	QE (%)
C1	> 600	3.5	124	125	0.38
C2	500	3.5	760	125	2.35
	500	3.4	762	125	2.36
	500	3.3	822	125	2.54
	500	3.2	850	125	2.63
	500	3.2	824	125	2.55
C3	410	3.4	1204	125	3.73
	400	3.3	1288	125	3.98
	400	3.3	1222	125	3.78
C4	300	3.5	20	51	0.15
	400	3.5	230	51	1.75
	500	3.6	570	51	4.33
C5	400	3.5	200	51	2.9
	400	3.5	230	51	3.00

Tab. A 5 Activation parameters of p-GaN on TiN samples.

sample	T (°C)	Cs current (A)	photocurrent (nA)	$P_{UV-Light}$ (μW)	QE (%)
D1	450	3.7	0	51	0
	530	3.7	450	51	3.41
	560	3.7	620	51	4.70
	0	3.7	535	51	4.06
D2	500	3.9	570	51	4.33
	550	3.8	565	51	4.28
	600	4.0	446	51	3.38
	650	4.1	390	51	2.96

Tab. A 6 Polishing steps that were used for achieving a mirror-like surface of the Cu plugs, used afterwards as a substrate for Cs_2Te.

polishing cloth	**suspension**
SiC #2000	H_2O
SiC #4000	H_2O
MD-DAC	diamont (3 µm)
MD-DAC	diamont (1 µm)
MD-NAP	non-dry

In the first step the Cu was polished with SiC #2000 foil of a grain size of 10 μm. The Cu was rotated with 150 revolutions per minute and pressed with a force of 30 N against the polishing clothes. In the first step only H_2O was used as a polishing solution. In the second step, a SiC foil #4000 was used with the same force parameters as in step 1. This foil included a grain size of 5 μm. In the third step an MD-DAC cloth was installed. This cloth was satin-woven acetate and was made wet with lubricant and a 3 μm diamond solution. In the 4th step only the diamond solution changed to 1 μm. At last a MD-NAP cloths with non-dry solution was used to finalize the polishing process. The MD-NAP was used in the final polishing step. Between each step the Cu plugs were rinsed with cold H_2O . All in all not more than 0.3 mm were removed from the initial Cu surface.

Tab. A 7 Studied Cs_2Te photocathodes on Cu substrate with the thickness of deposited Cs and Te layer and initial QE value.

sample	Te thickness (nm)	Cs thickness (nm)	QE (%)
E1	8	40	6.1
E2	6	32	6.5
E3	10	45	5.5

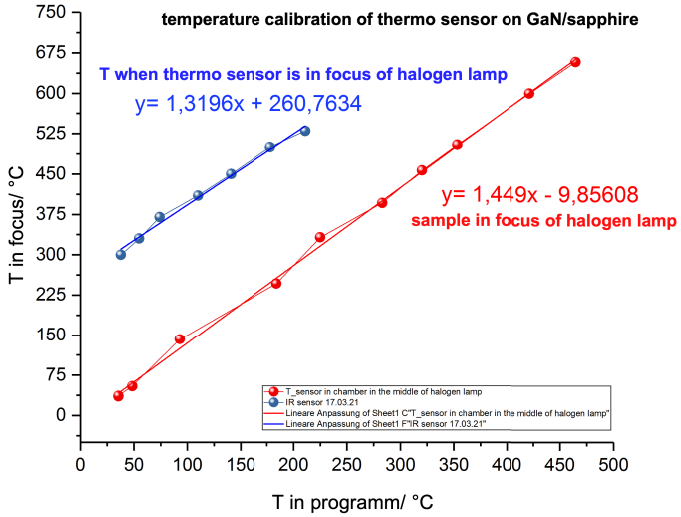

Fig. A 1 Temperature calibration of the thermo sensor when the sample (red) was in focus of the halogen lamp and when the thermo sensor (blue) was set in focus.

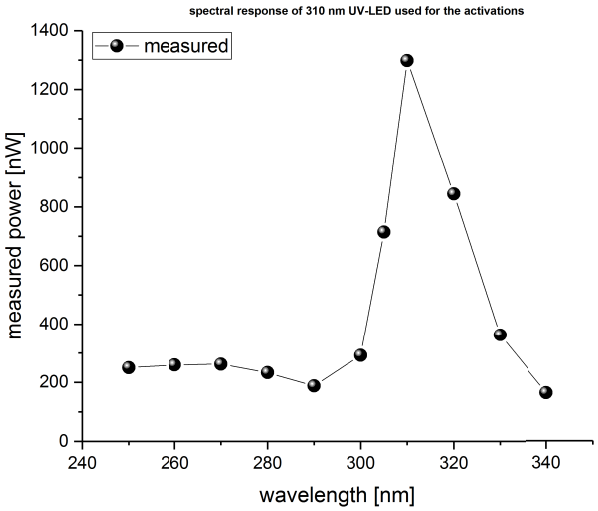

Fig. A 2 Measured spectral width of the commercially available UV-LED with a maximum λ at 310 nm.

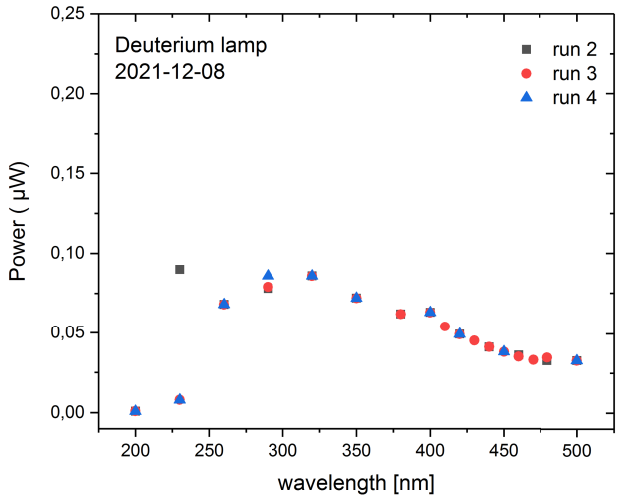

Fig. A 3 Measured output power of the deuterium lamp according to the used wavelength.

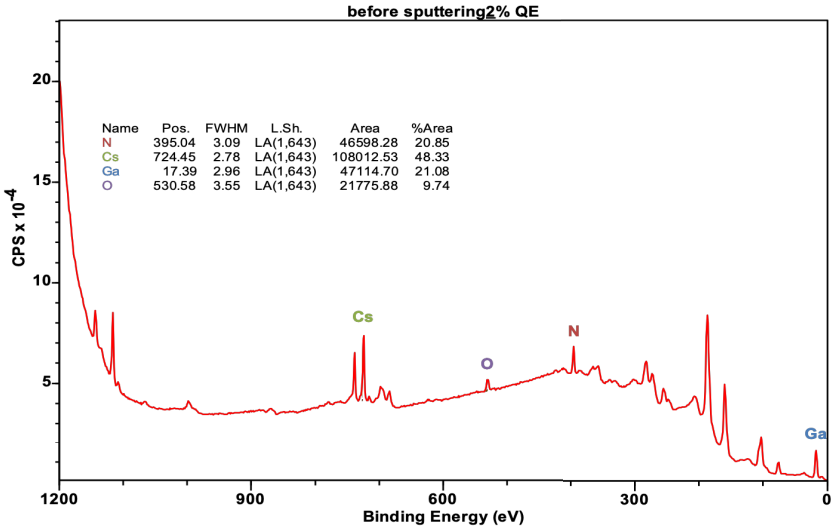

Fig. A 4 XPS survey spectrum of sample A13 with 2 % QE, before A13 underwent an Ar^+ irradiation.

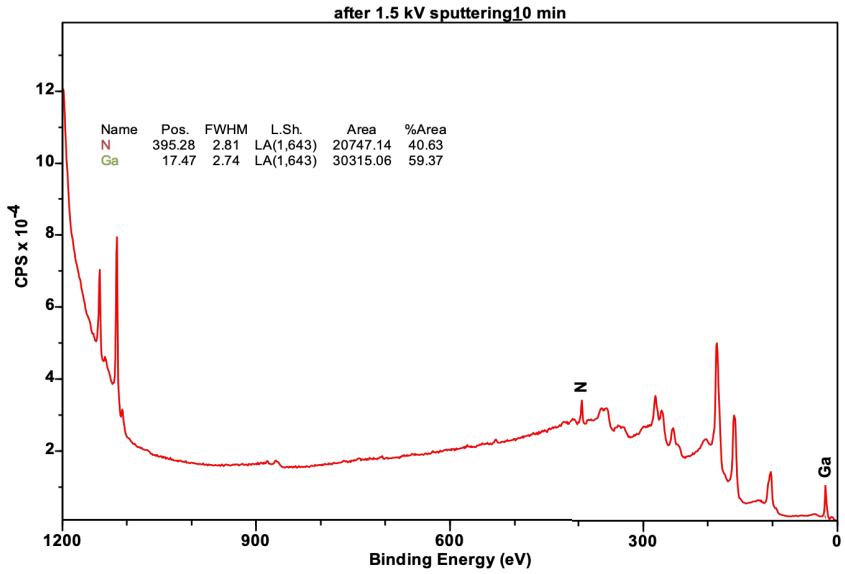

Fig. A 5 XPS survey spectrum of the surface of sample A13 after Ar^+ irradiation at an energy of 1.5 keV.

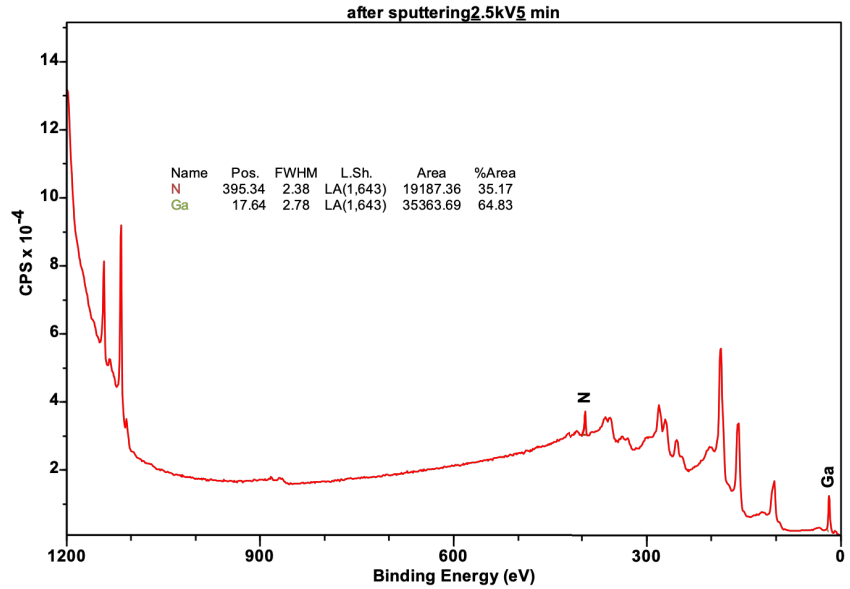

Fig. A 6 XPS survey spectrum of the surface of sample A13 after Ar^+ irradiation at an energy of 2.5 keV.

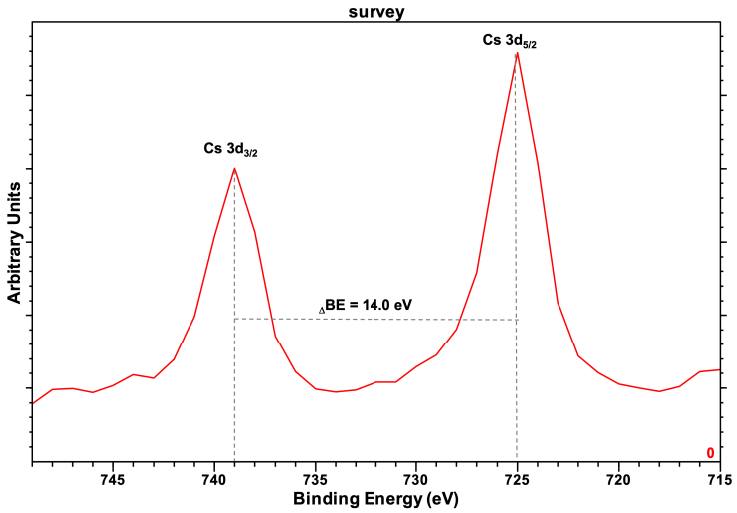

Fig. A 7 Cs 3d photoemission spectrum of the activated p-GaN surface, showing an Cs 3d spin–orbit splitting of exactly 14 eV between the $3d_{3/2}$ and $3d_{5/2}$ spin state.

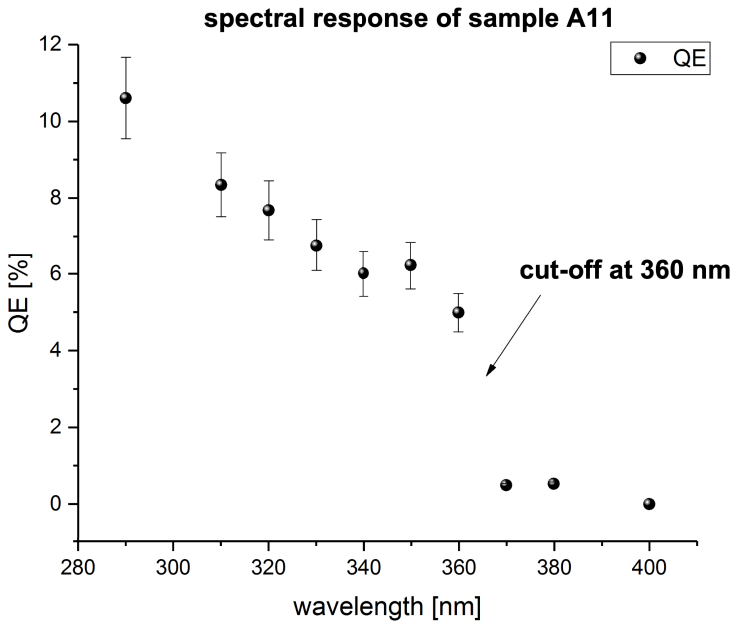

Fig. A 8 Spectral response of a p-GaN:Cs photocathode (sample A11) showing its cut-off edge at 360 nm, which is related to a band gap of 3.4 eV.

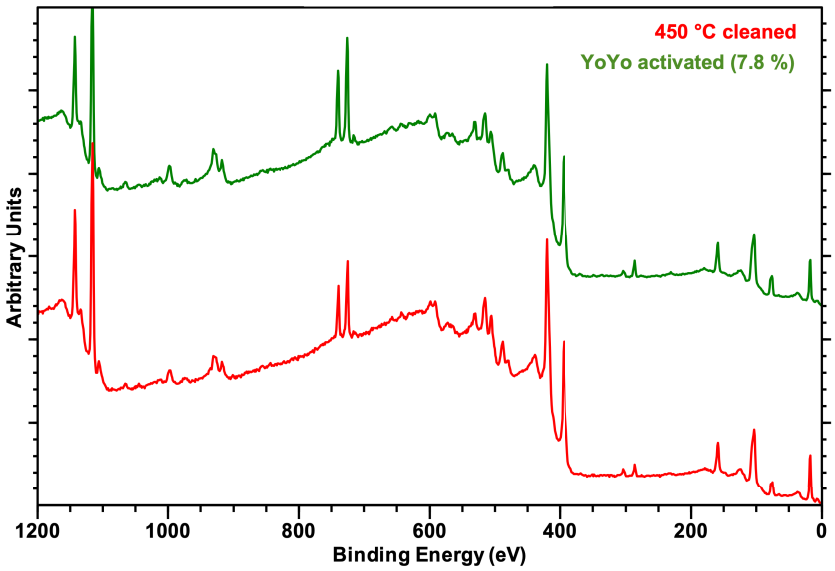

Fig. A 9 XPS survey spectra of the surface of sample A14 after thermally cleaned at 450 °C (red) and after YoYo activated (green).

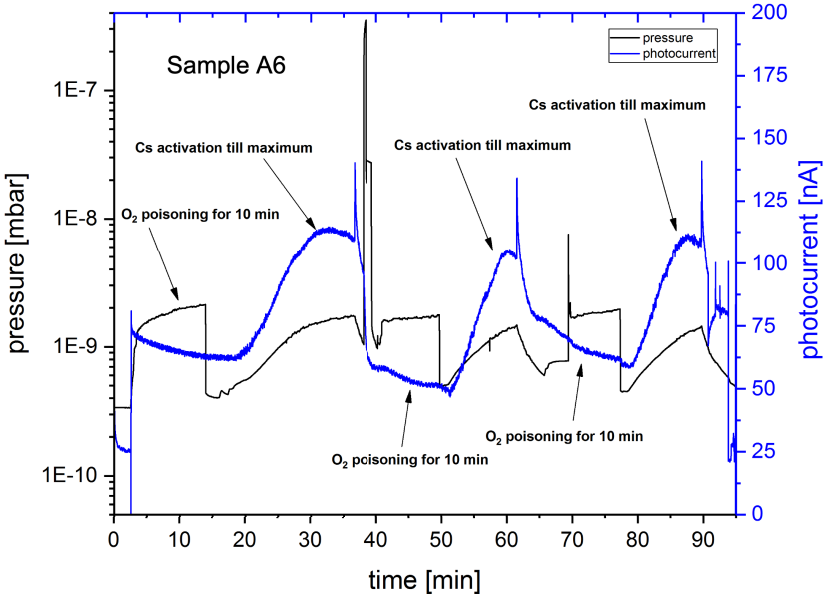

Fig. A 10 *In-situ* photocurrent curve of sample A6 during a YoYo activation; showing a photocurrent increase when Cs was applied and a decrease when O_2 was applied.

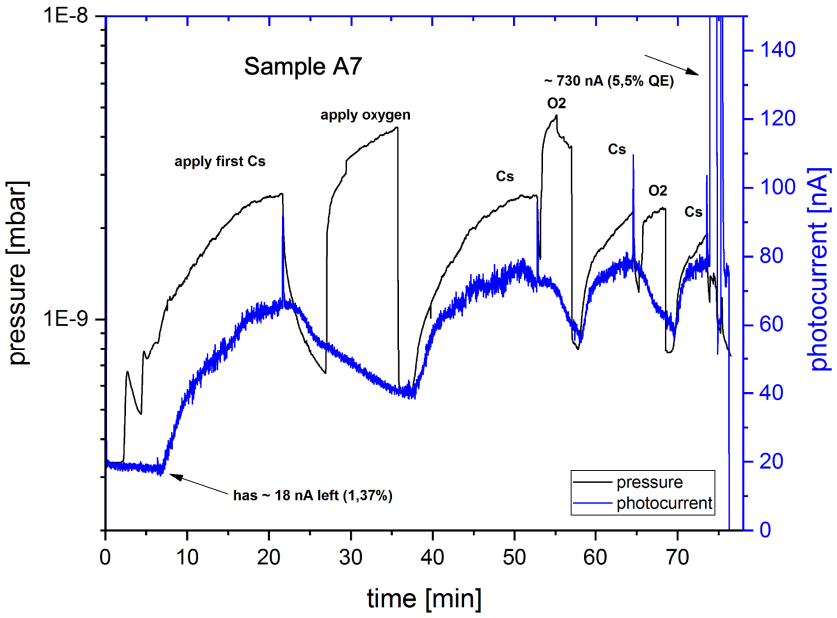

Fig. A 11 *In-situ* photocurrent curve of sample A7 during a YoYo activation; showing the influence of the alternating application of Cs and O_2 on the photocurrent of sample A7.

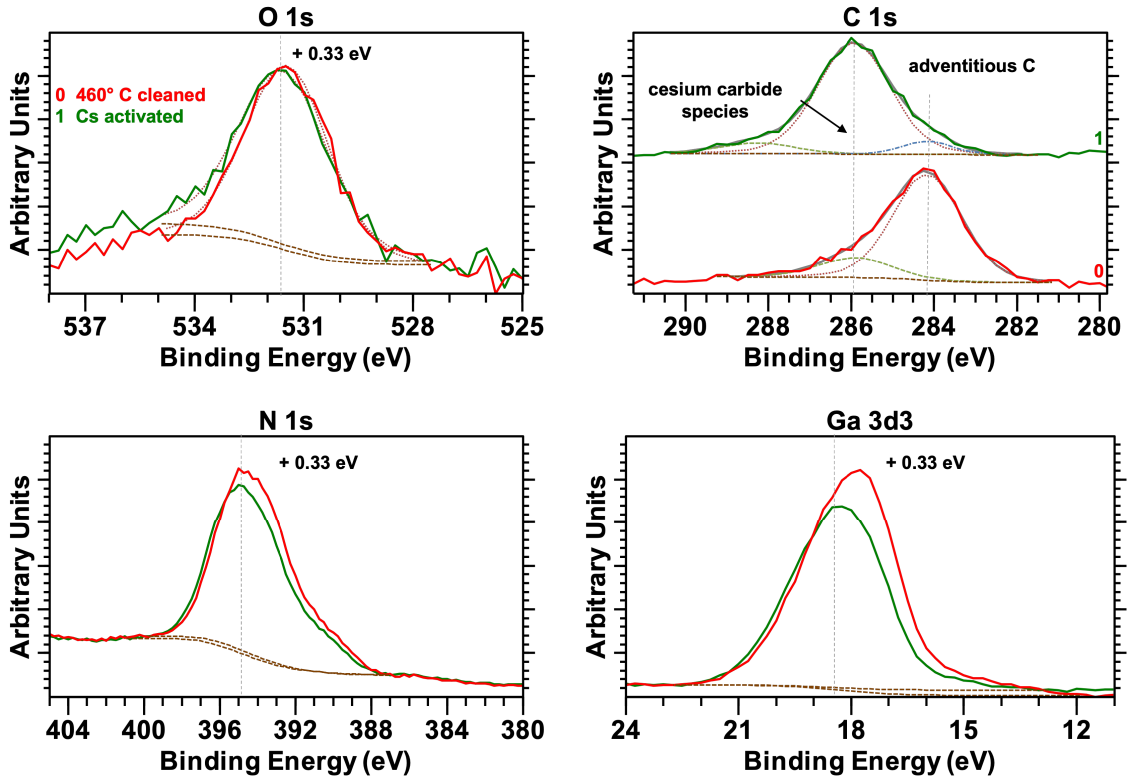

Fig. A 12 The Ga $3d_{3/2}$, Cs $3d_{5/2}$, O 1s, and C 1s photoelectron spectra of the p-GaN:Cs surface (sample A11) before (line 0) and after (line 1) renewed thermal cleaning at 500 °C

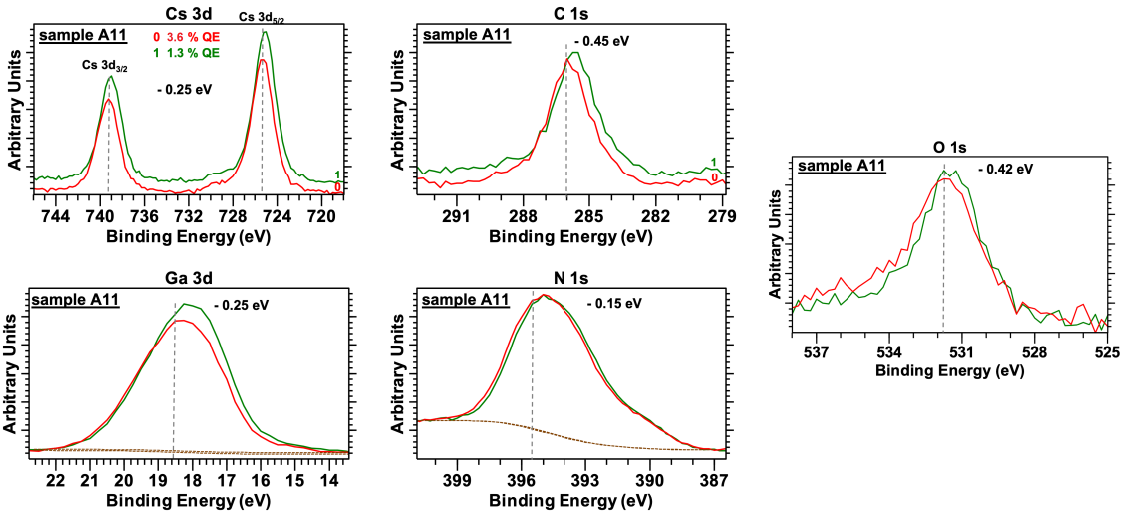

Fig. A 13 The Ga $3d_{3/2}$, Cs $3d_{5/2}$, O 1s, and C 1s photoelectron spectra of the p-GaN:Cs surface (sample A11) with 3.6 % QE (line 0, red) and with 1.3 % QE (line 1, green).

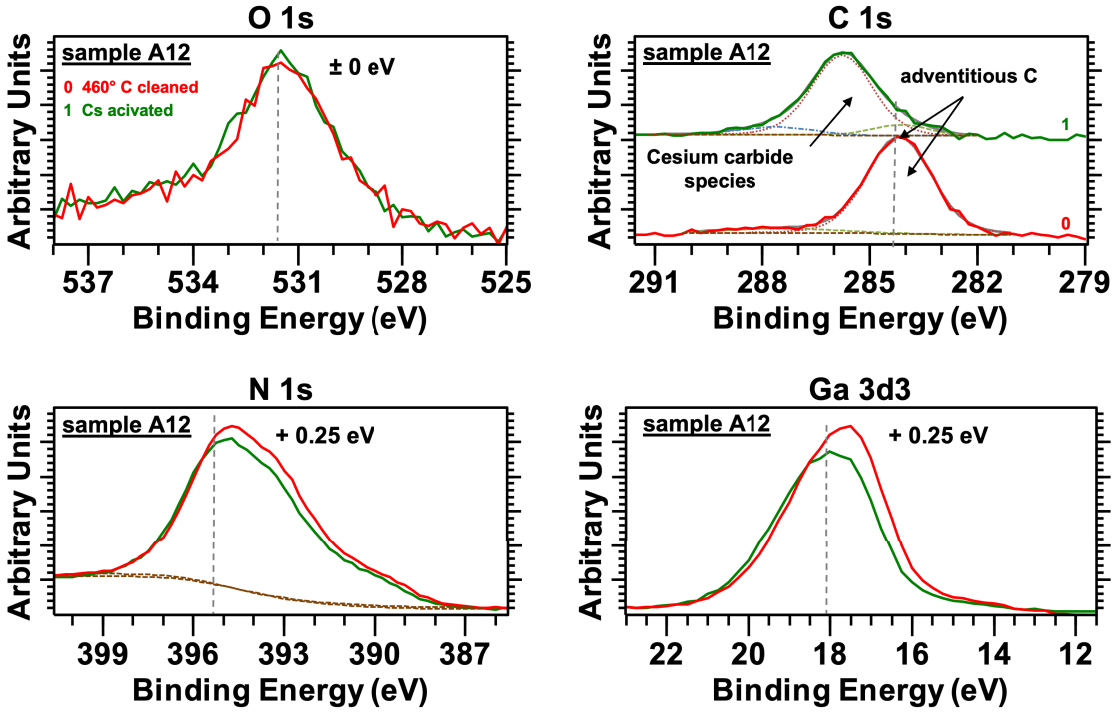

Fig. A 14 The Ga $3d_{3/2}$, Cs $3d_{5/2}$, O 1s, and C 1s photoelectron spectra of the p-GaN:Cs surface (sample A12) after thermal cleaning at 460 °C (line 0) and after Cs activation (line 1).

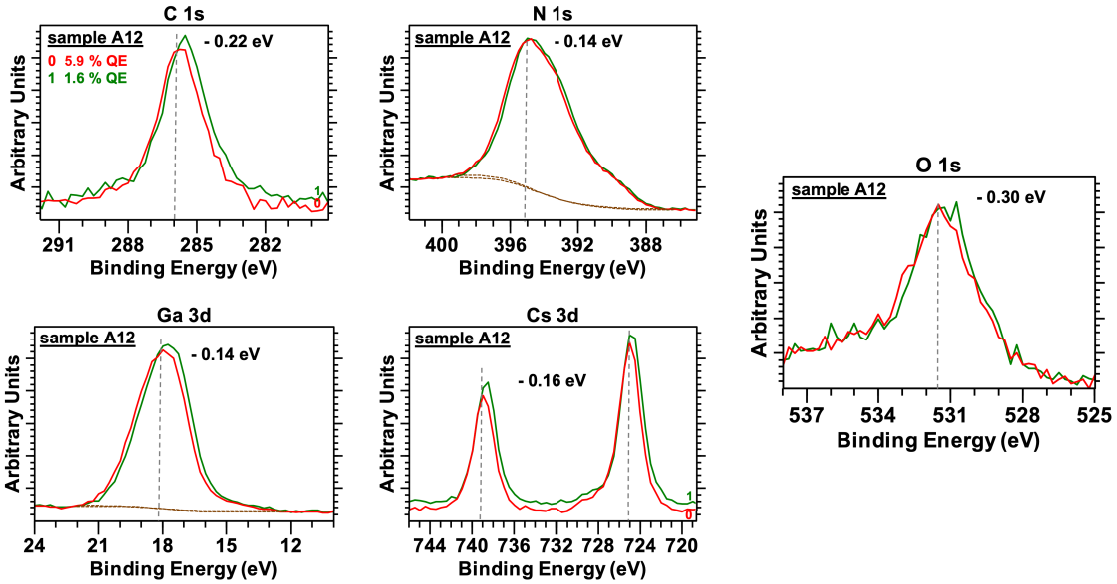

Fig. A 15 The Ga $3d_{3/2}$, Cs $3d_{5/2}$, O 1s, and C 1s photoelectron spectra of the p-GaN:Cs surface (sample A12) with 5.9 % QE (line 0) and with 1.6 % QE (line 1).

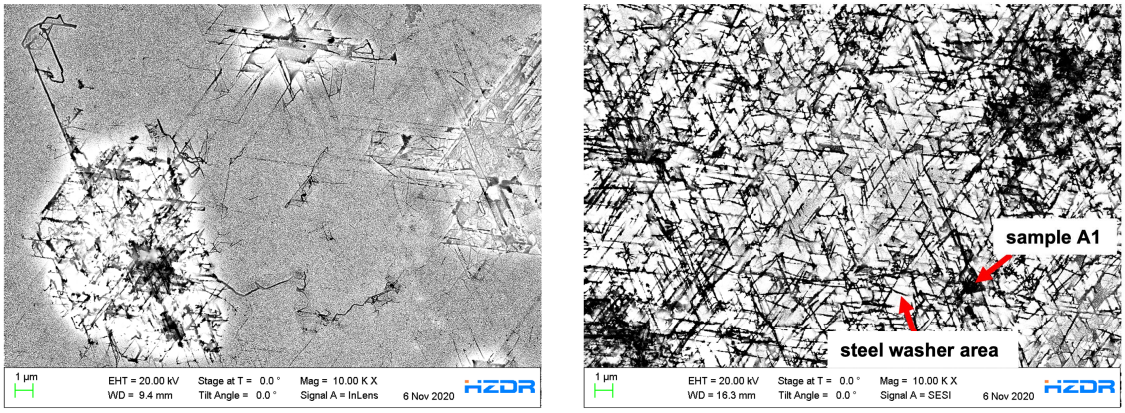

Fig. A 16 *Ex-situ* SEM images of the p-GaN:Cs on sapphire photocathode (sample A1) taken in the area where the steel washer fixed the sample on the sample holder and a higher magnification where the chemical composition by EDX (see Figure A 17) was measured.

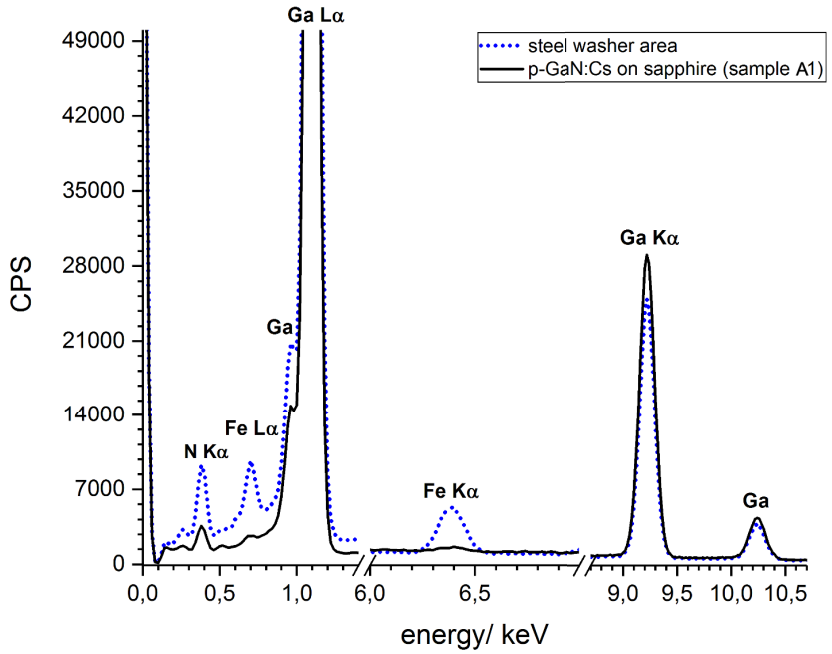

Fig. A 17 *Ex-situ* EDX measurement of p-GaN:Cs on sapphire photocathode (sample A1) showing the difference between the bright (steel washer area, blue dots) and dark area (p-GaN:Cs photocathode surface, black line); EDX was taken from SEM image (see Figure A 16).

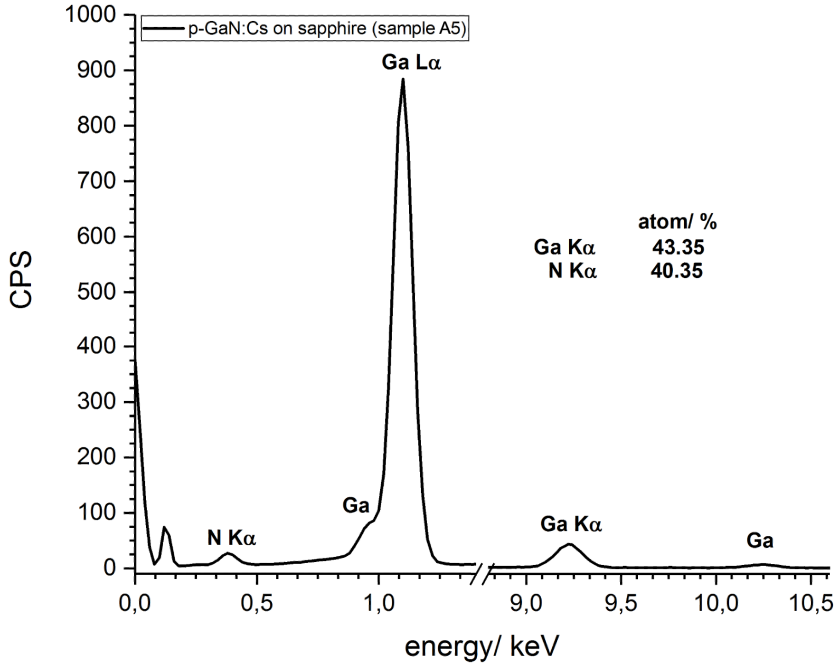

Fig. A 18 *Ex-situ* EDX measurement of p-GaN:Cs on sapphire photocathode (sample A5), showing a Ga:N ratio of approximately 1.

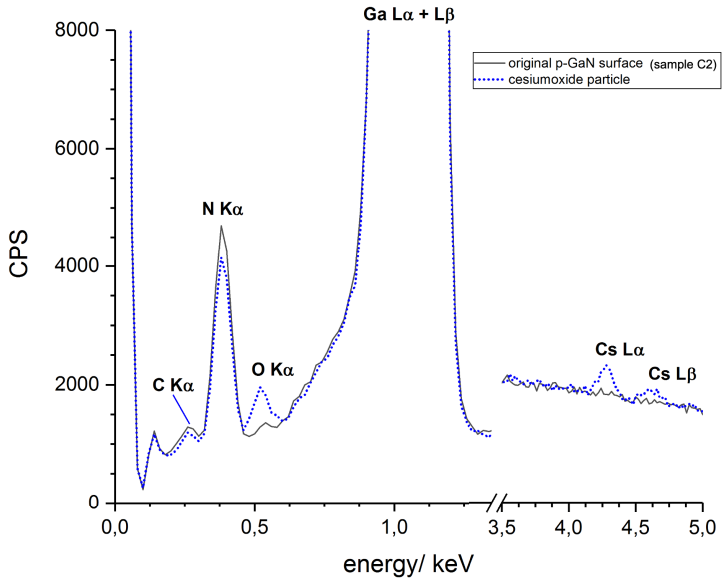

Fig. A 19 *Ex-situ* EDX measurement on the p-GaN:Cs on Si photocathode (sample C2), thermally cleaned at 500 °C and activated with Cs for five cycles; showing the EDX spectra of the original p-GaN surface (black line) and the Cs particle (blue dots), which was probably an CsOH particle.

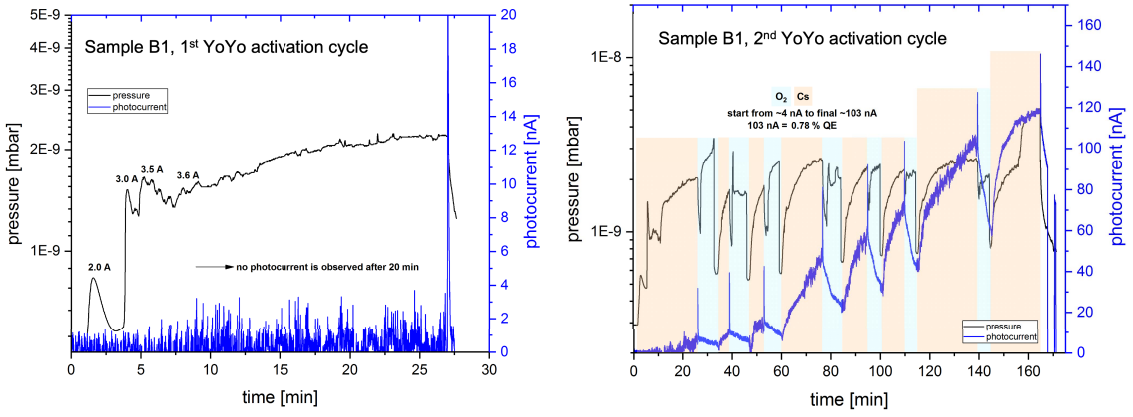

Fig. A 20 *In-situ* photocurrent curve of sample B1 during two YoYo activation cycles; the first cycle (left) resulted in no photocurrent while the second cycle (right side) shows the Cs application in orange and the O_2 application in blue; the *In-situ* photocurrent reached 120 nA.

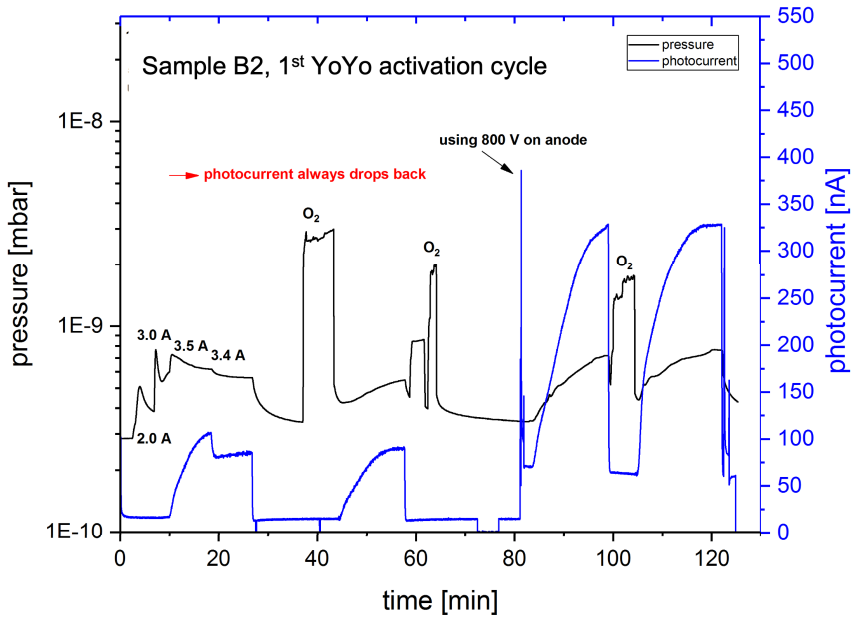

Fig. A 21 *In-situ* photocurrent curve of sample B2 during the first YoYo activation cycle.

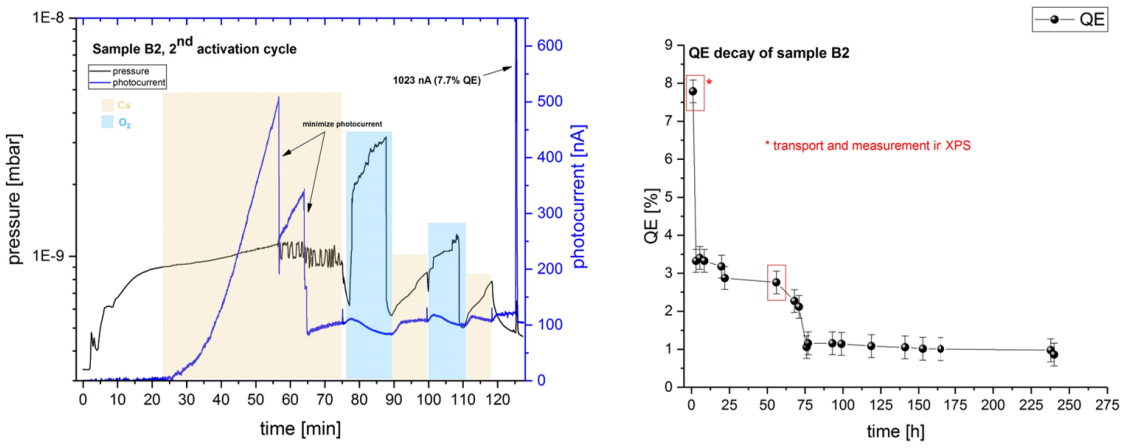

Fig. A 22 *In-situ* photocurrent curve of sample B2 during the second YoYo activation cycle (left); the Cs application is marked in orange, while the O_2 application is marked in blue; QE decay curve of the GaAs photocathode (right) with the QE points where the XPS measurements were taken (marked in red).

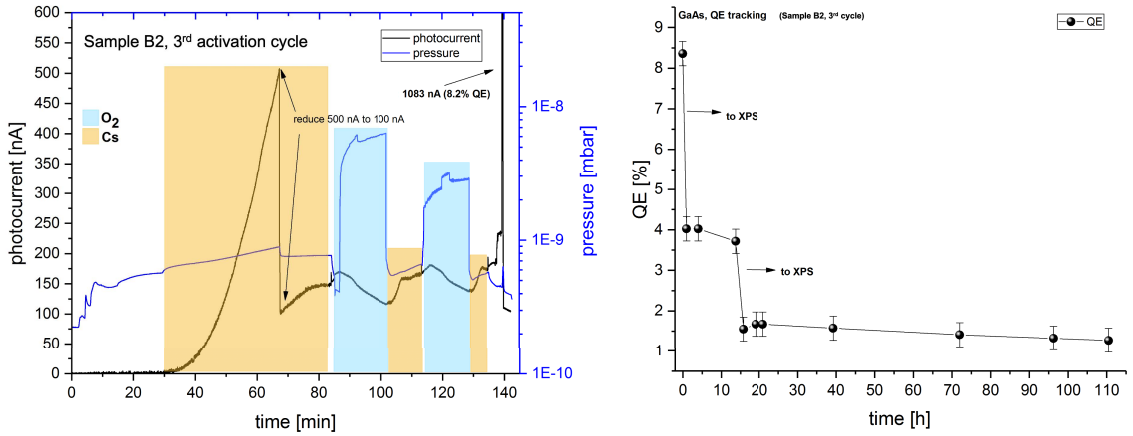

Fig. A 23 *In-situ* photocurrent curve of sample B2 during the third YoYo activation cycle (left); the Cs application is marked in orange, while the O_2 application is marked in blue; the QE decay curve of the GaAs photocathode (right) where the QE dropped significantly when XPS measurements were taken.

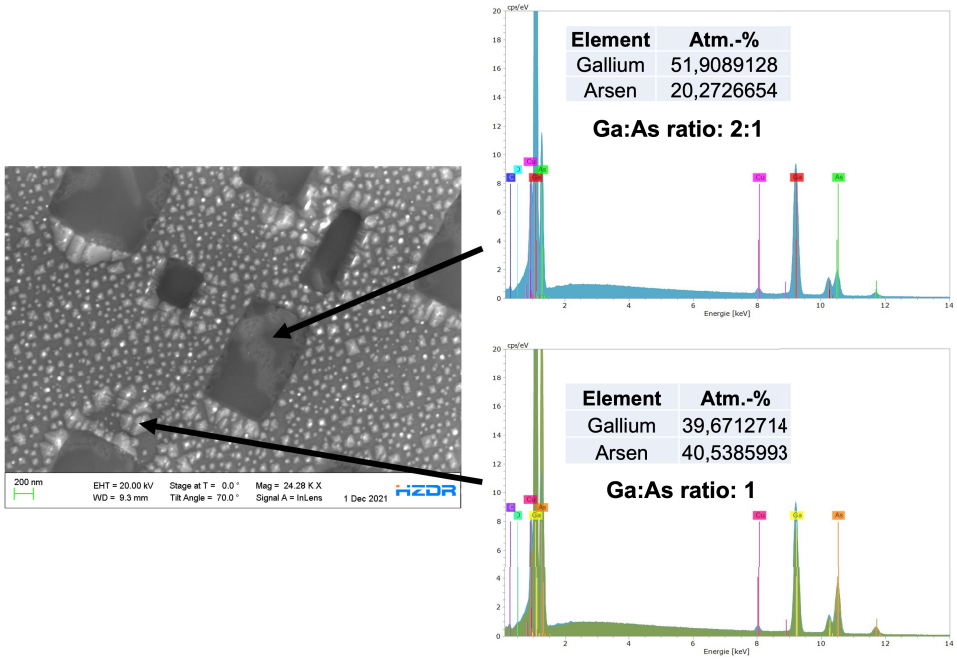

Fig. A 24 *Ex-situ* SEM of GaAs (sample B2) in the middle area, showing different crystal structures (left); EDX measurements (right) showed different Ga:As ratios inside the different crystal structures.

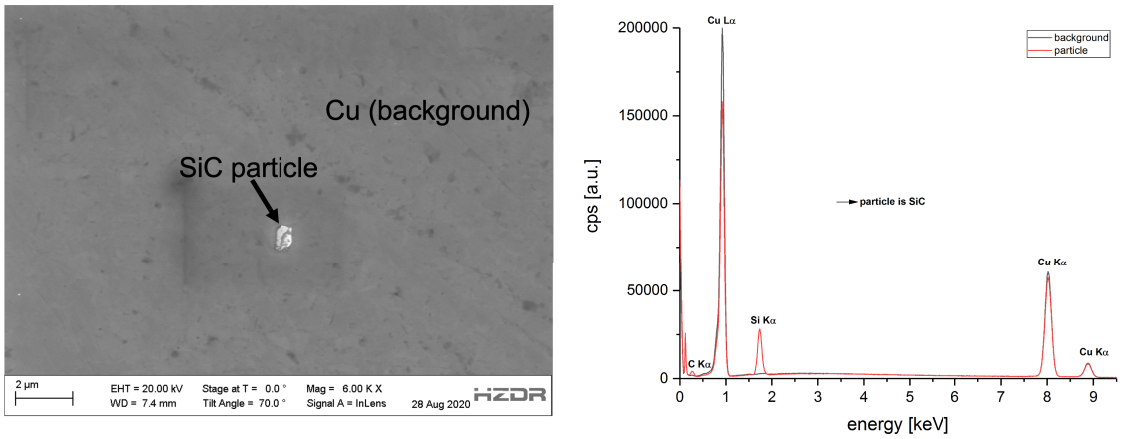

Fig. A 25 SEM Image of the surface of mirror-like polished Cu with a particle on the surface; EDX measurements identified the particle as a SiC particle from the polishing suspension.

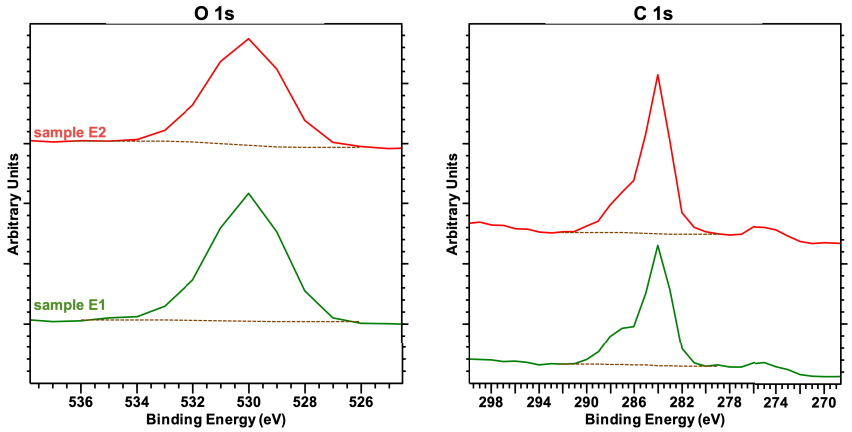

Fig. A 26 O 1s and C 1s photoemission spectra of sample E1 (green line) and sample E2 (red line); taken from the survey spectrum as a zoom of the sample E1 and E2.

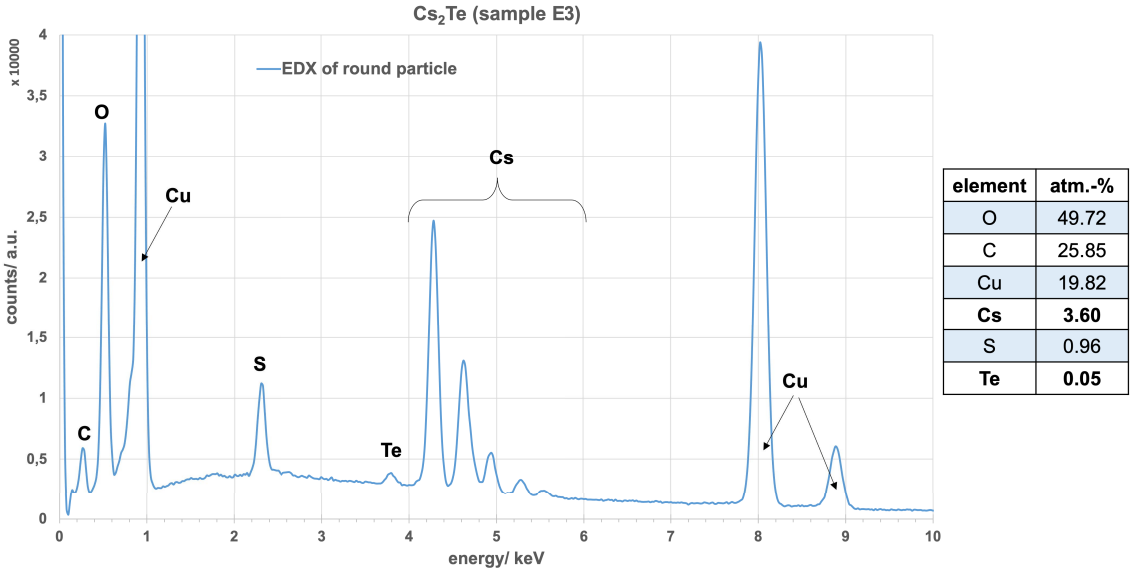

element	atm.-%
O	49.72
C	25.85
Cu	19.82
Cs	**3.60**
S	0.96
Te	**0.05**

Fig. A 27 *Ex-situ* EDX measurement; focussed on the particle on the Cs_2Te surface of sample E3; identifying the particle as a CsOH.

Erklärung

Die vorliegende Arbeit wurde am Institut für Strahlenphysik am Helmholtz Zentrum Dresden Rossendorf in der Zeit von Juni 2018 bis November 2022 unter der wissenschaftlichen Betreuung von Prof. Nikolai Gaponik und Dr. Rong Xiang angefertigt.

Versicherung

Hiermit versichere ich, dass ich die vorliegende Arbeit ohne zulässige Hilfe Dritter und ohne Benutzung anderer als der angegebenen Hilfsmittel angefertigt habe; die aus fremden Quellen direkt oder indirekt übernommenen Gedanken sind als solche kenntlich gemacht. Die Arbeit wurde bisher im Inland noch im Ausland in gleicher oder ähnlicher Form einer anderen Prüfungsbehörde vorgelegt.

Dresden, den 25.11.2022

Jana Schaber